Mesoporous Materials for Electrochemical Energy Conversion

by

Cüneyt Karakaya

A Dissertation Submitted to the
Graduate School of Sciences and Engineering
in Partial Fulfillment of the Requirements for
the Degree of

Doctor of Philosophy

in

Materials Science and Engineering

KOÇ ÜNİVERSİTESİ

October 1, 2021

Mesoporous Materials for Electrochemical Energy Conversion

Koç University

Graduate School of Sciences and Engineering

This is to certify that I have examined this copy of a doctoral dissertation by

Cüneyt Karakaya

and have found that it is complete and satisfactory in all respects, and that any and all revisions required by the final examining committee have been made.

Committee Members:

Assoc. Prof. Dr. Sarp Kaya (Advisor)

Prof. Dr. Havva Yağcı Acar

Assoc. Prof. Dr. Oktay Demircan

Prof. Dr. Can Erkey

Prof. Dr. Servet Turan

Date: 01.10.2021

ACKNOWLEDGMENTS

Foremost, I would like to express my deep gratitude to my supervisor Assoc. Prof. Dr. Sarp Kaya for his unlimited support, great scientific attitude, and enthusiasm which helped me a lot in completing my Ph.D. and widening my scientific view from different perspectives. I really admire and appreciate his patience and motivation while guiding me during my research.

My sincere thanks go to my thesis committee members; Prof. Dr. Havva Yağcı Acar, and Prof. Dr. Oktay Demircan for their useful comments and encouragement which helped me proceed in my research.

I would like to thank Turkish Petroleum Refineries Corporation (TÜPRAŞ) for the financial support for this study and its executives, Ersen Ertaş, R&D manager and İ. Serdar Kemaloğlu, assistant general manager.

I also appreciate my colleagues Dr. Cem Açıksarı and Dr. Serdar Çelebi for their useful comments and encouragement which helped me proceed in my research.

I would like to thank Prof. Dr. Servet Turan, Dr. Umut Savacı and Emre Keleş for their valuable collaborations.

In particular, I thank my fellow Navid Solati for helping in XPS and Raman measurements. In addition, I would like to thank Dr. Timuçin Balkan for his useful recommendations for my electrochemical experiments.

Last but not least, I would like to thank my wife for her support, care and patience, and my family for their endless love and encouragement from the distance which inspired me spiritually and helped me overcome the difficulties of being far from home during my Ph.D. period.

MESOPOROUS MATERIALS FOR ELECTROCHEMICAL ENERGY CONVERSION

Karakaya, Cüneyt

Ph.D., Materials Science and Engineering

Supervisor: Assoc. Prof. Dr. Sarp Kaya

October 2021, 140 Pages

Cheap, abundant, and easily manufactured electrocatalysts with high efficiency and stability are required for both hydrogen evolution reaction (HER) and oxygen evolution reaction (OER) to make renewable hydrogen production widespread. Transition metal chalcogenides and oxides have shown to be promising and versatile materials for catalyzing HER and OER in recent decades. Specifically, transition metal sulfides such as NiS_2 and MoS_2 offer great potential, their defective surface and edge site compositions, conductivities, and surface areas impose a significant effect on their electrochemical activities towards HER. On the other hand, mixed iron-nickel oxide based electrocatalysts have been intensively studied for OER. Engineering of abundant metal oxide/sulfide nanoparticles with a porous network by tuning the composition, structure, and morphology is highly promising to explore the most active and stable electrocatalyst. For this purpose, in this study, we developed a soft templating method to produce mesoporous nickel sulfides, mixed iron-nickel oxides, and molybdenum sulfide/oxide thin films. All synthesized materials were investigated by advanced characterization tools to identify their compositions, morphologies, and structures. Our soft templating method enables the production of mesoporous NiS_2, Ni_3S_2, NiS, Ni_7S_6, and mixed compositions by altering the starting precursor compositions. The performances of nickel sulfides were tested towards HER in both acidic and alkaline electrolytes. Electrochemical tests with tracking the samples by ex-situ advanced material characterization tools reveal that mesoporous nickel sulfides act as pre-catalyst that transforms into superior active sulfur deficient nickel sulfide with the collapse of the mesoporous structure under HER in an alkaline electrolyte. A similar observation was observed in electrochemical tests of mesoporous NiS_2 for OER. NiS_2 was converted to $Ni(OH)_2$ under a positive bias during OER. We synthesized the mesoporous $NiFeO_x$, $NiFe_2O_4$, and Fe_2O_3 thin films with tunable

compositions by changing the Ni/Fe precursors for OER in alkaline electrolytes. In the analysis of intrinsic activities, a peak in oxygen evolution activity was observed below %5 Fe content, leading to the formation of $NiFeO_x$, and it was noticed that futher Fe content decreases OER activity. The formation of $NiFe_2O_4$ slightly decreased OER activity, but mixed metal oxide was substantially more active than the pure NiO or Fe_2O_3. Fe impurities in KOH electrolyte electrochemical deposit on the electrocatalyst surface and enhance the OER activity of Ni-based electrocatalyst. With a cautious comparison of electrochemical tests results, Fe atoms in NiO lattice were found to boost OER activity substantially more compared to Fe deposition Ni-based metal oxide electrocatalyst. We also applied the soft templating strategy with minor modifications to produce mesoporous MoS_3-MoS_2-MoO_3 thin films for HER in acidic media. With ex-situ analysis of structure and activity, MoS_3 in the mesoporous framework was electrochemically reduced to more active MoS_2. Overall, the soft templating strategy is a facile and scalable fabrication method to develop a cheap and efficient electrocatalyst with an integrated film structure. In addition, the mesoporous structure of electrocatalysts provides insights into understanding structure-activity relation, changes in the surface composition or morphology, and durability of electrocatalysts owing to the high surface area with ultra-small crystal sizes.

Keywords: Hydrogen evolution reaction (HER), oxygen evolution reaction (OER), mesoporous, nickel sulfides, MoS_2, mixed iron-nickel oxide, pre-catalyst

ÖZETÇE

ELEKTROKİMYASAL ENERJİ DÖNÜŞÜMÜ İÇİN MEZO GÖZENEKLİ MALZEMELER

Karakaya, Cüneyt

Doktora, Malzeme Bilimi ve Mühendisliği Bölümü

Danışman: Doç. Prof. Sarp Kaya

Ekim 2021, 140 Sayfa

Yenilenebilir hidrojen üretimini yaygınlaştırmak için hem hidrojen oluşum reaksiyonu (HER) hem de oksijen oluşum reaksiyonu (OER) için ucuz, bol ve kolay üretilebilir, yüksek verimliliğe ve kararlılığa sahip elektrokatalizörlere ihtiyaç vardır. Geçiş metali kalkojenitler ve oksitlerin, son yıllarda HER ve OER'i katalize etmek için umut verici ve çok yönlü malzemeler olduğu gösterilmiştir. Özellikle, NiS_2 ve MoS_2 gibi geçiş metal sülfürleri büyük potansiyel sunar, kusurlu yüzey ve kenar bölgesi bileşimleri, iletkenlikleri ve yüzey alanları HER'e yönelik elektrokimyasal aktiviteleri üzerinde önemli bir etki yaratır. Öte yandan, OER için karışık demir-nikel oksit bazlı elektrokatalizörler yoğun olarak çalışılmıştır. Kompozisyon, yapı ve morfolojiyi ayarlayarak gözenekli bir ağ ile metal oksit/sülfür nanoparçacıklarının mühendisliği, en aktif ve kararlı elektrokatalizörü keşfetmek için oldukça umut vericidir. Bu amaçla, bu çalışmada, mezogözenekli nikel sülfürler, karışık demir-nikel oksitler ve molibden sülfür/oksit ince filmler üretmek için yumuşak bir kalıplama yöntemi geliştirdik. Sentezlenen tüm malzemeler; bileşimlerini, morfolojilerini ve yapılarını belirlemek için gelişmiş karakterizasyon araçlarıyla araştırıldı. Yumuşak şablonlama yöntemimiz, başlangıç bileşimlerini değiştirerek mezogözenekli NiS_2, Ni_3S_2, NiS, Ni_7S_6 ve karışık bileşimlerin üretilmesini sağladı. Nikel sülfürlerin performansları, hem asidik hem de alkali elektrolitlerde HER'e karşı test edildi. Gelişmiş malzeme karakterizasyon araçlarıyla numunelerin izlenmesiyle yapılan elektrokimyasal testler, mezogözenekli nikel sülfürlerin, alkali elektrolitte HER altında mezogözenekli yapının çökmesi ile üstün aktif kükürt eksikliği olan nikel sülfüre dönüşen ön katalizör görevi gördüğünü ortaya koymaktadır. Benzer bir gözlem, OER için mezo gözenekli NiS_2'nin elektrokimyasal

testlerinde gözlendi. NiS_2, OER sırasında pozitif voltaj altında $Ni(OH)_2$'ye dönüştürüldü. Alkali elektrolitlerde OER için Ni/Fe başlangıç oranları değiştirerek mezogözenekli $NiFeO_x$, $NiFe_2O_4$ ve Fe_2O_3 ince filmleri ayarlanabilir bileşimlerle sentezledik. Elektrotların aktivitelerin analizinde, oksijen oluşumu aktivitesinde $NiFeO_x$ oluşumuna sebep olan %5 Fe içeriğinin altında en yüksek performans gözlemlendi, ve Fe içeriğinin artmasıyla OER aktivitesinin azaldığı tespit edildi. $NiFe_2O_4$ oluşumu, OER aktivitesini azalttı, ancak karışık metal oksit, saf faz NiO veya Fe_2O_3'ten önemli ölçüde daha aktiftir. Elektrokatalizör yüzeyinde KOH elektrolitinden gelen Fe safsızlıkların depolandığı ve Ni bazlı elektrokatalizörün OER aktivitesini arttırdığı anlaşıldı. Elektrokimyasal test sonuçlarının dikkatli bir şekilde karşılaştırılmasıyla, NiO kristallerindeki Fe atomlarının, Fe kaplanan Ni bazlı metal oksit elektrokatalizörüne kıyasla OER aktivitesini önemli ölçüde artırdığı bulundu. Ayrıca asidik ortamda HER için mezogözenekli MoS_3-MoS_2-MoO_3 ince filmler üretmek için küçük modifikasyonlarla yumuşak şablonlama stratejisini uyguladık. Test sonrası yapı ve aktivite analizi ile, mezo gözenekli yapıdaki MoS_3, elektrokimyasal olarak daha aktif MoS_2'ye indirgendi. Genel olarak, yumuşak şablonlama stratejisi, entegre bir film yapısına sahip ucuz ve verimli bir elektrokatalizör geliştirmek için kolay ve ölçeklenebilir bir üretim yöntemidir. Ek olarak, elektrokatalizörlerin mezogözenekli yapısı, yapı-aktivite ilişkisini, yüzey bileşimindeki veya morfolojisindeki değişiklikleri ve ultra küçük kristal boyutlarına sahip yüksek yüzey alanı nedeniyle elektrokatalizörlerin dayanıklılığını anlama konusunda fikir verir.

Anahtar Kelimeler: Hidrojen oluşturma reaksiyonu (HER), oksijen oluşturma reaksiyonu (OER), mezogözenekli, nikel sülfürler, MoS_2, karışık demir nikel oksit, ön katalizör

TABLE OF CONTENTS

LIST OF FIGURES

LIST OF TABLES

1 INTRODUCTION

1.1 Motivation

Molecular hydrogen, H_2, is a critical chemical reagent, essential for various branches of industry. Around 75 million tons of hydrogen are produced from dedicated sources annually worldwide. In crude oil refining, fertilizer production, and methanol plants, hydrogen is consumed as a feedstock [1]. In crude oil refining, molecular hydrogen is used for hydrotreating of various refinery streams and hydrocracking of heavy products [2]. In the fertilizer industry, hydrogen is reacted with nitrogen to produce ammonia by the Haber-Bosch process, and ammonia is later converted into several types of fertilizers [3]. Hydrogen can also be reacted with CO and CO_2 to produce methanol in a catalytic reaction [4]. Approximately 95% of the hydrogen is produced by steam reforming from methane, oil, or coal, and the largest fraction comes from steam reforming of natural gas [5].

Hydrogen can be categorized according to the CO_2 balance such as gray, blue, and green based on public discussions [6]. For example, natural gas is converted at high temperature (> 700 ^oC) into CO_2 and 'gray' hydrogen leading to CO_2 emission at a rate up to 10 kg of CO_2 per kg H_2 [6]. If produced CO_2 is captured and stored or utilized (CCS or CCU), 'gray' hydrogen becomes 'blue' hydrogen [7]. However, the carbon capture rate is currently at a maximum of up to 90 %. Green hydrogen is produced by electrolysis of water, where water is electrochemically split into hydrogen and oxygen by an electric current and with the help of an electrolyte. If the electricity required for electrolysis comes exclusively from renewable, the entire production process is completely CO_2-free.

CO_2 emissions have accelerated during the 20^{th} century, rising to about 37 Gt per the year 2019, with global CO_2 atmospheric concentration reaching 415 ppm [8]. At current emissions levels, the remaining carbon budget to keep global warming below the +1.5 °C target could be exhausted in 10 years, which would have dramatic consequences on ecosystems and societies. Most greenhouse (GHF) emissions come from the production and transport of energy (about 40 %, including electricity and heat production, industry (23%), buildings (21%), and transport (16%) [9]. Hydrogen provides multiple pathways to reduce GHG emissions in these sectors and could address about half of their GHG emissions if produced, stored, and carried cleanly.

Hydrogen can be used either as a feedstock for various industrial and chemical processes. In steelmaking, hydrogen can work as a direct reducing agent, substituting for coal-based blast furnaces [10]. Grey hydrogen in the current production of methanol, ammonia, and liquid fuels could be replaced by green hydrogen with no changes in equipment or technology, eliminating the CO_2 emissions associated with the production of grey hydrogen. Hydrogen is also used to produce methane, synthetic naphtha, kerosene, and petrochemical feedstock such as olefin by using CO_2 captured from the air or emissions streams [11].

Hydrogen can be burned to release heat or converted into electricity using fuel cells. Therefore, hydrogen offers a broad range of applications for mobility services, especially trucks, buses, ships, trains, large cars, and commercial vehicles, where the performance of batteries is limited [12]. Hydrogen has a high gravimetric energy density of 120 MJ/kg and can be stored under multiple forms such as gaseous, liquid, or converted to other molecules (synthetic methane, synthetic liquid fuels, ammonia, and methanol) [13]. Therefore, hydrogen can be utilized as an intermediary vector between the energy systems (electric grid, gas grid, transportation, and industries) and intermittent renewable energy sources (wind and solar) [14].

Recent technological developments and mass production in wind turbines and photovoltaics have decreased renewable energy costs substantially in the last decades [15]. Electrolysis was the first H_2 production technology deployed but was overtaken by fossil fuel-based technologies in the early 1970s. With the continuously decreasing renewable electricity cost, the production of green hydrogen is increasingly economically attractive and has become a critical key to reach the net-zero target. IRENA Pathway claims that, by 2050, 30% of electricity use will be dedicated to green hydrogen production and its derivatives such as methanol and ammonia [16]. To achieve this, almost 5 000 GW of electrolyzer must be deployed by 2050. Therefore, all technical and economic barriers to electrolysis technologies must be overcome in order to make electrolyzers viable for widespread implementation.

1.2 Electrolysis of water

Several reviews of the electrolysis of water have been published elsewhere [17]–[20]. Here, we briefly describe the fundamentals and focus points of electrolysis of water relevant to this dissertation.

Electrolysis is done in an electrolysis cell that contains two electrically conductive electrodes (cathode and anode) separated by an electrolyte. The reaction and associated mechanisms depend on the pH of the electrolyte. In the alkaline type, a porous inorganic diaphragm (also called a separator) which is permeable to the OH^- ions, physically separates the electrodes and formed hydrogen and oxygen gases. In proton exchange membrane (PEM) electrolyzers, the electrodes are separated by an electron-insulating solid membrane, which is responsible for transporting H^+ ions from one electrode to the other and at the same time physically separating gases. For both systems, the hydrogen evolution reaction (HER) at the cathode and the oxygen evolution reaction (OER) at the anode take place [17], [20]. Water splitting occurs in acidic and alkaline media according to the reactions listed in Table 1.1.

Table 1.1 Hydrogen and oxygen evolution reactions for both acidic and alkaline media [21]

Acidic	Anode	: $2H_2O\ (l) \rightarrow\ 4H^+ +\ O_2\ (g) +\ 4e^-$
	Cathode	: $4H^+ +\ 4e^- \rightarrow 2H_2(g)$
	Overall reaction	: $2H_2O\ (l) \rightarrow\ 2H_2\ (g) + O_2\ (g)$
Alkaline	Anode	: $4OH^- \rightarrow\ 4H_2O +\ O_2\ (g) +\ 4e^-$
	Cathode	: $4H_2O +\ 4e^- \rightarrow H_2(g) + 4OH^-$
	Overall reaction	: $2H_2O\ (l) \rightarrow\ 2H_2\ (g) +\ O_2\ (g)$

The overall reactions in both alkaline and acidic media require a minimum energy input of ΔG = 237.1 kJ/mol at standard conditions corresponding to a standard voltage requirement of E =1.23 V [17]. The required voltage is much larger due to kinetic and transport limitations [17], [20].

The HER and OER proceed through reactive intermediates adsorbed at the cathode and anode surfaces, respectively. The electronic structure and atomic-scale morphology of the catalyst surface determine the strength of the interaction between

adsorbate and surface, and thus, accelerates or slows down the reaction rates. According to the Sabatier Principle, the case in which reactive intermediates neither too weakly nor too strongly bind to the surface is the most active for the electrochemical reaction [22], [23].

There are two plausible processes for HER mechanism in both acid and alkaline media: Volmer-Heyrovsky and Volmer-Tafel [19]. In acidic media, proton takes role itself, as a water molecule is a source of proton in alkaline media. In the Volmer step, proton adsorbs on the electrode surface regardless of the pH of the solution. Reaction further proceeds through either Tafel or Heyrovsky step. In the Tafel step, two adjacent protons adsorbed on the electrode surface react and form molecular hydrogen gas. In Heyrovsky step, another proton adsorbs by the adsorbed proton on the electrode and form molecular hydrogen. The Volmer-Tafel process is more favorable compared to the Volmer-Heyrovsky process. Proposed reaction steps are also indicated in Table 1.2.

Table 1.2 Processes of the mechanism during hydrogen evolution reaction

	Acidic	Alkaline media
Volmer	$H^+ + e^- \leftrightarrow H_{ads}$	$H_2O + e^- \leftrightarrow H_{ads} + OH^-$
Heyrovsky	$H_{ads} + H^+ + e^- \leftrightarrow H_2(g)$	$H_{ads} + H_2O + e^- \leftrightarrow H_2(g) + OH^-$
Tafel	$H_{ads} + H_{ads} \leftrightarrow H_2(g)$	$H_{ads} + H_{ads} \leftrightarrow H_2(g)$
	$\mathbf{2H^+ + e^- \leftrightarrow H_2(g)}$	$\mathbf{2H_2O + 2e^- \leftrightarrow H_2(g) + 2OH^-}$

The four-electron/proton transfer steps are widely accepted in both acidic and alkaline media for the OER mechanism [17]. However, the OER mechanism differs according to pH. Under acidic conditions,H_2O is oxidized, and electron and proton pairs andO_2 are formed. In contrast, under alkaline conditions, OH^- is oxidized to H_2O and O_2 with the formation of an electron. The bonding between intermediates (MOH, MO, and MOOH) and reactants (H_2O or OH^-) are crucial for the efficiency of OER. Proposed reaction steps are also indicated in Table 1.3.

Table 1.3 Processes of the mechanism during OER

Acidic	Alkaline media
$M + H_2O \leftrightarrow MOH + H^+ + e^-$	$M + OH^- \leftrightarrow MOH + H^+$
$MOH \leftrightarrow MO + H^+ + e^-$	$MOH + OH^- \leftrightarrow MO + H_2O + e^-$

$MO + H_2O \leftrightarrow MOOH + H^+ + e^-$	$MO + OH^- \leftrightarrow MOOH + e^-$
$MOOH \leftrightarrow M + O_2(g) + H^+ + e^-$	$MOOH + OH^- \leftrightarrow M + H_2O + e^-$
Total: $2\,H_2O \leftrightarrow O_2(g) + 4H^+ + 4e^-$	**Total: $4OH^- \leftrightarrow O_2(g) + 2H_2O + 4e^-$**

1.3 Ideal Electrocatalyst for a Water splitting

Platinum group metal electrocatalysts (Pt, Ru, Rh, Ir, and Pd) are the best known HER electrocatalysts regarding almost zero Gibbs free energy of adsorbed atomic hydrogen on their metallic sites [18]. Among them, Pt is used as a benchmark for the comparison of activities of other HER electrocatalysts. Nanostructured Pt on conductive support, generally carbon, is also one of the strategies to reduce the amount of Pt, as seen in commercial PEM electrolyzers [24]. Unfortunately, the widespread applications of PGM catalysts are limited by their high cost and scarcity.

Ni-based metal electrodes are a common choice in alkaline electrolyzers as cathodes for hydrogen evolution owing to their low cost and durability at alkaline media, 25 % KOH solution [25]. However, Ni usually suffers from the insufficient electrocatalytic activity and more importantly, progressive decay in the activity of HER upon continuous alkaline electrolysis because of reversible formation of inactive nickel hydride on the Ni surface [26].

Next-generation HER electrocatalysts are being researched intensively to fulfill some specifications such as being inexpensive, abundant, durable, and efficient for both alkaline and PEM electrolyzers [18], [20]. Substantial research effort has been devoted to investigating the HER activity of transition metal sulfides, selenides, nitrides, phosphides, and carbides to eliminate the problem discussed above [27].

The OER is often regarded as the main bottleneck in water splitting due to its slow kinetics of multiple reaction steps, as discussed above. RuO_2 and IrO_2 are commonly used to benchmark for OER electrocatalysts owing to their high electrocatalytic activities and corrosion stabilities in both acidic and alkaline solutions [28]. Unfortunately, the widespread applications of those two catalysts are limited by their high cost and scarcity. Because electrocatalysts must also be stable under acidic operating conditions, there has been no candidate except these two, RuO_2 and IrO_2 as the OER catalyst of PEM electrolyzer [29].

Ni-based metal electrodes are used instead of RuO_2 and IrO_2 in alkaline electrolyzers as anode for OER owing to their low cost and durability at alkaline media [25]. Comprehensive researches have been focused on investigating the OER activity of transition metal oxide catalysts, and various metal oxide families such as perovskite, spinels, and the layer structure type-family in order to increase activity toward OER [30].

Electrode fabrication always needs the tedious film casting or coating procedure with ion-conductive polymeric binders and extra conductive additives [31]–[33]. Usage of ion-conductive has risks that polymer can cover the active surface area of the electrocatalyst and interfere with the contact with conductive support. Electrocatalytically inactive conductive additive with a polymeric binder can limit electrochemical active surface area. Furthermore, continuous hydrogen and oxygen gas evolution cause the coated catalysts to peel off from electrodes, which adversely affects their catalytic activity and lifetime. The one-step production protocol enabling 3-D integrated porous structure without post-coating process does not require nonconductive organic binders. This can ensure good electron conductivity and support the high mechanical stability of catalysts for long-term and cyclic use. Appropriate porous structure also fastens the reactions on the electrode by easy electrolyte penetration, diffusion of ions (e.g. OH^-, H^+) through electroactive sites, and rapid release of reaction products [33].

1.4 Mesoporous Inorganic Materials

Porous materials can be classified according to their pore size: microporous (≤ 2 nm), mesoporous (2-50 nm), and macroporous materials (≥50 nm) [34]. The first known example of mesoporous inorganic material, M41S family (MCM-41, MCM-48, and MCM-50), is discovered by Kresge et. al. in Mobil Oil Company [35]. M41S family has a silica framework, synthesized by self-assembly of surfactant, above its critical micelle concentration (CMC), and silica precursors in an acidic or basic aqueous media. The other types of mesoporous silica materials with having various pore sizes, morphology, surface area, and wall thickness were synthesized by changing surfactant hydrophobic and hydrophobic lengths, solvent, and type of silica and surfactant type such as SBA family [36]–[38]. Since then, mesoporous materials have been intensively studied to discover advanced energy materials with high surface area, accordingly more active sites, for applications such as green energy, energy storage, batteries, and catalysts [39]–[42].

SBA and M41S families are in powder forms due to the nature of their synthesis protocols in which dilute concentrations of silica precursor and surfactant are used. Later, Attard and coworkers introduced a novel method that uses the liquid crystalline region of a surfactant rather than CMC and a higher concentration of silica precursor in order to obtain silica monoliths [43]. Thin-film technologies of mesoporous materials had become critical for many applications such as sensors, electrocatalysts, and solar cells [44]–[48]. In this aspect, Brinker and coworkers have introduced, for the first time, the evaporation induced self-assembly (EISA) method to create the ordered mesoporous silica thin films by controlling the self-assembly of surfactant and inorganic precursor with an oriented replica of liquid crystal template [49].

Surfactant templating methods were extended to obtain non-siliceous mesoporous materials (known as soft templating) and also rationally designed mesoporous silica thin films, powders and monoliths have been used as a template to produce non-siliceous mesoporous materials (known as nanocasting or hard-templating) [50]–[53]. The electrodes showing outstanding performance and durability for both HER and OER can be generated by utilizing either hard or soft templating methods.

1.5 Mesoporous Metal Oxides via Hard Templating Method

Hard templating is based on a casting process that results in the negative replica of the template materials [51]. That's why it is also named as 'nanocasting' in the literature. The hard templating method for providing ordered mesoporous metal oxides usually uses ordered mesoporous silica and carbon as the hard template for providing ordered mesoporous metal oxides. The precursor of the target material is tried to fill all voids in the mesoporous structure. The precursor of target material in the mesoporous template is converted to the metal oxide by calcination to replicate the shape of pores of the template. The silica template is lastly etched by HF and highly concentrated NaOH/KOH solutions to obtain the final mesoporous metal oxide [51], [52]. Schematic illustration of nanocasting is indicated in Figure 1.1.

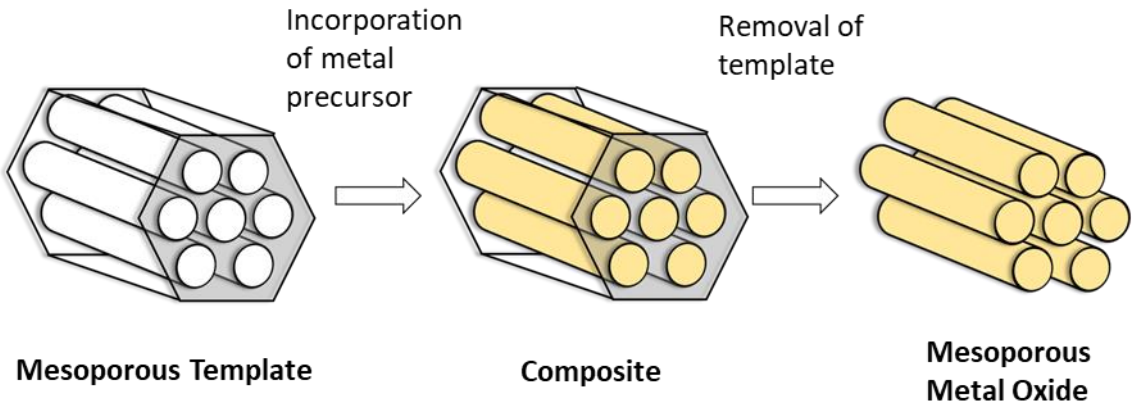

Figure 1.1 Schematic illustration of nanocasting method by using hexagonal mesoporous silica as a template.

The first example of mesoporous transition metal oxides via nanocasting was the mesoporous Cr_2O_4 developed by Zhu *et al.* in 2003 [54]. Since then, many mesoporous metal oxides and mixed oxides were developed by using hard templating [55], [56]. A major drawback in the synthesis of mesoporous metal oxides using the hard templating method is the large volume difference between the common metal precursors (i.e., nitrate salts) and their oxide form upon the calcination process. Up to 90% contraction in volume makes creates isolated small islands instead of interconnected networks. Therefore, the hard templating method is not suitable for preparing thin-film transition metal oxide electrocatalyst on any conductive support.

1.6 Mesoporous Metal Oxides via Soft Templating Method

As discussed above, surfactant templating can be applied for the synthesis of mesoporous powders, monoliths, and thin films. Herein, we will discuss liquid crystalline templating methods in detail. The surfactant molecules that consist of hydrophobic and hydrophilic groups above critical micelle concentration, assemble into a micelle. At higher concentrations, micelles start to aggregate and then form a lyotropic liquid crystals (LLC) mesophase. The structure depends strongly on the concentration of solvent as well as temperature. The main LLC mesophases are lamellar (surfactant bilayers separated by aqueous layers), hexagonal (hexagonal arrangement of cylindrical micelles), and cubic structures. Incorporation of metal oxide precursor into solvent can place between micelle groups. This LLC mesophase is utilized as a structure-directing agent to form mesoporous materials. Schematic illustration of the LLC templating method is indicated in Figure 1.2.

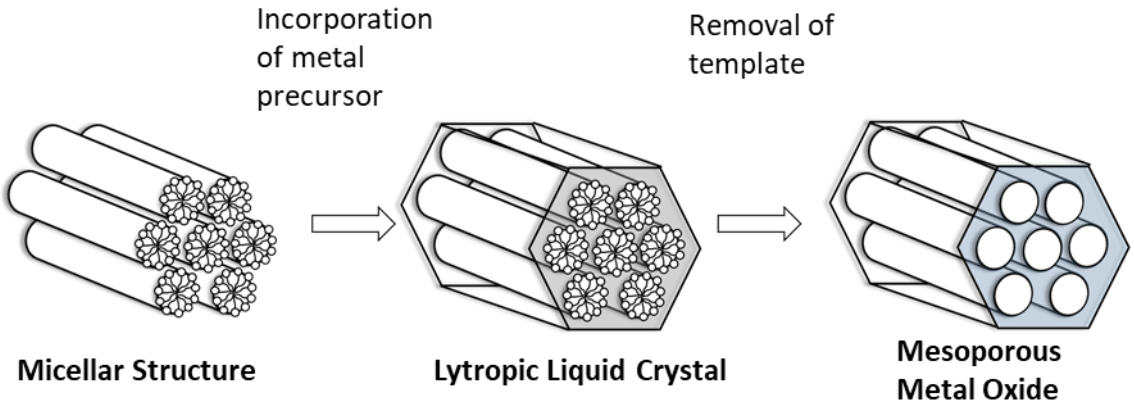

Figure 1.2 Schematic illustration of soft templating method.

In the first example of synthesized mesoporous silica, sodium and tetranethylamonnium silicate were used as an inorganic metal precursor with lyotropic liquid phase of quaternary ammonium surfactant with water [57]. Mesoporous non-siliceous metal oxides, including TiO_2, ZrO_2, Al_2O_3, Nb_2O_5, Ta_2O_5, WO_3, HfO_2, SnO_2, and their mixed oxides were synthesized by using amphiphilic poly(alkylene oxide) block copolymers as structure-directing agents with their transition metal chloride (i.e. $TiCl_4$) in non-aqueous solutions [58]. Dip coating of the sol was applied to prepare transparent thin films after removal of surfactant via calcination at 400 ^oC for 5 h in air.

The evaporation of the volatile compounds during dip-coating starting from dilute solution forms a well-ordered gel-like mesostructure. Spray and spin coating show the same mechanism. While surfactants form micelles, inorganic species locate among the micelles. The semi-crystalline or non-crystalline structure of desired metal oxide is formed by hydrolysis and condensation reaction. Therefore, this method is called EISA [49].

Controlled condensation of metal oxide is very critical to form a mesostructured framework. The condensation of transition metal chlorides, MCl_4, could be controlled at slow rate due to the formation of stable chloroalkoxy complexes of metals in the presence of hydrochloric acid with ethanol. Metal alkoxides ($M(OR)_4$, i.e. $Si(OMe)_4$, $Ti(OBu)_4$, (where Me: Methyl and Bu: Butyl) are hydrolyzed into MOH_4 in a controlled manner with aid of tuning the acid content of the solvent of alcohol [59]. The use of them in liquid

templating shows better control on the condensation reaction. After condensation, the surfactant template can be removed by chemical and thermal methods according to desired properties of mesoporous metal oxide.

1.7 Molten Salt Assisted Self Assembly (MASA)

The liquid templating method with the incorporation of alkoxides cannot be applied for all transition metal oxides because of the lack of their alkoxides. For instance, Ni, Co, Zn, Cd, and Fe are in the form of salts, such as nitrates, chlorides, and sulfates. Hydrolysis and condensation reactions do not take place in the assemble of mesophase because of the formation of stable solutions in various solvents. Decomposition of metal salts into metal oxides can rigidify the mesostructured framework upon calcination if surfactant assembly holds the mesophase at moderate calcination temperatures.

A novel LLC method, molten salt self-assembly (MASA) was discovered, for the fabrication of mesoporous silica-CdO and silica-ZnO composite thin films [60]. They used the aqueous solution in which consists of two surfactants, one of them is charged, cetylammonium bromide (CTABr), and the other one is nonionic, oligo (ethylene oxide), silica precursor, (tetraetylene orthosilicate (TEOS), and Zn nitrate or Cd nitrate. After evaporation of water via spin and spray coating, hydrolyzed silica precursor and transition metal oxide precursor with these two surfactants forms mesophase. Upon controlled calcination starting from room temperature to 450 ^{o}C, condensation of silica rigidifies the mesoporous framework and metal nitrates decomposes into metal oxide flakes over the silica framework. By changing the surfactant/metal salt ratio, the porosity and thickness of the metal oxide in the mesoporous framework were tuned in this study.

Later, they discovered that mesoporous $LiCoO_2$, $LiMn_2O_4$, and mixed $LiMn_{2-x}Co_xO_4$ have been fabricated without using titania or silica precursor as a rigidifying agent [61]. Upon calcination, the anionic part of metal nitrates salts can be easily started to decompose at low temperature, above 90 ^{o}C, where surfactant assembly can stand at higher temperatures, up to 200 ^{o}C without decomposition. By using this property, transition metal oxide moiety can rigidify among the surfactant domains, and further increase in calcination temperature can provide the removal of surfactant domains and form mesopores.

MASA process is strongly dependent on the robust and stable LLC phase of transition metal salts and surfactants. In 2001, Dag et al. showed Cd, Zn, and Co nitrate

salt could make cubic and hexagonal lyotropic liquid mesophase with non-ionic surfactant [62]. With the addition of a second surfactant, which is anionic or cationic, the amount of transition metal salt among the surfactant domains is increased as keeping mesophase stable [63]. The function of charged surfactant is to balance the total charge of the interface between surfactant domains and metal salt species among those surfactant domains. As indicated in Figure 1.3-a, the metal salt is confined in a very narrow space, 2-3 nm. The high surface area of confined salt species neutralized by charged surfactant shows a lower melting point compared to the bulk state, even liquid or molten below 0 ^{o}C. The stable lyotropic liquid mesophase with two surfactants and various transition metal nitrate have been converted to mesoporous $MnCo_2O_4$, $NiCo_2O_4$ $LiMn_2O_4$, $ZnCo_2O_4$ and NiO for many applications [61], [64]–[66]. The general MASA method is described as Figure 1.3-b. In this thesis, the fundamentals of MASA were used to develop the mesoporous metal oxide and sulfide thin films.

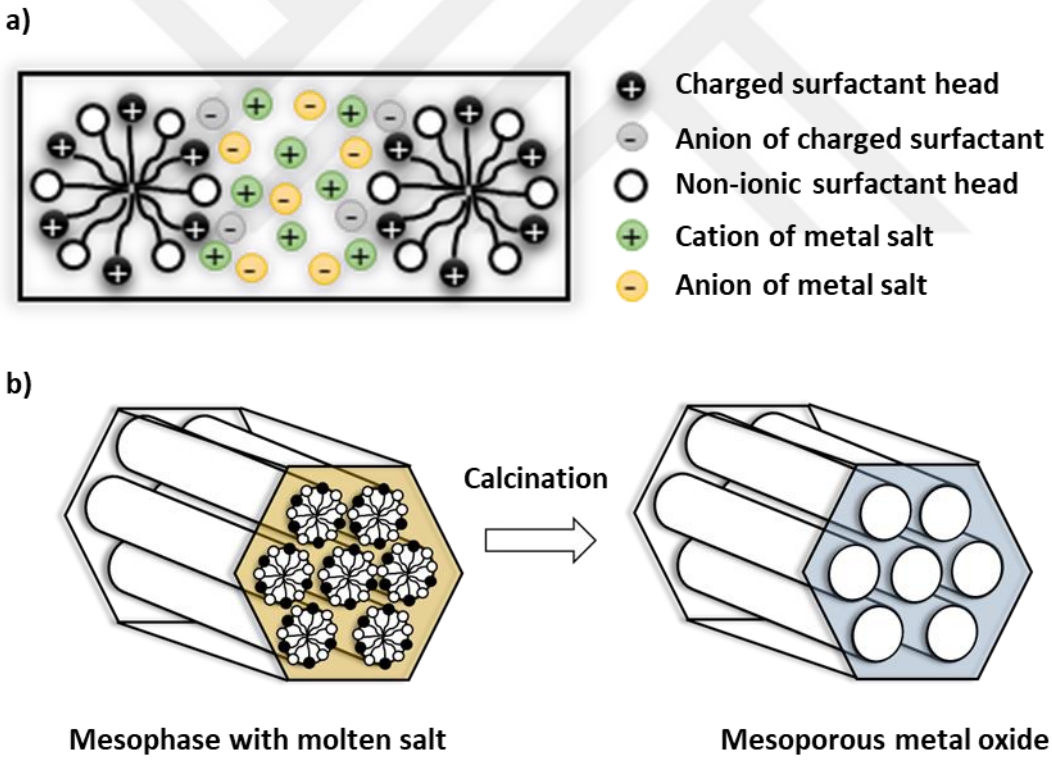

Figure 1.3 a) Schematic illustrations of mesophase of two surfactants and metal salt. b) MASA method

1.8 Mesoporous Metal Sulfides

Mesoporous transition metal sulfides have attracted great attention owing to their superior performance as catalysts, electrodes, and photocatalytic materials [67]–[71]. As discussed in the synthesis of mesoporous metal oxide via hard templating, the same strategy was applied for the synthesis of mesoporous metal sulfides such as FeS_2, CoS_2, NiS_2, WS_2, and MoS_2.[72], [73] Two kind of hard templating method was applied to obtain mesoporous metal sulfides. Metal nitrates in mesoporous silica are converted to interconnected metal oxide composite by calcination and then reacted with H_2S to obtain its metal sulfide form. On the other hand, metal nitrates in mesoporous silica are directly reacted with H_2S to obtain its metal sulfide form. In both strategies, the silica framework is removed by etching HF or concentrated KOH solution. Schematic illustrations of two strategies are depicted in Figure 1.4.

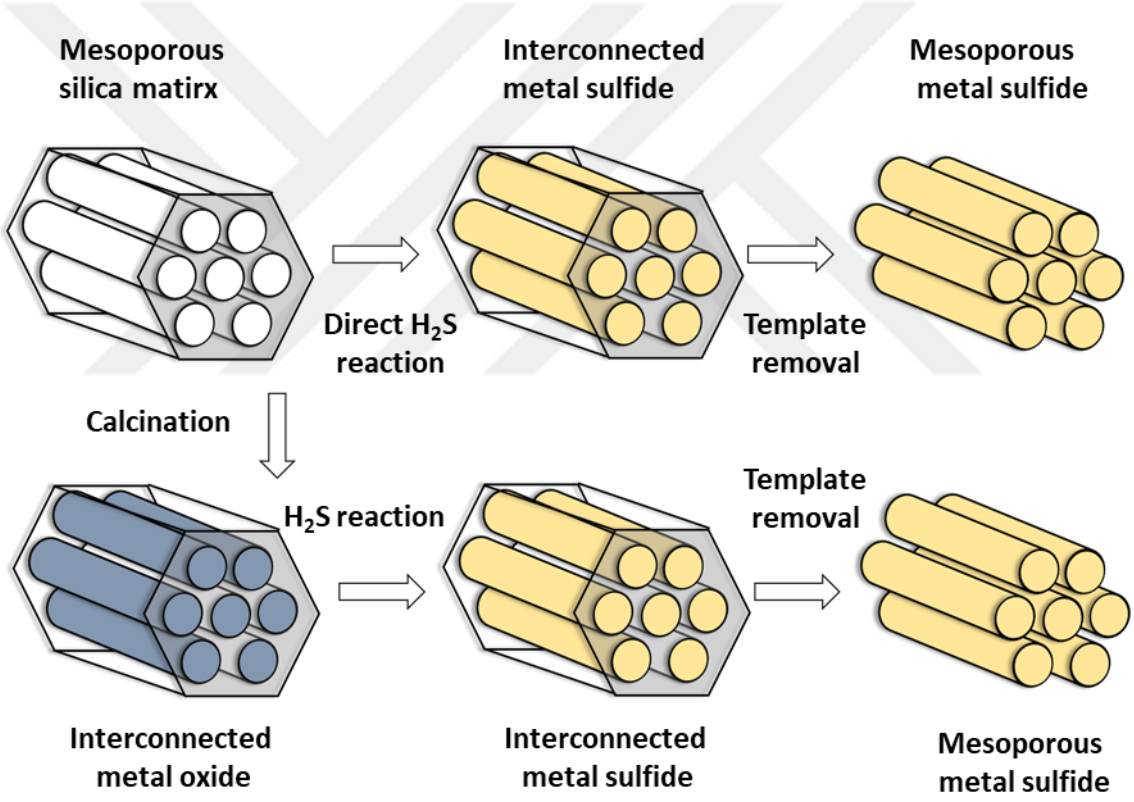

Figure 1.4 Schematic illustration of nanocasting method form mesoporous metal sulfides

Likewise, in the hard templating method for mesoporous metal oxides, the volume contradiction of metal precursor after conversion from metal oxide to sulfide or direct conversion into metal sulfide outcome the disconnected mesoporous metal sulfide powders, even if thin-film silica template is used. Only electrodeposition of metal

precursor into mesoporous silica was able to fill all pores without disconnection along with porous media [74]. However, all nanocasting method has long-lasting multi-steps that take 1-7 days to obtain final products. Dag et. al. also showed that mesoporous silica-CdO and ZnO thin films prepared by MASA method were easily converted into mesoporous silica-CdS and ZnS films in an H_2S environment [75]. With the aid of dilute HF solution, silica was etched and mesoporous CdS and ZnS thin films consist of weakly connected and nanoflakes were formed. Another disadvantage could be the corrosion of metal sulfides during the removal of the silica template.

The other method to produce mesoporous transition metal sulfides is the oxide-to-sulfide conversion strategy. Suib *et. al.* introduced that amorphous mesoporous Fe_2O_3 prepared by surfactant templating sol-gel method can be converted into mesoporous FeS_2 in an H_2S environment [68]. This was also a two-step protocol consuming time and enabling only mesoporous FeS_2 powders samples without risk of corrosion. Tolbert *et. al.* showed that mesoporous MoS_2 thin film samples were synthesized by thermal sulfurization of mesoporous MoO_2 thin film prepared by the EISA method [76]. However, produced mesoporous MoS_2 thin film has thicker walls, about 85 nm with 5 nm pore size, lead to a low accessible surface. The gas-phase oxide-to-sulfide conversion process typically requires a long reaction time under a highly poisonous H_2S atmosphere.

Synthesis of mesoporous metal sulfide by soft templating is still very challenging due to the uncontrollable fast precipitation process between metal salts and the S_2^- ions. Early examples of the soft templating method were prepared ordered mesostructures composed of CdS and ZnS materials using nonionic surfactant as a structure-directing agent [77], [78]. However, other transition-metal sulfides (e.g., CoS, NiS) is a lot more challenging due to the uncontrollable precipitation speed between metal salts and the S^{2-} ions and low affinity between metal salts. Yamuchi showed that diblock copolymer polystyrene-block-poly(acrylic acid) (PS-b-PAA) templates could be used to direct the assembly of Co nitrate, phosphomolybdic acid hydrate, and dithiooxamide as sulfur precursor at room temperature [79]. After annealing in N_2 environment, $MoS_2/CoMoS_2$ mesoporous powder containing an interconnected network of pores was obtained. However, a very expensive PS-b-PAA polymer was used and this method enables only powder samples.

1.9 Aim of the Study

This study aims to develop a one-step protocol enabling mesoporous metal sulfide and oxide thin films and investigate their electrochemical activity towards HER and OER. The protocol for mesoporous sulfide offers a novel understanding of the soft templating method to the literature. The durability of developed electrocatalysts is investigated in detail towards HER and OER by combining electrochemical tests and structural characterizations after and before various performance tests of HER and OER.

The outline of the thesis is as follows:

Chapter 2 –Methodology is given to have a basic theory about the instruments used for characterization and electrochemical activity tests. First, the theoretical background of characterization instruments was introduced. Final, the theoretical background for electrochemical activity tests was explained.

Chapter 3 –Synthesis of mesoporous NiS_2 thin films describes the optimization of soft templating method for mesoporous nickel sulfides.

Chapter 4 –Mesoporous nickel sulfides thin films for a hydrogen evolution reaction describes the performance and durability of meseporous nickel sulfides in different phases toward HER in both alkaline and acidic electrolyte.

Chapter 5 –Mesoporous thin films for an oxygen evolution reaction describes the performance and durability of meseporous NiS_2 and iron nickel oxides in different phases toward OER in alkaline electrolyte.

Chapter 6 –Mesoporous MoS_2 thin films describes the optimization of soft templating method for mesoporous MoS_2, and their performance and durability toward HER in acidic electrolyte.

2 METHODOLOGY

2.1 Characterization Techniques

2.1.1 X-ray Diffraction (XRD)

X-ray diffraction is a common technique for the determination of crystal structures and atomic spacing. The interatomic distances in crystals and molecules between 0.15 and 0.4 nm corresponding to the electromagnetic spectrum with the wavelength of x-rays having photon energies between 3 and 8 keV. X-ray diffraction is relying on constructive interference of monochromatic X-rays and an ordered crystal structure. Monochromatic X-rays are directed toward the sample. Only X-rays that obey Bragg's Law ($n\lambda=2d \sin \theta$) undergo constructive interference with the sample. This law relates the wavelength of X-ray to the diffraction angle and the lattice spacing of crystals or long-range orderly periodic arrangements, see Figure 2.1.

In this thesis, we explored the LLC mesophases arrangement as in Figure 2.1b and the crystal structures of the final materials obtained as in Figure 2.1a, such as mesoporous nickel sulfides and NiFeoxides by using XRD.

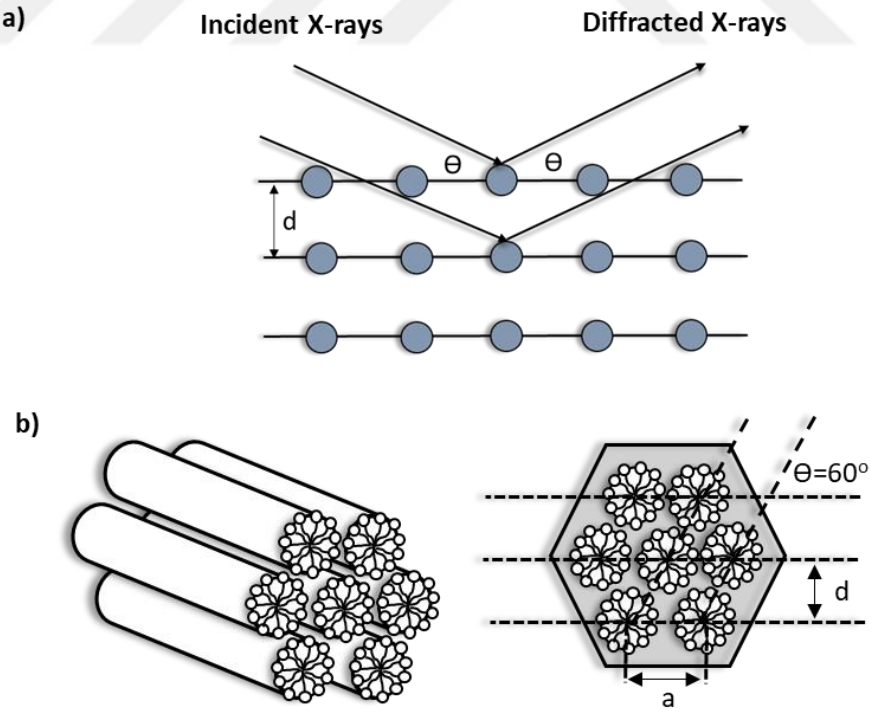

Figure 2.1 The Schematic illustration of how Braggs law work in a crystal (a) and a hexagonally ordered LLC mesophase (b).

2.1.2 Fourier Transform Infrared Spectroscopy (FT-IR)

FT-IR spectroscopy is a powerful tool for identifying organic and inorganics compounds because, except for a few homonuclear molecules such as CO_2, N_2 and Cl_2, all molecular species absorb light in the infrared region. Infrared spectroscopy offers the potential for determining an unusually large number of substances because each molecular species has a unique infrared absorption spectrum.

The energy of infrared radiation can excite vibrational and rotational transitions, but it is not enough to excite electronic transitions. Therefore, it is one of the harmless characterization tools. In addition, infrared absorption occurs not only with organic molecules but also with covalently bonded inorganics, which are generally active in the longer wavelength of the infrared region.

In this thesis, FT-IR spectroscopy was used for the optimization of the development of mesoporous materials such as the analysis of the lyotropic liquid crystalline mesophase, the surface purity of the obtained final materials, tracking the decomposition or calcination of surfactants after thermal treatments.

2.1.3 Scanning Electron Microscopy (SEM), Transmission Electron Microscopy (TEM), Scanning Transmission Electron Microscopy (STEM), and Energy Dispersive X-ray Spectroscopy (EDS)

The scanning electron microscope (SEM) produces images by scanning the sample with a high-energy beam of electrons. The electrons interact with matter in number ways as seen Figure 2.2. SEM uses secondary and backscattered electrons to create the visual images of the sample. These electrons are counted by several detectors to form signals. When the electron beam strikes the specimen, it penetrates the sample to a depth of a few microns, depending on the energy of electron beam and the density of the sample. Many signals, like secondary electrons and X-rays, are produced as a result of this interaction inside the sample.

The maximum resolution obtained in an SEM depends on multiple factors, like the electron spot size, types of used dedectors, conductivity of the specimen and interaction volume of the electron beam with the specimen. With technological

developments, new brands of SEMs can reach the resolution below 1 nm but not atomic resolution.

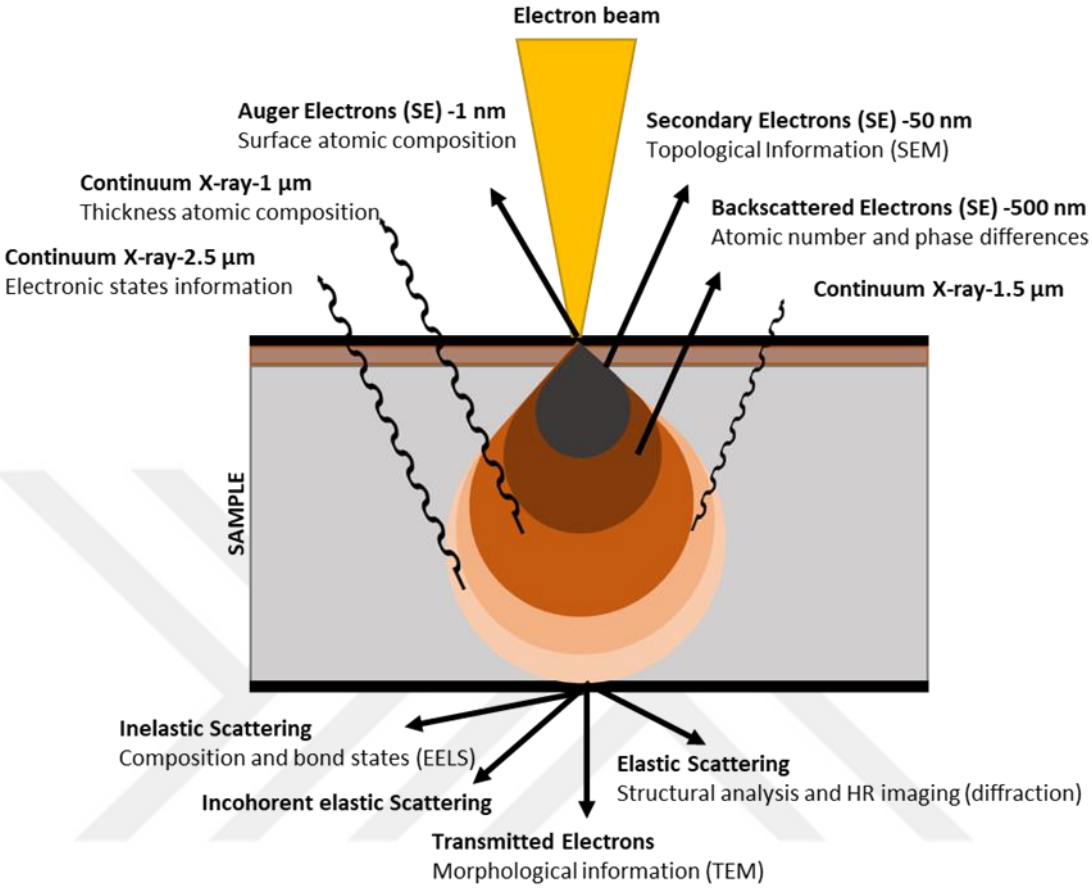

Figure 2.2 Signal emitted from different parts of the interaction volume.

In transmission electron microscopy (TEM), beams of electrons interact with the sample as the beam is transmitted through the specimen. The transmitted electrons form the bright field image. Regions that are thicker, have a higher atomic number, or higher density will appear darker. The image is a two-dimensional projection of the specimen. In dark field images, the aperture while one blocks the direct beam or more diffracted beams are allowed to pass the objective aperture. Since diffracted beams have strongly interacted with specimen, very useful information is present in dark-field images, e.g., about planer defects, impurities.

Scanning transmission electron microscopy (STEM) is a combination of the SEM and TEM, it gives the significant advantage such as allowing for a correlation between surface and bulk information in a higher resolution. For both SEM and STEM, X-rays

produced by the interaction of electrons with specimens are used for elemental characterization of the samples in energy-dispersive x-ray spectroscopy. (EDS) All possible electron sample interactions was illustrated in Figure 2.2.

In this thesis, SEM was used for the topological analysis of as-prepared or tested mesoporous electrodes like porosity, the thickness of the films. EDS was used for the compositional analysis of as-prepared or tested electrodes. While HR-TEM was used for the structural analysis of as-prepared or tested electrodes, STEM was used for the topological analysis of as-prepared or tested mesoporous electrodes, especially mesoporosity.

2.1.4 N_2 Sorption Analysis

Molecules and atoms can attach to any surface in two ways, physisorption and chemisorption. In physisorption, there is a van der Waals interaction between the adsorbate and the substrate. In N_2 sorption analysis in which the physisorption is utilized, the sample is degassed to ensure that its surface is totally clean and a N_2 gas at a series of pressures which will adsorb to the surface and to the walls of the pores is dosed. The free gas and the adsorbed nitrogen gas are in dynamic equilibrium, and the fractional coverage of the surface depends on the pressure is called the sorption isotherm.

The simplest physically plausible isotherm, Langmuir isotherm, is based on three assumptions:

1. Adsorption cannot proceed beyond monolayer coverage.
2. All sites are equivalent, and the surface is uniform.
3. There is no interaction between adsorbed molecules.

If the initial monolayer can behave as a substrate for further adsorption, rather than the isotherm decreasing to some saturated value at high pressures, it can rise indefinitely. The most widely used isotherm engaging in multilayer adsorption was described by Stephen Brunauer, Paul Emmett, and Edward Teller and is named the BET isotherm. A BET isotherm is not accurate at all pressures, but is widely used in this thesis at low relative pressures (P/P^o) to determine the surface area of the mesoporous samples.

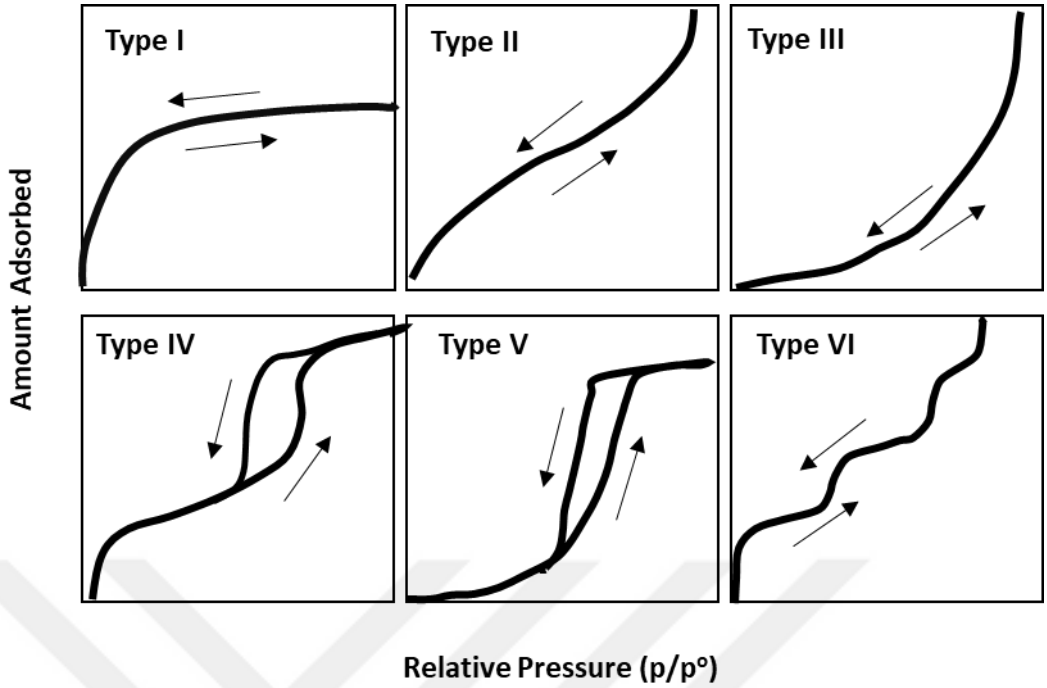

Figure 2.3 IPUAC Classification of isotherms [80]

A classification of physisorption isotherms (Figure 2.3) which are broadly useful in the characterization of subcritical isotherms on rigid adsorbents has been standardized by the IUPAC. The mesoporous materials, the main focus of this thesis, show the type IV isotherm since a hysteresis loop occurs due to capillary condensation in the adsorption and desorption isotherms.

2.1.5 X-ray Photoelectron Spectroscopy

XPS is a surface-sensitive spectroscopic technique often used to investigate the chemical composition as well as the electronic structure. X-rays are emitted onto the sample surface. XPS, based on the photoelectric effect, was developed in the mid-1960's as a practical technique by Kai Siegbahn and his research group at the University of Uppsala, Sweden.

In XPS, an incident X-rays excites a photoelectron, and this photoelectron escapes with the kinetic energy that is equal to how much energy that X-ray gives minus how tightly the electrons itself to nucleus (binding energy) and the calibration factor, work

function. Generally, XPS is presented on a binding energy scale in which the binding energies are characteristic for the elements. If the upper shell electrons fill at the place of the exited electrons, the energy is released and excites the upper shell electrons, called Auger electron emissions. These two processes are represented in the Figure 2.4. XPS using soft X-rays can probe all of the orbitals in only the light elements.

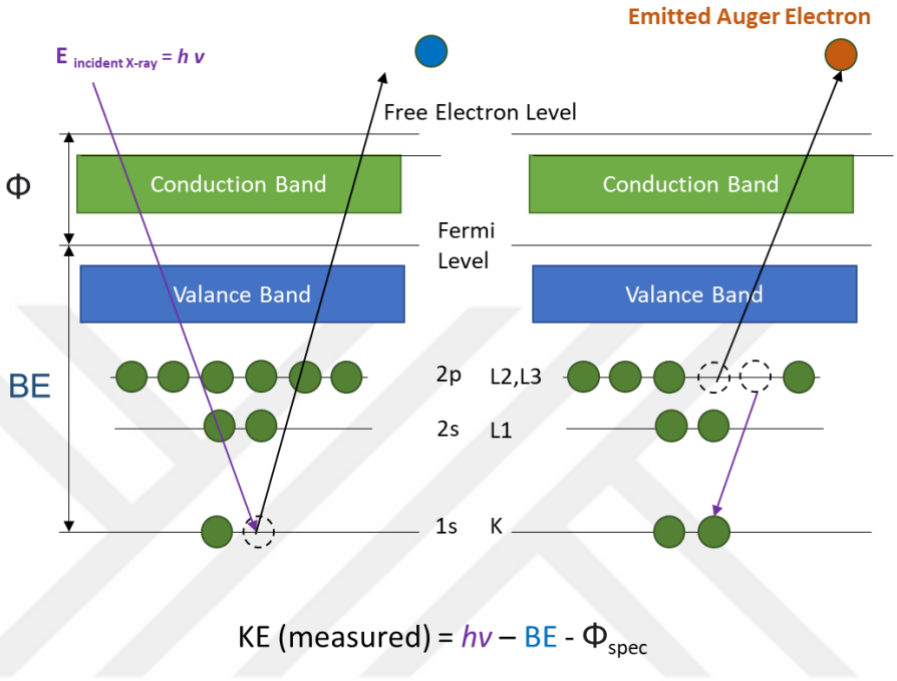

Figure 2.4 The photoelectron and Auger Electron Emission

The inelastic mean free path of the electrons is dependent on the kinetic energy of X-ray and the composition of elements. XPS is a surface-sensitive since electrons travel only a few nanometers through solid materials. %95 of the signal comes from within 5 nm of the surface or less.

The binding energy is dependent on electron-electron repulsion and electron-nucleus attraction. For a given orbital, binding energy will increase with atomic number. When the orbitals' angular momentum couples with the orbital spin, spin-orbit coupling occurs, resulting in the lifting of the degeneracy of the energy levels of the electrons in the same orbital. The oxidation number and the total electron density cause the chemical shift of the binding energies. In this thesis, XPS was used intensively to investigate the chemical composition of as-prepared and tested electrodes.

2.1.6 Inductively Coupled Plasma - Optical Emission Spectrometry (ICP-OES)

ICP-OES is a type of spectrometer that allows the simultaneous identification and quantification of trace elements in aqueous samples. The analysis is mainly used to test elements in liquid samples down to parts per billion detection limits (ppb). ICP-OES consists of two defining components, inductively coupled plasma and optical emission spectroscopy. The plasma, is a state of matter that is formed at very high temperatures, is used as the source for the spectrometer. The temperature of the plasma is approximately 7000 K, causing gas to ionize and become electrically conductive. In practice, the liquid sample is first turned into an aerosol by a nebulizer. Then, the sample gets injected into the plasma torch. The plasma torch ionizes or breaks the sample down to its individual ions and atoms which are in an energized state. They will eventually return to their lower energy state and emits light in the process. The wavelength of the light is related to the type of the elements and its intensity is related to the concentration elements in the sample. The wavelengths and intensities of these spectra are then measured by the detector and converted into various elements and concentrations.

In this thesis, ICP-OES was intensively used for the elemental composition of as-prepared and tested electrodes. In addition, it was used to detect any contamination of the electrodes coming from the electrolyte or counter electrode and the quantification of dissolved elements of the electrodes in the electrolyte during electrochemical performance test runs in ppb level.

2.1.7 Polarized Optical Microcopy (POM)

A simple polarizing microspore is an optical microscope composed of a detector, lenses and polarizing filters as represented in Figure 2.5. A first filter selects a polarization, which means a single orientation among all waves, which compose light. A second polarizing filter selects a single orientation. When the oriantations of two filters are perpendicular, no wave can transmit anymore. A sample is positioned along the light beam. If it is birefringent, it will split the light by polarization into two ways with different delays. The second filter transmits only the waves whose polarization was tilted by the sample. The sample becomes visible. The POM allows to visualize and characterize birefringent samples. To illustrate, as the hexagonally ordered LLC mesophase shows a texture under a POM, the cubic NaCl crystals are invisible. In this thesis, the POM

technique was used intensively to characterize the structure and stability of LLC mesophases.

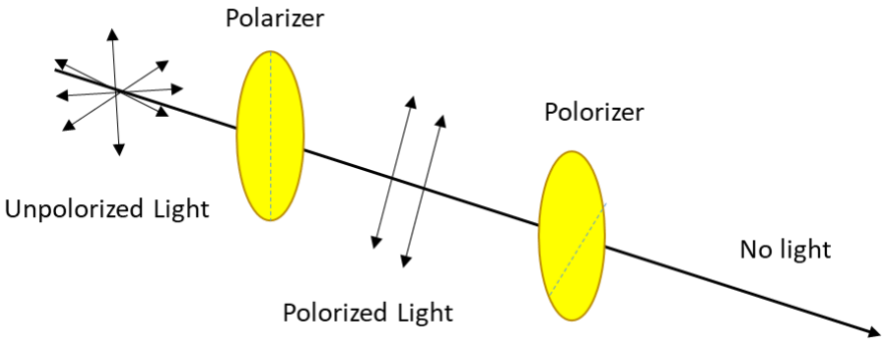

Figure 2.5 The polarized optical microscope setup

2.2 Electrochemical Tests

2.2.1 Linear Seep Voltammetry (LSV) and Cyclic Voltammetry (CV)

The kinetics of the electrode process can be studied by the voltammetry in which the current is monitored as the potential is changed. Depending on the type of the potential signal, many voltammetric methods are available. In this thesis, the linear sweep voltammetry (LSV) and cyclic voltammetry (CV) intensively were used to investigate the electrochemical activities and properties of the electrodes such as capacitance for hydrogen evolution or oxygen evolution reactions.

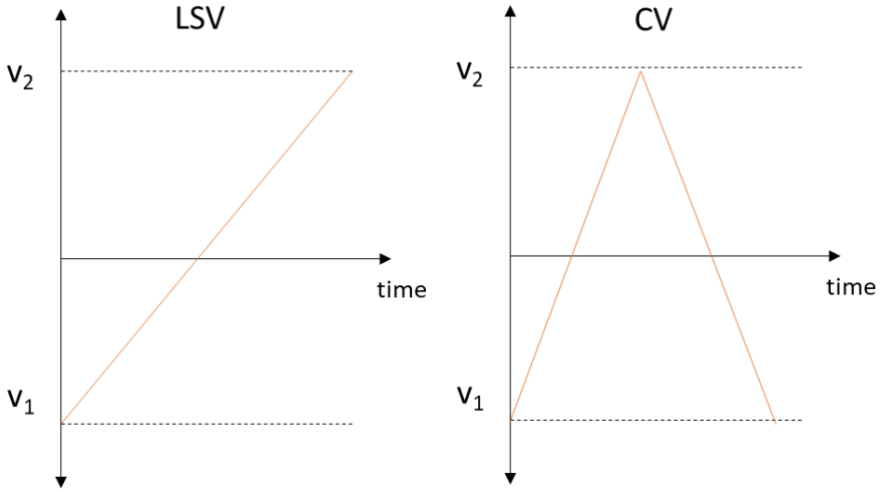

Figure 2.6 The applied potential diagram with time for LSV and CV

In LSV, the potential of the working electrode is ramped from the initial potential to the final potential. The way direct current potential of the indicator electrode varies with time is a potential ramp. In LSV, the potential linearly varies with time. In cyclic voltammetry, the potential is similarly ramped from an initial potential but at the end of its linear sweep, called forward scan, the direction of the potential san is reversed usually stopping at the initial potential, called reverse scan. The potential at which reverse occurs is known as switch potential.

2.2.2 Chronoamperometry (CA)

Chronoamperometry is an electrochemical technique in which the constant potential of the working electrode is applied and the resulting current from faradaic reactions occurring at the electrode is recorded as a function of time. In this thesis, chronoamperometry was intensively used to test the durability of the electrodes during HER and OER.

2.2.3 Electrochemical Impedance Spectroscopy (EIS)

The term impedance refers to the frequency-dependent resistance to the current flow of a given circuit element such as a resistor, capacitor, inductor, etc.

Impedance: $Z\omega=E\omega/I\omega$

- $E\omega$=Frequency-dependent potential and $I\omega$=Frequency-dependent potential

Ohm's Law: R=E/I

- R= impedance at the limit of zero frequency

EIS can determine diffusion-limited reactions and give information on the capacitive behavior of the electrochemical system. The measurement of impedance is conducted by applying an oscillating bias and measuring the oscillating current response. The equation of oscillating voltage can be written down

$$E(\mathrm{t}) = |E| \sin(\omega t)$$

where |E| is the amplitude of the voltage signal and ω=2πf (the angular frequency). The response will be a current with an amplitude |*I*|, which is also shifted in phase from the applied signal:

$$I\,(\mathrm{t}) = |I|\,\sin(\omega t + \theta)$$

The current shifted in phase because of reactance in addition to the resistance. The impedance is expresses as:

$$Z = \frac{E(t)}{I\,(t)} = \frac{|E|\,\sin\omega t}{|I|\,\sin(\omega t + \theta)} = |Z|\,\frac{\sin\omega t}{\sin(\omega t + \theta)} = |Z|\,e^{i\theta}$$

EIS data may be represented as either a vector or a complex quantity. A vector is described by the impedance magnitude and the phase angle. As a complex quantity, total impedance is the sum of the real and imaginary parts of impedance, Z real and Z imaginary. This is the basis for the Nyquist plot, which is the plot of the real and imaginary parts of the impedance that often used for the characterization of resistance of electrocatalysts as used in this thesis. Both are different representations of the impedance and are mathematically equivalent. Electrochemical cells can be modelled as a network of passive electrical circuit elements like resistance, capacitance, etc. A network is called an equivalent circuit. The EIS data of an equivalent circuit can be calculated and compared to the actual EIS data of the electrochemical cell as seen in the Figure 2.7.

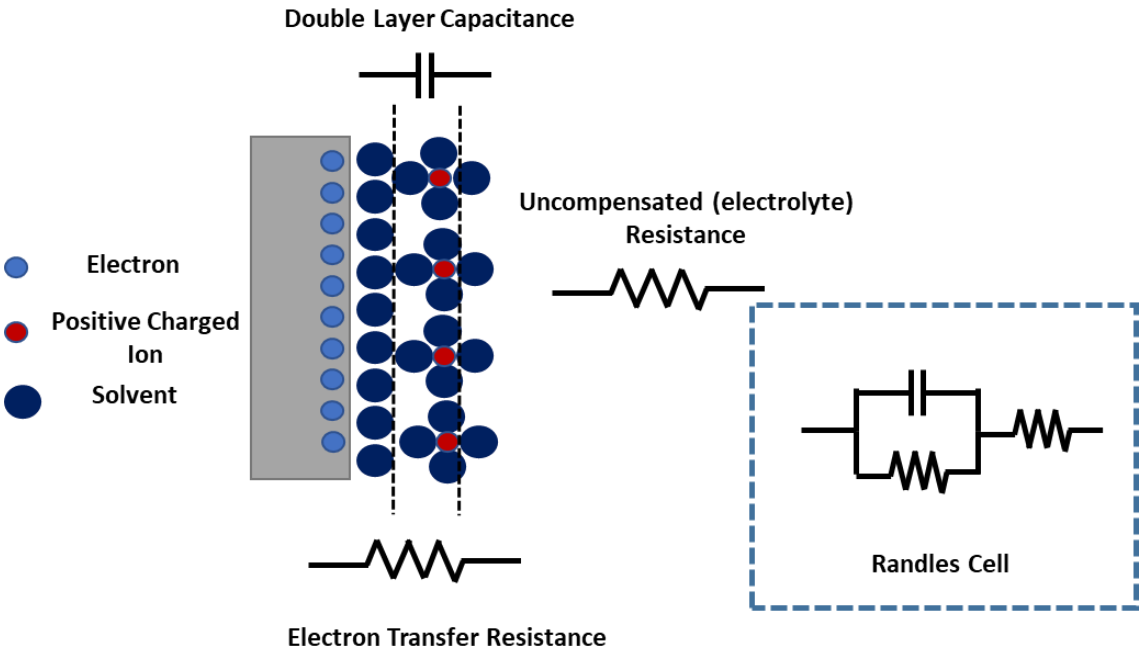

Figure 2.7 The electrochemistry on an electrode surface as a circuit

3 MESOPOROUS NICKEL SULFIDES

3.1 Introduction

As discussed in the first chapter, the synthesis of mesoporous metal sulfides by soft templating is still very challenging. In this chapter, we described a facile method to fabricate the mesoporous nickel sulfides based on the LLC soft templating of nickel nitrate and thiourea with two surfactants. The effects of the annealing temperature and starting Ni/S precursor ratio on the morphology, crystal stucture and composition were investigated in detail by using many characterization tools such XRD, BET, TEM, SEM and etc.

3.2 Experimental Section

All chemicals, cetyltrimethylammonium bromide (CTAB), polyoxyethylene (10) lauryl ether ($C_{12}EO_{10}$), nickel nitrate hexahydrate ($Ni(NO_3)_2.6H_2O$) and thiourea (CH_4N_2S) were purchased from Sigma-Aldrich unless otherwise specified.

3.2.1 Preparation of Solutions of Nickel and Sulfur Precursor and Surfactants

In a typical solution preparation, CTAB, $C_{12}EO_{10}$, nickel nitrate hexahydrate, and thiourea are mixed in a 25 ml vial with deionized water. The solution is stirred for one day in order to make sure it is homogenous and clear (green). A Schematic illustration of the typical solution preparation is indicated in Figure 3.1.

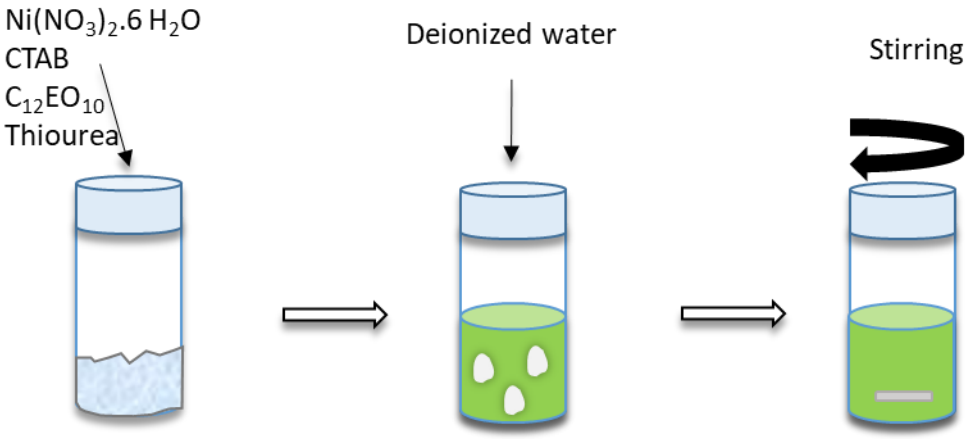

Figure 3.1 Schematic illustration of the preparation of Ni and S precursors and surfactants solution

The amounts of each ingredient for the preparation of all solutions are tabulated in Table 2.1. Deionized water was kept constant in all solutions, 5 g. As CTAB/ $C_{12}EO_{10}$ mole ratio was kept being 1.0 for all solutions, nickel salt/CTAB and thiourea/CTAB mole ratios were altered. The mole ratio nickel salt and thiourea to CTAB mole ratios were used for labeling the solution.

Table 3.1 The amounts of CTAB, $C_{12}EO_{10}$, nickel nitrate hexahydrate, thiourea and deionized water for each solution

Notation of solutions Mole ratios (Ni salt/Thiourea)	**Nickel nitrate (g)**	**Thiourea (g)**	**CTAB (g)**	**$C_{12}EO_{10}$ (g)**	**Deionized water (g)**
06/00	1.392	0.000	0.291	0.500	5.0
06/06	1.392	0.364	0.291	0.500	5.0
06/09	1.392	0.546	0.291	0.500	5.0
06/12	1.392	0.729	0.291	0.500	5.0

3.2.2 Preparation of Lyotropic Liquid Crystalline (LLC) Mesophase

The mesophases were prepared by spin coating of solutions their ingredients are given in table 3.1 for thin LLC films. Spin coating was applied to prepare LLC and further mesoporous nickel sulfide thin films. A few drops of the solution were placed on the FTO or microscopic glass and it was spun for 20 s at 1000 rpm by a spin coater. To obtain

thicker mesophase, drop-cast coating on the microscopic slides was also applied. Drop-casting was applied by placing a few drops of solutions and aged for evaporation of deionized water. Schematic illustration of both drop-casting and spin coating methods are indicated in Figure 3.2.

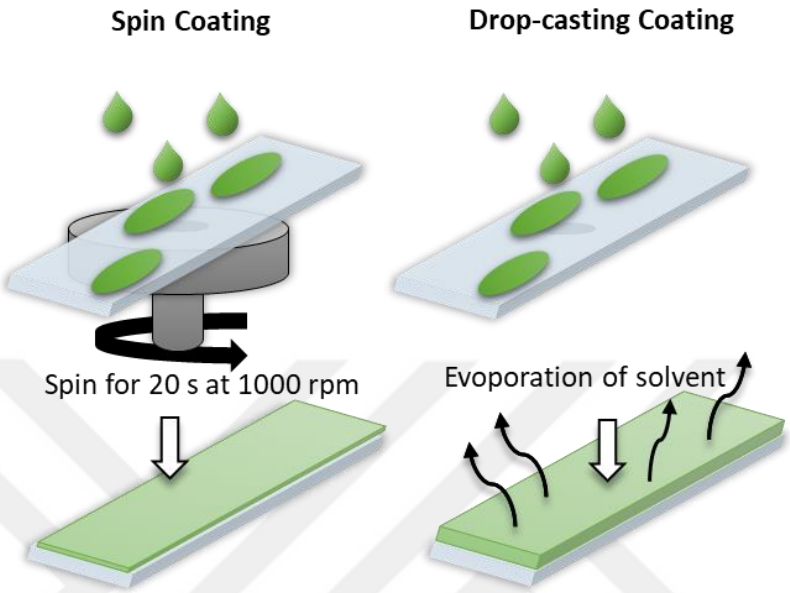

Figure 3.2 Schematic illustration of spin coating and drop-casting casting methods.

3.2.3 Synthesis of Mesoporous Nickel Sulfides

Mesoporous nickel sulfide thin films were prepared via annealing at various temperatures in an inert N_2 atmosphere. Spin-coated samples were sandwiched by another glass slide placed on top and for example, they are annotated as Ni06-S12-200C-capped, where 06 and 12 are mole ratios of Ni salt and thiourea to CTAB, 200C is the final annealing temperature (200 °C). The samples annotated as 300C, 400C and 500C were initially annealed at 130 °C for 2 hours and then annealed at notated temperature for another 2 hours. The case that samples were not sandwiched was annotated as Ni06-S12-200C-2h-nocapped. In order to get a large amount of samples, drop-casted samples without capping were annealed and annotated as Ni06-S12-200C-2h-dropcasted. The films were scrapped from the glass slides by using a razor for the TEM and BET analysis. The Schematic illustration of the synthesis of mesoporous Ni sulfide thin film is depicted in Figure 3.3.

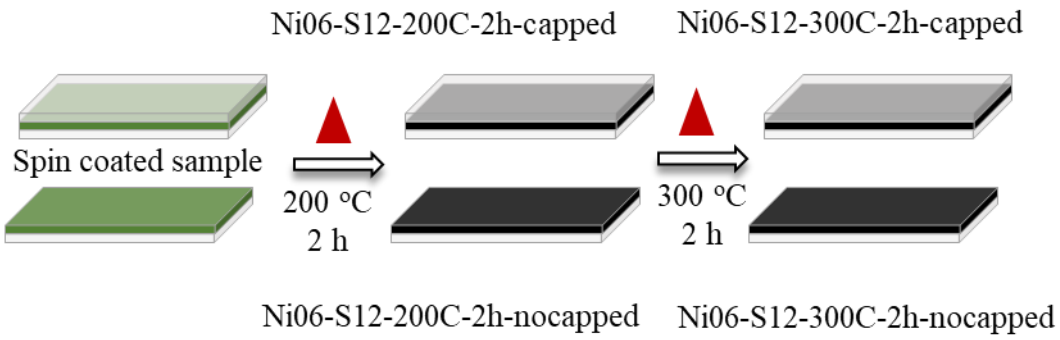

Figure 3.3 Schematic illustration of the synthesis of mesoporous Ni sulfide thin films

3.3 Instrumentation

Powder X-ray diffraction (XRD) measurements were performed at room temperature on a Bruker D-8 diffractometer (Cu Kα radiation, λ = 1.5406 A). A beam voltage of 40 kV and a current of 40 mA were used. The powder sample was collected by scratching films from the glass slides. The phase identification of patterns recorded by X-ray diffractometers was done by using PDF cards of Bruker EVA software program with international center for diffraction data (ICDD). FTIR spectra of the mesophase, heat-treated, and washed samples were recorded by using Perkin Elmer Frontier MIR-ATR Spectrometer with 4 cm^{-1} spectral resolution. A Zeiss Supra 50VP SEM with an accelerating voltage of 20 kV equipped with an energy dispersive spectrometer (EDX) was used to analyze the film morphology and composition of the samples. Low and high-resolution TEM images were performed on a Jeol JEM 2100F field emission electron microscope under 200 kV. BET surface area and BJH pore-size distribution of all synthesized materials were measured using a Micromeritics ASAP 2020 automated gas sorption analyzer.

3.4 Liquid Mesophase of Nickel Nitrate-Thiourea System with Two Surfactants

Thiourea was one the most widely used sulfur precursor in the synthesis of metal sulfides due to high solubility in various solvents (e.g. water, alcohols), air stability, commercial availability, and low decomposition temperature. The addition of thiourea into LLC mesophase of nickel nitrate with CTAB and $C_{12}EO_{10}$ surfactants is very critical to obtain mesoporous nickel sulfides. Therefore, the formation and stability of the liquid

mesophase of nickel nitrate-thiourea system with two surfactants were investigated extensively.

3.4.1 Liquid Mesophase Formation and Characterization

Nickel nitrate salt with two surfactants forms LLC mesophase. Nickel nitrate species fill among the surfactant domain aggregated upon evaporation of water. The sulfur precursor, thiourea, which is also soluble in water, can place next to nickel nitrate salt species among the hydrophilic space of surfactant domains. The LLC mesophases of nickel nitrate salt/CTAB and thiourea/CTAB mole ratios are investigated by a small angle XRD measurement and POM, see Figure 3.4 and Figure 3.5, respectively.

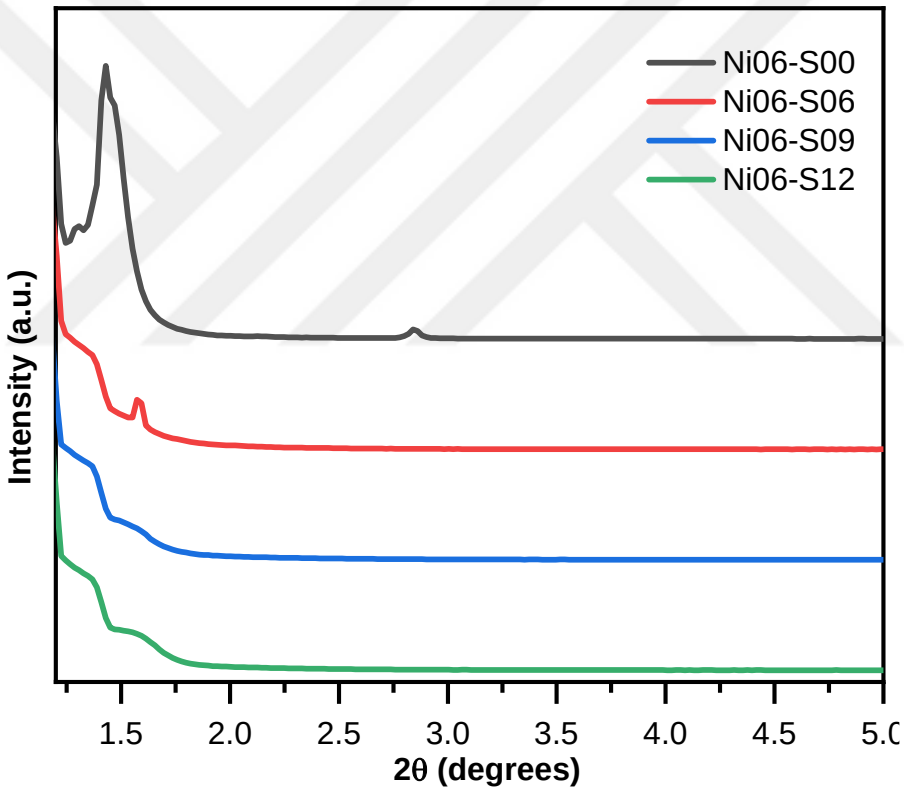

Figure 3.4 Small-angle XRD patterns of LLCs of various nickel nitrate and thiourea mole ratios

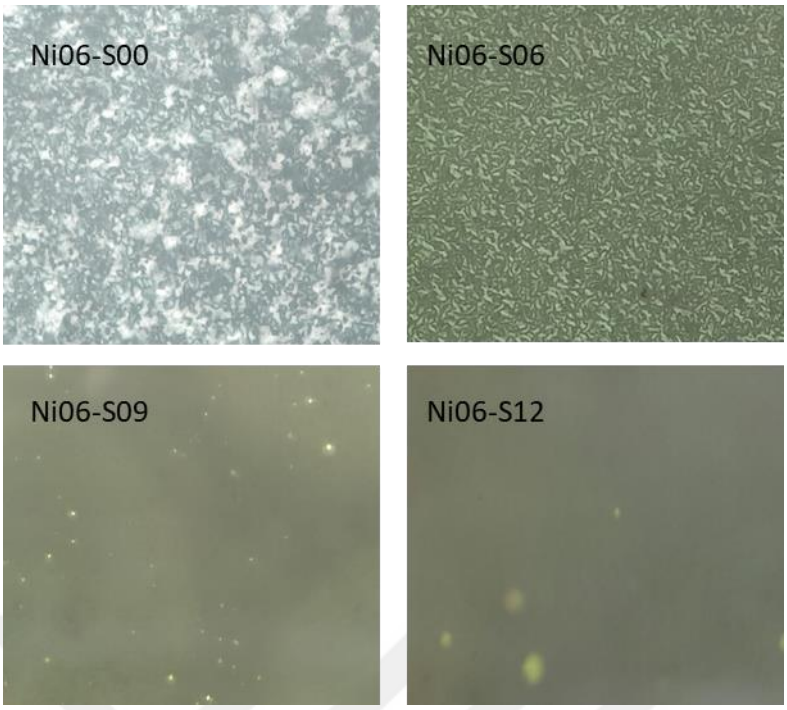

Figure 3.5 POM images of LLCs of various nickel nitrate and thiourea mole ratios

Ni06-S00 and Ni06-S06 samples display the fan texture under a polarized optical microscope (POM), typical characteristics of an ordered 2D-hexagonal LLC mesophase. They also present the diffraction lines at between 1° and 2°, indicating the formation of ordered LLC mesophase. Increasing thiourea content distracts the LLC mesophase because the diffraction line at a small angle is mostly weakened and the fan texture under a POM vanishes for Ni06-S09 and Ni06-S12 samples. Besides, the LLC mesophases with higher content of thiourea can keep the whole inorganic species in the mesophase. The stability of LLC mesophase is very critical to keep the mesostructure upon annealing intact. As any inorganic species leach out from the liquid crystalline mesophase, the inorganic compound with targeted stoichiometry in the mesoporous structure cannot be formed. The decomposition of inorganic species must be in the confined space among the surfactant domains.

3.5 Optimization of the Synthesis of Mesoporous Nickel Sulfides

Nickel sulfides can naturally be occurring and can have various artificial phases and stoichiometries such as NiS, NiS_2, Ni_3S_2, Ni_3S_4, Ni_7S_6, Ni_6S_5, and Ni_9S_8. The phase diagram of the nickel and sulfur reveals that temperature and Ni/S mole ratio present in

the reaction system are key parameters for the phase of nickel sulfide. The lowest obtainable Ni/S stoichiometric ratio is belonging to pyrite NiS_2. Hence, the liquid crystalline mesophase of which Ni/S ratio is 1/2 was extensively studied to optimize the protocol allowing mesoporous nickel sulfide.

3.5.1 Annealing of Liquid Crystalline Mesophase

Non-identical thermal stability of components of the nickel nitrate salt, thiourea, and surfactants in the liquid crystalline mesophase is useful for designing the synthesis protocol of mesoporous nickel sulfide. The late decomposition temperature of surfactants comparing to nitrate ion and thiourea provide time for the formation of nickel sulfide crystallites among the surfactant domains. For identification of the composition, particle size, and crystal structure of the annealed sample, diffraction patterns of as-prepared sample and samples annealed at selected temperatures were recorded, see Figure 3.6. To reveal the underlying mechanism in the formation of mesostructured nickel sulfides, temperature-dependent analysis, DSC and TGA, were performed, see Figure 3.7.

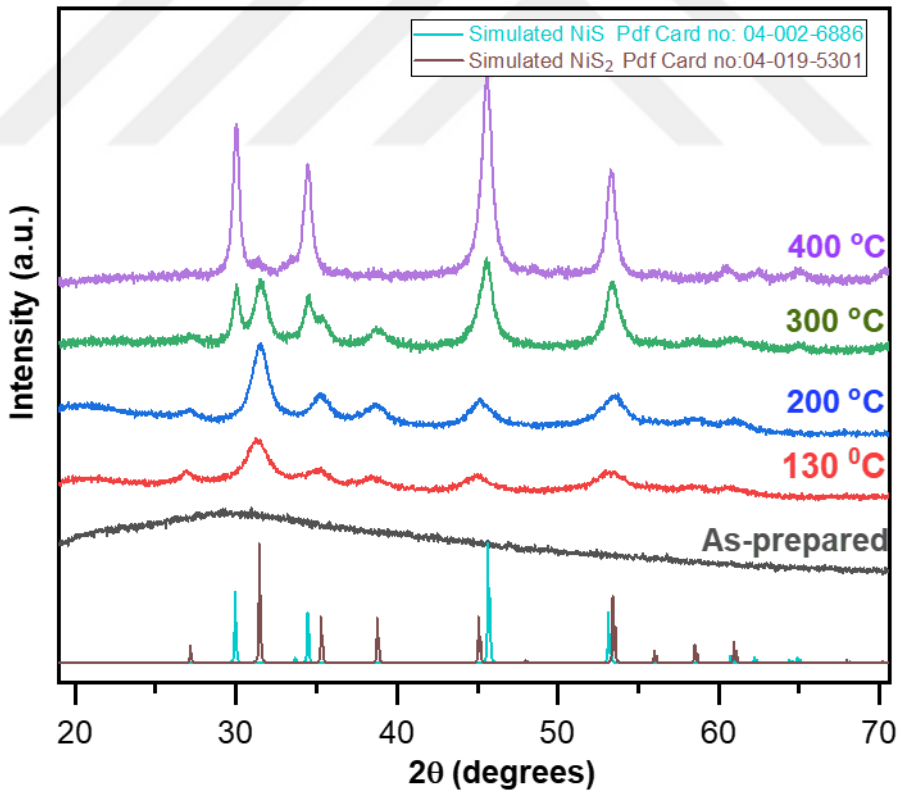

Figure 3.6 XRD patterns of Ni06-S12-dropcasted at room temperature and annealed at different temperatures 130 ℃ and 400 ℃ and the simulated NiS_2 and NiS XRD patterns

According to the XRD patterns of Ni06-S12-dropcasted sample, the mesophase was transformed to pyrite NiS_2 at an annealing temperature of 130 ℃. The broad diffraction lines belonging to reference PDF-04-019-5301 points out the NiS_2 nanocrystallites. With increasing temperature up to 200 ℃, the diffraction lines get sharper, indicating an increase in the crystal size. At an annealing temperature of 300 ℃, nearly half of pyrite NiS_2 started to decompose into NiS. Full conversion of NiS from NiS_2 is achieved at 400 ℃. The diffraction lines of NiS are matched with the reference PDF 04-002-6886.

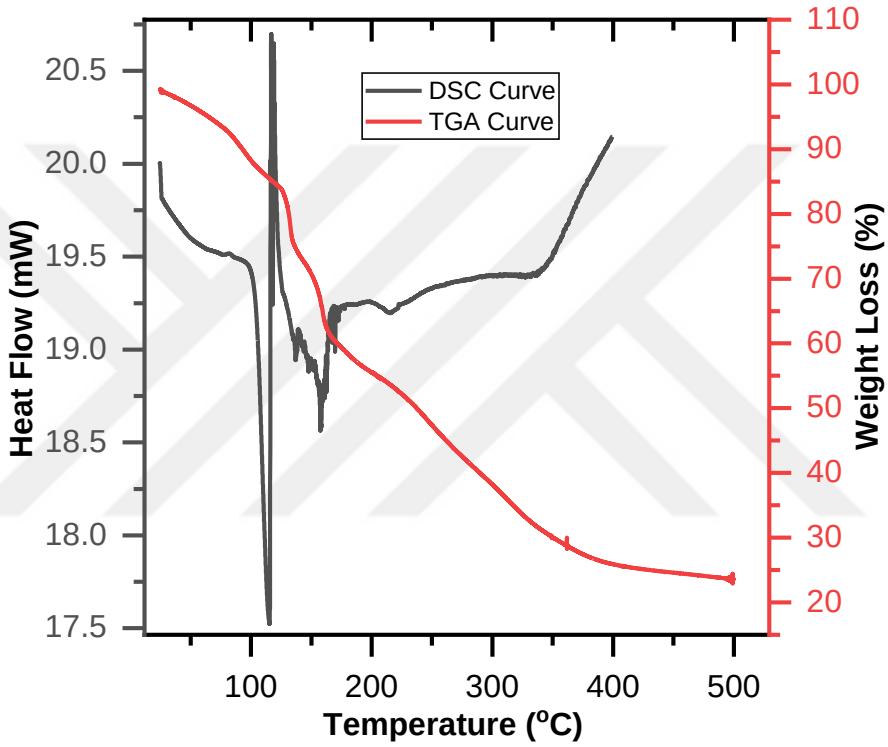

Figure 3.7 TGA/DSC data of Ni06-S12-dropcasted

DSC curve of Ni06-S12-dropcasted sample represented sharp endothermic and subsequent exothermic peaks between temperatures of 100 ℃– 130 ℃. The endothermic peak is most probably corresponding to the decomposition of thiourea. Then, the sulfurous products such as H_2S, CS_2, and SCN react with Ni^{2+} and form pyrite-type NiS_2 compounds that correspond to the subsequent exothermic peak. Following endothermic peaks may belong to nitrate decomposition at mainly between 140 ℃ and 185 ℃, the transformation of NiS_2 into NiS and surfactant carbonizatiın at between 210 ℃ and 300 ℃. TGA curve of Ni06-S12-dropcasted sample has three decomposition steps that

consistent with the decomposition of thiourea, the transformation of NiS_2 into NiS and surfactants carbonization.

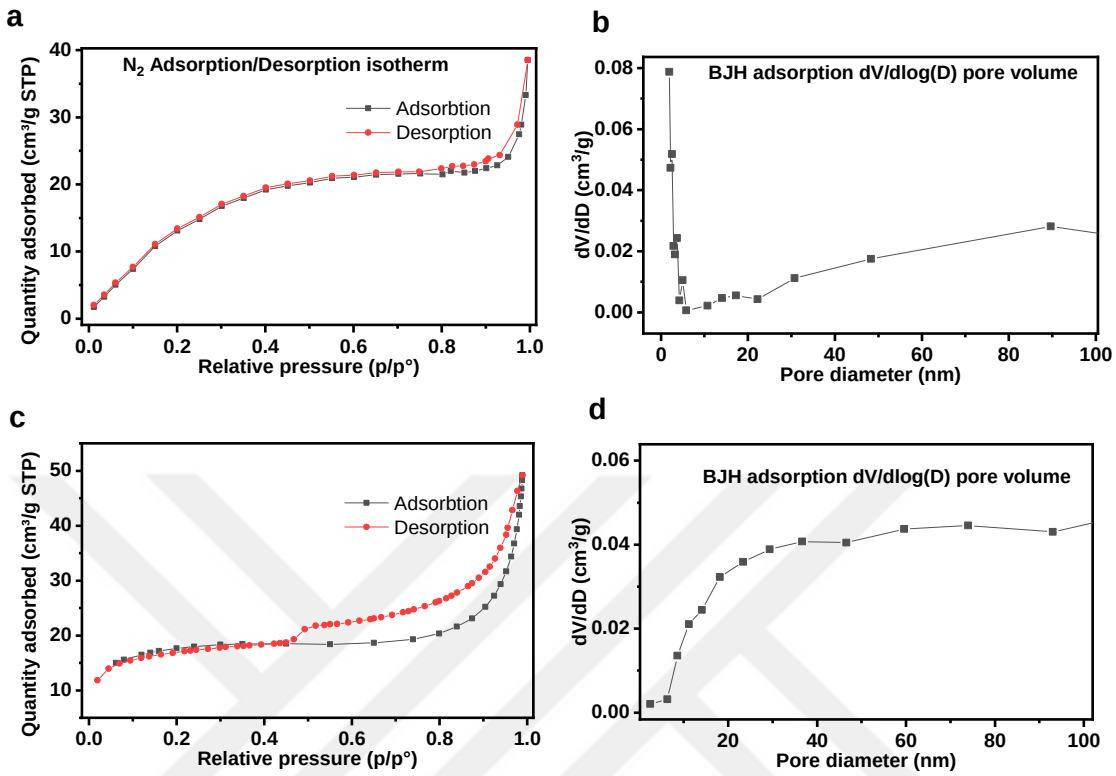

Figure 3.8 N_2 adsorption−desorption analysis and pore size distribution of (a-b) Ni06-S12-185C-dropcasted and (c-d) Ni06-S12-400C-dropcasted

To prove mesoporosity of the samples after annealing the liquid crystalline mesophase of nickel nitrate, thiourea, and two surfactants, N_2 adsorption-desorption isotherms of Ni06-S12-dropcasted samples annealed at 185 ℃ and 400 ℃ were recorded, see Figure 3.8. Ni06-S12-dropcasted sample annealed at 185 ℃ was washed initially in order to remove surfactants and obtain mesoporous structure. The hysteresis on the adsorption and desorption behavior confirms the mesoporosity. The type IV isotherm observed is characteristic of the mesoporous materials.[81] The Brunauer-Emmett-Teller (BET) surface area is about 69 m^2/g. The Barrett-Joyner-Halenda (BJH) analysis exhibits narrow pore-size distribution peaking around 3 nm and a broad pore-size distribution starting 20 nm to above 100 nm. Mesopores size (3 nm) is consistent with the size of surfactant domains in the liquid crystalline mesophase of nickel nitrate, thiourea, and two surfactants. Larger pore size distribution may be originating with the mass and volume contradiction induced by annealing.

The surfactants' carbonization by annealing the sample at further temperatures may induce porosity owing to the volume shrinkage and decomposition of surfactants. Ni06-S12-dropcasted samples annealed at 400 °C also the hysteresis on the adsorption and desorption. However, BET surface area is decreased to about 62 m^2/g, and narrow pore-size distribution peaking around 3 nm vanishes. Instead, it shows a broad pore-size distribution shows starting about 5 nm to above 100 nm. Both phase transformation from NiS_2 to NiS and increase in the crystal size demolish the small mesopores and collapse into bigger ones.

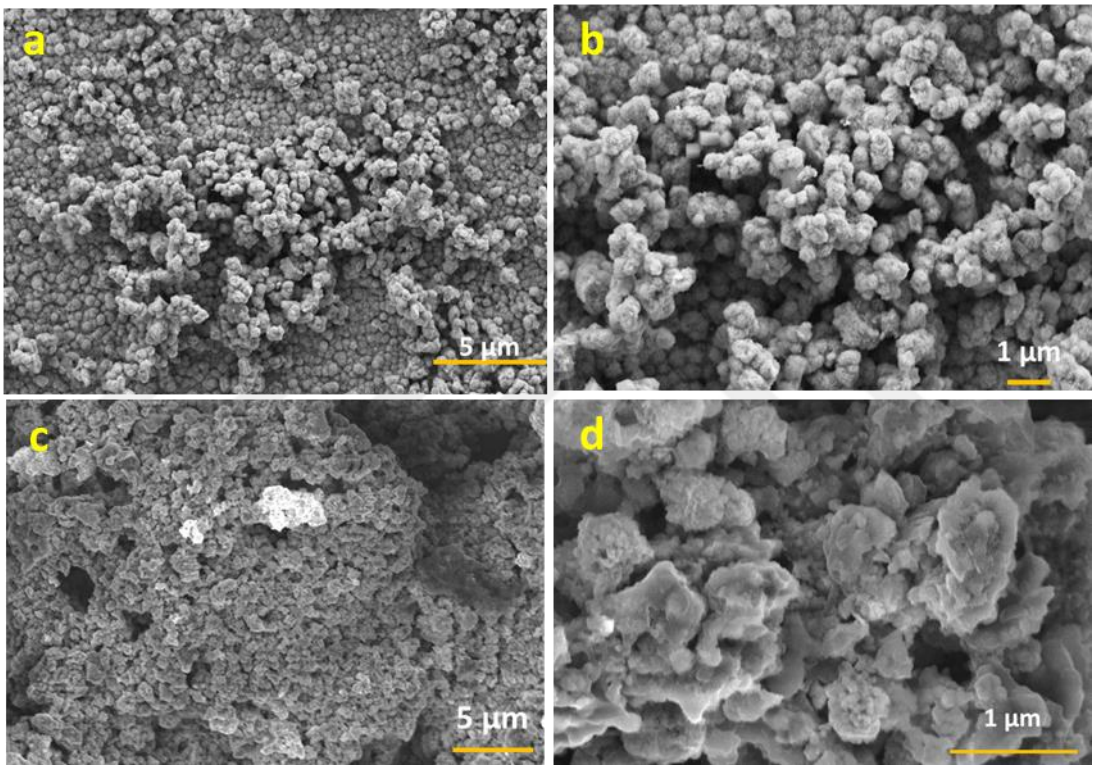

Figure 3.9 Low and high magnification SEM images of (a-b) Ni06-S12-185C-dropcasted and (c-d) Ni06-S12-400C-dropcasted samples

In the SEM images of the drop-casted sample annealed at 185 °C and 400 °C (see Figure 3.9), agglomerated powder particles are observed. Even if the capability resolution of the microscope is not enough to image in detail, mesopores openings have been detected for both samples. As annealing at low temperature provides more mesoporous texture, an increase in annealing temperature diminishes porous structure and enlarging pore openings, which is consistent with their N_2 sorption analysis.

The decomposition of nitrate and thiourea and formation of NiS_2 cause the large volume difference between the precursors (nickel nitrate hexahydrate and thiourea) and NiS_2, resulting in the shrinkage of the liquid crystalline mesophase and solidification as spherical particulates, justifying broad pore-size distribution starting 20 nm to above 100 nm as seen N_2 adsorption−desorption analysis. Further annealing promotes the carbonization of surfactants, generating additional shrinkage but sintering agglomerated particles.

Drop-casting method is useful for structural characterizations and porosity analysis due to the high amount of sample requirement of those analyses conducted. For many applications, as discussed in the literature, thin films are preferred rather than powder samples [44].

3.5.2 Annealing of capped and non-capped samples for mesoporous nickel sulfides

Spin coating is one of the powerful cheap techniques for the production of uniform thin films. The thickness of the film can be tuned by changing the angular speed of sniping or the concentration of the solution. Liquid mesophase of nickel nitrate-thiourea system produced by spin coating have usually below micron thickness. As discussed above, thermal treatment of the mesophase produces mesostructured NiS_2 and transforms into mesoporous NiS with the help of the reaction between mostly gaseous sulfurous products formed by thiourea decomposition and nickel cation. The thicker mesophase sample obtained by drop-casting may create inhomogeneity during the decomposition of precursors and the reaction among them. However, bulk or micro characterizations are not useful for detecting inhomogeneity on powder samples. Therefore, we applied the spin coating of the mesophase and later annealed samples with or without capping another glass slide to obtain mesoporous NiS thin films on glass slides. The capping aimed to apply the sandwich structure, preventing the escape of sulfurous gasses (CS_2, H_2S and etc.) from the mesophase without reacting nickel cations. The annealing temperature was selected to be 500 ℃ to secure the complete formation of all precursors into detectable final phases by the characterization. Characterization of the annealed spin-coated films was done by using the XRD data and SEM imaging to determine the morphology and composition of the final products.

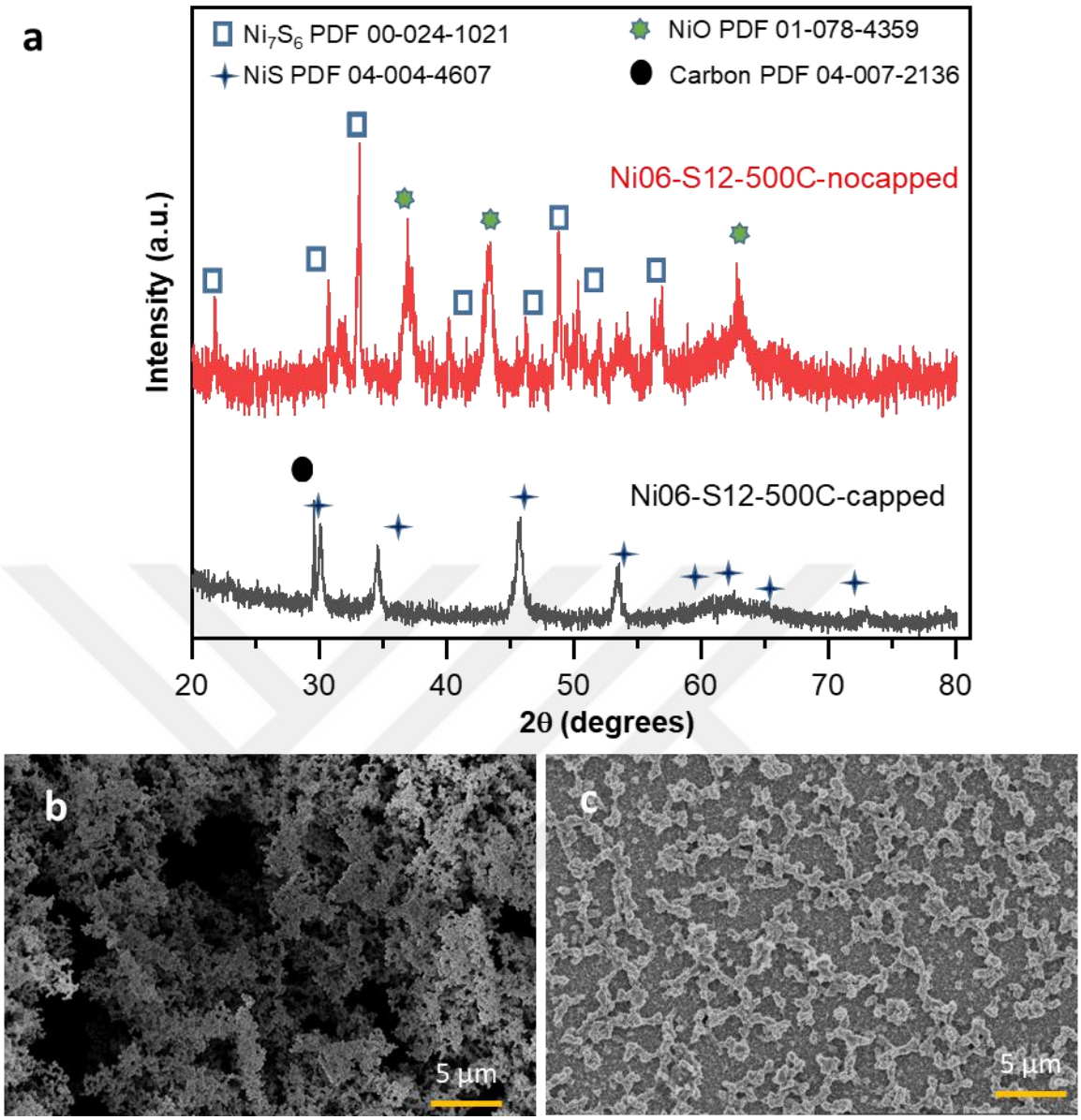

Figure 3.10 (a) XRD pattern of Ni06-12-500C-capped and Ni06-12-500C-nocapped sample. The SEM images of (b) Ni06-12-500C-nocapped and (c) Ni06-12-500C-capped.

The diffraction patterns of Ni06-12-500C-capped and Ni06-12-500C-nocapped are very different from each other, see Figure 3.10a. Ni06-12-500C-capped sample has two crystalline compounds; one of them is NiS as similar to the one obtained by the application of the drop-casting method and the other one is crystalline carbon unlike the drop-casting method. On the other hand, Ni06-12-500C-nocapped sample has mainly NiO and slightly Ni_7S_6 crystalline compounds. The annealing thin film of mesophase without blocking the escape of gaseous sulfurous compounds results in an incomplete

reaction between nickel cation and gaseous sulfurous compounds. Only a small amount of nickel cation forms nickel sulfide and the remaining ones just decompose into nickel oxide. The carbonization of surfactant is also justified by the observation peak at 29.5 degrees attributed to crystalline carbon. Remind that the transformation of NiS_2 in NiS lowered slightly the BET surface area per gram even though small mesopores is collapsed. This is because of the fact that carbon gives the extra surface area in the porous structure and decreases the bulk density. In the SEM images of annealing without capping, Figure 3.10b, the agglomerated particulate powders with large voids are observed. On the other hand, the formation of NiS_2 and even transforming into NiS provides long-ranged continuous film framework when the capping is applied, see Figure 3.10c.

3.6 Obtaining different mesoporous nickel sulfides

As observed in the effect of unequal mole ratio of nickel sulfide precursors on the final structure for uncapped samples such as Ni_7S_6, changing nickel to sulfur precursor mole ratio may enable the formation of the various phases of nickel sulfide. To test our protocol for mesoporous nickel sulfide thin films other than NiS_2 and NiS, the spin-coated liquid crystalline mesophases having three different Ni/S precursor mole ratios were initially converted to NiS_2 at 135 ℃ and then annealed at various temperatures. Note that all samples were capped during annealing for the full reaction between nickel and sulfur precursors. X-ray diffraction patterns of prepared samples were collected to reveal the final phase and composition, see Figure 3.11. The diffraction patterns of the samples were compared with the reference patterns by using ICDD database.

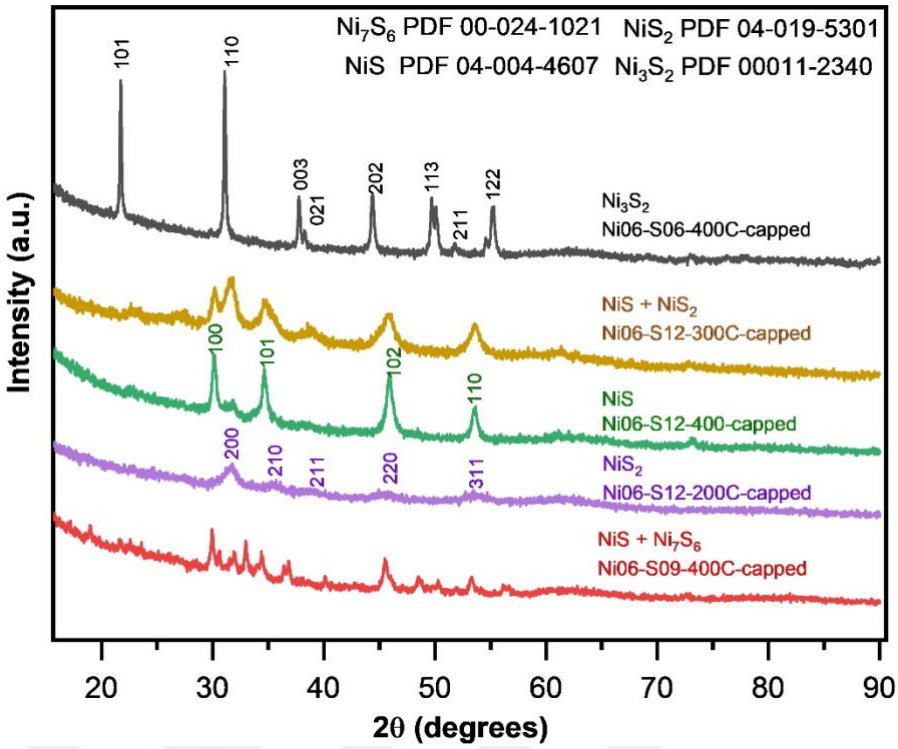

Figure 3.11 XRD patterns of the samples containing different nickel salt to thiourea mole ratios (Ni salt/Thiourea) annealed at various annealing temperatures

In the diffraction patterns of the Ni06-S12 thin film annealed at 200 ℃, 300 ℃, and 400 ℃, pure NiS_2, a mixture of NiS_2 and NiS and pure NiS phase of nickel sulfide were obtained, respectively. Decreasing thiourea content in the liquid crystalline mesophase, Ni06-S09, gives a mixture of NiS and Ni_7S_6 phases of nickel sulfides at 400℃. For one-to-one precursor mole ratio, Ni06-S06, pure Ni_3S_2 phase of nickel sulfide was obtained. It is obvious that NiS_2 is the starting phase and not stable above 200 ℃. The mesoporous pyrite NiS_2 displays broader diffraction lines, the grain size is found to be around 8-9 nm by applying the Scherrer equation. The transformation of NiS_2 into NiS may produce elemental sulfur. The NiS phase is still stable at high temperatures. Mesoporous NiSshows much sharper diffraction lines with grain sizes larger than 25 nm. As the NiS_2 phase is annealed with non-sulfurous Ni species, the reaction undergoes among non-sulfurous Ni species, elemental sulfur, and NiS phase, leading to the formation of sulfur deficient nickel sulfides such as Ni_7S_6 and Ni_3S_2. The formed phase of nickel sulfide is dependent on the amount of Ni species and elemental sulfur produced by the decomposition of NiS_2. The annealing temperature, sample preparation method,

nickel salt to thiourea mole ratios (Ni salt/Thiourea), and obtained nickel sulfide phase are tabulated in the Table 3.2.

Table 3.2 The annealing temperature, sample preparation method, nickel salt to thiourea mole ratios (Ni salt/Thiourea), and obtained nickel sulfide phase for each sample

Notation of solutions Mole ratios (Ni salt/Thiourea)	**Annealing temperature (°C)**	**Sample preparation method**	**Nickel sulfide phase**
06/12	135	capped	NiS_2
06/12	185-200	capped	NiS_2
06/12	300	capped	Mainly NiS + NiS_2
06/12	400	capped	NiS
06/12	500	capped	NiS
06/12	500	no capped	Mainly NiO + Ni_7S_6
06/06	400	capped	Ni_3S_2
06/09	400	capped	Mainly NiS + Ni_7S_6

3.7 Detailed Characterization of Mesoporous NiS and NiS_2 thin films

The aim of this study is to develop a facile and one-step method for the mesoporous metal sulfide thin films and their application of water splitting as electrodes. Up to now, we have discussed the flexibility and limits of our novel protocol by using common characterization tools used for mesoporous materials. According to the N_2 sorption and XRD analysis of synthesized samples, mesoporous NiS_2 thin film shows the most mesoporous thin film characteristic in accordance with the main purpose. Hence, we focused on the detailed characterization of especially mesoporous NiS_2 thin films by utilizing high-resolution TEM, STEM, and SEM (with EDS) in order to reveal their all structural and morphological properties.

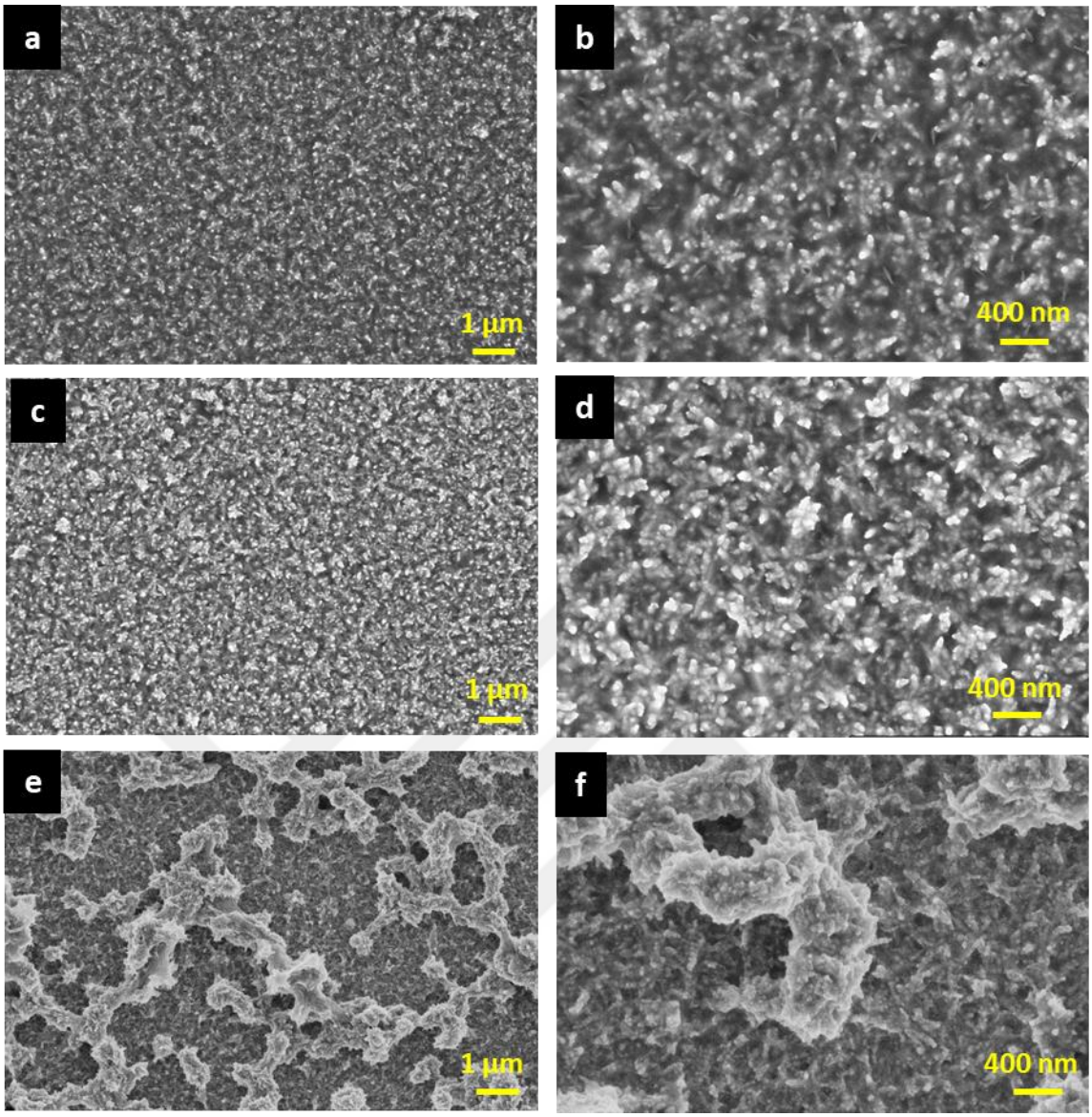

Figure 3.12 Low and high magnification of SEM images (a-b) non-washed Ni06-S12-185C-capped, (c-d) washed Ni06-S12-185C-capped and (e-f) Ni06-S12-300C-capped samples

SEM images of non-washed mesoporous NiS_2 thin film sample, see Figure 3.12a-b, show less textured surface features with 20-25 nm sized NiS_2 crystals. Removing surfactant via washing makes those features more visible due to most probably an increase in the conductivity of the film, see Figure 3.12b-c. Further annealing, 300 ℃, the size of crystals is decreased, and the film's texture is becoming much more perforated see Figure 3. 12d-e. This may be the result of the decomposition of many parts of NiS_2 into NiS.

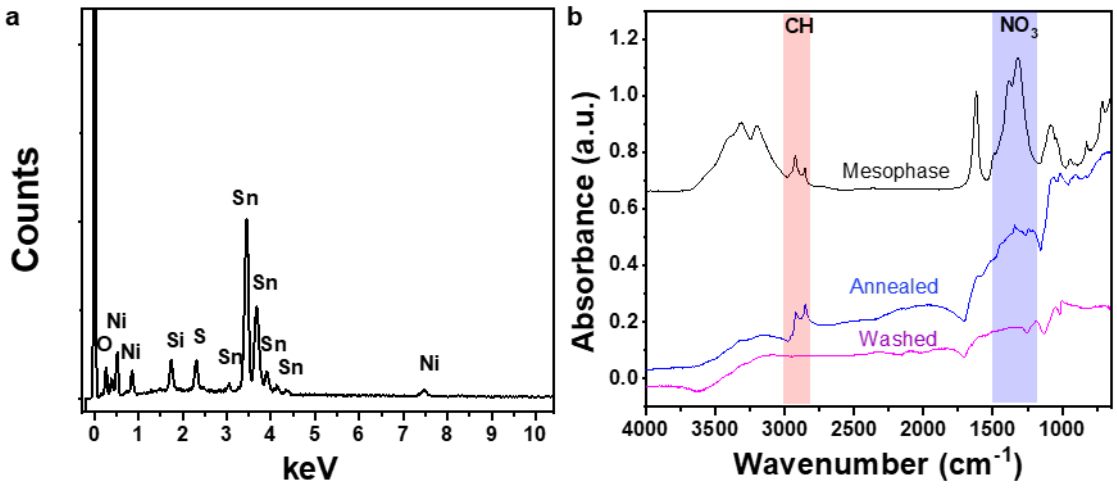

Figure 3.13 (a) EDS spectrum of non-washed Ni06-S12-185C-capped, washed Ni06-S12-185C-capped and Ni06-S12-300C-capped samples. (b) FT-IR spectrum of Ni06-S12 mesophase, non-washed Ni06-S12-185C-capped, and washed Ni06-S12-185C-capped samples

The EDS was also performed on the samples imaged by SEM (Figure 3. 13a) for compositional analysis. The Ni/S atomic ratios of both washed and non-washed mesoporous NiS_2 are the same and about 1/2. This ratio is reduced to 1/1.2 for the sample annealed at 300 ℃. It is expected that the sample consists of a mixture of mainly NiS phase and less amount of NiS_2. Surfactants were washed out by dipping the samples into distilled water. As indicated in the FTIR spectra (Figure 3.13b), the symmetric and anti-symmetric stretching modes of C-H at around 2820 and 2920 cm^{-1} vanish after washing, confirming the complete removal of surfactants.

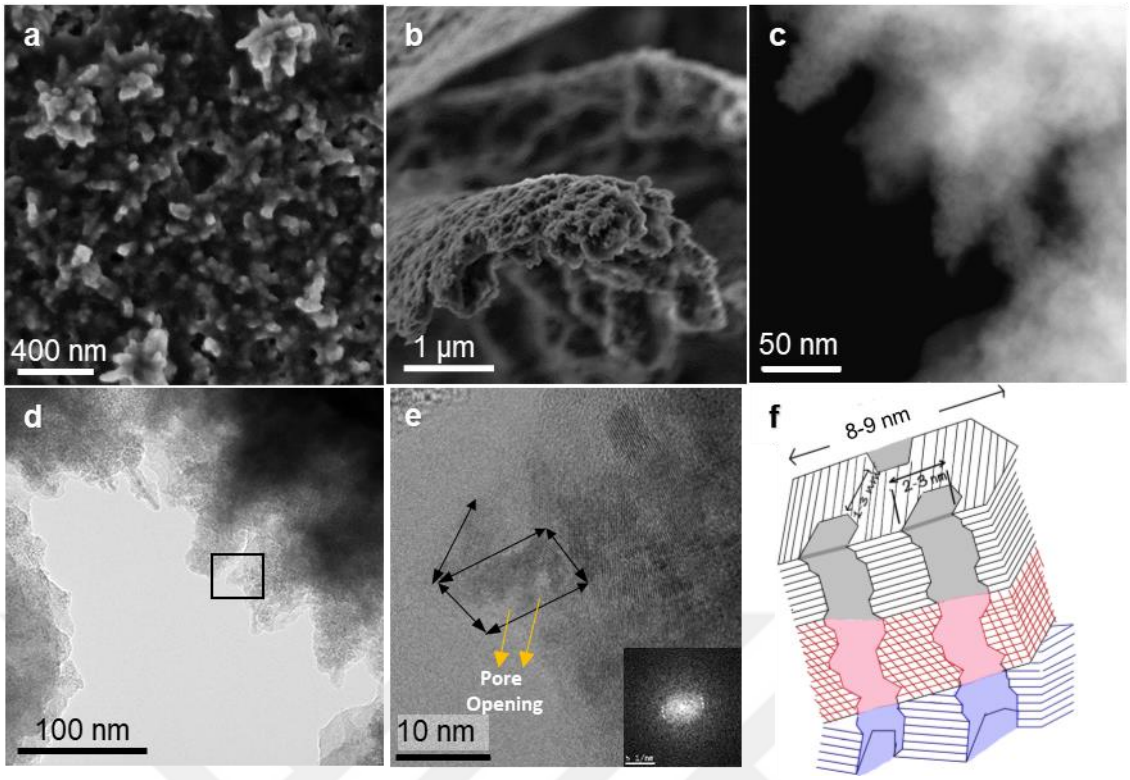

Figure 3.14 (a-b) SEM, (c) HAADF-STEM, and (d-e) low and high magnification TEM images of washed Ni06-S12-185C-capped. TEM image shown in (e) is obtained from the region indicated by a black rectangle in (d). The inset is the FFT of the image (e). (f) Schematic illustration of mesoporous NiS_2.

The washed mesoporous NiS_2 thin film, seen in the panoramic SEM image of Figure 3.14a, was scrapped by using a razor blade. The film thickness varies from 300 to 500 nm and films appear to be integrated (Figure 3.14b). To further understand the structural details of the mesoporous NiS_2 films, a series of STEM and TEM mages have also been collected. HAADF-STEM images, in Figure 3.14c, and TEM images, in Figures 3.14d-e, display the sponge-like disordered mesoporosity created by agglomerated ultra-small NiS_2 nanocrystals (3-5 nm) with pore openings 3-5 nm wide. The value of pore openings is consistent with the size of the micelles formed by CTAB and $C_{12}EO_{10}$. In the HR-TEM images (Figure 3.14e), the lattice fringes of NiS_2 crystals can be observed. The lattice spacing estimated by FFT (fast Fourier Transform) pattern is 0.285 nm which represents the (200) lattice plane of the NiS_2 nanocrystallites in the pyrite structure. Combining STEM/TEM morphological analysis with the XRD and BET data, we can visualize the mesoporous film structure as depicted in Figure 3.14f. The wall thickness of

2-3 nm is much smaller than typical mesoporous NiS_2 prepared by using hard templating method (9-10 nm), whereas both methods yield NiS_2 with similar BET surface areas.[82]

3.8 General Summary of Novel Liquid Templating Method for Mesoporous Nickel Sulfide

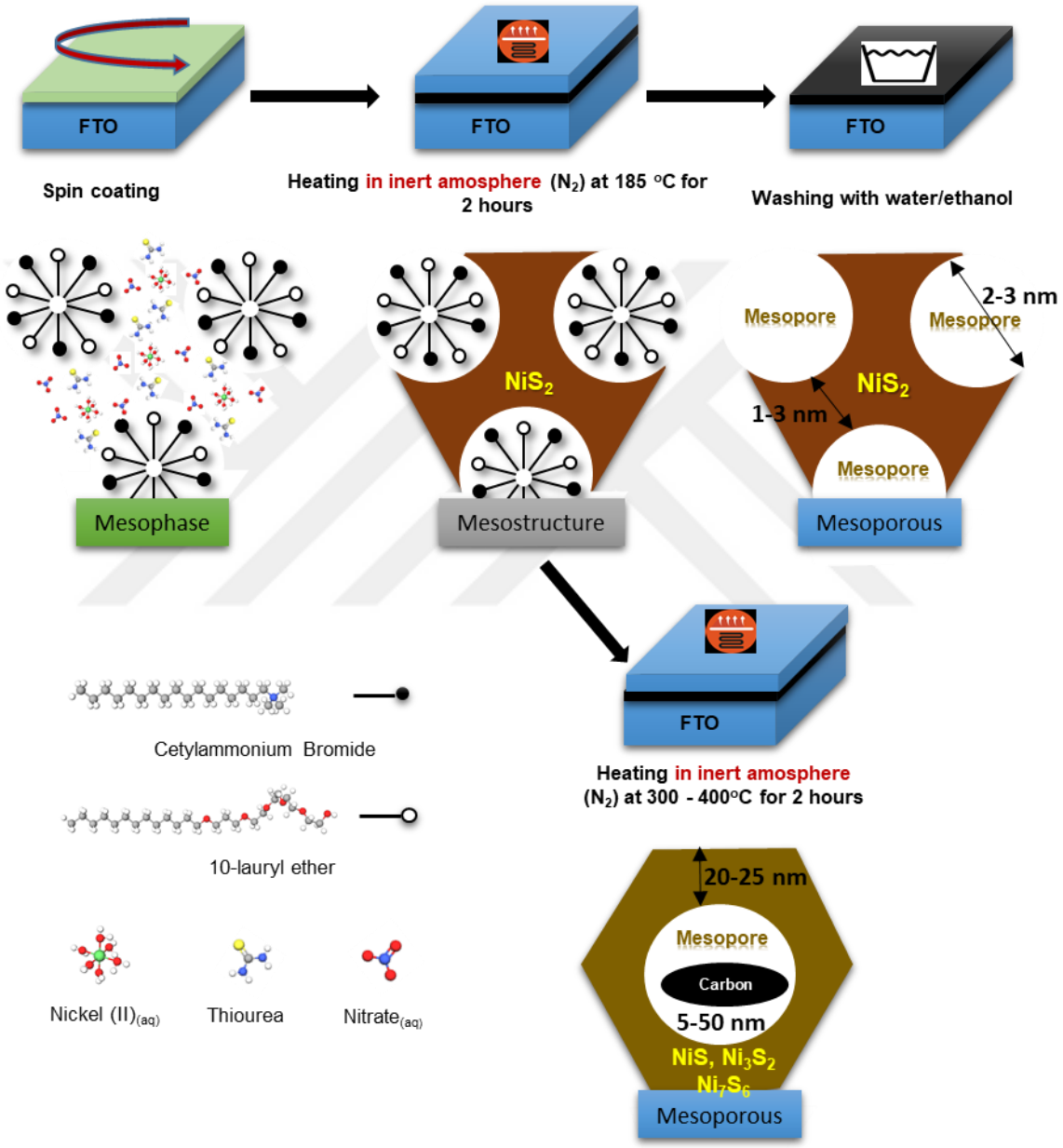

Figure 3.15 The schematic diagram of the liquid templating method for mesoporous nickel sulfide

As a summary, we developed a novel and facile one-step protocol that could be classified as a truly soft-templating method without any post-sulfurization process to

obtain mesoporous nickel sulfide thin films, as summarized schematically in Figure 3.15. To illustrate, our protocol provides NiS_2 thin films with high surface area and narrow pore size distribution, which are crucial material properties for many advanced applications, especially electrodes in electrolysis.

4 MESOPOROUS NICKEL SULFIDES THIN FILMS FOR A HYDROGEN EVOLUTION REACTION

4.1 Introduction

Noble metal-based electrocatalysts, such as platinum, show superior catalytic activity and stability;[83] however, their high cost and scarcity severely limit their widespread utilization in electrochemical applications.[84] HER electrocatalysts that are fulfilling all requirements (inexpensive, abundant, durable, and efficient) are being researched intensively and recently the focus has been directed into transition metal (TM) sulfides,[85]–[93] selenides,[94]–[98] nitrides,[99]–[101] phosphides,[102]–[106] and carbides[107]–[109] that demonstrate a potential to eliminate noble metals. Among the reported materials, the cubic pyrite-phase TM dichalcogenides (MX_2 where M = Fe, Co, or Ni and X = S or Se) have been identified as a family of very promising earth-abundant and low-cost HER electrocatalysts.[110]

Various synthesis strategies yield Ni sulfides in different chemical compositions and morphologies. Recent studies show that most of those phases are active toward HER.[88], [111]–[117] It is however challenging to compare the activities of TM sulfide electrocatalysts on the same basis, the geometric current densities rather than specific current densities are commonly reported.[118] The onset potentials, the potential at which 10 mA/cm^2 is reached, and the results of the kinetic analysis (Tafel plots) are taken as activity measures. It is also well-acknowledged that electrochemical surface areas (ECSAs), conductivities of the electrodes, and different morphologies (films, nanorods, nanoflakes, etc.) strongly influence the activities. For example, pure NiS_2 in different morphologies show varying activities in alkaline media with overpotentials between 67 and 220 mV to reach 10 mA/cm^2.[111], [112] A detailed investigation performed by Jiang et al. compares HER activities of Ni_3S_2, NiS, and NiS_2 crystals of similar sizes and identifies Ni_3S_2 as a superior electrocatalyst in alkaline media owing to its higher ECSA and conductivity.[88] Ni_3S_2 nanosheets,[113], [114] films grown by atomic layer deposition,[115] and nanowires[116] have been shown as the active structural phase, similar to flower-like β-NiS.[117] In a recent review by Siegmund et al., more emphasis has been placed on the activities of the metal-rich phases like Ni_3S_2. More specifically, pentlandite type of structures (Ni_9S_8) has been shown to exhibit better HER activities due to intrinsic high conductivity.[39]

The active sites of Ni sulfides for HER show surface chemical composition dependence. The results of the density functional theory (DFT) calculations indicate that Ni-S coordination could be an activity descriptor in Ni sulfides in general.[119] It has been suggested that high electronegativity of S could be the origin of high activity of Ni sulfides, but it could be a more relevant hypothesis for HER in an acidic environment where H^+ adsorption is the first step of the two-electron transfer mechanism.[120] In alkaline media, Volmer-Heyrovsky ($H_2O + e^- \rightarrow H_{ad} + OH^-$, $H_2O + H_{ad} + e^- \rightarrow H_2 + OH^-$) and Volmer-Tafel ($H_2O + e^- \rightarrow H_{ad} + OH^-$, $H_{ad} + H_{ad} \rightarrow H_2$) processes are plausible,[120] however, H adsorption (H_{ad}) on both processes is expected to be dependent on the active surface site. On NiS surfaces, favored H adsorption on Ni sites has been found critical for higher H_2 turnover.[121] Calculations also suggest that both S and Ni sites on (001) terminated NiS_2 could be active but free energy of H adsorption on Ni sites is smaller.[122] Creation of S vacancies and facilitated H_2O dissociation in alkaline and acidic media further point out the importance of the under-coordinated Ni sites on the surface.[123], [124]

Despite the high HER activity of the transition metal sulfides, less work has focused on evaluating their stability and degradation behavior.[112], [125]–[131] In the course of HER, the surface compositions (1-2 nm depth) of the electrocatalyst are generally prone to modification while their inner structures remain intact, leading to alteration of the surface morphology and active surface area.[126] The durability of electrocatalysts is tested by a high number of repeated linear/cyclic voltammetry scans or long period chronoamperometry (CA)/chronopotentiometry (CP). However, the initial changes in the surface compositions and the morphologies, which are generally ignored, could mislead the determination of the active phase that is responsible for the high HER activity. For instance, Hofmann et al. have shown that the apparent electrochemical stability of Co_2P in alkaline media could be attributed to the increased ECSA by the formation of surface hydroxyl groups.[130] Similar alternations in the surface regions have also been reported for the TM sulfides. V-incorporated Ni_xS_y nanowires and CoMnS electrocatalyst have been shown to undergo instantly electrochemical cathodic reduction followed by the generation of surface hydroxyl groups.[128], [129] On the contrary, Zheng et al. have reported that NiS_2 flakes are electrochemically reduced to metallic Ni in alkaline media.[112] These studies indicate that NiS_2 could be identified as a pre-catalyst for HER,

but the mechanism behind the formation of new surface composition and corresponding activity is still unclear.

The mesoporous thin films have received growing attention for the electrochemical HER catalysis owing to their abundance of accessible mesopores, self-supporting nature, high surface area, and exposure of active sites, which can facilitate the charge transfer and reactant/product diffusion.[132]–[137] It has been shown that mesoporous CoS_2 microspheres provide superior HER activity compared to most of the previously reported catalysts and commercial CoS_2.[138]

Herein, we developed a novel and facile one-step protocol that could be classified as a truly soft-templating method without any post-sulfurization process to obtain mesoporous nickel sulfides electrodes. The self-assembly of surfactants with TM salts and S precursor (thiourea) have been soft-templated into the liquid crystalline system and turn into the mesoporous nickel sulfides electrodes with ultra-thin pore walls after heat treatment. We compared the electrochemical HER activities of mesoporous metal sulfides electrodes including the phases of NiS_2, NiS, Ni_3S_2, Ni_7S_6 and mixed of some of them in alkaline and acidic electrolyte. We revealed that the mesoporous nickel sulfides undergo the dissolution toward HER in the acidic electrolyte. The mesoporous NiS_2 shows the best HER activity in alkaline electrolyte compared to other mesoporous nickel sulfides electrodes. Mesoporous NiS_2 films show a dynamic HER activity with overpotential ranged between 160 and 260 mV for 10 mA/cm^2 in an alkaline media while providing a platform to reveal the roles of the surface structures in the activity. It has been found that mesoporous NiS_2 experiences instant transformations from the mesoporous crystalline phase into a Ni enriched amorphous sulfide film structure. The surfaces of the latter are prone to a reaction with OH^- under open-circuit conditions, resulting in a temporary enhancement in the HER activity.

4.2 Experimental Section

4.2.1 Preparation of Mesoporous Metal Sulfide Electrodes on FTO

The metal sulfides, synthesized using liquid crystalline templating over a flat fluorine doped tin oxide (FTO) coated glass slides, were used for hydrogen evolution reaction (HER). Before spin coating, FTO (1 cm × 2 cm) substrates were cleaned by ultra-sonication in absolute ethanol. The electrodes were prepared by spin coating the solutions of the corresponding composition as given in Chapter 3. Scotch-tape was used to make

an area of 1 cm^2 on FTO for spin-coating. A few drops of the solution described above was placed on the FTO and it was spun for 30 s at 1000 rpm by a spin coater. After spin coating, the films were sandwiched between FTO and another glass slide placed on top to prevent the release of sulfurous gas without reacting with Ni^{2+}. The mesophase film over the FTO was annealed at various temperatures in a nitrogen (N_2) atmosphere for 2 hours. The heat-treated films below 300 °C were dipped into deionized water for 3 times to wash the surfactants. The electrochemical measurements like LSV, CV and CA and also the analysis such as ICP, XPS, TEM, SEM, EDX, etc. were conducted using the electrodes. Schematic illustration of the fabrication of electrodes are presented in Figure. 4.1. The mesoporous films are labelled according to their nickel sulfide phase. In Table 4.1, the annealing process, the composition of the nickel sulfide phase and the Ni/S ratio are tabulated.

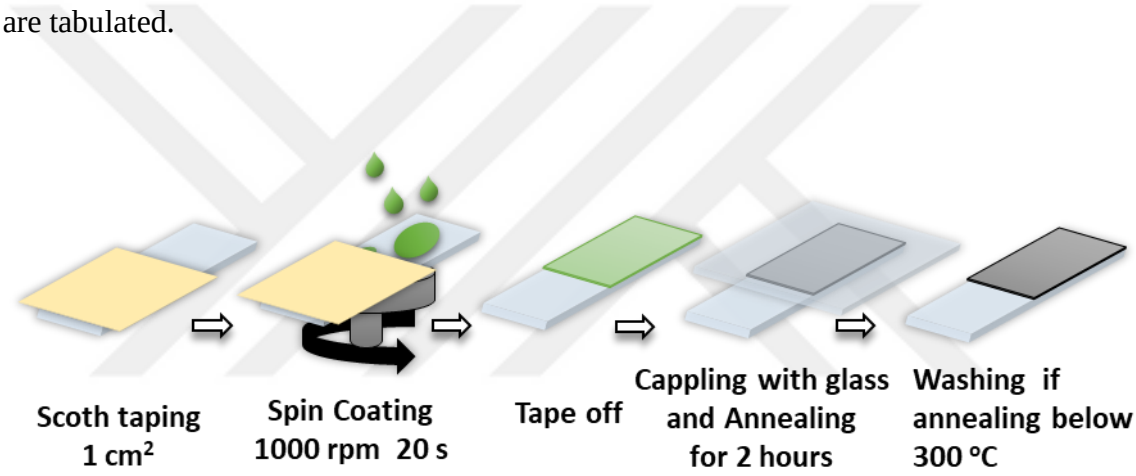

Figure 4.1 Schematic illustration of the fabrication of mesoporous metal sulfides electrodes on FTO substrates

Table 4.1 The notation of the mesoporous nickel sulfide electrodes by mole ratios of Ni/S, annealing temperature and nickel sulfide phase

Mole ratios (Ni salt/Thiourea)	**Annealing temperature (°C)**	**Nickel sulfide phase**	**Notation for electrodes**
06/12	185	NiS_2	Mesoporous NiS_2
06/12	300	Mainly NiS + NiS_2	Mesoporous NiS + NiS_2
06/12	400	NiS	Mesoporous NiS
06/06	300	Ni_3S_2	Mesoporous Ni_3S_2
06/09	300	Mainly NiS + Ni_7S_6	Mesoporous NiS + Ni_7S_6

4.2.2 Preparation of Mesoporous NiS_2 on Ni Foam

A similar procedure has been applied for the preparation of mesoporous NiS_2 on Ni foam. Ni foam (99.99% purity, 346 g/m2 of surface density, and 1.6 mm of thickness) were purchased from MTI corporation. Before spin-coating, Ni foam pieces (1 cm × 1 cm) were well-cleaned by ultra-sonication in absolute ethanol for 5 minutes. A few drops of the solution described for mesoporous NiS_2 on the Ni foam (20 s at 1000 rpm). Then, the sample was placed into the paraffin oil at 185 °C for 2 hours. The heat-treated samples were dipped into deionized water for 3 times to wash the surfactants.

4.3 Instrumentation

A Zeiss Supra 50VP SEM with an accelerating voltage of 20 kV equipped with an energy dispersive spectrometer (EDX) was used to analyze the film morphology and composition of the samples on FTO after and before HER activity tests. Low- and high-resolution TEM images and EDX elemental mapping were performed on a Jeol JEM 2100F field emission electron microscope under 200 kV. X-ray photoelectron spectroscopy (XPS) measurements were conducted using a Thermo K-alpha spectrometer system with Al Kα radiation as the excitation source. Binding energies for the XPS spectra were calibrated by setting C 1s binding energy to 284.5 eV. BET surface area and BJH pore-size distribution of all synthesized materials were measured using a Micromeritics ASAP 2020 automated gas sorption analyzer. Ni and S contents in the electrolyte were determined using a Perkin Elmer Optima 8300 ICP-OES analyzer. Polarized optical microscopy (POM) images of the mesophases were recorded using a ZEISS Axio Scope A1 polarizing optical microscope.

4.4 Electrochemical Measurements

All electrochemical measurements were performed in a three-electrode setup using a GAMRY Reference 3000 and Biologic VSP 300 potentiostat/galvanostats. Pt wire was used as a counter electrode. The reference electrode was Ag/AgCl/KCl (sat.d), activity measurements were performed in 1 M KOH and 0.5 M H_2SO_4. The standard potential of a reference electrode was checked relative to another reference electrode that was never used in experiments and was always properly stored. The measured potentials vs. Ag/AgCl were converted to the reversible hydrogen electrode (RHE) scale according to the Nernst equation: $E_{RHE} = E_{Ag/AgCl} + 0.059 \times pH + E^{\circ}_{Ag/AgCl}$ where E_{RHE} is the converted

potential vs. RHE, $E°_{Ag/AgCl}$ = 0.198 V at 25 °C, and $E_{Ag/AgCl}$ is the experimentally measured potential against Ag/AgCl reference electrode

4.4.1 Linear Sweep Voltammetry

A scan rate of 5 mV/s was used in the linear sweep voltammetry (LSV) measurements. All LSV plots were corrected with %100 iR compensation for ohmic losses. Current interrupt iR compensation mode in the software of GAMRY Reference 3000 potentiostat/galvanostat was selected. LSV plots with and without iR compensation are shown in Figure 4.2 for clarity. Current Interrupt IR Compensation was used for %100 iR compensation. In this technique, a current interrupt measurement is after each point, and a determination of the uncompensated resistance is made based on the drop in the voltage measurement. This technique is more reliable for any case in the instability of catalyst during electrochemical reactions due to instant changes in impedance.

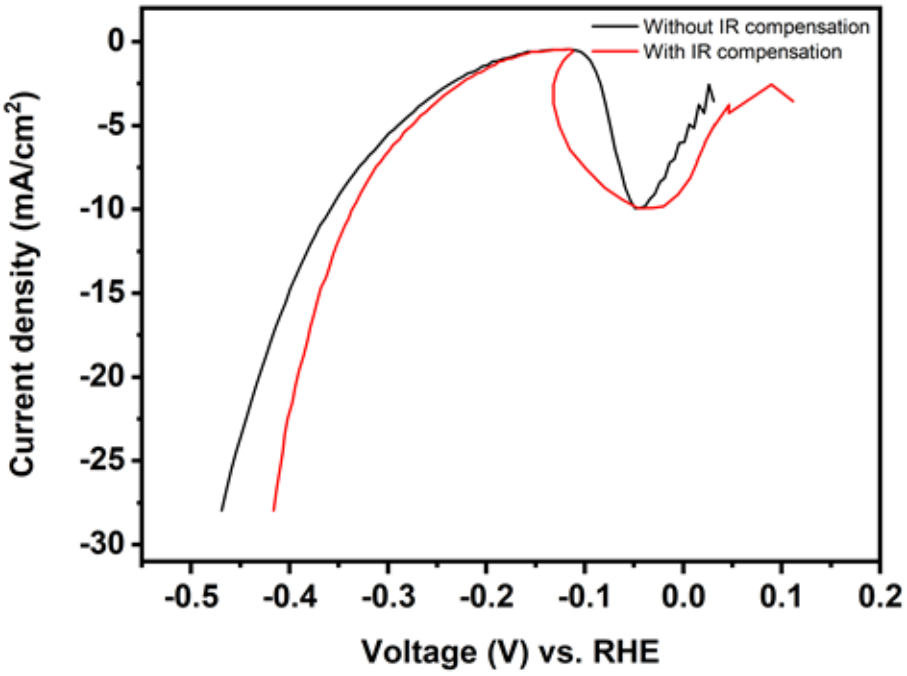

Figure 4.2 The first LSV run of the mesoporous NiS_2 with and without iR compensation in 1 M KOH.

4.4.2 Chronoamperometry (CA)

Chronoamperometry (CA) tests were performed at a constant potential of -0.4 mV without iR compensation by using Pt counter electrode for long-term durability tests over HER in a glass electrochemical cell. The CA tested electrode investigated by using Pt counter electrode was digested to demonstrate the absence of Pt deposited on the working electrodes by ICP-OES, see Figure 4.3.

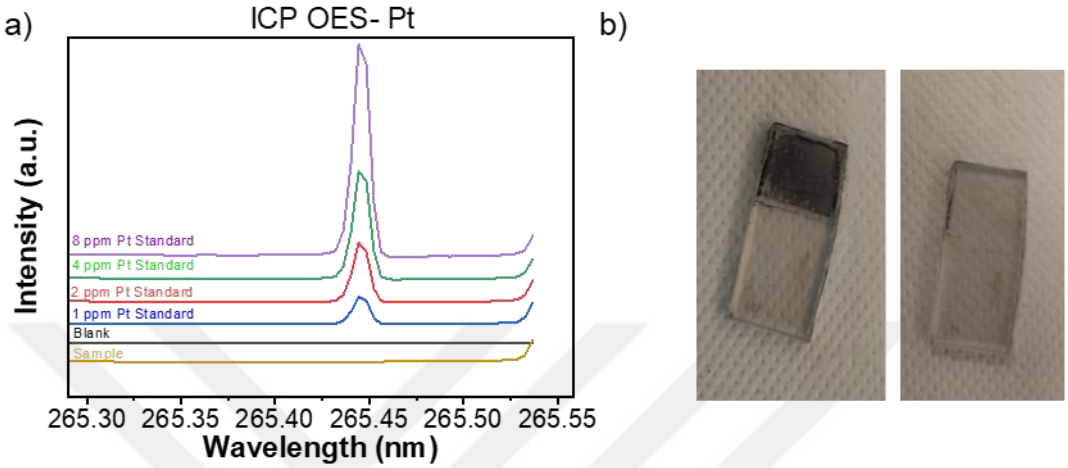

Figure 4.3 (a) The ICP-OES spectrum of the sample CA tested by using Pt as counter electrode confirming the absence of Pt.(b) The CA tested electrode before (left) and after (right) acid digestion in 6 M HNO_3.

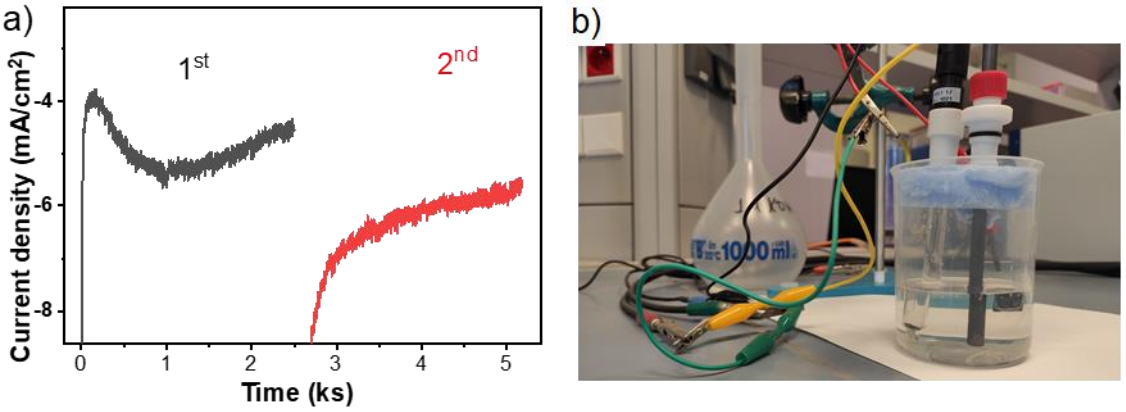

Figure 4.4 (a) CA runs under a static potential of -0.4 V vs. RHE in a plastic cell using graphite rod as a counter electrode. (b) The photo of the plastic cell.

A CA test was also conducted in a plastic electrochemical cell with a graphite counter electrode (see Figure 4.4b) to confirm that silicates that could potentially dissolve in the presence of KOH electrolyte have no effect on the activity. As seen in Figure 4.4a,

the first and following CA runs show current density behavior identical to the ones presented in Figure 4.11, ruling out the contribution of elements dissolved from glass cells and Pt counter electrode to the presented results. Moreover, CA tested NiS_2 coated on the FTO was digested in 6 M HNO_3 in order to check plausible trace elements deposited during electrochemical tests by ICP-OES (see Figure 4.5). Sigma-Aldrich multi-element VIII calibration standard solution for ICP-OES was used to detect metal contents in the digested CA tested sample. Only Ni metal was detected.

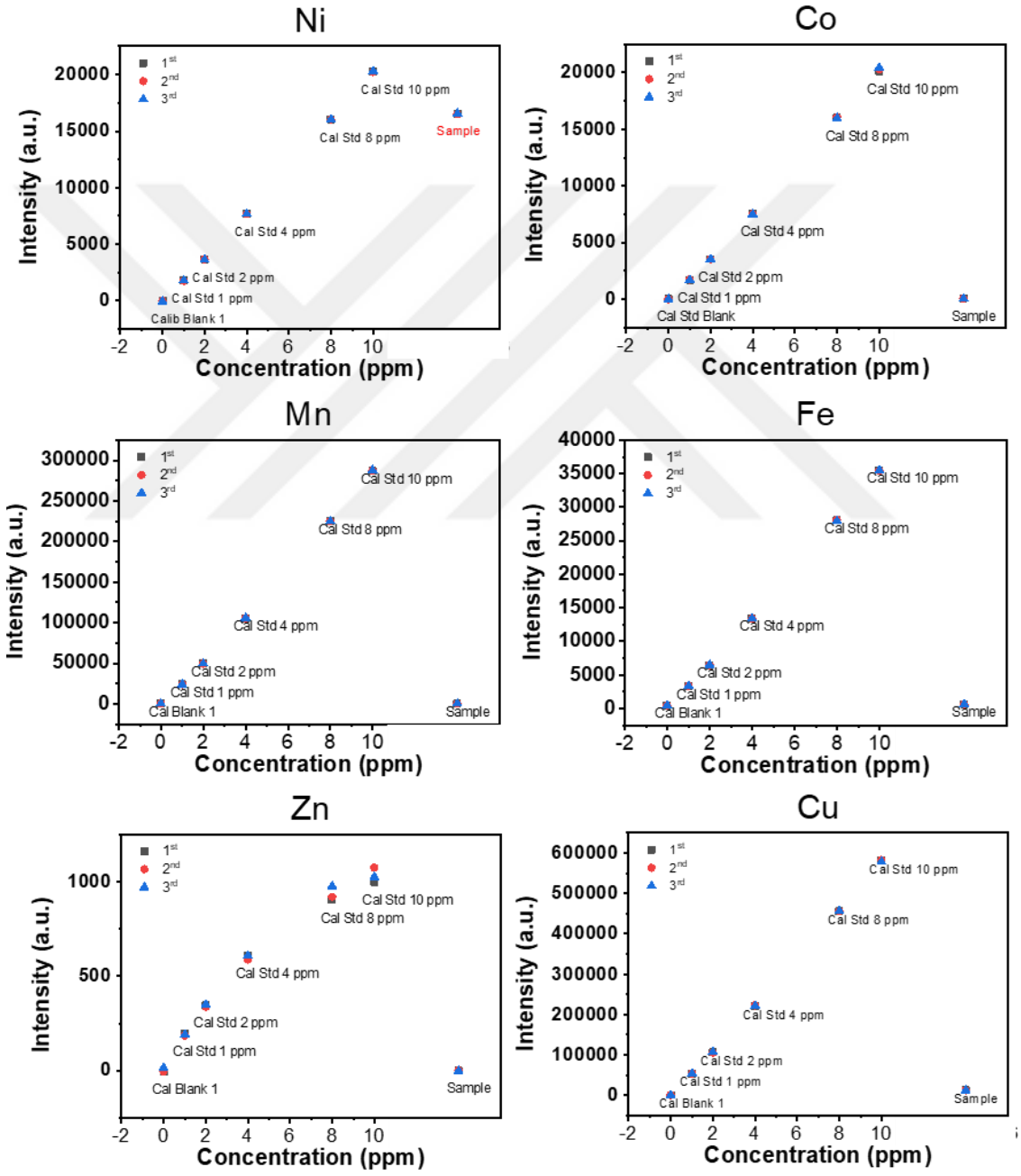

Figure 4.5 The concentrations of some trace metals that could be considered as electrochemically active impurities. They were obtained by ICP-OES measurements from the CA tested electrodes that were acid-digested.

4.4.3 Double-layer Capacitance

CV for the determination of double-layer capacitance was carried out from 0.18 to 0.30 V vs. RHE in 1 M KOH solution where no obvious Faradic reaction took place. The cyclic voltammograms was taken by increasing scan rate from 50 mV/s to 250 mV/s with the interval of 50 mV/s. The capacitive current density was measured from the CVs at different scan rates, as shown in Fig 4.6a. The relation between current density, the scan rate and the double-layer capacitance (C_{dl}) was given in eq 4.1.

$$\text{The current density} = \text{The scan rate} \times C_{dl} \quad (4.1)$$

Therefore, the slope of current density as a function of scan rate gives a straight line with the slope equal to C_{dl}. For calculation of double-layer capacitance, the capacitive current densities at 0.24 V vs. RHE were used in the plots of capacitive currents vs. scan rates, see Figure 4.6b.

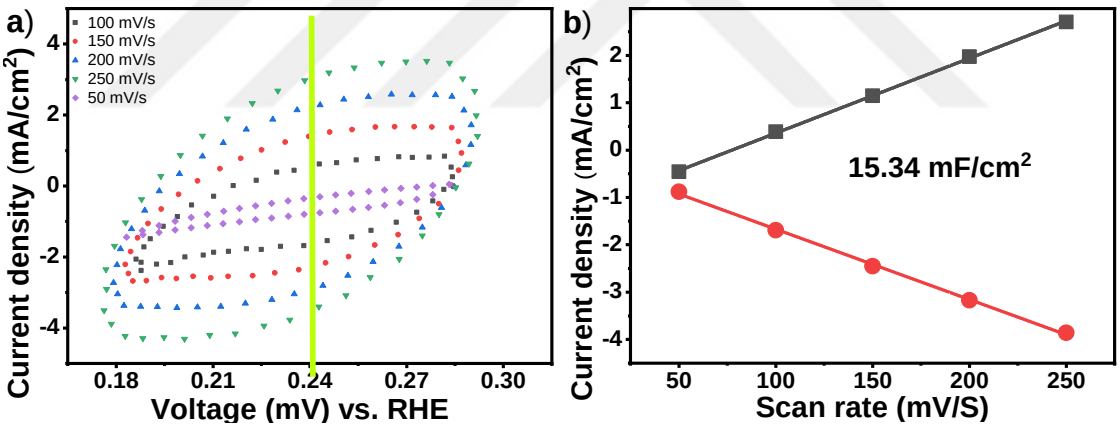

Figure 4.6 (a) An example of CV curves of electrode in a non-faradic region in 1.0 M KOH at the scan rates of 50, 100, 150, 200, and 250 mV/s. (b) Capacitive currents are plotted as a function of the scan rate.

4.4.4 Electrochemical Impedance Spectroscopy (EIS)

The electrochemical impedance spectroscopy (EIS) measurements were carried out under a static potential of -0.4 V vs. RHE for the frequency regime between 0.1 Hz and 100 kHz. The electrolyte solution was purged with N_2 for 30 min before each test.

4.4.5 Faradaic Efficiency (FE) Calculations

Product analysis and Faradaic efficiency (FE) calculations were performed via collecting gaseous species in the headspace of the sealed electrochemical cell by means of a Hiden HPR 20 mass spectrometer. The electrolyte solution was purged with N_2 extensively for 30 min before the measurements. A three-electrode setup was used. The gas collection was performed on-line by attaching the head of the capillary tube of the mass spectrometer to the electrochemical cell. FE was calculated using the formula given below:

$$FE = \frac{n_{H_2}}{\frac{Q}{eF}} \quad (4.2)$$

In this formulation n is the number of moles of H_2 produced, Q is the charge (C), e is the number of electron transfer (2 for HER), and F is the Faraday's constant. Q was calculated by multiplying electrochemical current recorded by time. To determine n, H_2 pressure signal in the mass spectrometer was calibrated against H_2/Ar gas mixture with known composition fed into the mass spectrometer. A calibration plot was obtained by adjusting the H_2 amount in H_2/Ar gas mixture and was used to quantify H_2 produced in HER.

4.5 Hydrogen Evolution Reaction (HER) Activity of Mesoporous Nickel Sulfide Thin Films in an Acidic Media

We investigated the HER activities of mesoporous nickel sulfide thin films electrodes on FTO in an acidic electrolyte, 0.5 M H_2SO_4. Seven consecutive LSV scans were recorded for each electrode with different nickel sulfide composition, see Figure 4.7.

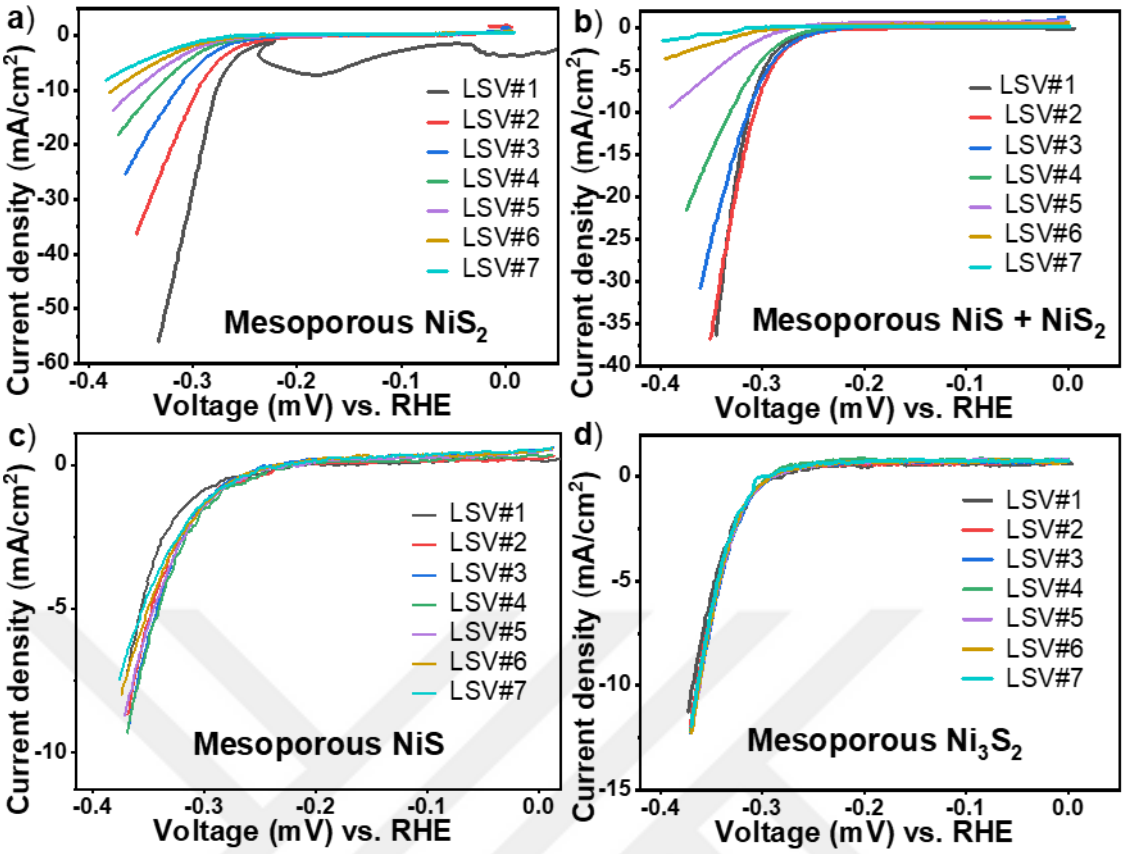

Figure 4.7 Consecutive LSV plots for (a) mesoporous NiS_2, (b) mesoporous NiS + NiS_2, (c) mesoporous NiS and (d) mesoporous Ni_3S_2 on FTO in 0.5 M H_2SO_4.

At the beginning of the first LSV scan set, a cathodic current is observed at the potentials spanned between 0 and 150 mV for mesoporous NiS_2 on FTO. Mesoporous NiS_2 shows the best HER activity, the follows mesoporous NiS+ NiS_2, mesoporous Ni_3S_2 and mesoporous NiS. In addition, we noticed that all phases of nickel sulfide electrodes in order of NiS_2, NiS + NiS_2, NiS and Ni_3S_2 is not stable under HER. The activity decreases after each LSV cycle. The most marked decrease in activity are for mesoporous NiS+ NiS_2 and mesoporous NiS_2. Therefore, we have initially conducted a visual analysis on those tested samples for the observed enormous decrease in activity, mesoporous NiS_2 and NiS+ NiS_2. Later, extended the comprehensive analysis with SEM with EDS in order to understand the changes in HER activity, see Figure 4.8.

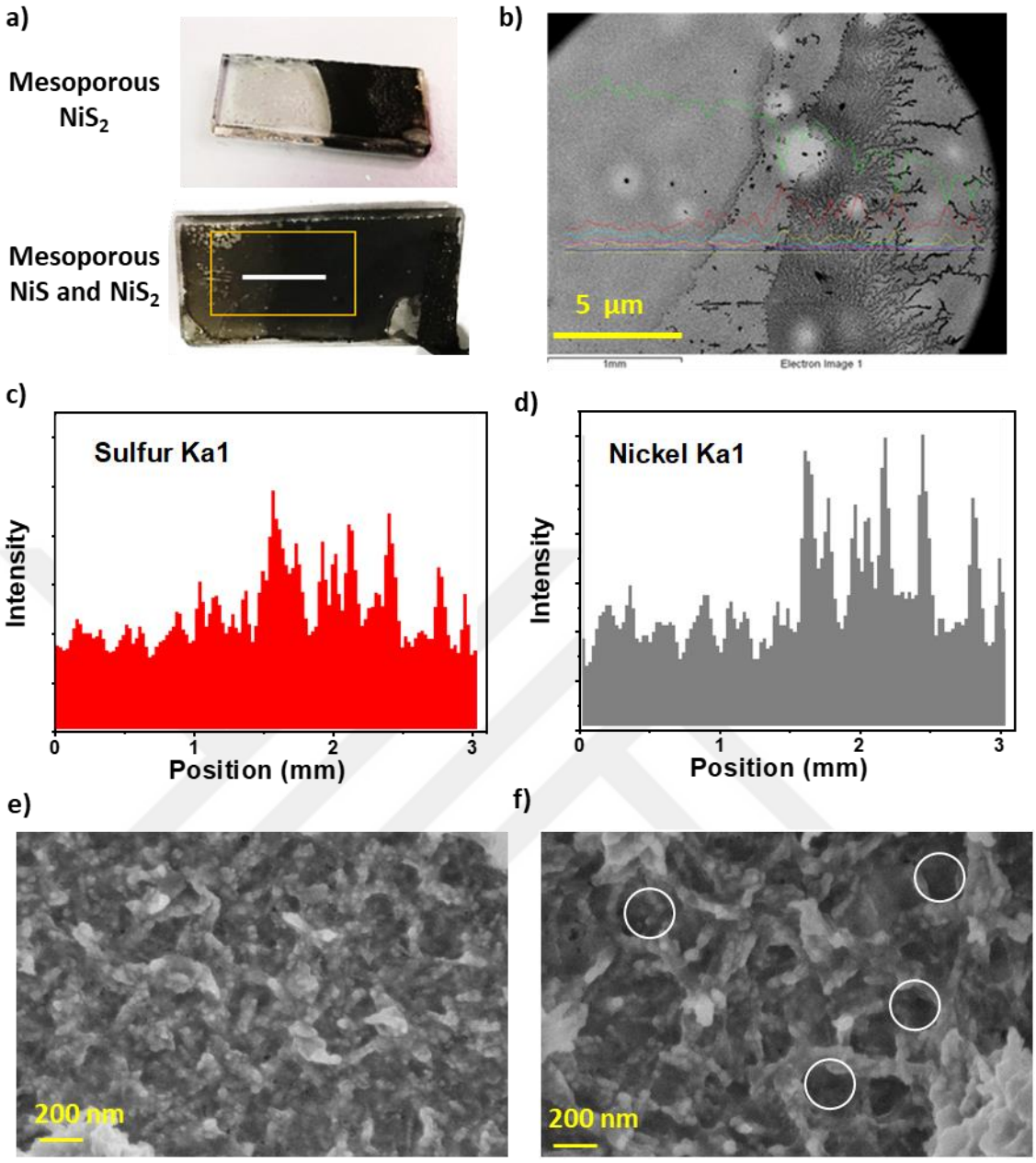

Figure 4.8 (a) The photograph of mesoporous NiS_2 and NiS + NiS_2 on FTO after seven LSV. The left side of rectangular yellow area is dipped into electrolyte and right side is not dipped into electrolyte. (b) SEM image of rectangular are of mesoporous NiS +Ni_3S_2. The EDS line analysis for sulfur Ka1 (c) and nickel Ka1 (d). High-resolution SEM image of as-prepared (e) and LSV tested sides (f) of mesoporous NiS + NiS_2 thin film on FTO.

In the photographic images of HER tested of mesoporous NiS_2 and NiS +NiS_2 on FTO, Figure 4.8a, rigorous dissolution in acidic environment dismantles the nickel sulfides from the FTO. Dipped into the electrolyte and HER tested side of mesoporous NiS_2 electrode almost was vanished. The decrease in the contrast between HER tested and not sides of other electrode was detectable by the naked eye, justifying dissolution of nickel sulfide species. In the detailed SEM analysis with EDS on the interphase of HER tested and not tested sides of mesoporous NiS + NiS_2, the intensities of nickel and sulfur decrease where the sample are tested, see Figure 48c-d. Remember that the surfactants are carbonized in this sample and form carboneous framework along with the film. When we compare the tested and non-tested part of the detailed high-resolution SEM images of mesoporous NiS and NiS_2, around 200 nm voids were formed during HER and some 20-25 nm features still remained, see Figure 4e-f.

After seven consecutive LSV scan, HER activity of the sample almost disappeared. We can assume that those nickel sulfide species are covered by carbon, preventing leaching out. Due to blockage of contact with electrolyte by carbon, they are not active anymore. On the other hand, the pure washed mesoporous NiS_2 electrode does not contain carbon because of low temperature annealing. All NiS_2 crystallites have accessible mesopores and high surface area therefore; exposure to acidic electrolyte consequently dissolves stoichiometrically in acid. Pure mesoporous NiS and Ni_3S_2 have larger crystallites, carbon framework and lower accessible surface due to higher annealing temperature as discussed in the previous chapter. This may be an explanation of higher durability and lower activity compared to other electrodes. To sum up, nickel sulfides are active on HER but not stable electrocatalyst in acidic environment contrary to many examples in the literature. The ideal electrocatalysts, like mesoporous NiS_2, are not only significant for high activity, but also for straightforward understanding of stability. If they are not stable against corrosion in the electrolyte, they disappeared even in a short period of electrochemical reaction. Our results are also consistent with the dissolution of Co_2P electrocatalyst under HER in acidic environment.[133]

4.6 Hydrogen Evolution Reaction (HER) Activity of Mesoporous Nickel Sulfide Thin Films in an Alkaline Media

After we investigated the HER activities and stabilities of mesoporous nickel sulfide thin films electrodes on FTO in the acidic electrolyte, 0.5 M H_2SO_4, we have decided to investigate HER activities of them in alkaline electrolyte,1 M KOH.

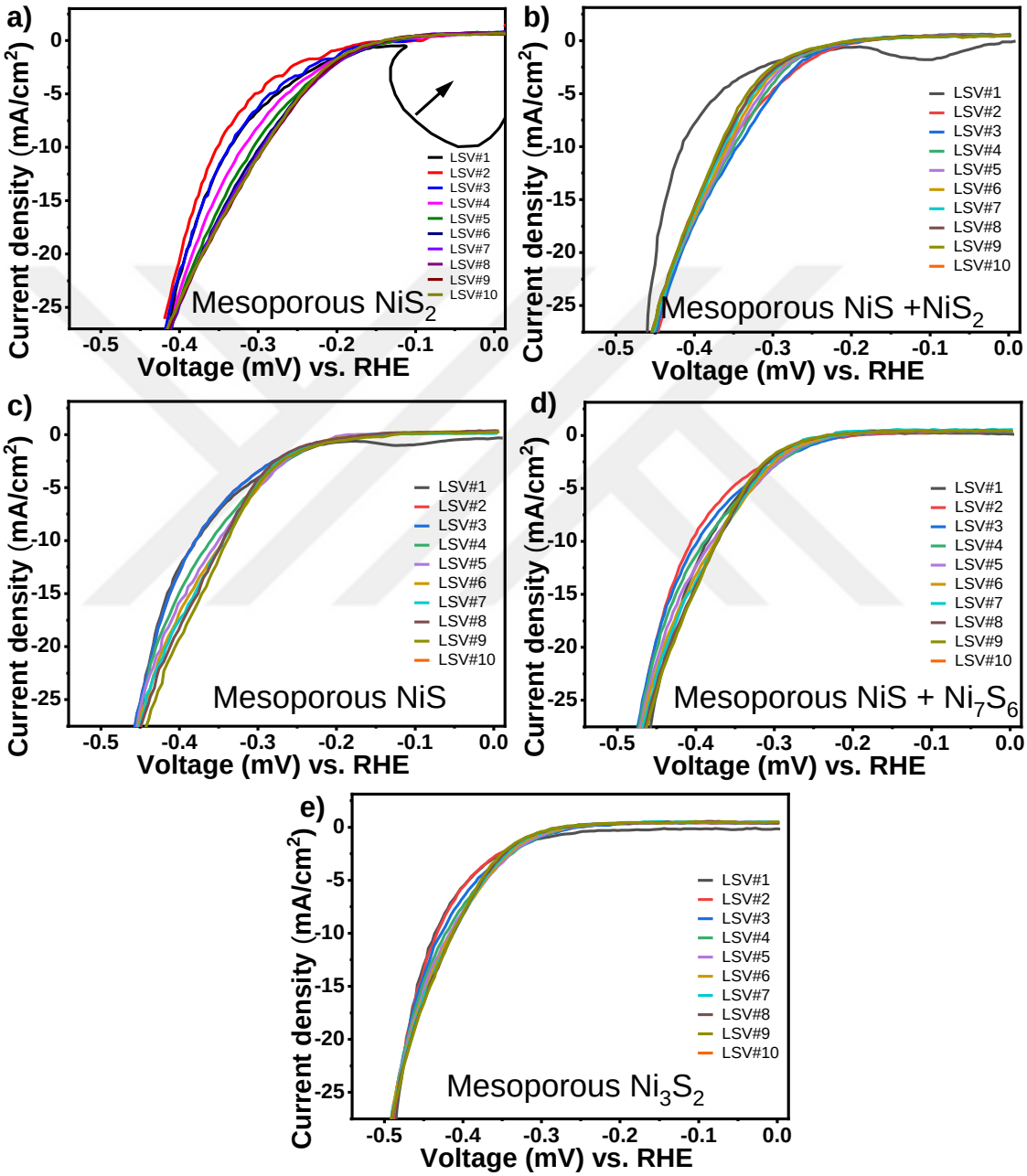

Figure 4.9 Consecutive LSV plots for (a) mesoporous NiS_2, (b) mesoporous NiS + NiS_2, (c) mesoporous NiS,(d) mesoporous NiS and Ni_7S_6 and (e) mesoporous Ni_3S_2 on FTO in 0.5 M H_2SO_4.

Ten consecutive LSV scans were recorded for each electrode with different nickel sulfide composition, see Figure 4.9. The most active phase towards HER in alkaline environment again is belonging to the mesoporous NiS_2 electrode. At the beginning of the first LSV scan set, a cathodic current is observed at the potentials spanned between 0 and 150 mV for mesoporous NiS_2 and mesoporous NiS+ NiS_2 electrodes on FTO. However, it is observed that HER activity is dynamic; each LSV scan shows deviations for all phases of mesoporous nickel sulfide electrodes. On the contrary, their HER activities are increased with each LSV scan. If dissolution happens on the nickel sulfide phases, they must lose their HER activity. As discussed earlier, mesoporous NiS_2 electrodes are likely to be close to an ideal electrocatalyst; therefore we have decided to investigate its activity and stability towards HER in an alkaline environment in detail to reveal this unusual change.

4.7 Mesoporous NiS_2 as an Idealized Pre-electrocatalyst for Hydrogen Evolution Reaction

We investigated the HER activities of mesoporous pyrite NiS_2 thin-film electrodes in alkaline electrolytes. In addition to FTO, Ni foam was used as a substrate to increase the geometrical surface area and the mass loading of catalyst. The polarization curves of bare Ni foam, mesoporous NiS_2 on Ni foam are compared with those of crystalline NiS_2 and commercial Pt/C on Ni foam in Figure 4.10a. The mesoporous NiS_2 appears to exhibit rather high activity with lower onset potential for HER compared to other reported pure NiS_2 electrocatalysts.[111], [112], [122], [139]–[142] However, it is observed that HER activity is dynamic, each LSV scan shows deviations for both mesoporous NiS_2 on Ni foam and FTO, as seen in Figure 4.10b and c, respectively. After the first set of consecutive LSV scans, the electrodes were kept in the electrolyte for 3 minutes without any bias. Then, the second set of LSV scans were recorded, consecutively. At the beginning of the first LSV scan set, a cathodic current is observed at the potentials spanned between 0 and 150 mV for both mesoporous NiS_2 on Ni foam and FTO. Note that H_2 bubble formation was not observed despite a high current density recorded (~10 mA/cm^2). The initial LSV scan of the second set shows the best activity, however, the activity deteriorates after subsequent scans.

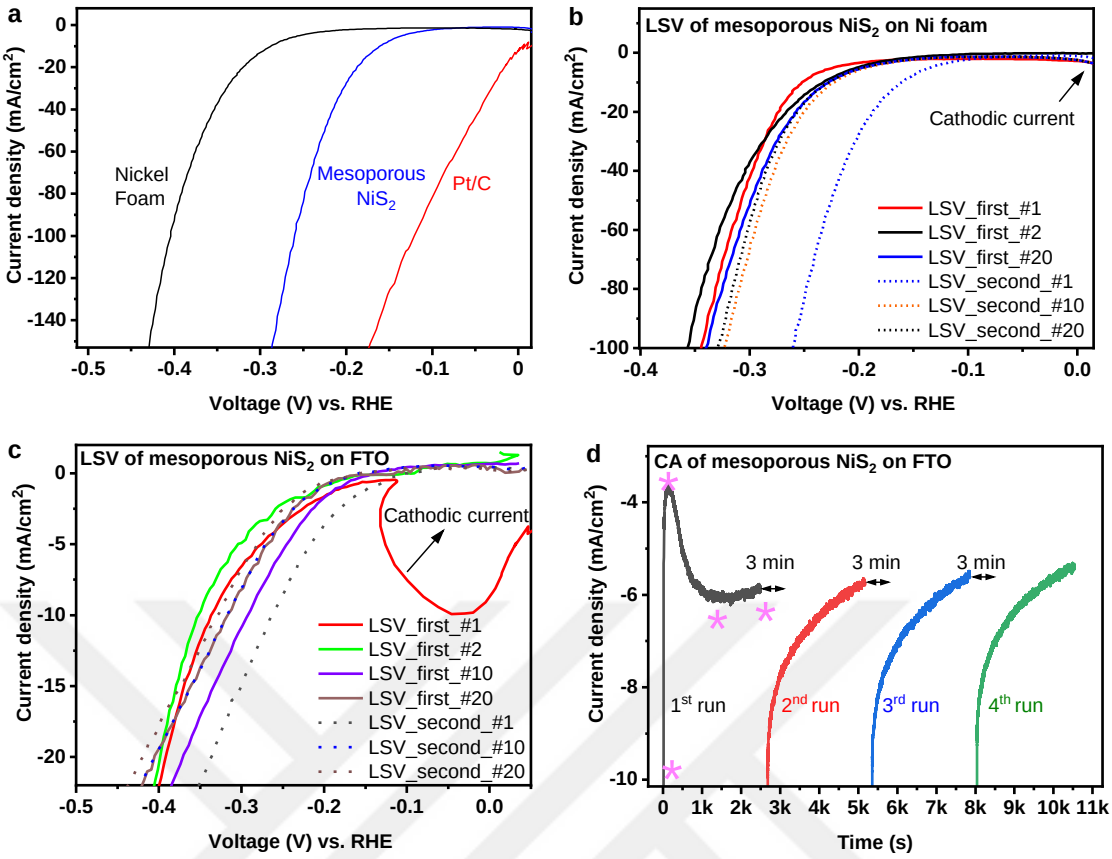

Figure 4.10 (a) LSV plots for bare Ni foam, mesoporous NiS_2 and commercial %20 Pt/C on Ni foam in 1 M KOH. (b) Consecutive LSV plots for mesoporous NiS_2 on Ni foam in 1 M KOH. (c) Consecutive LSV plots for mesoporous NiS_2 on FTO in 1 M KOH. (d) Four consecutive CA runs under a static potential of -0.4 V vs. RHE for the mesoporous NiS_2 on FTO. Between each run, the electrode is rested for 3 min under open-circuit conditions.

To understand the dynamic changes in HER activity, CA curves under a static potential of - 0.4 V vs. RHE were recorded (Figure ***4.10***d). We adapted the consecutive LSV analysis therefore mesoporous NiS_2 on FTO was kept in the electrolyte for 3 min without applying any bias between each measurement. The CA behavior matches well with the dynamic activity changes observed in successive LSV scans. As in the initial LSV scans of the first set, a significant cathodic current is observed in the first CA run. The current density suddenly decreases and reaches a minimum at -3.6 mA/cm^2 within a few minutes. Then, it shows a more gradual increase, reaches ~-6 mA/cm^2 in 1500 s, and subsequently decreases in time. In the second CA run, the highest current density is reached initially, but it does not go through a minimum as in the first CA run. For each CA run after resting under unbiased conditions the same trend is observed (3^{rd} and 4^{th} CA

runs), similar behavior in the extended number of runs can be seen in Figure 4.11. These observations suggest that the dynamical CA behavior observed for the mesoporous phase is unique and critical for its HER activity.

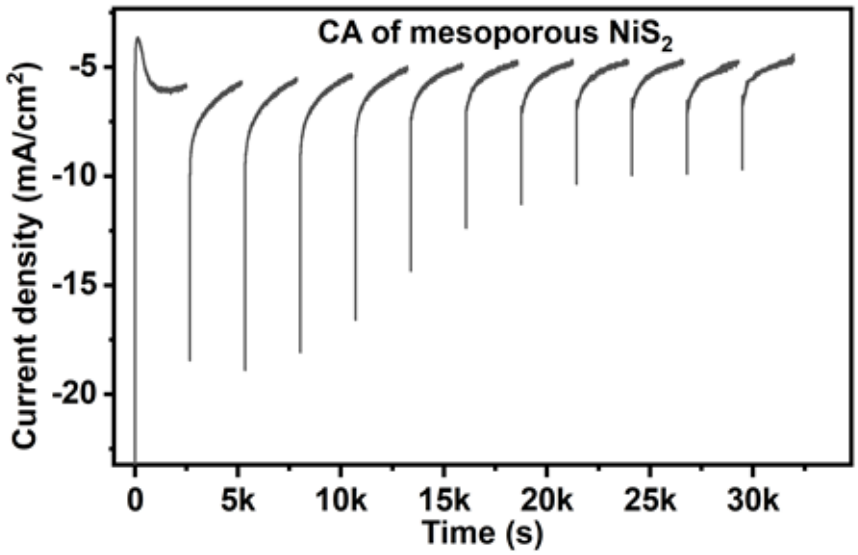

Figure 4.11 12 consecutive CA runs under a static potential of -0.4 V vs. RHE.

To elucidate the dynamic behavior in HER, the morphological and compositional analysis was performed using SEM and EDX. Pink stars in Figure 4.10a shows four significant points in the first CA run selected to determine the Ni/S atomic ratios. Detailed SEM images and their EDX spectra are given in Figure 4.12a-d. As the negative bias is applied, the Ni/S atomic ratio of as-prepared mesoporous NiS_2 changes from 1/2 to 1/1, manifesting a significant compositional change. Recent investigations show that NiS_2 undergoes a structural and compositional change during HER in alkaline conditions and the HER has been associated with the metallic Ni generated under reaction conditions rather than the surface of NiS_2.[112] Initially, the disulfide (S_2^{2-}) are electrochemically reduced to sulfide (S^{2-}), generating the cathodic current (Figure 4.10c), and consequently sulfurous species are leached into the electrolyte,[128] which lead to amorphization of NiS_2.

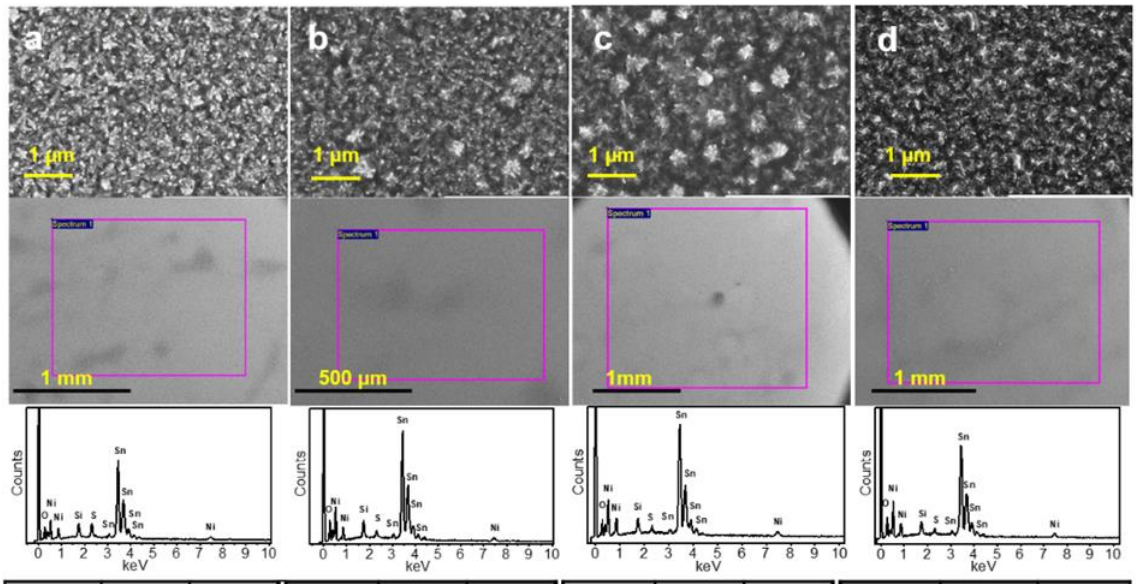

Element	Weight %	Atomic %
S K	51.07	65.65
Ni K	48.93	34.35
Total	100	

Element	Weight %	Atomic %
S K	29.72	43.63
Ni K	70.28	56.37
Total	100	

Element	Weight %	Atomic %
S K	21.23	33.04
Ni K	78.77	66.96
Total	100	

Element	Weight %	Atomic %
S K	23.90	36.51
Ni K	76.10	63.49
Total	100	

Figure 4.12 SEM and EDX analysis on mesoporous NiS_2 on FTO after CA test under a static potential of -0.4 V vs. RHE. (a) t=0 s, (b) t=100 s, (c) t=1000 s, and (d) t= 2500 s.

The HR-TEM images presented in Figure 4.13a demonstrate amorphization, the lattice fringes clearly visible in as-prepared NiS_2 completely disappear. HAADF images taken from the electrodes CA tested for 100 s (Figure 4.13c) show that the mesoporosity still exists even after electrochemical reduction. When the HER activity gets enhanced, the Ni/S atomic ratio become 2/1. This suggests that leaching of the sulfurous species into the electrolyte continues over time in CA runs. Later, Ni/S atomic ratio remains unchanged, and yet the HER activity slightly decreases. HAADF image shown in Figure 4.13d evidences the modification of the mesoporous structure within 1000 s of the CA run, which is further confirmed by the detailed HRTEM investigations on the structural changes (Figure 4.13b).

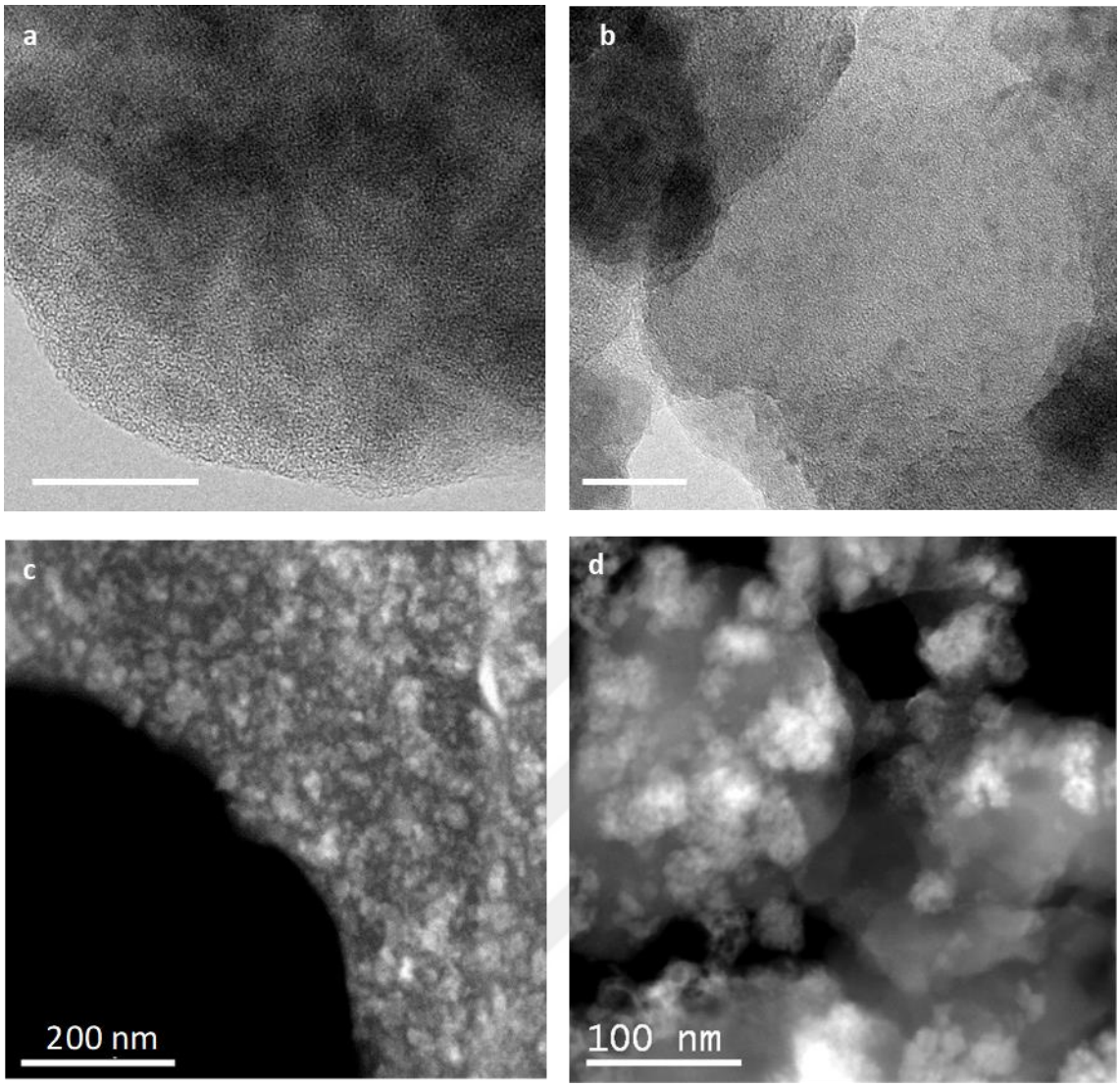

Figure 4.13 . HR-TEM images of the mesoporous NiS_2 after CA at -0.4 V vs. RHE. (a) t=100 s and (b) t=1000 s. HAADF TEM images of electrodes. (c) t=100 s and (d) t=1000 s.

The Ni and S concentrations in the electrolyte analyzed by ICP-OES at the selected regions of CA test demonstrate that Ni leaching is negligible whereas S concentration increases over time (Figure 4.14). Ni, S, and O atomic fractions determined by TEM/EDX analysis shown in Figure 4.15 confirm Ni enrichment in the course of CA, also consistent with the SEM/EDX findings. Only a small region in the HAADF-TEM image show higher S content with mesoporosity.

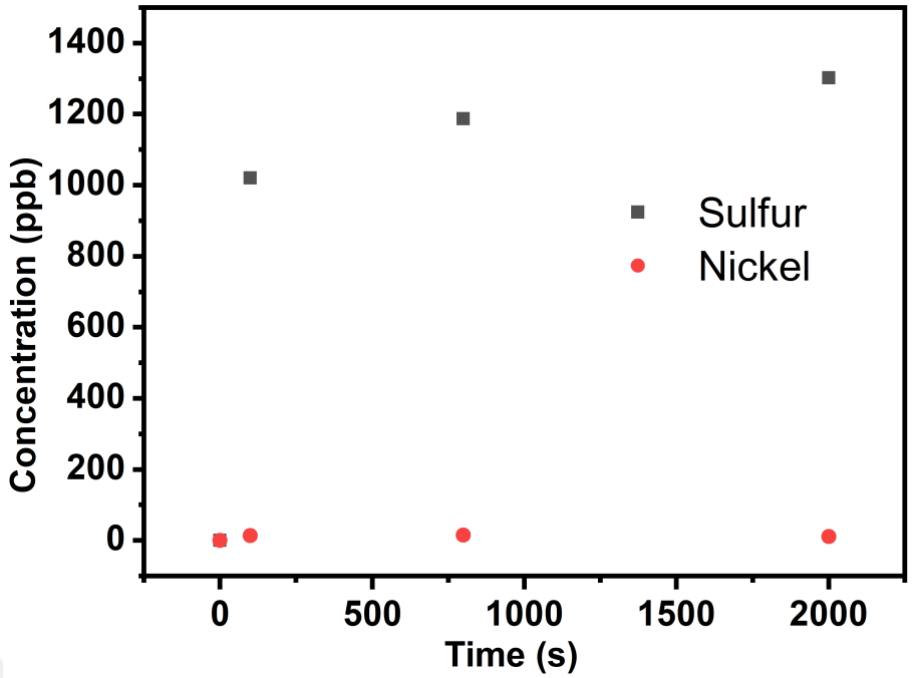

Figure 4.14 ICP-OES analysis on the concentration of nickel and sulfur in the electrolyte during CA at -0.4 V vs. RHE.

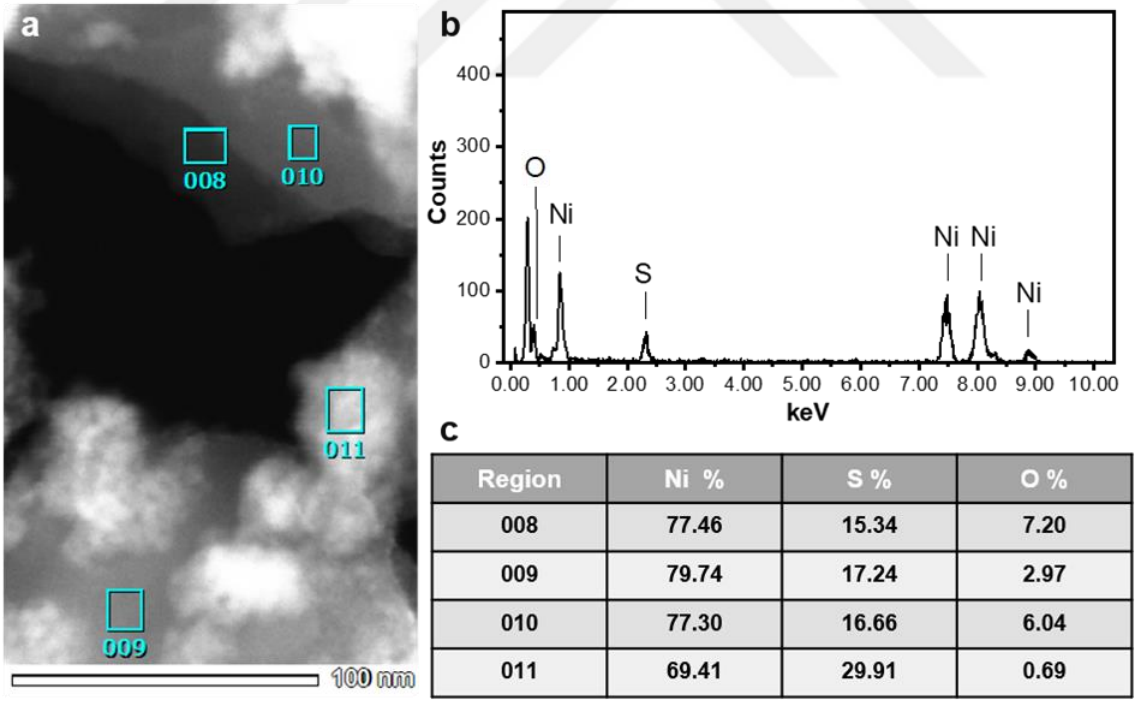

Region	Ni %	S %	O %
008	77.46	15.34	7.20
009	79.74	17.24	2.97
010	77.30	16.66	6.04
011	69.41	29.91	0.69

Figure 4.15 (a) HAADF image of the mesoporous NiS_2 on FTO after CA test at -0.4 V vs. RHE for 2500 seconds (b) EDX spectrum of a selected region (008). (c) Nickel, sulfur, and oxygen atomic ratios for the selected regions.

ECSAs of the electrodes are typically proportional to the electric double-layer capacitance (C_{dl}), which can be derived from the CV curves in a non-faradaic region. Therefore, we also track the changes in the C_{dl} of mesoporous NiS_2 in the course of cathodic reduction in CA runs. As seen in Figures 4.16a-f, the C_{dl} of the mesoporous NiS_2 decreases from 15.34 mF/cm^2 to 3.63 mF/cm^2 after 100 s.

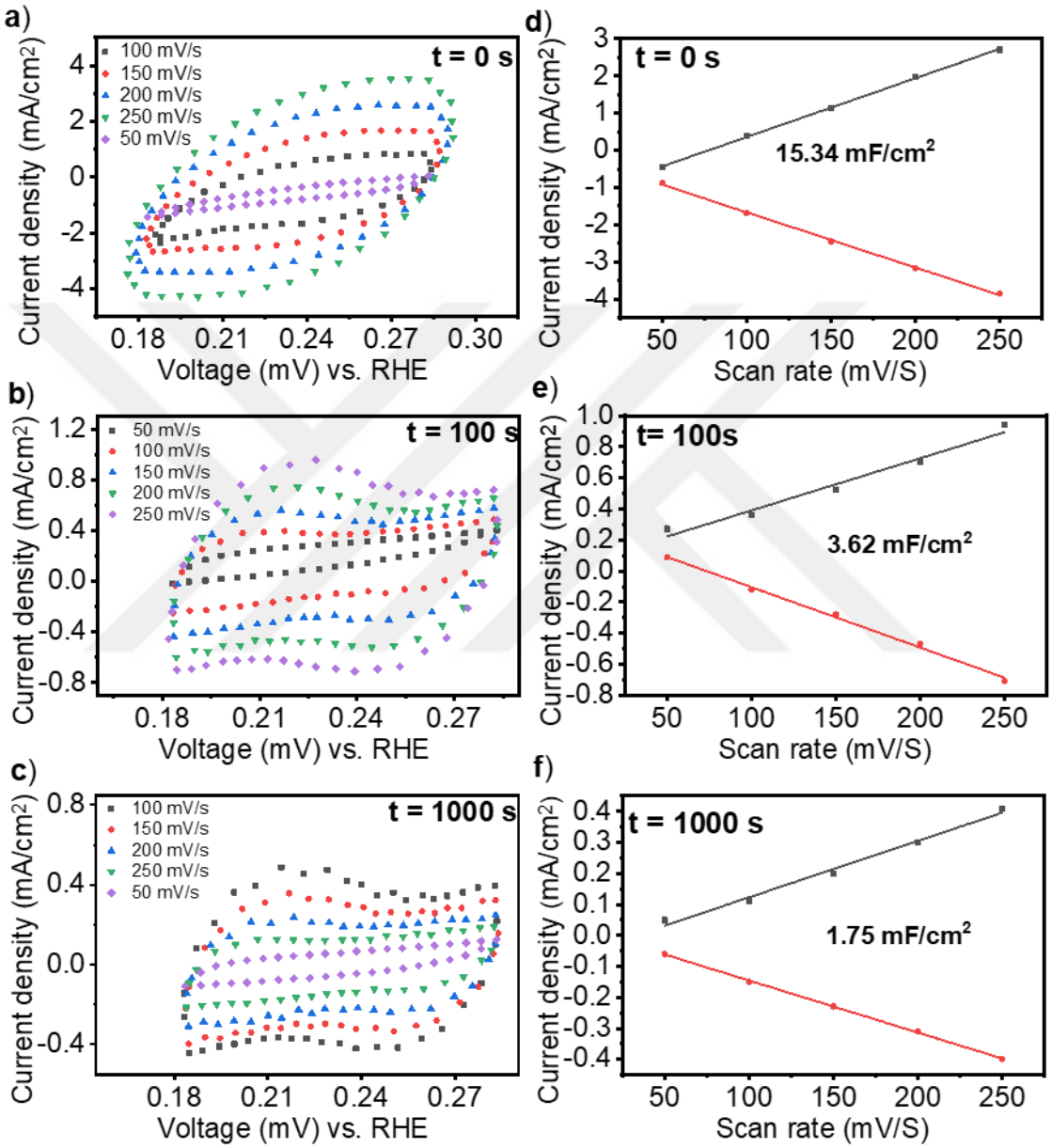

Figure 4.16 CV curves of the mesoporous NiS_2 on FTO electrode in a non-faradic region in 1.0 M KOH at the scan rates of 50, 100, 150, 200, and 250 mV/s. Capacitive currents are plotted as a function of the scan rate

Also, electrochemical impedance spectroscopy (EIS) was conducted to explore the charge transfer kinetics of the electrocatalysts during CA runs. The Nyquist plots

shown in Figure 4.17a indicate that charge-transfer resistance (R_{ct}) of the mesoporous NiS_2 decreases during HER. The R_{ct} is the highest for as-prepared mesoporous NiS_2, the application of cathodic potential leads to a drop in R_{ct} value and a minimum is achieved after 1000 sec. This behavior is consistent with the change in the current densities during the first CA run. In the second CA run, the lowest R_{ct} is achieved after resting under unbiased conditions and it gradually increases with time (Figure 4.17b).

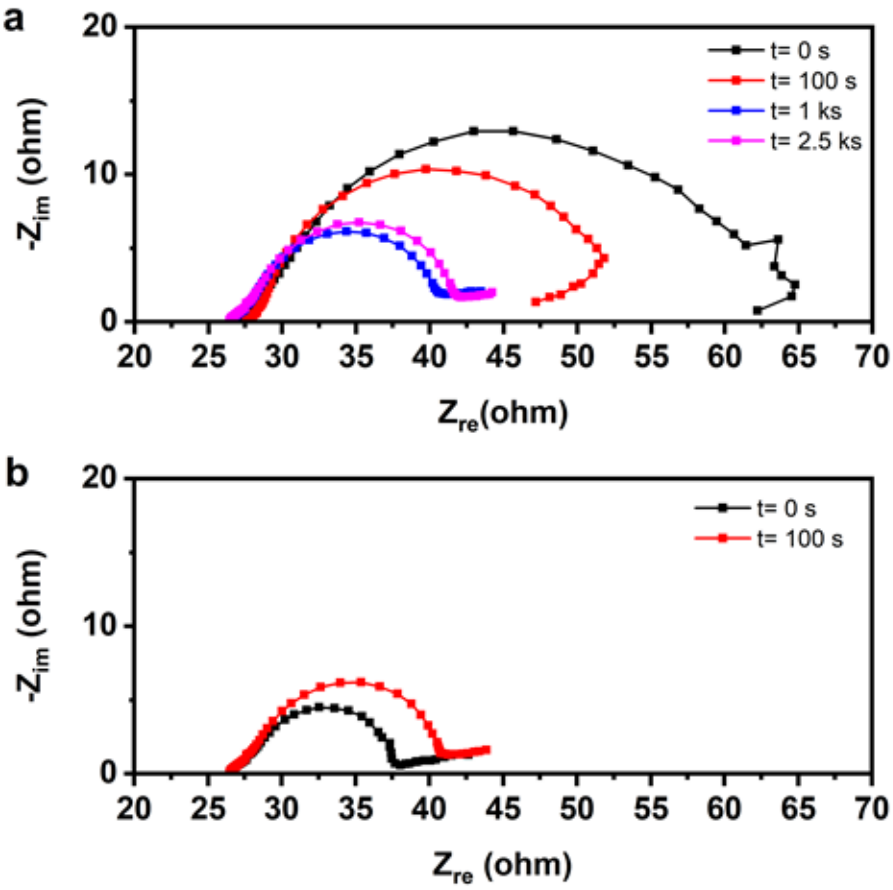

Figure 4.17 Nyquist plots of the mesoporous NiS_2 on FTO electrode for (a) first and (b) second CA runs in 1.0 M KOH. The measurements were carried out under a static potential of -0.4 V vs. RHE for the frequencies between 0.1 Hz and 100 kHz. Semicircles in Nyquist plots are distorted because of the dynamical changes on the electrocatalysts.

It is plausible that the leaching of sulfurous species and amorphization reduce the ECSA and increases the conductivity of the electrode. Prolonged cathodic bias brings C_{dl} to very low levels, 1.75 mF/cm^2. This value was expected due to the transition to the film from the mesoporous structure. During the first CA run, current density values normalized by ECSA (Figure 4.18) exhibit that the real HER activity is enhanced under cathodic bias,

which can be explained by the increase in the conductivity of the electrodes. BET surface area, pore size distribution, onset potentials, and ECSA of the electrodes subjected to the CA tests are summarized in Table 4.2.

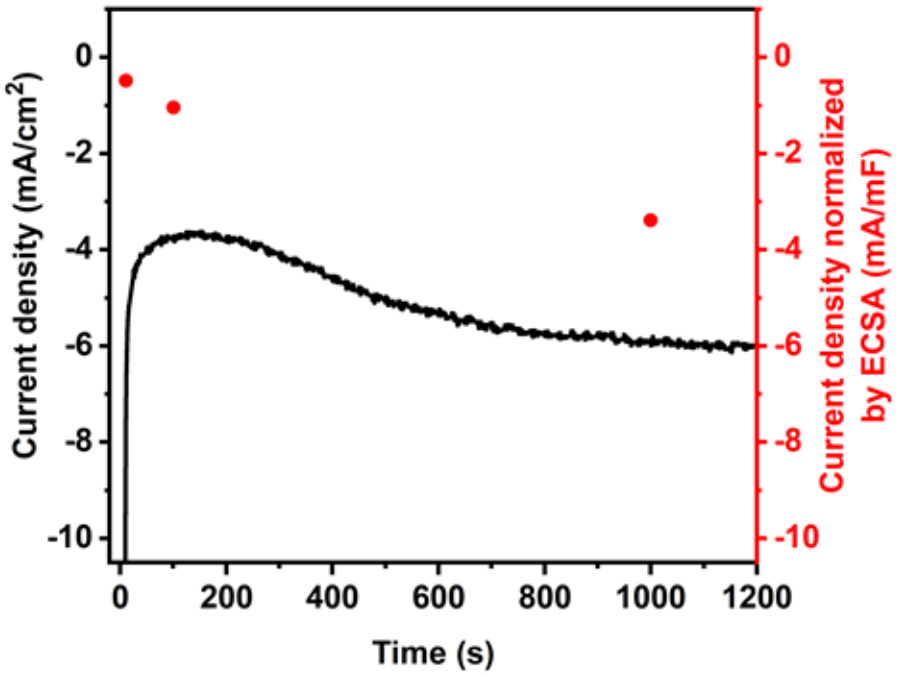

Figure 4.18 The ECSA normalized current density increase during the first CA run presented in Figure 4.10d.

Table 4.2 Comparison of reported pure NiS_2 for HER in 1.0 M KOH electrolyte

Morphology	**Synthesis method**	**Surface area (g/cm^2)**	**Thickness (nm)**	**Overpotential (mV)**	**ECSA (mF/cm^2)**	**Catalyst Amount (mg/cm^2)**	**Reference**
Hallow sphere Powder	Hydrothermal	20.8	200	174 (at 10 mA/cm^2)	6.18	0.7	[141]
Nanosheet array on Ti mesh	Hydrothermal	N/A	100	320 (at 200 mA/cm^2)	N/A	1.2	[140]
Hallow sphere powder	Hydrothermal	15,4	100	219 (at 10 mA/cm^2)	N/A	0.5	[112]
Nanosheet on Ni foam	Hydrothermal	N/A	10	67 and 122 (at 10 mA/cm^2)	239.5 and 566.5	0.5	[143]
Mesoporous film	Soft Template	69	2-3	250 (at 10 mA/cm^2)	1.75	N/A	This study

Despite electrochemical leaching of sulfur and surface reduction, the Faradaic efficiency of HER is close to unity. As shown in Figure 4.19, the amount of hydrogen evolving gradually increases as the potential is raised in the cathodic direction. Faradaic efficiency was calculated to be 0.96 at -0.4 V vs. RHE, suggesting that the observed electrochemical currents are related to HER rather than surface reduction, corrosion, or other non-Faradaic events.

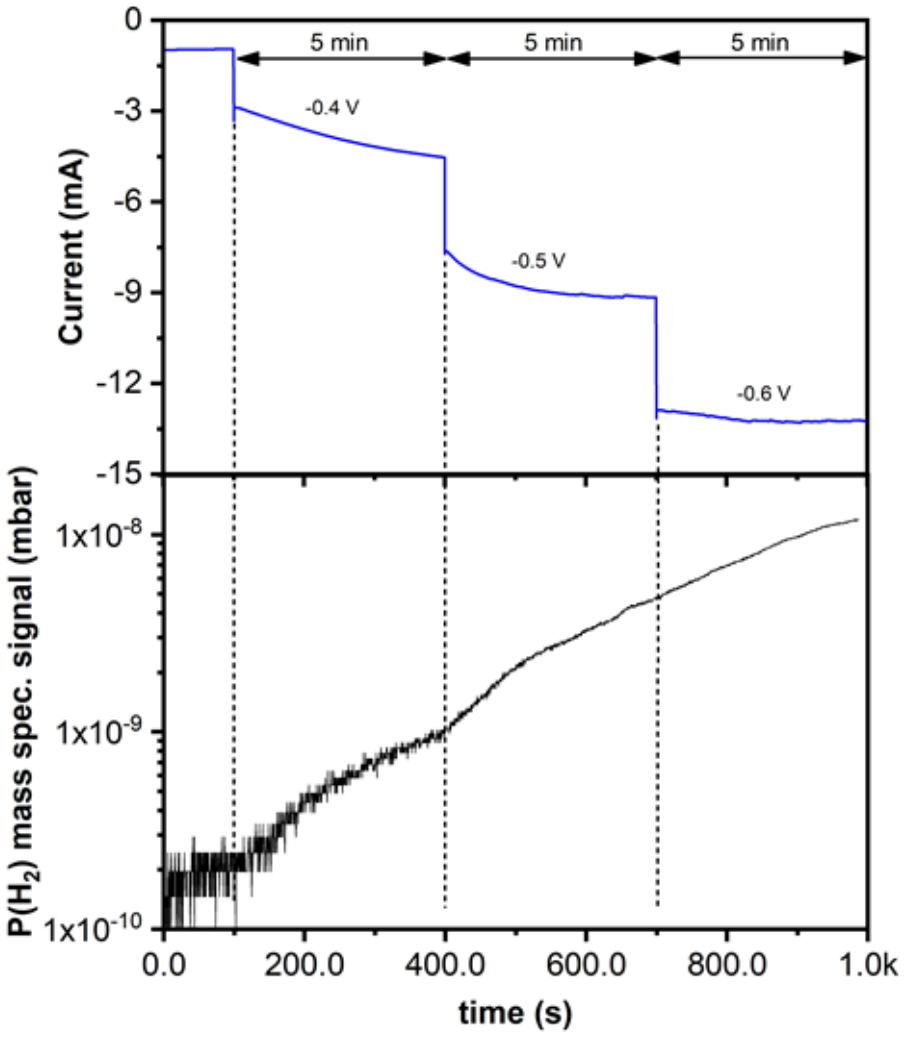

Figure 4.19 H_2 evolution is monitored by a mass spectrometer. CA runs at various potentials (-0.4, -0.5, -0.6 V vs. RHE) were sequentially performed, the duration of each CA run was 5 min. Due to the capillary tube used to collect gases from the headspace of the electrochemical cell, approximately 1 min delay was observed in the detection of the masses. This delay was compensated by shifting the mass spectrometer signal and matching them with the changes in the current jumps.

The results of the XPS analysis of as-prepared mesoporous NiS_2 and NiS_2 in the course of the first CA run are shown in Figures 4.20a-c. For the Ni 2p region (Figure 4.20a), the spectrum exhibits two major peaks at 854.8 and 872.0 eV assigned to Ni $2p_{3/2}$ and Ni $2p_{1/2}$, respectively. For Ni $2p_{3/2}$ (Ni $2p_{1/2}$), a high binding energy shoulder at 857 (874) eV and a broad satellite feature at ~861 (880) eV are also seen. The binding energy positions of the main peaks and satellite features as well as their intensities are rather sensitive to the structure and the composition of late TM compounds. They appear due to the different final states of photo-ionized Ni 2p orbitals and ligand atoms (O, S, P, etc.) coordinated to them which have a strong influence in the screening of the core hole.[144] 2p XPS spectra of Ni sulfides are distinguishable from those of oxides and hydroxides because of both their metallic nature and little effect of S 3p orbitals on the final state.[145] After the application of the cathodic bias, Ni 2p peaks slightly shift to the lower binding energies with no major change in the intensities of high binding energy and satellite features. In the S 2p spectra in Figure 4.20b, it is possible to identify different surface species, the peaks at 167.5/168.7 eV are assigned to S $2p_{3/2}/2p_{1/2}$ doublets of the sulfite (SO_3^{2-}) species caused by surface oxidation in ambient air. The doublet peaks at 161.3/162.5 eV are ascribed to the S_2^{2-} while the major doublets at 163.8/165.0 eV were attributed to S^{2-} neighboring oxidized S species.[139] After applying cathodic bias, the intensity of S_2^{2-} species significantly decreases while those of the S^{2-} ions remain largely unchanged. It is clear that S_2^{2-} species are prone to electrochemical leaching. In 100 s, a fraction of SO_3^{2-} groups is also lost, but longer cathodic treatments result in low binding energy shift in all spectra suggesting a mild reduction. Another doublet attributed to sulfate (SO_4^{2-}) species also appears at 169.0/170.1 eV. It can be expected that undercoordinated Ni atoms become available upon reductive dissolution of the S_2^{2-} species, which then could be terminated by hydroxyl (-OH) groups readily available in KOH electrolyte at unbiased conditions. The O 1s component at 530.8 eV assigned to –OH groups (Figure 4.20c) gains intensity at the initial stages of the CA run. All the reductive surface changes demonstrated by XPS coincide with the HER onset shifting to lower overpotentials. Similar behavior has been observed on amorphous Co-Ni sulfides during HER.[131] An overall assessment of XPS findings reveals that NiS_2 is only a pre-electrocatalyst for HER in alkaline media.[146] Dissimilarity in the final surface compositions of crystalline and mesoporous NiS_2 after the cathodic dissolution of sulfurous species can be explained by the difference in the leaching mechanisms. The

collapse of the mesoporous structure inhibits facile leaching of sulfurous species while the process continues for nonporous larger NiS_2 crystallites without any termination.

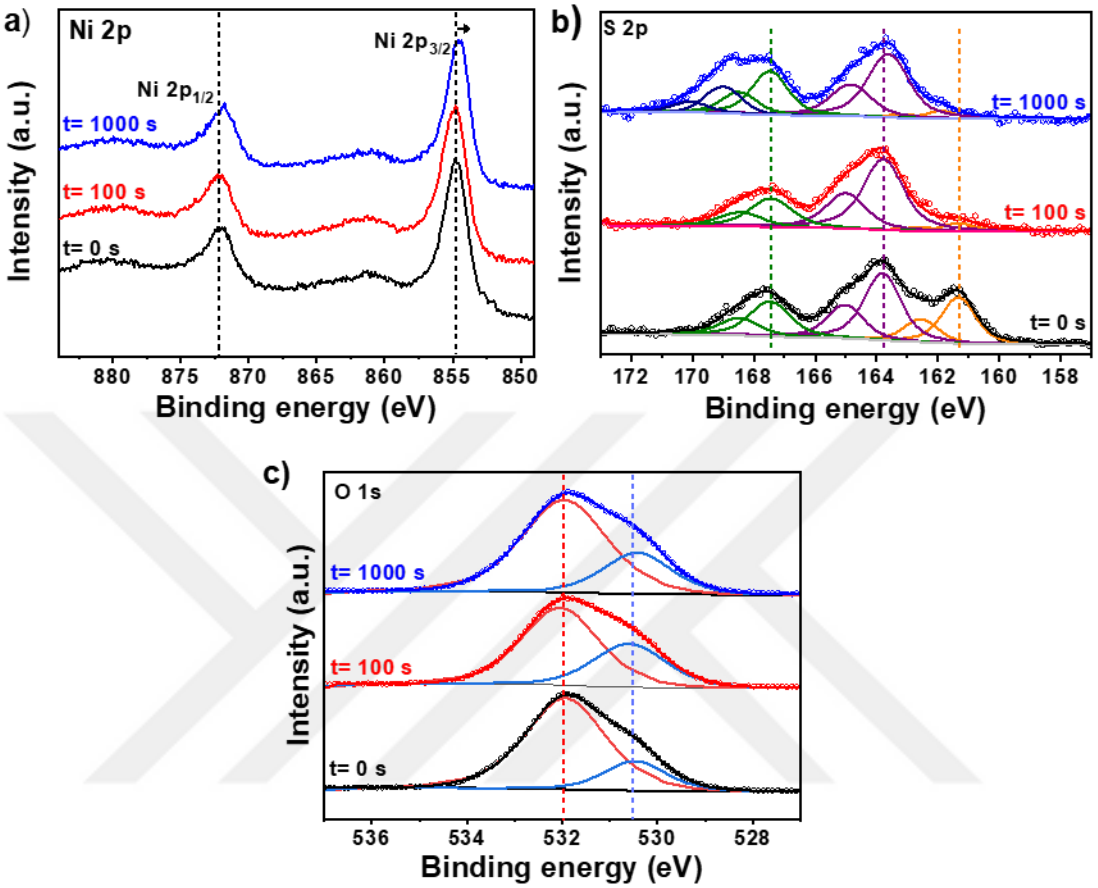

Figure 4.20 (d) Ni 2p, (e) S 2p, and (f) O 1s XPS spectra of the as-prepared and CA tested NiS_2 on FTO. The deconvolution of the spectra was performed by using the Doniac-Sunjic line profile. A Shirley type of background was used in all spectra. The S 2p spectra were deconvoluted using a doublet with a splitting of 1.2 eV and a 2:1 $2p_{3/2}$:$2p_{1/2}$ area ratio.

Resting mesoporous NiS_2 electrodes in the electrolyte after the first CA run improves the activity in terms of the reduction reaction onset but both mesoporous and crystalline NiS_2 eventually deactivate. The standard reduction potential of $Ni(OH)_2$ in alkaline media (pH 14) resides on the reduction potential of water regarding the Paurbaix diagram of the Ni-H_2O system (Figure 4.21). The surface of the Ni foam can reversibly be hydroxylated and reduced back to Ni electrochemically, giving the same HER activity consequently (see Figure 4.22). For Ni sulfides, the activity depends on the abundance of undercoordinated Ni sites and surface –OH groups, which can simply be recovered by

turning off the bias in the electrolyte. We show that the activity induced by the surface –OH groups is temporary for the mesoporous NiS_2 electrode . However, the crystalline NiS_2 shows the enhancement of HER activity at the end of the second CA run. Dynamic HER activities of NiS_2 electrodes are correlated with the equilibrium between the number of undercoordinated Ni sites and hydroxylated Ni species. It can be speculated that initial H_2O adsorption is facilitated in the presence of the -OH groups due to more effective hydrogen bonding. Besides, the existence of S in the amorphous Ni structure is required for higher HER activity. The mesoporous structure with very small crystallites and narrow pores is ideal to maintain the S in the electrode structure. For further understanding of the role of S in HER kinetics, operando X-ray spectroscopy analysis and detailed DFT studies are required.

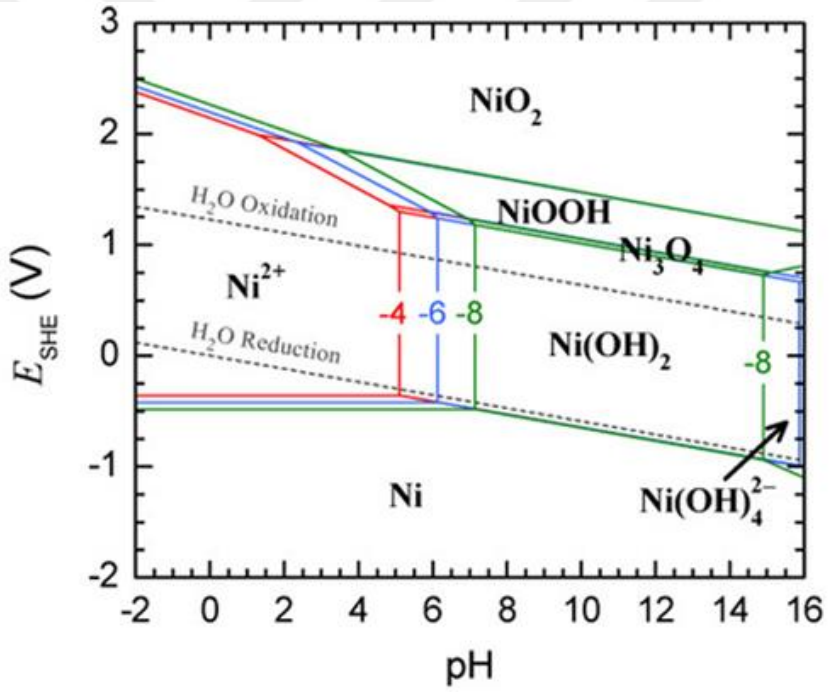

Figure 4.21 The Pourbaix diagram of the Ni-H2O system *[147]*. Adapted with permission from (J. PHYS. CHEM. C 2017, 121 (18), 9782–9789). Copyright (2017) American Chemical Society.

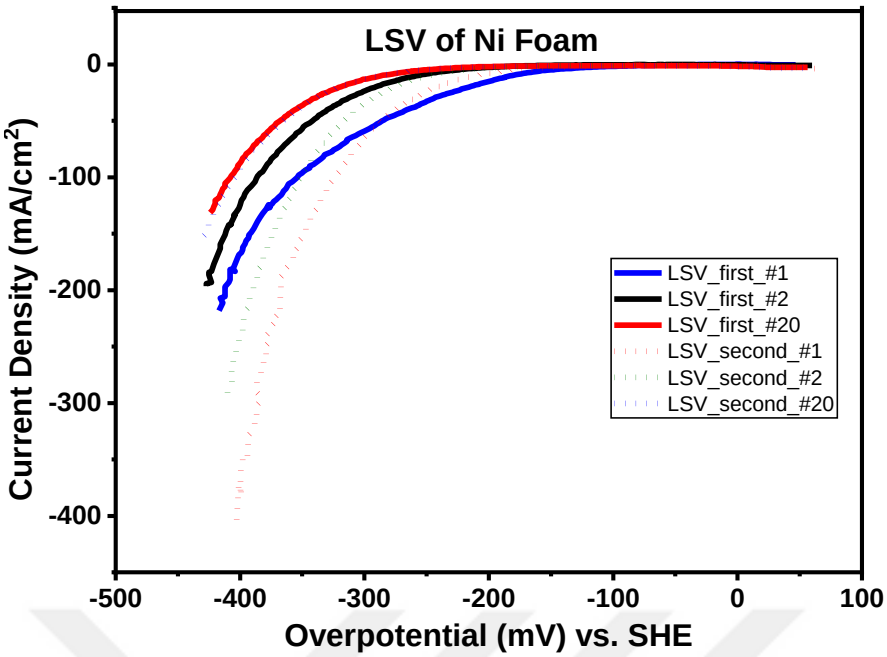

Figure 4.22 The consecutive LSV plots for Ni Foam in 1 M KOH. Between two sets, Ni Foam waited in 3 minutes without applying negative bias.

In summary, we show that the mesoporous, high surface area thin-film NiS_2 electrocatalyst with small pore walls and narrow pore size distribution is ideal to reveal the dependence of the activities on the robustness of the structural phase and surface composition. NiS_2 surface is very dynamic during HER in alkaline media, amorphization along with sulfurous ions leaching out changes the HER activities. Partially hydroxylated, undercoordinated Ni sites formed upon sulfurous ions leaching provide the most active surface for HER. The presence of S on the surface is critical for the stimulation of HER activity.

4.8 General Overview on Mesoporous Nickel Sulfides for Hydrogen Evolution Reaction in Both Alkaline and Acidic Media

Developing active, durable, and inexpensive electrocatalyst is critical for hydrogen production to meet ever-growing sustainable energy needs. Nickel sulfides offer significant potential as electrocatalysts for hydrogen evolution reaction (HER), however, the active phase governing the electrochemical conversion is still under debate.

We show that mesoporous thin-film NiS_2 synthesized by a novel soft-templating method without post-sulfurization exhibit superior HER activity in alkaline media after a preconditioning step that results in sulfur leaching, amorphization of the surface and collapse of the mesoporous structure. A comparative analysis with crystalline NiS_2 reported in the literature reveals that partial hydroxylation of the under-coordinated Ni sites is responsible for the superior HER activity rather than metallic nickel. Such transformations are summarized and schematically represented in the Figure 4.23. On the other hand, the nickel sulfides are active for HER but not durable in acidic media and they do not undergo any transformation and just dissolves in the electrolyte.

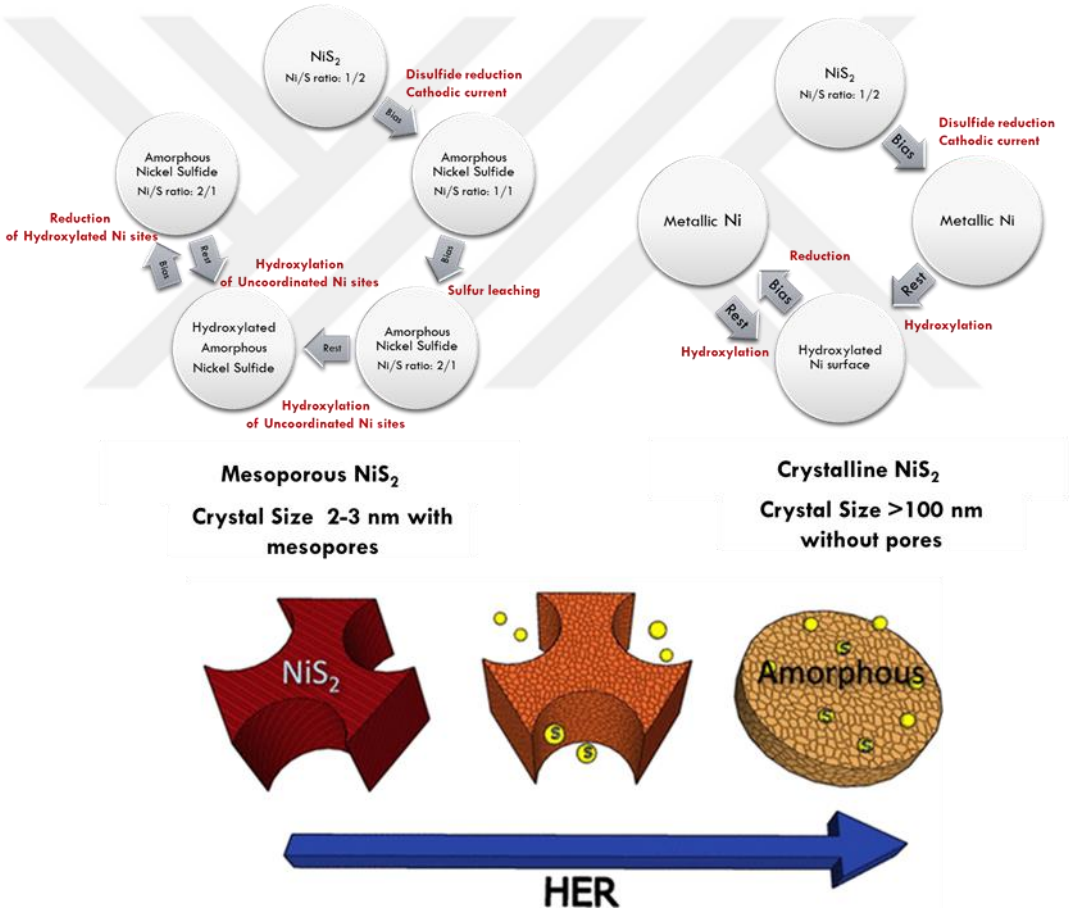

Figure 4.23 A summary of preconditioning steps of nickel sulfides during HER in alkaline media.

5 MESOPOROUS THIN-FILMS FOR AN OXYGEN EVOLUTION REACTION

5.1 Introduction

Developing the abundant and cheap electrocatalysts for both HER and OER that minimize overpotential and Tafel slope is a challenge standing over against the efficient electrolyzers. MoS_2 type-based electrocatalysts can compete with platinum group materials (PGM) electrocatalyst for HER [90]. The kinetics of OER is the bottleneck for the water splitting due to the slow four-electron transfer process [148], [149]. Ir-and Ru-based electrocatalysts are represented as a benchmark of OER electrocatalyst in terms of performance and durability in both alkaline and acidic electrolyte, however, their large-scale application is limited due to their high cost and low-abundance [150]–[153]. Therefore, there has been comprehensive research on exploring alternative earth-abundant catalysts with outstanding performance and long-term durability. The transition metals (Fe, Ni, Co and etc.) based phosphides [154]–[156], oxides [65], [157]–[159], oxyhydroxides [160]–[162], perovskites [163], [164], nitrides [165], [166] and sulfides [165], [167] have been extensively reported to be possible candidates for apprehending preferred activity and durability in alkaline media.

Recent studies have been focusing on the mixed transition metal-based oxide electrocatalysts such as (CoFe, NiFe MnNi, or FeCoNi) and layered double hydroxides (LDH) due to better performance and stability rather than pure forms [168]–[171]. Among them, NiFe oxide electrocatalysts have been come into prominence owing to superior long-standing activity [172]. An enhanced OER activity obtained by incorporating Fe at even very low concentrations into nickel oxide had been demonstrated by Corrigan for the first time [173]. The Fe impurities in KOH used in the preparation also enhanced Ni-based OER electrocatalyst [174]–[176]. Identifying the real role of Fe in the NiFe-based electrocatalyst has not yet been fully understood due to complicated kinetics and limitations of existing characterization methods [149], [158].

Most NiFe-based electrocatalysts undergo structural and compositional self-reconstruction under applied anodic potential; usually result in a dynamic activity in OER [177]. The surface of the electrocatalyst is very prone to these dynamic structural and compositional changes rather than of the bulk state. The surface and bulk structure of as-prepared and electrochemically tested catalysts should be fully unveiled in order to reveal

the structure-activity relation [174], [175], [177]. Therefore, a high surface area catalyst with uniform morphology is very critical in defining the exact structure and compositions for as-prepared and tested electrocatalysts [46]. Because of the structural and compositional changes that occurred at the electrode-electrolyte interface, the mass transfer of gas and electrolyte should be homogenous during OER in order to monitor the effect of dynamic structural and compositional changes [178]–[180]. To illustrate, NiFe-based nanocatalysts in carbon layers protect against degradation under continuous OER operating conditions [181].

Bell and co-workers reported that Fe doping NiOOH improves OER activity and Fe^{3+} species on the surface are active sites for OER through monitoring operando X-ray absorption spectroscopy and proving DFT calculations. Fe^{3+} sites provided optimum adsorption sites for OER intermediates [170]. On the contrary, Stahl and co-workers extended research by monitoring NiFe LDH using operando Mössbauer spectroscopy [182]. The OER takes place near the Fe^{4+} species generated at the edge, corner, and defect sites within NiFe LDH. Li and Selloni reported that Fe incorporation into the NiOOH lattice enhances the internal electronic conductivity in the film, where Ni species are activated by partial-charge transfer induced by Fe [183]. Furthermore, enhanced OER activity comes from the formation of Ni^{4+} induced by Fe^{3+}. As seen in many studies, the structure-activity relation for NiFe-based electrocatalysts differs by DFT studies and used operando techniques. Those inconsistent efforts to reveal the underlying mechanism of the structure-activity relation are most probably due to the dynamic changes in the structure and composition of the surface or dissolution/redeposition of active species during OER.

The next-generation water alkaline electrolyzer system has been shifted to alkaline exchange membrane electrolysis technology [184]. The electrocatalysts were generally immobilized on the membrane with ionomers, however, the ionomers in alkaline conditions under anodic potential suffer from the stability [185]. Ionomers can affect the performance and durability of OER electrocatalysts adversely by changing mass diffusion behavior and blocking the surface of electrocatalysts [186]. Constructing self-supported electrocatalysts with uniform morphology and structure is of importance for scaling up cheap and efficient electrolyzer technology.

NiFe-based electrocatalysts with several structures, various morphologies, adjustable stoichiometries, modified electronic structures, abundant active sites, and long-range order can be synthesized in many synthesis protocols [152], [157], [159], [169], [175], [187]–[190]. Mesoporous metal oxide thin film electrodes can satisfy many requirements for the next generation electrolyzer technology and the understanding of triangle among the structure-stability-activity relations. In addition, creating more surface area with interconnecting conductive networks increases the number of active sites and improves charge transfer kinetics and reagent/product diffusion as their mesoporous analogues [46], [64]–[66], [79], [190], [191]. The stable lyotropic liquid mesophase with two surfactants and various transition metal nitrate have been converted to mesoporous $MnCo_2O_4$, $NiCo_2O_4$ $LiMn_2O_4$, $ZnCo_2O_4$, and NiO thin films for many applications [64], [65]. Herein, our study was firstly focused on the OER performance of mesoporous NiS_2 thin films and then the development of mesoporous NiFe oxides thin films and their activities and stabilities toward OER. Mesoporous NiS_2 thin films undergo rapid and severe structural transformations during OER, formation of nickel oxide/hydroxide structure, resulting in the collapse of the mesoporous structure. We applied a similar approach to the liquid crystal templating method to produce mesoporous more durable iron-nickel oxide thin film electrodes. The mesoporous $NiFeO_x$, $NiFe_2O_4$, and Fe_2O_3 thin films electrodes having tunable compositions and a high surface area were successfully synthesized and comprehensively characterized. OER activities and stabilities of the electrodes were compared by numerous electrochemical tests in both Fe-free and non-purified electrolytes. The best OER performance shows mesoporous $NiFeO_x$, $NiFe_2O_4$, NiO, and Fe_2O_3, respectively. Uniform and highly porous nano-sized metal oxide framework allowed the understanding of the OER mechanism of NiFe based electrocatalysts in which insertion of an infinitesimal number of Fe atoms in NiO lattice boosts the OER activity of Ni sites by altering its electronic structure.

5.2 Experimental Section

5.2.1 Preparation of Mesoporous NiS_2 Electrodes on FTO

The preparation of mesoporous NiS_2 electrode on FTO was prepared by following the protocol described in Chapter 4.

5.2.2 Preparation of Solutions of Nickel and Iron Precursors and Surfactants for Mesoporous NiFe Oxide Thin Films

In a typical solution preparation, CTAB, $C_{12}EO_{10}$, nickel nitrate hexahydrate, and iron nitrate nonahydrate are mixed in a 25 ml vial with deionized water. The solution is stirred for one day in order to make sure that it is homogenous and clear.

The amount of each ingredient for the preparation of all solutions is tabulated in Table 5.1. Deionized water was kept constant in all solutions, 5 g. As CTAB/ $C_{12}EO_{10}$ mole ratio was kept being 1.0 and total transition metal (iron and nickel nitrate)/CTAB mole ratio was kept to be 9.0 for all solutions, nickel/iron salt mole ratios were altered. The nickel to iron salt mole ratios were used for labeling the solution.

Table 5.1 The amounts of CTAB, $C_{12}EO_{10}$, $Ni(NO3)_2.6H_2O$, $Fe(NO3)_2.9H_2O$ and deionized H_2O for each solution

Notation of solutions Mole ratios (Ni/Fe salt)	**$Ni(NO_3)_2.6H_2O$ (g)**	**$Fe(NO_3)_3.9H_2O$ (g)**	**CTAB (g)**	**$C_{12}EO_{10}$ (g)**	**Deionized H_2O (g)**
Ni9.0/Fe0.0	2.087	0.000	0.291	0.500	5.0
Ni8.9/Fe0.1	2.064	0.032	0.291	0.500	5.0
Ni8.0/Fe1.0	1.856	0.546	0.291	0.500	5.0
Ni7.0/Fe2.0	1.624	0.644	0.291	0.500	5.0
Ni6.0/Fe3.0	1.392	0.967	0.291	0.500	5.0
Ni4.5/Fe4.5	1.044	1.450	0.291	0.500	5.0
Ni3.0/Fe6.0	0.696	1.933	0.291	0.500	5.0
Ni0.0/Fe9.0	0.000	2.900	0.291	0.500	5.0

5.2.3 Preparation of Lyotropic Liquid Crystalline (LLC) Mesophase for Mesoporous NiFe Oxide Thin Films

The mesophases were prepared by spin coating of solutions their ingredients are given in table 5.1 for thin LLC films. Spin coating was applied to prepare LLC and further mesoporous NiFe oxide thin films. An adequate amount of the solution was placed on the FTO or glass lamels and it was spun for 20 s at 1000 rpm by a spin coater. To obtain thicker mesophase, drop-cast coating on the microscopic slides was also applied. Drop-casting was applied by placing solution and aged for evaporation of deionized water. The spin-coated samples were used for XRD analysis. The samples prepared by drop-casting

were collected from the glass slides for the FTIR and POM analysis. Schematic illustrations of both drop-casting and spin coating methods are indicated in Figure 5.1.

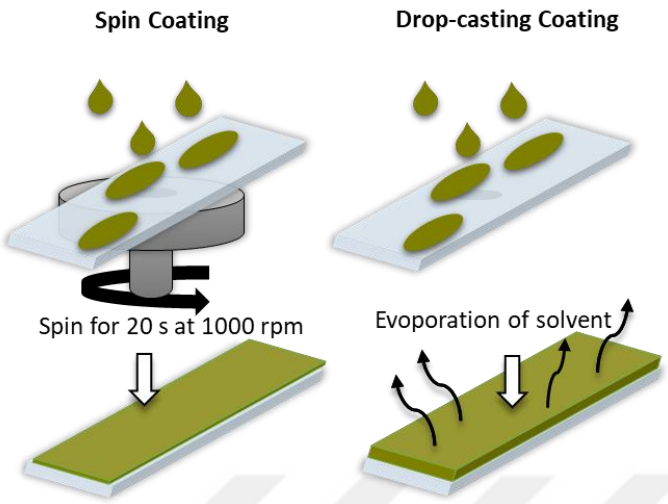

Figure 5.1 Schematic illustration of spin coating and drop-casting casting methods.

5.2.4 Synthesis of Mesoporous NiFe Oxides

Mesoporous NiFe oxide thin films were prepared via calcination of LLC prepared by spin coating or drop-casting coating. The calcination procedure was carried out starting from room temperature up to 300 ^{o}C with a ramp of 2 ^{o}C/min and keeping at 300 ^{o}C for 2 hours. The samples were annotated as mesoporous Ni_x/Fe_y, where x and y are the mole ratios of nickel nitrate and iron nitrate to CTAB, respectively. The films prepared by drop-casting were scrapped from the glass slides by using a razor for the XRD, FTIR, and BET analysis. The films prepared by spin-coating were scrapped from the glass slides by using a razor for the SEM/EDX, TEM, and XPS analysis. The Schematic illustration is depicted in Figure 5.2.

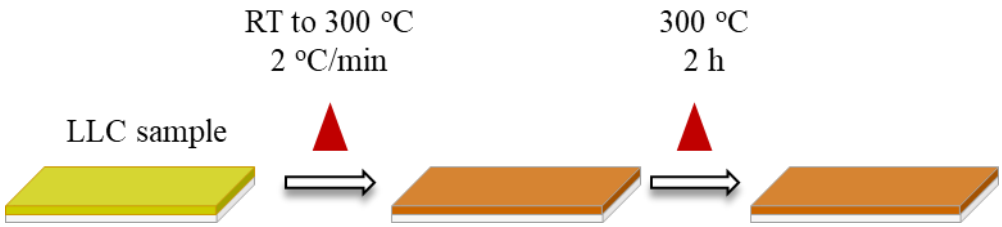

Figure 5.2 Schematic illustration of synthesis of mesoporous NiFe oxide thin films

5.2.5 Preparation of Mesoporous NiFe Oxide Electrodes on FTO

The spin coating protocol described above was applied for the preparation of mesoporous NiFe oxide electrodes on FTO. Before spin coating, FTO (1 cm × 2 cm) substrates were cleaned by ultra-sonication in absolute ethanol. A scotch tape was used to make an area of 1 cm^2 on FTO for spin-coating. A few drops of the solution described above were placed on the FTO and it was spun for 30 s at 1000 rpm by a spin coater. LSV, CV, and CA measurements and the analysis of Raman spectroscopy were conducted by using electrodes. Schematic illustration of the preparation of electrodes and the photograph of prepared samples on FTO with different compositions are presented in Figure. 5.3.

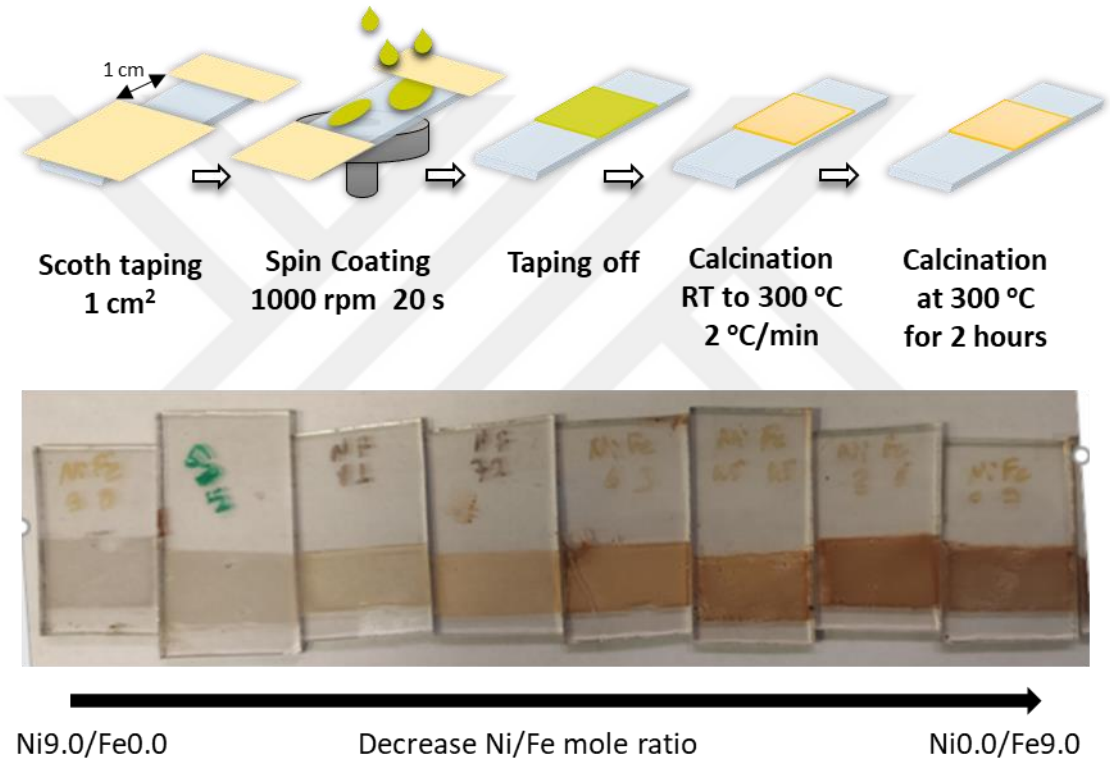

Figure 5.3 Schematic illustration of the preparation of mesoporous NiFe oxide electrodes on FTO substrates (upper part). The photograph of mesoporous NiFe oxide on FTO electrodes with various Ni/Fe compositions (lower part).

5.3 Instrumentation

The instrumentation that used in this chapter was described in the previous chapters.

5.4 Electrochemical Measurements

The electrochemical measurements conducted in this chapter are described in Chapter 4.

5.5 Liquid Mesophase of Nickel Nitrate-Iron Nitrate System with Two Surfactants

Pure or mixed nickel nitrate and iron nitrate salt with two surfactants form LLC mesophase after spin coating. Salt species fill among the surfactant domain aggregated upon evaporation of water. The LLC mesophases of various nickel nitrate salt/iron nitrate mole ratios were investigated by a small angle XRD measurement and POM, see Figure 5.4.

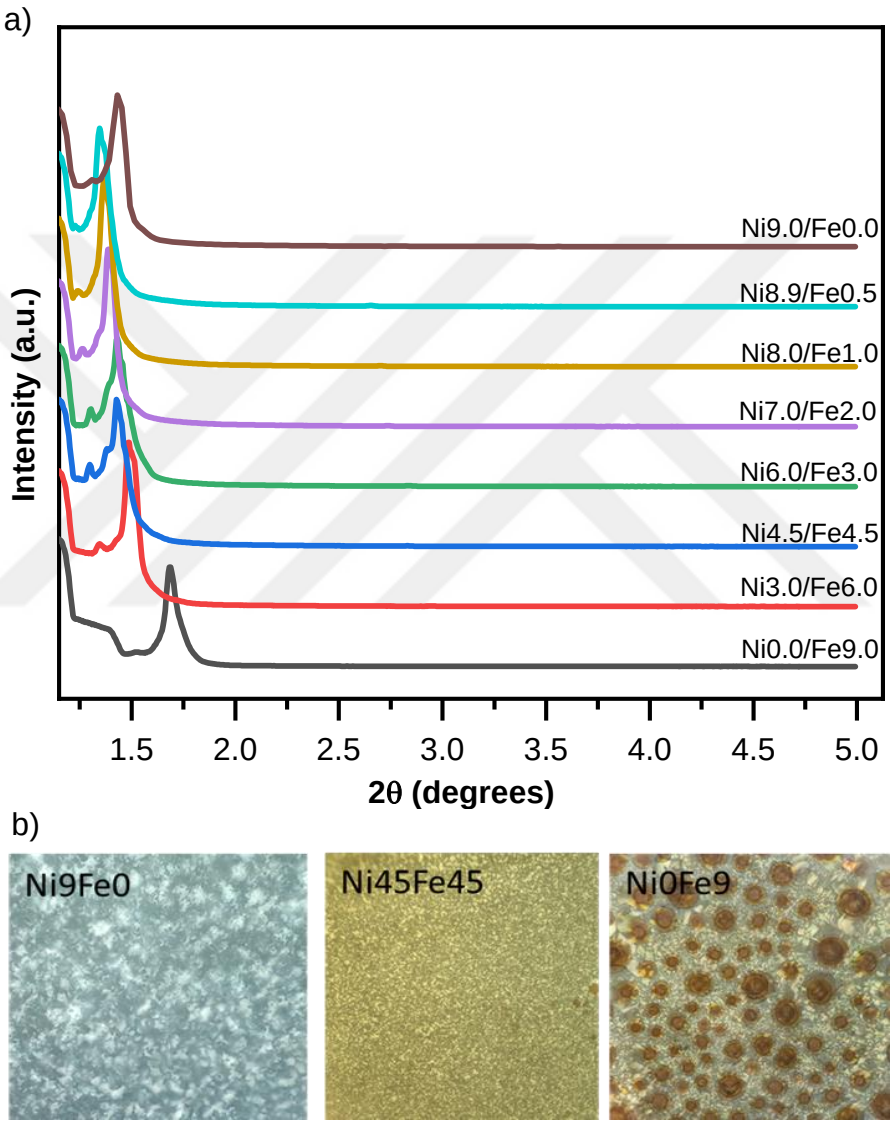

Figure 5.4 (a) Small-angle XRD patterns and (b) POM images of various Ni/Fe salt mole ratio mesophase

All samples prepared by spin coating present the diffraction lines at between 1° and 2°, indicating the formation of ordered LLC mesophase. The thick gels prepared by

drop-casting show the fan texture under a polarized optical microscope (POM), typical characteristics of an ordered 2D-hexagonal LLC mesophase. The addition of iron nitrate salt into nickel nitrate LLC mesophase at low quantities increases the distance between surfactant domains. The distance between surfactant domains decreases with decreasing Ni/Fe mole ratio. The pure iron nitrate LLC mesophase displays the shortest distance between surfactant domains among various Ni/Fe salt mole ratios LLC mesophase. In the POM images of the samples, the dark brown spots showing no textured features are detected after the Ni/Fe mole ratio becomes 4.5/4.5. Some iron nitrate salt species may leach out from the LLC mesophase. This causes the differentiation of Ni(II) and Fe(III) cations mole ratio in the confined space between surfactant domains with starting compositions.

5.6 Characterization of Mesoporous NiFe Oxide

The calcination of LLCs mesophase of nickel and iron nitrate salt is applied in order to obtain mesoporous pure and mixed NiFe oxide samples. Calcined samples are characterized by comprehensive analysis tools such as XRD, FTIR, N_2 sorption analysis, SEM/EDX, TEM, and STEM.

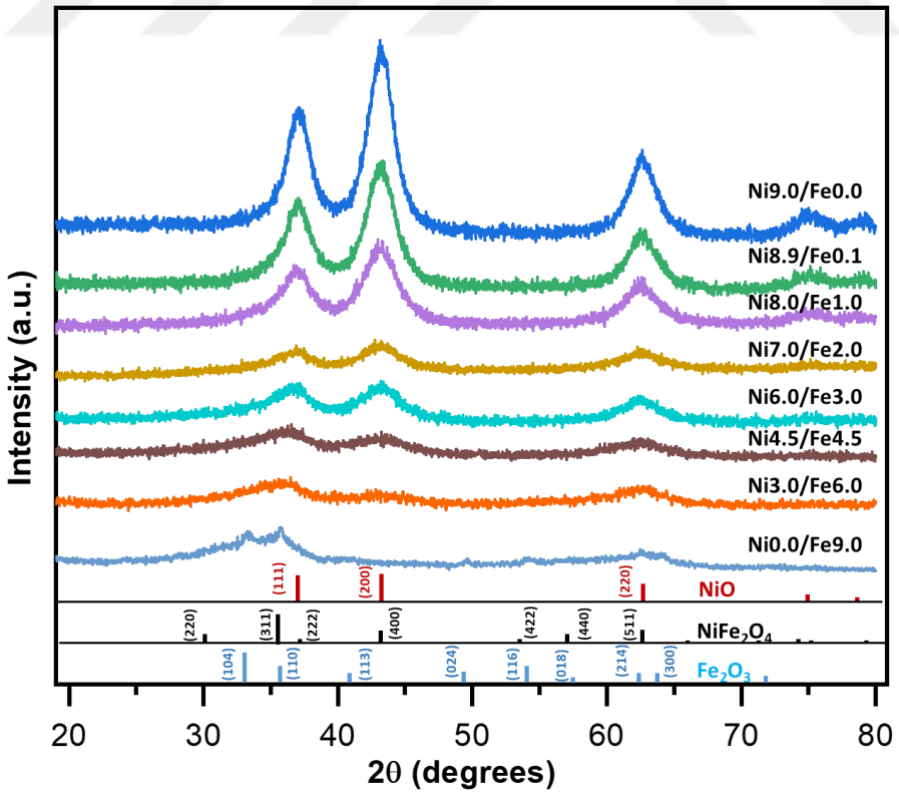

Figure 5.5 XRD patterns of the calcined samples of various Ni/Fe salt mole ratio mesophases

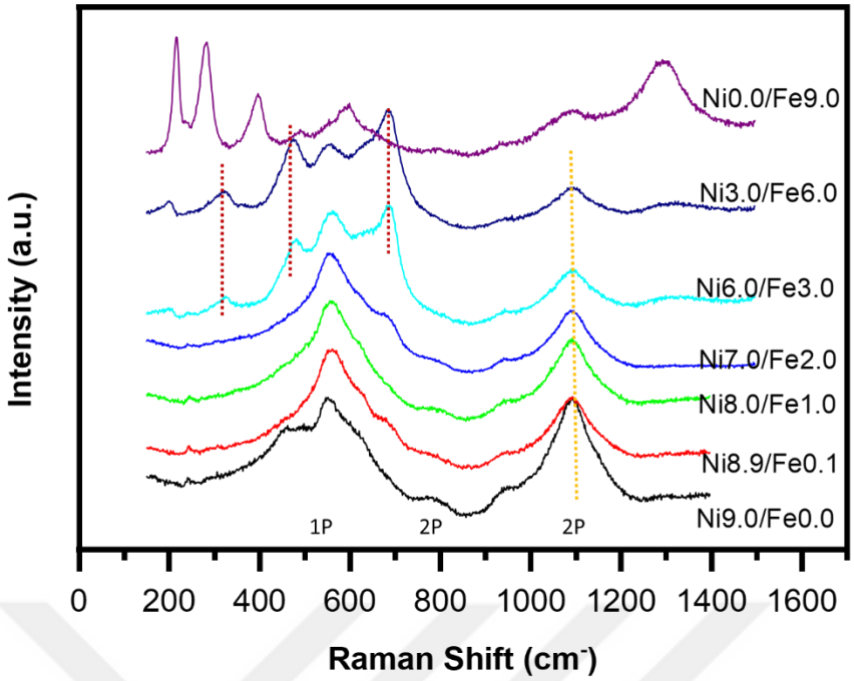

Figure 5.6 Raman spectrum of the calcined samples of various Ni/Fe salt mole ratio mesophases

Figure 5.5 shows the XRD patterns of calcined samples of various Ni/Fe salt mole ratio mesophases. As calcined pure nickel nitrate salt mesophase sample has cubic NiO, calcined pure iron-nickel salt mesophase has α-Fe_2O_3 structure. The crystallite size of the calcined pure nickel sample is calculated by the Scherrer equation, found to be around 3.7 nm. The diffraction lines get broader with decreasing Ni/Fe salt mole ratio, indicating smaller crystallite size or amorphous Fe_2O_3. The calcined pure iron-nickel mesophase displays sharper diffraction lines belonging to Fe_2O_3 and very broad diffraction lines around them. This represents that the sample contains both nanocrystalline and relatively bulk Fe_2O_3 crystallites. The leached iron nitrate salt species may result in the formation of bulk Fe_2O_3 crystals since they are not confined among surfactant domains during calcination. We note that the crystallization at the same temperature, 300 ^oC, does not process for both NiO and Fe_2O_3. We found that the insertion of Fe (III) into NiO lattice hinders crystallization. Moreover, until the Fe/Ni atomic ratio becomes 6.0/3.0, the intensity ratio of diffraction lines belonging to lattice planes of (111) and (200) are the same. We can say that the dominant phase seems cubic NiO and Fe(III) cations are substituted with Ni(II) in the lattice. Raman analysis is a powerful technique to detect smaller crystalline nanoparticles (<4 nm) or amorphous phases that cannot be determined

by XRD. Raman analysis was conducted to figure out the oxide phases present in critical synthesized mesoporous samples, Figure 5.6. The intensity of the main peak of NiO at 1100 cm^{-1} is decreased with iron content in the oxide phase. When the sample content becomes Ni6.0/Fe3.0, three new peaks are appeared at 320, 467, and 688 cm^{-1} , belonging to spinel structured $NiFe_2O_4$. At Ni3.0/Fe6.0, the NiO peak at 1100 cm^{-1} has low intensity compared to other peaks. The sample of pure Fe directly matches with α-Fe_2O_3. In conclusion, Up to Ni/Fe ratio, 7/2, iron atom are mixed in the rock salt type NiO, and then the formation of spinel $NiFe_2O_4$ structures starts at higher iron contents until the main oxide phase become spinel mixed oxide structure at Ni3.0/Fe6.0. TEM/STEM experiments were performed to examine the more detailed structural and morphological analysis in selected samples at the nanoscale, Figure 5.7. Pure and mixed samples show a sponge-like mesoporous framework as seen in STEM images. High-resolution TEM images and selected area electron diffraction patterns (SAED) of Ni9.0/Fe0.0 and Ni8.9/Fe0.1 samples are consistent with XRD and Raman analysis. Iron atoms substitute with nickel atoms in cubic NiO crystalline structure with particle sizes around 5-10 nm. At Ni6.0/Fe3.0 sample, electron diffraction pattern differs from other mixed oxide phases with the circle indexed as (111) lattice plane of spinel $NiFe_2O_4$ with a yellow arrow as detected in Raman analysis. The pure iron sample displays an α-Fe_2O_3 nanocrystalline structure, having a particle size smaller than 5 nm.

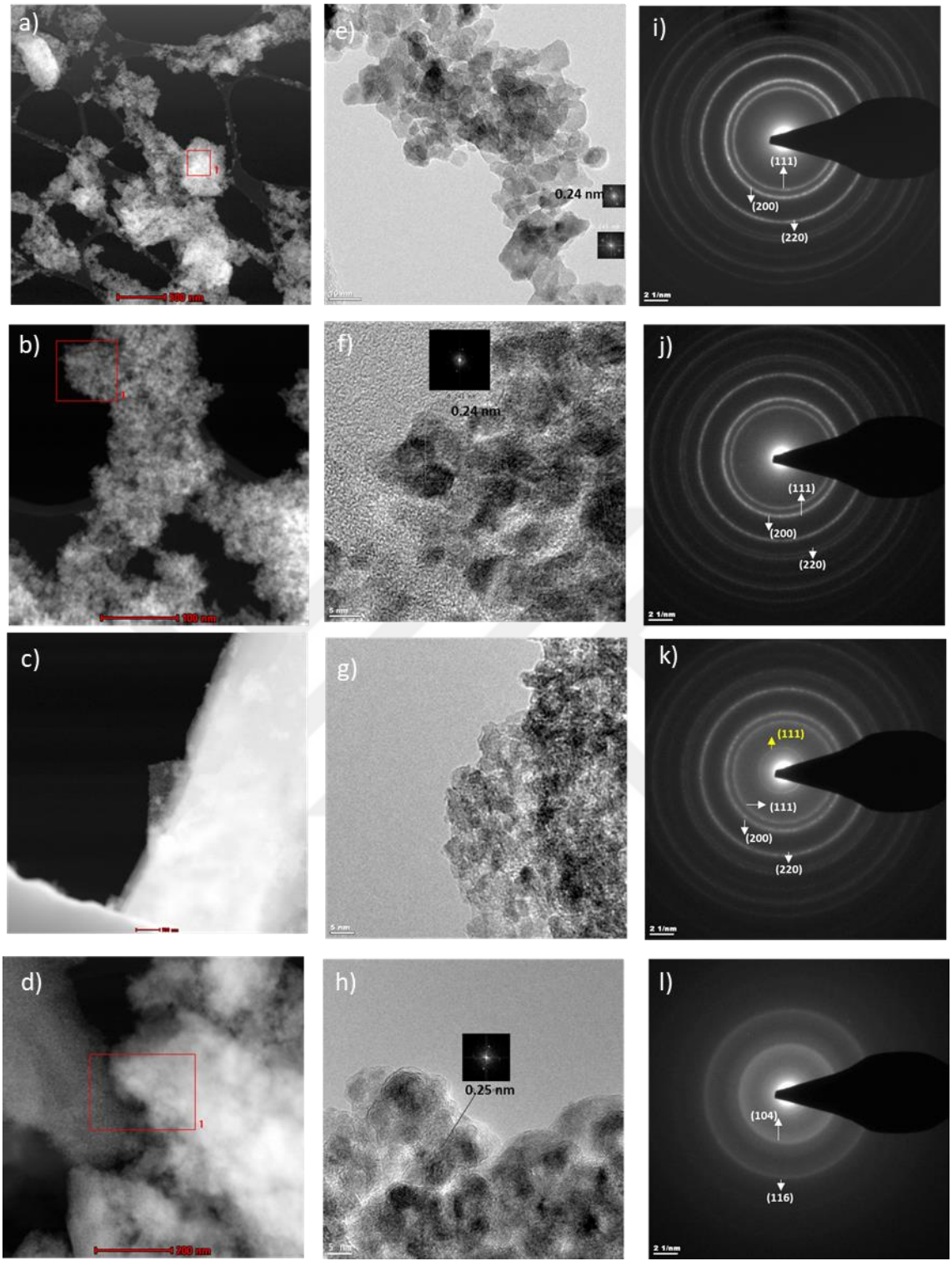

Figure 5.7 STEM (a-d), high resolution TEM (e-h) and selected area electron diffraction pattern (SAED) (i-l) of calcined samples of Ni9.0/Fe0.0, Ni8.9/Fe0.1, Ni60/Fe3.0 and Ni0.0/Fe9.0, respectively

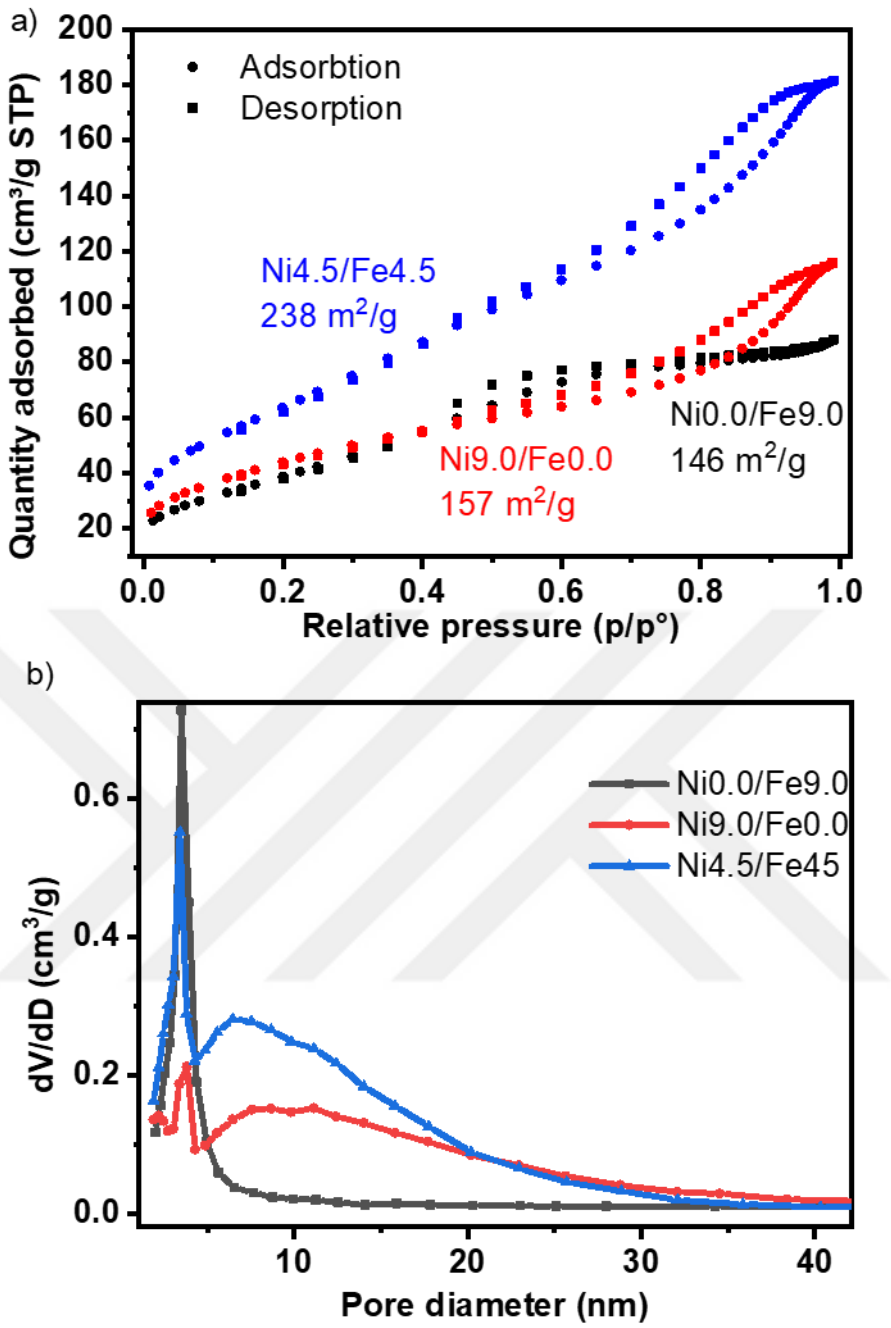

Figure 5.8 (a) N_2 sorption isotherms and (b) pore size distributions of calcined Ni0.0/Fe9.0, Ni4.5/Fe4.5, and Ni9.0/Fe0.0 samples

Figure 5.8 shows N_2 sorption isotherms and pore size distributions of selected samples; mesoporous Ni0.0/Fe9.0, Ni4.5/Fe4.5, and Ni9.0/Fe0.0. All N_2 sorption isotherms display type IV hysteresis, which is characteristic of mesoporous materials. Mesoporous pure nickel and iron oxide samples have similar BET surface areas, 157 and 146 m^2/g, respectively. Mesoporous mixed NiFe oxide interestingly has a higher surface

than pure phases, 238 m^2/g. Pore size distribution of mesoporous nickel oxide, iron oxide, and mixed NiFe oxide are sharply centered at around 3.8 nm. For mesoporous nickel oxide and mixed NiFe oxide, second broader pore size distribution is observed. The calcination process of mesophases at 300 °C provides clearing out the surfactant domains by burning, leading to the formation of mesopores and decomposition transition metal nitrate salt. All other parameters of N_2 sorption analysis of selected samples are tabulated in Table 5.2. The FT-IR spectrum of all mesophases and calcined samples, seen in Figure 5.9, confirms the burning out of all surfactants and nitrates by disappearing the peaks at around 1100 and 2800 cm^{-1} due to surfactants and nitrates. However, surfaces of nano-sized metal oxides particles are contaminated by carboxyl groups during calcination. The further crystallization of amorphous phases creates broader pore size distribution because of the rearrangement of decomposed metal oxide species. The low crystallization tendency of iron oxide compared to nickel oxide inhibits the enlarging pore media. The crystallite size calculated XRD data by the Scherrer equation is consistent with this observation. The leaching of iron salt species resulting in the formation of bulk oxide most probably decreases the overall surface area while it does not affect the pore size distribution.

Table 5.2 All parameters of N_2 sorption analysis of selected samples

Mole ratios (Ni/Fe)	**BET Surface Area m^2/g**	**Pore Volume cm^3/g**	**Average Pore Size nm**
Ni9.0/Fe0.0	157	0.157	4.49
Ni8.9/Fe0.1	185	0.200	4.07
Ni6.0/Fe3.0	220	0,314	5.05
Ni4.5/Fe4.5	238	0.270	4.69
Ni0.0/Fe9.0	146	0.133	3.68

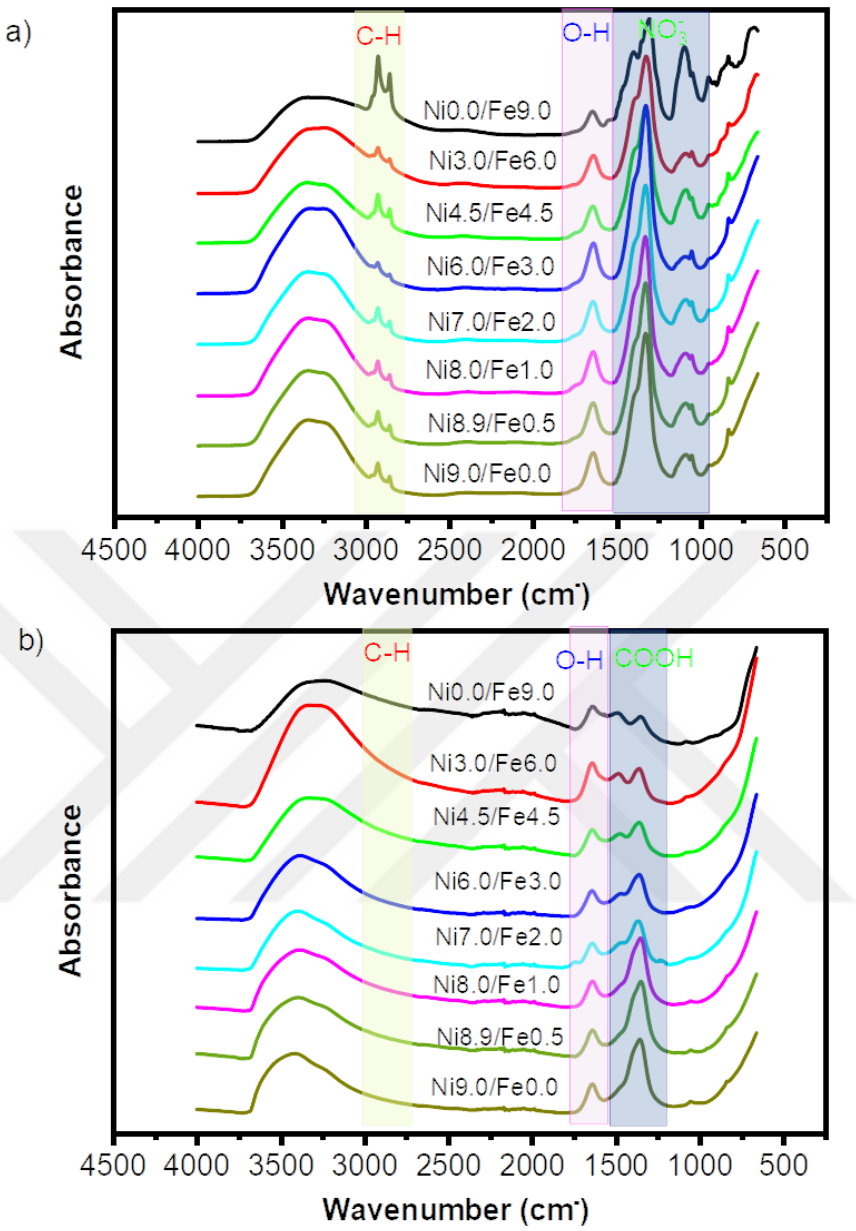

Figure 5.9 (a) FT-IR spectrum of as-prepared mesophase and (b) calcined samples at 300 °C

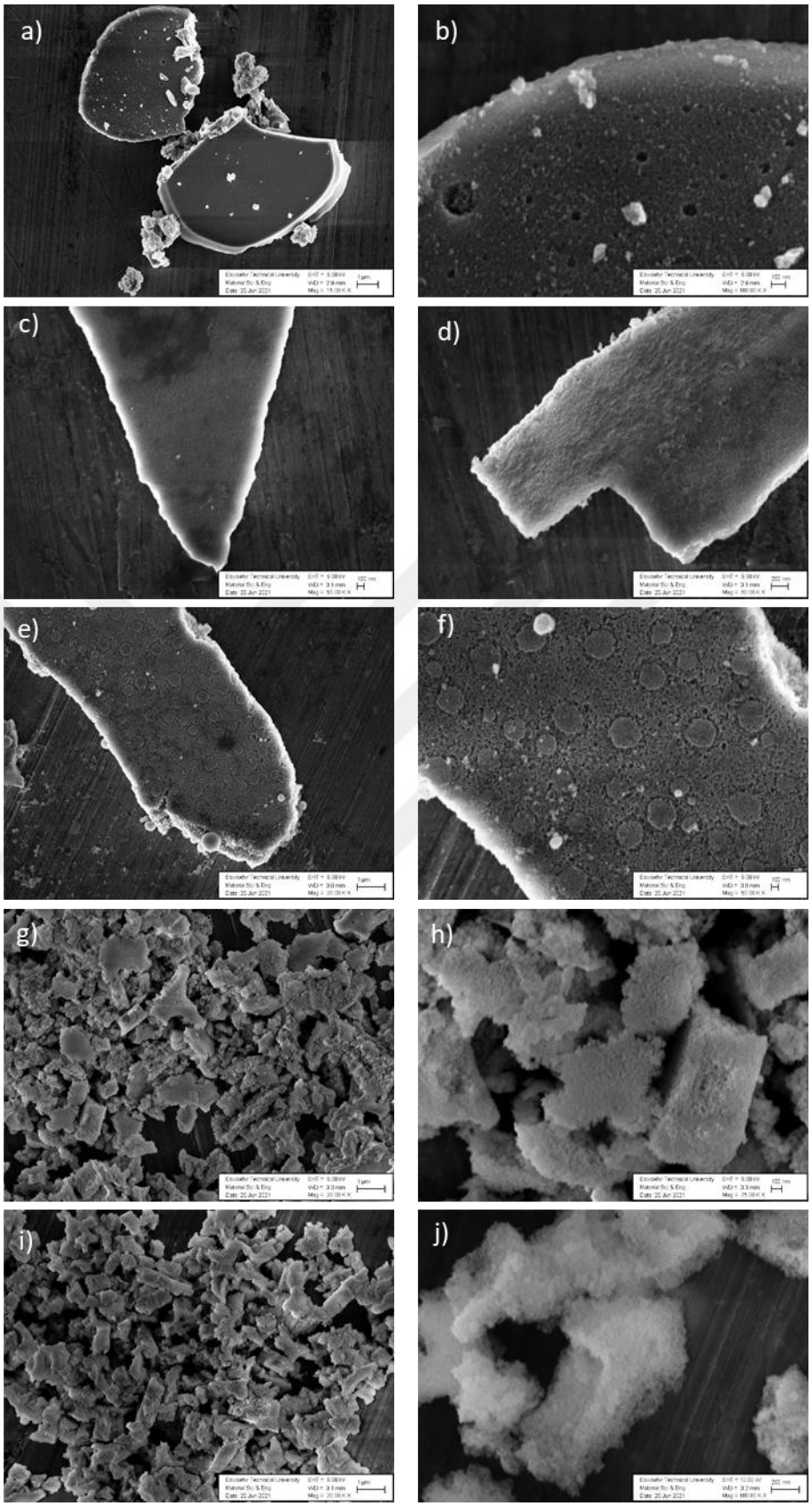

Figure 5.10 SEM images of mesoporous (a and b) Ni0.0/Fe9.0, (c and d) Ni3.0/Fe6.0 (e and f) Ni4.5/Fe4.5, (g and h) Ni6.0/Fe3.0 and (i and j) Ni9.0/Fe0.0

In the SEM images of scrapped samples from glass slides, see Figure 5.8, the mesoporous structures are clearly observed. The N_2 sorption analysis is consistent with SEM analysis, decreasing Ni content in the samples provides a broader porous framework. However, the instability of mesophase at higher Fe content samples caused by leaching iron salt out from mesophase results in nonporous regions after calcination, as seen in Figure 5.10c-d. For the mesoporous Ni.4.5/Fe4.5, some circular islands having different pore size distributions are formed. We further investigated the elemental compositions of all calcined samples by using EDS, which is tabulated in Table 5.3 to understand the distribution of oxide phases at the macroscale. The instability of mesophases slightly alters the uniform distributions of mixed oxides. Starting compositions of ingredients outcomes nearly the same compositions of iron and nickel atoms after calcination of mesophases.

Table 5.3 The elemental compositions of calcined samples from SEM/EDS

Mole ratios (Ni/Fe)	Atomic Ni %	Atomic Fe %
Ni9.0/Fe0.0	50.00	0.00
Ni8.9/Fe0.1	47.86	2.14
Ni8.0/Fe1.0	44.87	5.13
Ni7.0/Fe2.0	37.61	12.39
Ni6.0/Fe3.0	34.13	15.87
Ni4.5/Fe4.5	23.97	26.03
Ni3.0/Fe6.0	17.08	32.92
Ni0.0/Fe9.0	0.00	31.62

5.7 Mesoporous NiS_2 Thin films for Oxygen Evolution Reaction in Alkaline Media.

OER activity of mesoporous NiS_2 on FTO electrode in an alkaline media, 1 M KOH, was investigated by CV, see Figure 5.9a. Notice that mesoporous NiS_2 electrodes in an alkaline media show a dynamic HER activity and act as a pre-catalyst that transformed into sulfur deficient amorphous nickel sulfide by sulfur ions leaching. Mesoporous NiS_2 electrodes having high surface area, very small nano-crystalline structure, and narrow pose size distribution is an ideal platform to underly the structure-activity relation for OER as well understood in the HER.

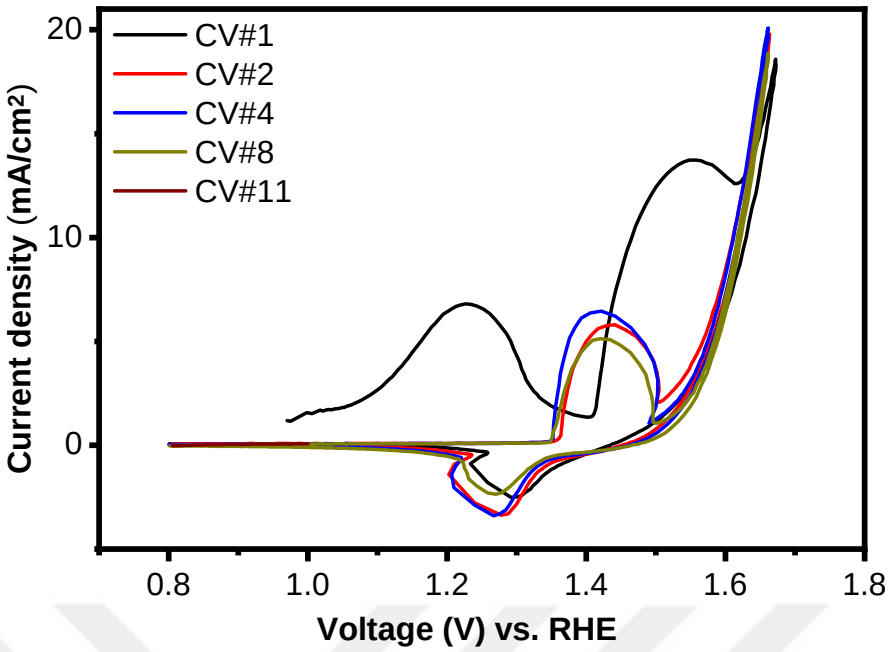

Figure 5.11 CV curves of the mesoporous NiS_2 on FTO electrode in 1.0 M KOH with the scan rate 5 mV/s.

In the first CV scan of the mesoporous NiS_2 electrode, two anodic peaks spanned between 1.0-1.4 V and 1.4-1.6 are observed during the initial forward scan. For consecutive forward CV scans, only one anodic peak spanned between 1.35-1.5 V is observed. For all reverse scans, one cathodic peak spanned between 1.2 -1.4 V is observed. Therefore, we presume that while the initial anodic peak is irreversible, the second peak is reversible. The initial anodic peak is most probably associated with the oxidation of $NiS_2$and in-situ transformation to $Ni(OH)_2$. As seen in Ni-based electrocatalyst, $Ni(OH)_2$ transforms into NiOOH with further bias at peaked potential, 1.4V which is characteristic for the redox potential of reaction of $Ni^{2+} \rightarrow Ni^{3+}$. Another proof for this transformation is that the phase change deduced by the cyclic voltage between $Ni(OH)_2$ and NiOOH is reversible. The content that undergoes reversible changes between $Ni(OH)_2$ and NiOOH is increased with the number of CV cycles. After the second anodic peak, the oxygen evolution reaction starts and its activity does not alter enormously with the number of CV cycles.

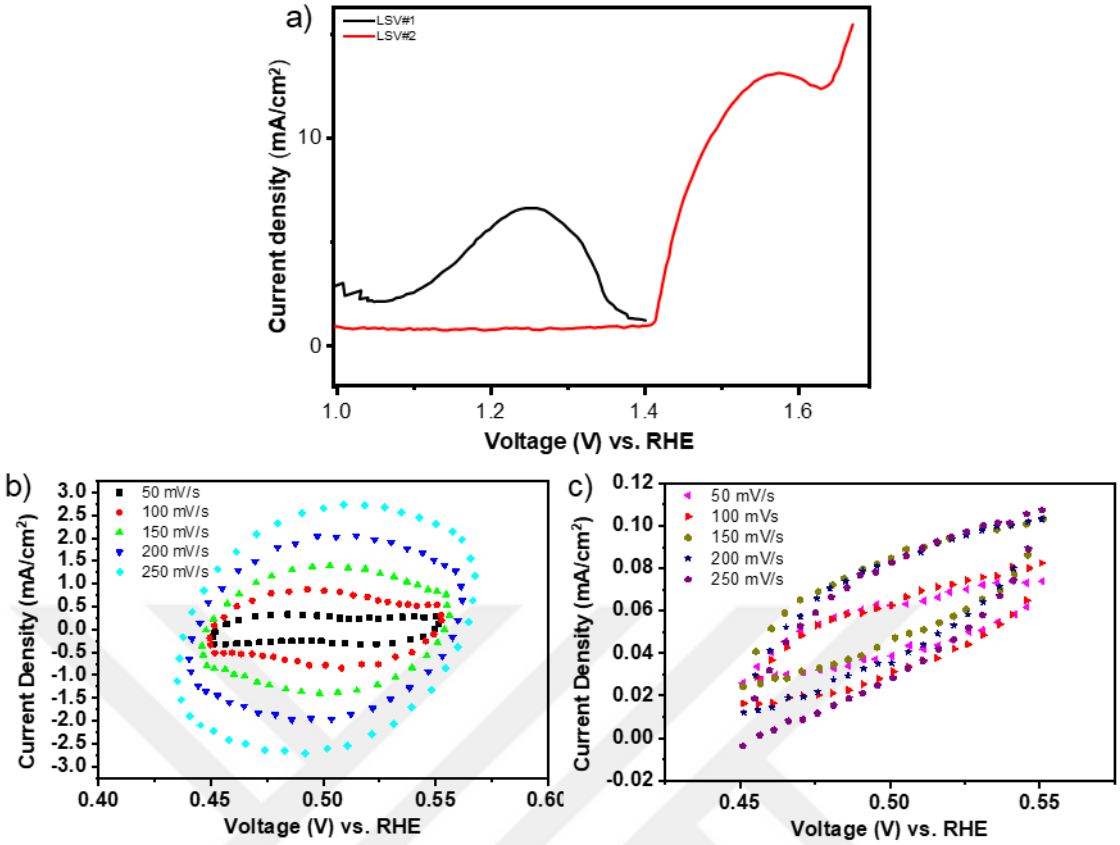

Figure 5.12 (a) LSV plots for mesoporous NiS_2 in 1 M KOH. (b-c) CV curves of as-prepared mesoporous NiS_2 and one LSV tested on FTO electrode in a non-faradic region in 1.0 M KOH at the scan rates of 50, 100, 150, 200, and 250 mV/s, respectively

In order to verify the oxidation of NiS_2 and understand the morphological alteration, we carried out LSV measurements in which the first LSV covers only the oxidation of NiS_2 and the second LSV includes the oxidation of nickel hydroxide species and oxygen evolution reaction, seen Figure 5.10a. We also recorded CV curves of as-prepared and first LSV tested electrodes in a non-faradaic region with various scan rates to understand the change in the electrochemically active surface area after the oxidation of NiS_2, seen Figure 5.10b-c. The second LSV scan does not show any oxidative peak that belongs to the oxidation of NiS_2. Therefore, available NiS_2 crystallites in the mesoporous framework are electrochemically converted into $Ni(OH)_2$. The electrochemical active surface area of the as-prepared electrode derived from the area of CV scans is dramatically decreased after the first LSV, indicating the collapse of the mesoporous framework. The in-situ transformation makes the surface of the electrode nonporous $NiOH_2$.

5.8 Mesoporous NiFe Oxide Thin films for Oxygen Evolution Reaction in Alkaline Media.

After mesoporous NiS_2 electrodes are found to be not durable under OER in alkaline media, we have decided to apply the LLC method to obtain active and more significantly durable mesoporous NiFe oxide electrodes for OER. We investigated the OER activities of mesoporous NiFe oxide electrodes having different compositions in alkaline electrolytes. First, we carried out 20 consecutive LSV measurements to determine the OER activity and stability.

In the consecutive LSV plots for mesoporous NiFe oxides electrodes, Figure 5.13, the activities and stabilities of all electrodes towards OER in alkaline electrolytes were investigated. Oxidation peak at around 1.30-1.45 V is observed for the electrodes up to the iron content, Ni/Fe atomic mole ratio of 3/6. Pure mesoporous nickel oxide electrodes exhibit the most intense oxidative current density and increasing iron content in the electrodes weaken the oxidative current density. In addition, its intensity increases with the number of LSV scans. Based on the literature and the findings, this is corresponding to $Ni(OH)_2/NiOOH$ conversion. While pure nickel and iron oxide electrodes show superior and inferior stabilities toward OER respectively, other electrodes with intermediate compositions are nearly durable against the phase changes and OER. However, the oxidation peaks of $Ni^{2+} \rightarrow Ni^{3+}$ for all electrodes shift to a higher potential. It has been reported in numerous recent studies that Fe impurities in KOH at even ppm levels deposits on the surface and increase drastically OER activities of Ni based electrocatalyst. The metal having higher oxidation states such as Fe^{3+} only shift the oxidation potential of Ni^{2+}.

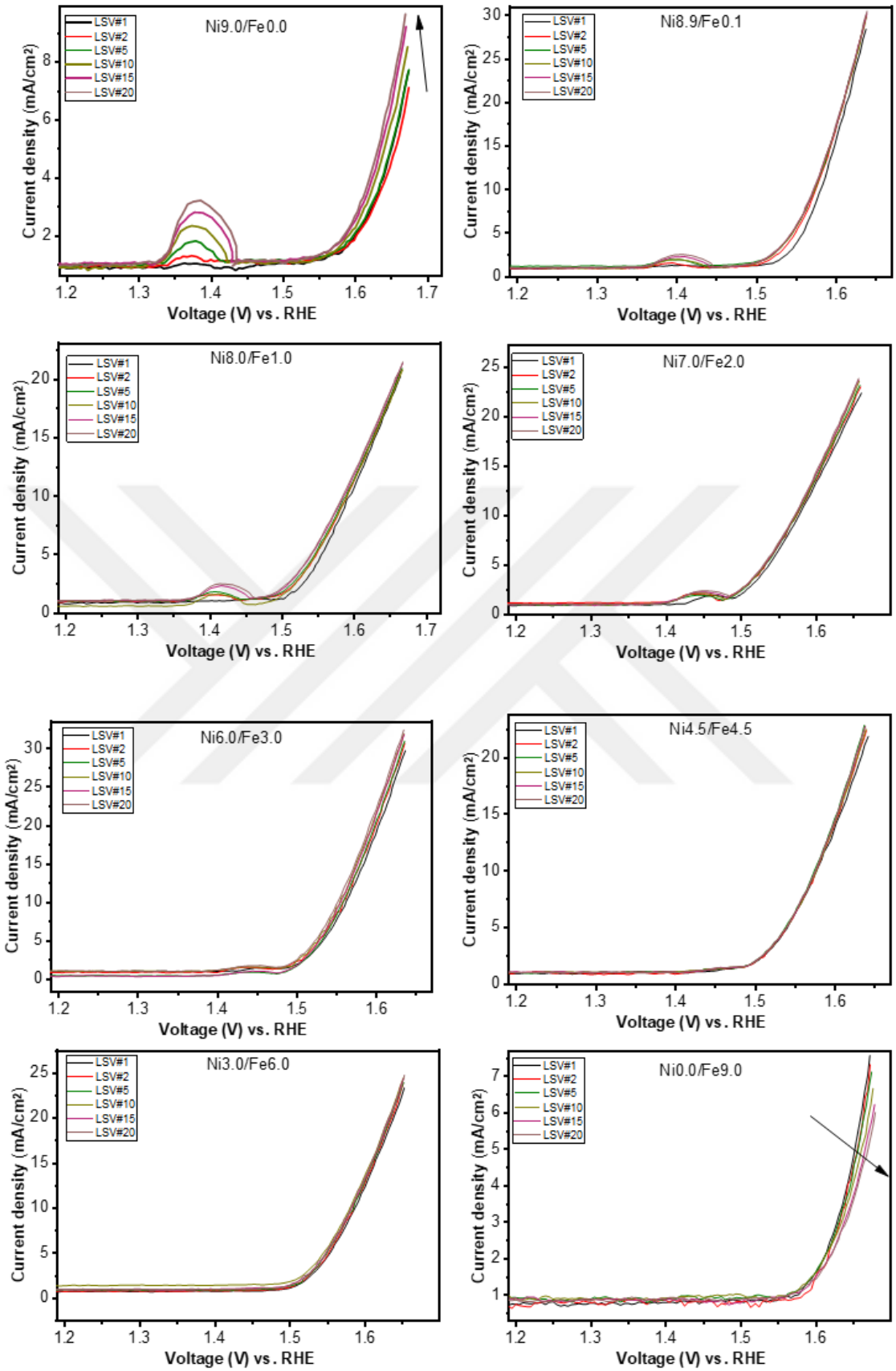

Figure 5.13 Consecutive LSV plots for mesoporous NiFe oxide electrodes having various compositions in alkaline electrolyte, 1.0 M KOH.

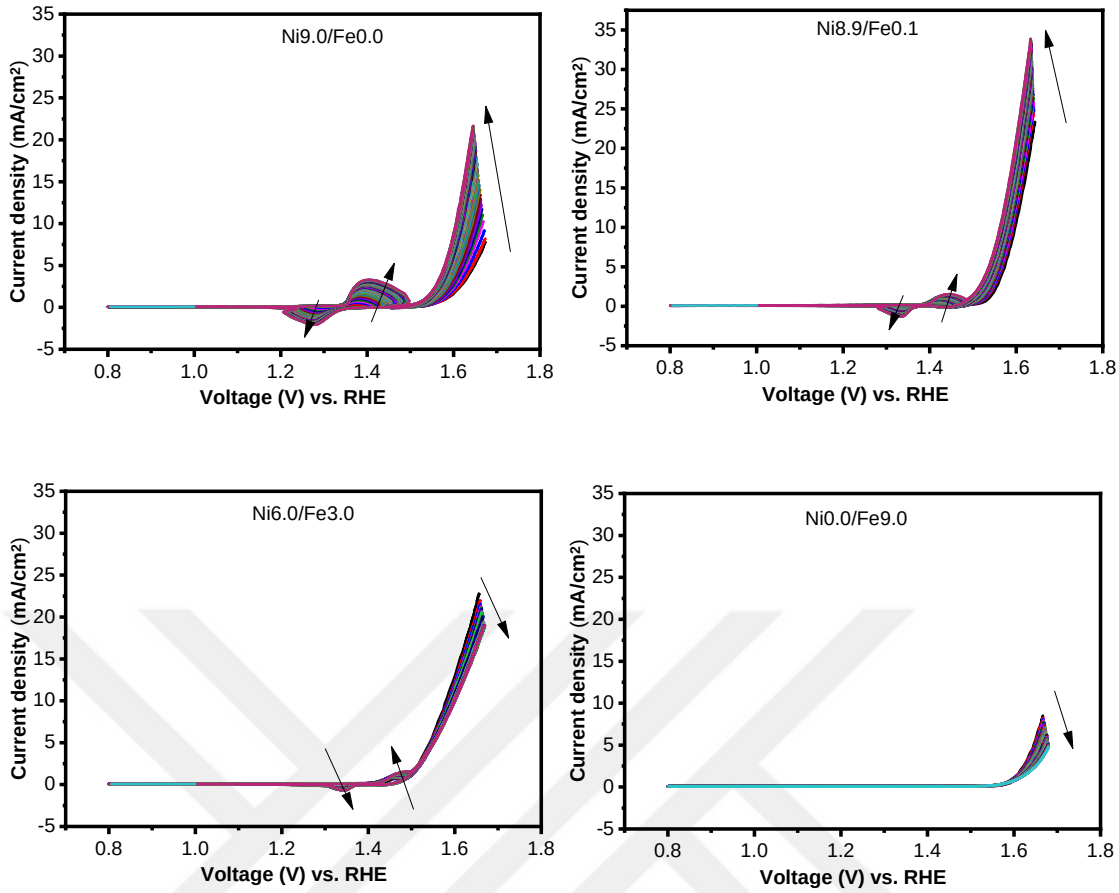

Figure 5.14 Consecutive CV plots for mesoporous NiFe oxide electrodes having various compositions in alkaline electrolyte, 1.0 M KOH.

In order to verify the compositional change which is responsible for $Ni(OH)_2$/NiOOH and Fe impurities in KOH, cyclic voltammetry plots were recorded for selected electrodes in Figure 5.15. The observed oxidative peak is reversible due to appearing opposite reductive peak at lower potentials in the reverse cycle, evidence for the change of $Ni(OH)_2$/NiOOH. Interestingly, the OER activity of mesoporous pure nickel electrode increases with CV scans intenser than the observations in LSV measurements. Another abnormality is that the steady activities in LSV measurements of mesoporous NiFe oxide electrodes present the enhancing or diminishing trends with CV cycles accompanying alterations of oxidation/reduction potentials nickel in even pure NiO. CA tests of selected electrodes display mild changes as their LSV tests, see Figure 5.15. In order to reveal the activity-structure relations regarding composition, the electrochemical tests should be conducted in Fe-free KOH electrolyte.

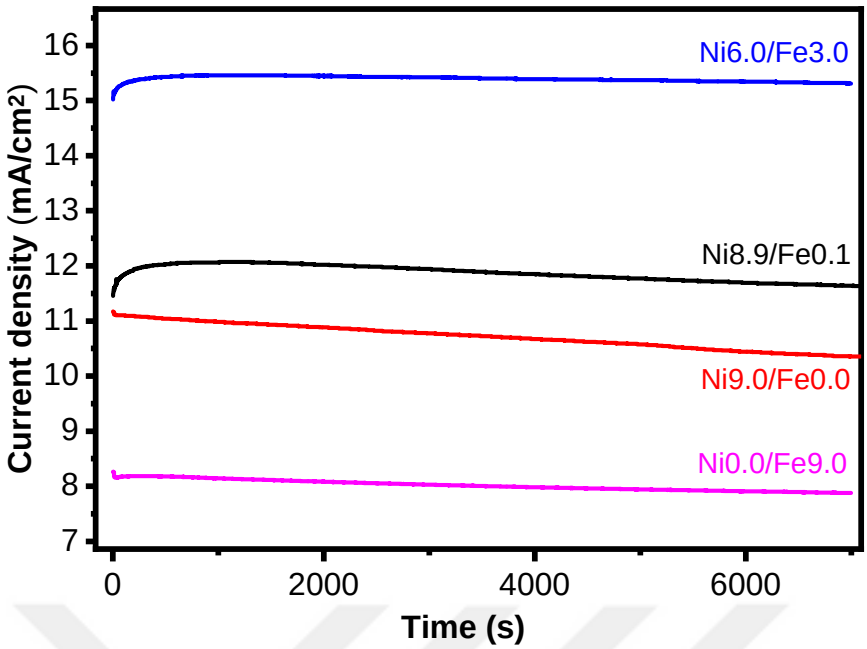

Figure 5.15 Chronoamperometry (CA) of selected mesoporous NiFe oxide electrodes under applied bias 1.0 V vs. RHE without IR compensation in 1.0 M KOH

5.9 Electrochemical tests in Fe-free KOH electrolyte

KOH solution was purified by $Ni(OH)_2$ for obtaining Fe-free KOH electrolyte. Compared with consecutive LSV tests in non-purified KOH electrolytes, the LSV plots become steady state after the first LSV run for nearly all electrodes as seen in Figure 5.16. The oxidative peak intensity of Ni9.0/Fe0.0 only increases with LSV cycles. In addition, the alteration of peak maxima was not observed for all electrodes, confirming used KOH electrolyte was impurity-free, especially Fe. In order to compare the activity of electrodes, 20^{th} LSV runs are selected and plotted in Figure 517.

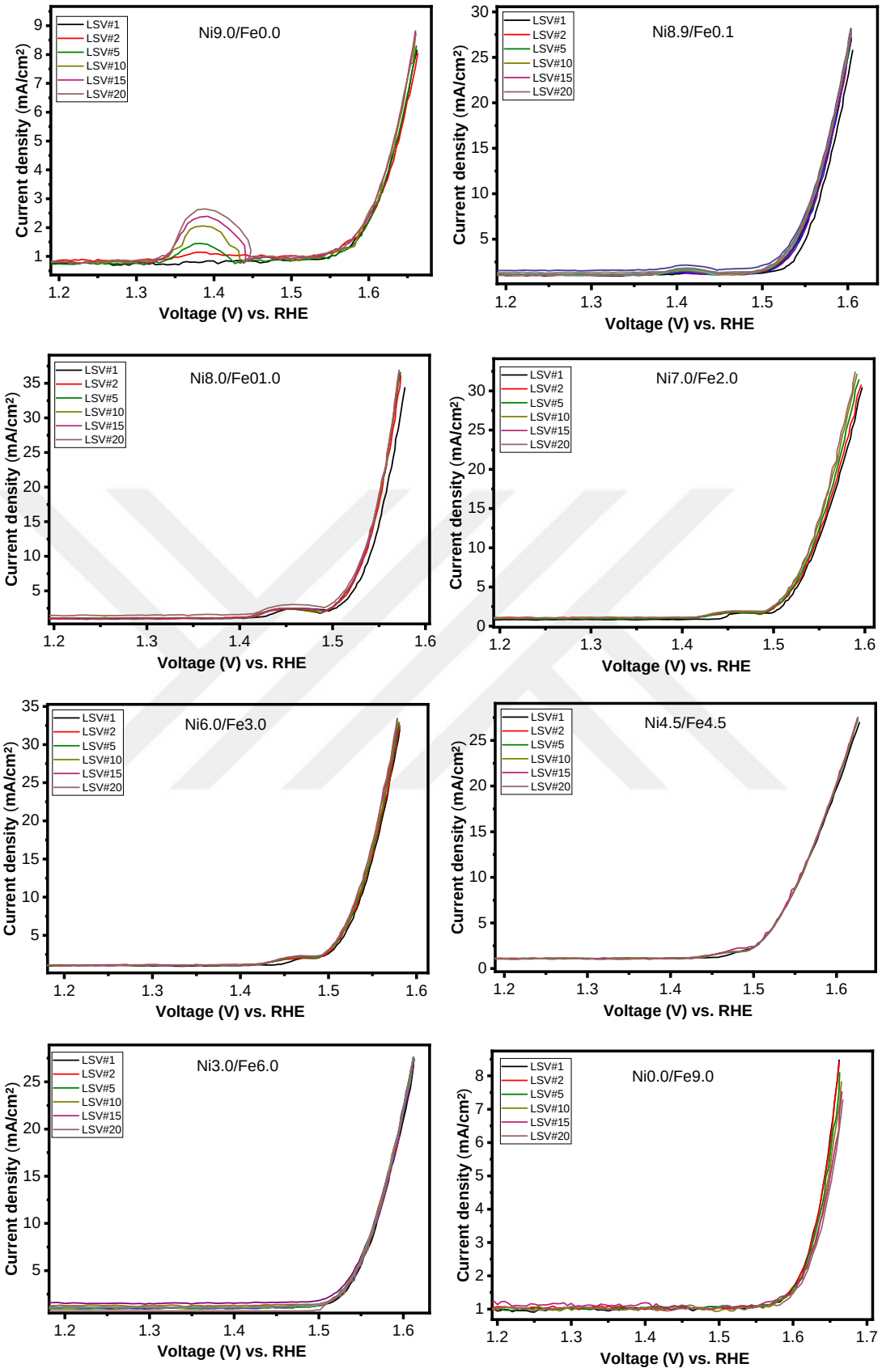

Figure 5.16 Consecutive LSV plots for mesoporous NiFe oxide electrodes having various compositions in alkaline electrolyte, Fe-free 1.0 M KOH.

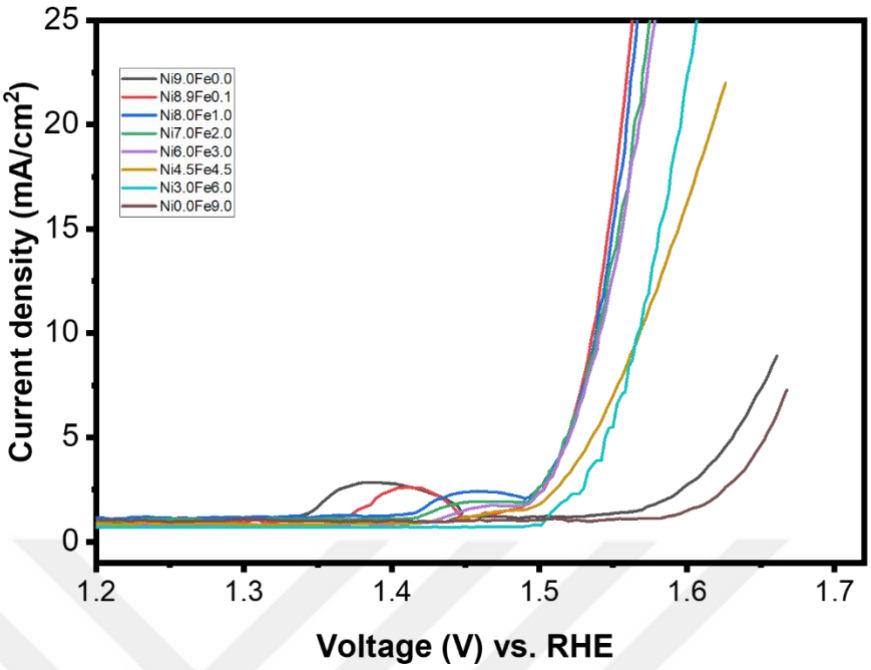

Figure 5.17 20th LSV runs for comparison of mesoporous NiFe oxide electrodes having various compositions in alkaline electrolyte, Fe-free 1.0 M KOH.

The alterations of viscosities of the typical solutions for preparation of metal oxides and random roughness of the FTO may change the loading amount and thickness of the catalyst film. Therefore, we normalized LSV plots according to the oxidative peak areas for Ni oxidation per the total content of Ni derived from EDS analysis, Figure 5.17. The Ni8.9/Fe0.1 gives a positive shift (20 mV) for the Ni oxidation peak compared with Ni9.0/Fe0.0. Up to content Ni4.5/Fe4.5, the positive shift for the Ni oxidation peak is constant (60 mV). The Ni8.9/Fe0.1 shows the highest OER activity and a large current density of 20 mA/cm^2 at 1.55 V vs. RHE, about 14 times higher than Ni9.0/Fe0.0. An increase in Fe content decreases slightly OER activity up to Ni4.5/Fe.45. A major drop in OER activity is observed where the composition comes to Ni4.5/Fe4.5. The worst OER activity is that of Ni0.0/Fe9.0. In Figure 5.18, the Raman spectrum of LSV tested electrodes having even strong Ni oxidation peak, Ni9.0/Fe0.0 and Ni8.9/Fe0.1, display nearly no changes, a slight increase in the shoulder band between at 449 and 495 cm^{-1}. Bell and *et. al.* showed that β-$Ni(OH)_2$ phase has a characteristic band the Raman bands at 449 and 495 cm^{-1} [192]. We find that the transformation of NiO to $Ni(OH)_2$ and Ni(OOH) is limited by the surface of the oxide particles. Fe-doped NiO enhances OER activity significantly with Ni oxidation. When the phase of the electrodes becomes the spinel structure of $NiFe_2O_4$, the OER activity is worsened. It can be deduced that Fe itself

cannot act as the active site. Fe in NiO lattice modulates the electronic structure of nickel oxide/hydroxide/hydroxide phases. Another supportive finding could be that the boost of OER activity is much larger for consecutive CV tests rather than LSV tests in non-purified KOH electrolytes. When the cyclic phase changes in CV tests promote the insertion of Fe atom in NiO lattice, the forward positive bias can foster the electrochemically deposition of Fe impurities in KOH electrolyte on the NiO crystals. The deposited and isolated Fe species should activate its neighbors of NiO active sites. The trends in the enhancement of incorporation content of iron into NiO lattice differentiate in the reported studies. While Rohlfing et. al. find $Fe_{0.1}Ni_{0.9}O$ showing the best OER performance [193], Kaufman reported $NiFeO_x$, where 29 % Fe [194]. Comparison of the overpotential at a specific current density with literature is controversial due to uncertain validations of the catalyst amount, substrate geometry, and conductivity. Contrary, we conclude that a small number of Fe introduction in the NiO lattice, such as $Ni_{0,043}Fe_{0.957}O$, is adequate to boost supreme OER activity. The OER activity trend follows $NiFeO_x$ > $NiFe_2O_4$ > NiO > Fe_2O_3..

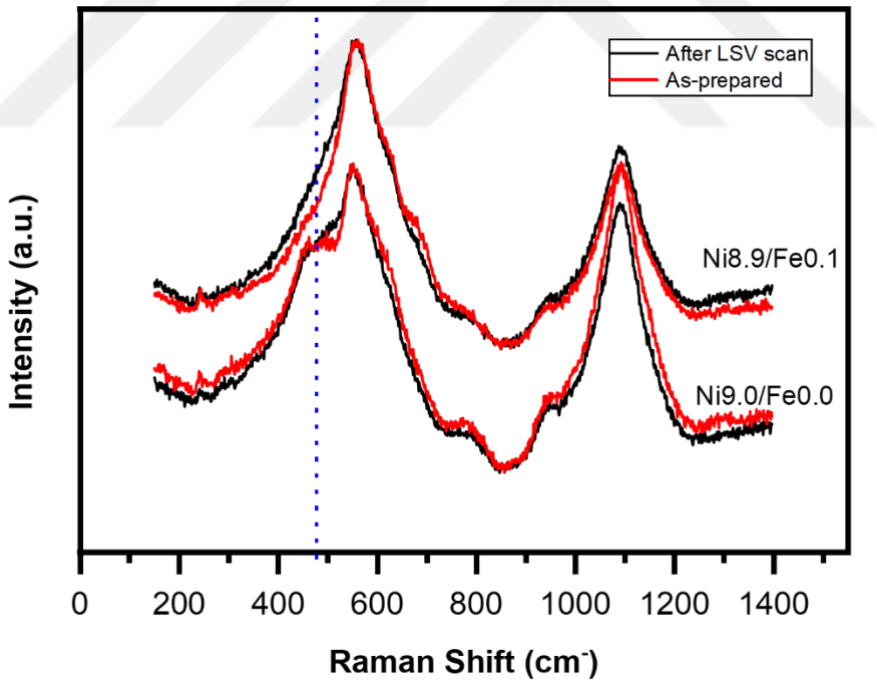

Figure 5.18 Raman spectrum of Ni9.0/Fe0.0 and Ni8.9/Fe0.1 electrodes after and before LSV runs

5.10 Mesoporous Materials for Overall Water Splitting

We showed that mesoporous NiFe oxides and pyrite nickel disulfide exhibit superior performance for OER and HER, respectively, in alkaline environment. Nickel or

stainless steel foam typically is used for the substrate for commercial alkaline electrolyzer. We prepared electrodes of one of the most active mesoporous NiFe oxide, Ni6.0/Fe3.0, on nickel foam and nickel disulfide, NiS_2, on carbon cloth for overall water splitting in alkaline electrolyte, 1.0 M KOH.

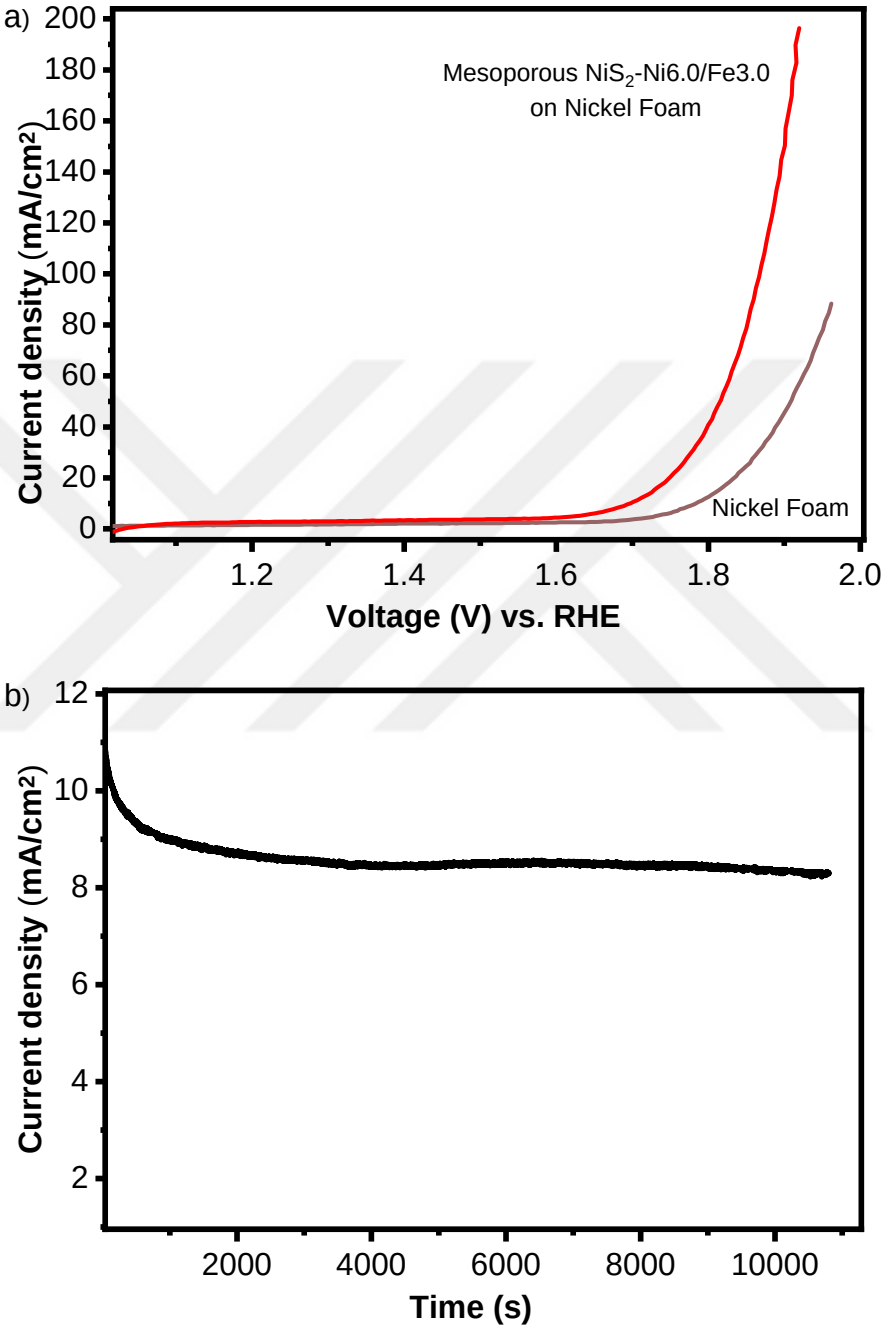

Figure 5.19 a) Polarization curves of mesoporous NiS_2 // mesoporous NiFe oxide on Ni foam and Ni foam//Ni foam and (b) CA of mesoporous NiS_2 on carbon cloth and mesoporous NiFe oxide, Ni6.0/Fe3.0 on nickel foam electrodes in alkaline electrolyte, 1.0 M KOH.

The polarization curve of mesoporous NiFe oxide, Ni6.0/Fe3.0, on nickel foam and nickel disulfide, NiS_2, on carbon cloth, see Figure 5.19a, was recorded after CA test conducted about 3 hours, see Figure 5.19b. Our electrolyzer requires only a cell voltage of 1.816 V to achieve a water-splitting current density of 50 mA cm^2 compared with a cell voltage of 1.904 V of Ni foam electrodes at the same current density. Ren showed (Ni,Fe)OOH/$MoNi_4$ electrodes show the lowest cell voltage, 1.454 V at 50 mA/cm^2 current density. The benchmark electrodes IrO_2/Pt for water splitting displayed a1.652 V of cell voltage at 50 mA/cm^2 current density. Our electrodes exhibit a close electrolysis performance. If mesoporous NiS_2 electrodes do not collapse and lose its high surface area during HER, the performance will be superior.

5.11 General Overview

After the investigation of the instability of OER activity in alkaline electrolytes, we have used a lyotropic liquid crystalline templating method to produce mesoporous iron nickel oxide thin film electrodes for OER. Nickel and iron nitrate salt with two surfactants (CTABr and $C_{12}E_{10}$) form nearly homogenous lyotropic liquid crystalline mesophases. The calcination temperature of 300 ^oC is adequate to burn off surfactants, obtaining 3-5 nm-sized pores. We reveal the exact structure and morphology of all produced mesoporous metal oxide thin film electrodes by using electron microscopy and spectroscopic techniques. The walls of the mesoporous framework consist of integrated metal oxide crystallites of around 5 nm. Mesoporous $NiFeO_x$, $NiFe_2O_4$, and Fe_2O_3 thin film electrodes with tunable phases and compositions were obtained. We investigated the OER performance and stabilities of mesoporous electrocatalyst thin films. Pure mesoporous NiO electrocatalyst shows an overpotential of around 470 mV at the current density of 10 mA/cm^2. The Fe-doped NiO boost the OER performance by decreasing an overpotential of around 1700 mV at the current density of 10 mA/cm^2. While $NiFe_2O_4$ exhibits a moderate OER performance, the lowest OER activity is belonging to Fe_2O_3. Fe impurities in KOH deposits on metal oxide electrodes under a positive bias and enhances the OER activity. When constant a positive bias enables the deposition of Fe islands on metal oxide particles, a cyclic voltage results in the insertion of Fe atoms into a metal oxide lattice. The enhancement in OER activity is larger in the case of the insertion of Fe atoms into metal oxide lattice. Those experimental results find out Fe is not the active site of mixed oxides for OER, Fe atoms just activate Ni centers via a partial charge transfer mechanism.

6 MESOPORUS MoS_2 THIN FILMS

6.1 Literature Overview

Platinum is the best electrocatalyst for HER, however, its large-scale application is limited due to its high cost and low abundance [195]. MoS_2, a significant member of two-dimensional (2D) transition metal dichalcogenides, has been used as a hydrodesulfurization catalyst in the petroleum refinery industry for decades due to its abundant, inexpensive, and reversible hydrogen desorption properties [196]. It has also exhibited strong electrochemical activity, it has been shown by theoretical calculations that S-terminated edge sites of MoS_2 might be active for the HER [197], which has later been confirmed experimentally [198]. S-terminated edge sites are active whereas the basal planes and Mo terminated edges, which compose the majority of the sites, are inert for HER [198] . The relative activities of edge sites, vacancies, and grain boundaries of MoS_2 have been determined by Tafel analysis and the slopes have been calculated to be 65-75 mV/dec. for edge sites, 65-85 mV/dec. for sulfur vacancies, and 120-160 mV/dec. for grain boundaries [199].

One strategy for elevating the HER activity is to generate an amorphous catalyst because a disordered atomic orientation may induce more electrochemically active sites [200]. However, amorphous MoS_3 has been shown to undergo a structural transformation towards MoS_2 under HER conditions [201]. Operando ambient pressure X-ray photoelectron spectroscopy (APXPS) has been used to demonstrate the conversion from MoS_3 to MoS_2, Mo 3d and S 2p spectral changes under negative bias show progressive compositional change and put forward MoS_2 phase critical for enhanced HER activity [202]. Further evidence for structural modification has been provided by *in situ* TEM. Amorphous MoS_2 simultaneously crystallizes under negative bias [203].

2D layered structures lack the electrical conductivity required for electrochemical applications owing to the weak electronic coupling between van der Waals layers. The electrocatalytic activity of a single layer MoS_2 for the HER decreases with the addition of a second layer, adding the potential barrier of 0.119 V [204]. The nanostructured crystalline MoS_2 is very useful in terms of accelerating the mass transfer, improving electron conductivity, and avoiding restacking [205]. Therefore, many nanostructured MoS_2 based electrocatalysts, i.e., hierarchical structures [206], quantum dots [207],

micro-nano spheres [208], and flower-like nanoflakes [209] were designed, synthesized, and tested for HER.

Preparation of catalyst ink from 2D materials is troublesome due to restacking of the layers [210]. 3D structures of nanostructured MoS_2 with an interconnected conductive network are crucial to prevent restacking and provide a high specific surface area with improved conductivity [211]. For this reason, carbon-based support materials such as carbon nanofibers [212], [213], carbon cloths [214], [215], carbon papers [216], carbon nanotubes [217], and graphene foams [218] have been used. For example, W-doped MoS_2 and MoO_2 heterostructures on carbon nanotubes exhibit Pt-like HER activity [219]. The more conductive MoO_2 bridges the less conductive MoS_2, and the carbon matrix, facilitate the charge transport between MoS_2 and carbon nanotubes. Doping high valance atom, W, into the MoS_2 lattice also activates the basal plane S atoms and results in an enhanced HER activity. Another strategy to boost the HER activity is to activate the basal planes of MoS_2 by creating sulfur vacancies [220]–[223]. The concentration of sulfur vacancies that maximizes the HER performance is between 12.5% and 15.62% [223].

The porous electrocatalysts provide better mass transport and are beneficial for large-scale electrocatalyst fabrications. The high porosity potentially increases the surface area that further leads to the exposure of abundant internal sulfur terminated edge sites. For this reason, mesoporous transition metal sulfides have attracted great attention owing to their superior performance as catalysts, electrodes, and photocatalytic materials [68]–[72]. The hard templating method has been applied for the synthesis of mesoporous metal sulfides such as FeS_2, CoS_2, NiS_2, WS_2, and MoS_2 [73], [74]. There are several examples of mesoporous MoS_2 thin films prepared by using this method [74] whereas the synthesis of mesoporous metal sulfides by soft templating is still very challenging due to the uncontrollable fast precipitation process between metal salts and the S_2^- ions. Mesoporous iron-doped $MoS_2/CoMo_2S_4$ powder electrocatalyst that shows superior HER activity in alkaline media have been developed [79]. However, the synthesis of mesoporous MoS_2 thin-film electrocatalysts via the soft templating route remains challenging.

The one-step production protocol enabling the formation of 3D integrated porous structures without a post-coating process does not require nonconductive organic binders and offers a robust alternative for efficient electrode preparation. The stable lyotropic liquid mesophase with two surfactants and various transition metal nitrates have been converted to mesoporous $MnCo_2O_4$, $NiCo_2O_4$ $LiMn_2O_4$, $ZnCo_2O_4$ and NiO thin films for

many applications [61], [64]–[66]. The same strategy has been adopted to prepare mesoporous NiS_2 electrodes for HER [46]. Mesoporous MoS_2 thin-film electrodes are ideal for improved mass transfer and the number of HER active sites. To the best of our knowledge, a one-step method that enables mesoporous MoS_2 thin film coating with narrow pore sizes for HER has not been developed. Herein, we modified the liquid crystalline templating strategy to obtain mesoporous MoS_2 thin-film electrodes for HER.

6.2 Experimental

6.2.1 Preparation of Solutions of Molybdenum and Sulfur Precursor and Surfactants

In a typical solution preparation, CTAB, $C_{12}EO_{10}$, ammonium heptamolybdate tetrahydrate, and thiourea are mixed in a 25 ml vial with deionized water. Later, the ammonia solution is added by dropping pipette. When ethylene glycol is used for preparation of solution, ethylene glycol is added before addition of ammonia solution. The solution is stirred for one day in order to make sure it homogenous and clear (transparent and colorless). A Schematic illustration of the general solution preparation is indicated in Figure 6.1. Amount of each ingredient for the preparation of solutions with/out ethylene glycol are tabulated in Table 6.1 and Table 6.2, respectively.

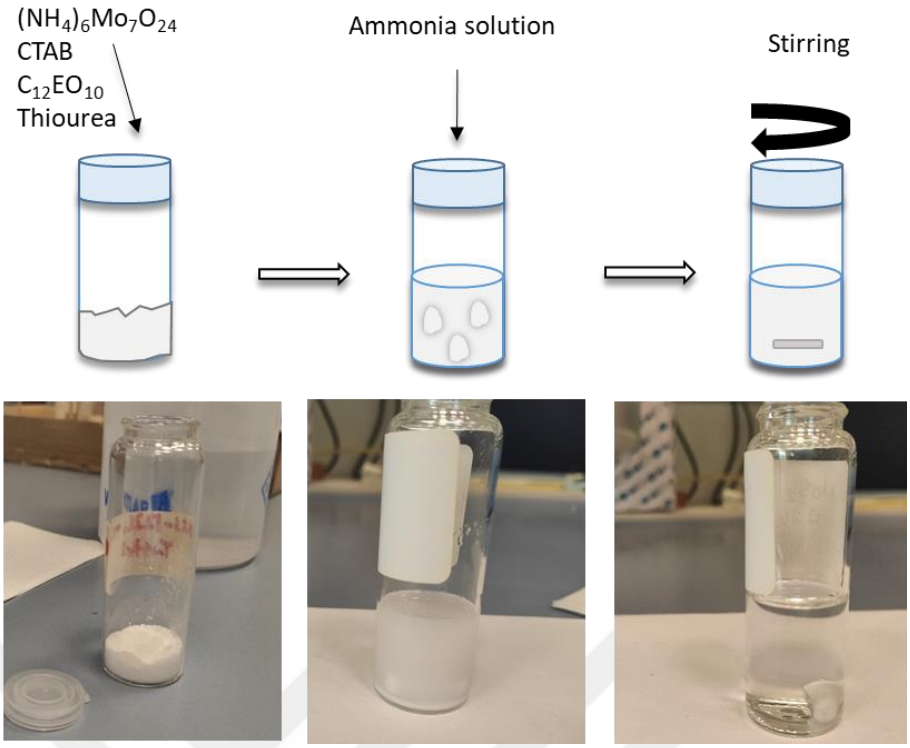

Figure 6.1 Schematic illustration of the preparation of Mo and S precursor and surfactants solution

Table 6.1 The amounts of CTAB, $C_{12}EO_{10}$. $(NH_4)_6Mo_7O_{24}.4H_2O$, thiourea, NH_4OH and deionized H_2O.

$(NH_4)_6Mo_7O_{24}.4H_2O$	Thiourea	CTAB	$C_{12}EO_{10}$	NH_4OH	H_2O
2.495 g	1.457 g	0.291 g	0.500 g	4.000 g	5.000 g

Table 6.2 The amounts of CTAB, $C_{12}EO_{10}$. $(NH_4)_6Mo_7O_{24}.4H_2O$, thiourea, NH_4OH, deionized water and ethylene glycol.

$(NH_4)_6Mo_7O_{24}.4H_2O$	Thiourea	CTAB	$C_{12}EO_{10}$	NH_4OH	H_2O	Ethylene glychol
2.495	1.457	0.291	0.500	4.000	5.000	4.000

6.2.2 Instrumentation

The instrumentation that used in this chapter was described in the previous chapters.

6.2.3 Preparation of Lyotropic Liquid Crystalline (LLC) Mesophase

The mesophases were prepared by spin coating of solution their ingredients are given in table for thin LLC films. Spin coating was applied to prepare LLC and further mesoporous MoS_2 thin films. A few drops of the solution were placed on the FTO or microscopic glass and it was spun for 20 s at 1000 rpm by a spin coater. To obtain thicker mesophase, drop-cast coating on the microscopic slides was also applied. Drop-casting was applied by placing a few drops of solutions and aged for evaporation of deionized water. Schematic illustration of both drop-cast and spin coating methods are indicated in Figure 6.2.

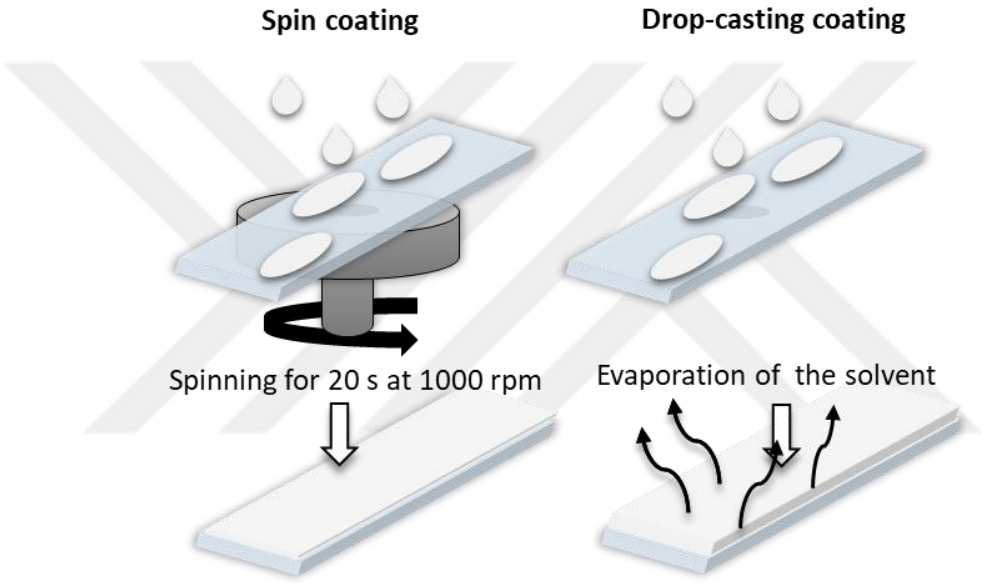

Figure 6.2 Schematic illustration of spin coating and drop-casting casting methods.

6.2.4 Preparation of Mesoporous MoS_2 on FTO

The mesoporous MoS_2 electrodes, synthesized using liquid crystalline templating which described in the same protocol above over a FTO, were used for HER. Before spin coating, FTO (1 cm × 2 cm) substrates were cleaned by ultra-sonication in absolute ethanol. The electrodes were prepared by spin coating the clear solutions of the corresponding composition as given in Chapter 6.3.2. Scotch-tape was used to make an area of 1 cm^2 on FTO for spin-coating. The mesophase film over the FTO was annealed at 170 ℃ and 300 ℃ in a nitrogen (N_2) atmosphere for one hour and two hours, respectively. The as-prepared samples were also further annealed at 400 and 500 ℃ for

two hours. The electrochemical tests like LSV, CV, etc. and the advanced characterizations like XPS, SEM, EDX, etc were conducted. Schematic illustration of the preparation of electrodes are presented in Figure. 6.3.

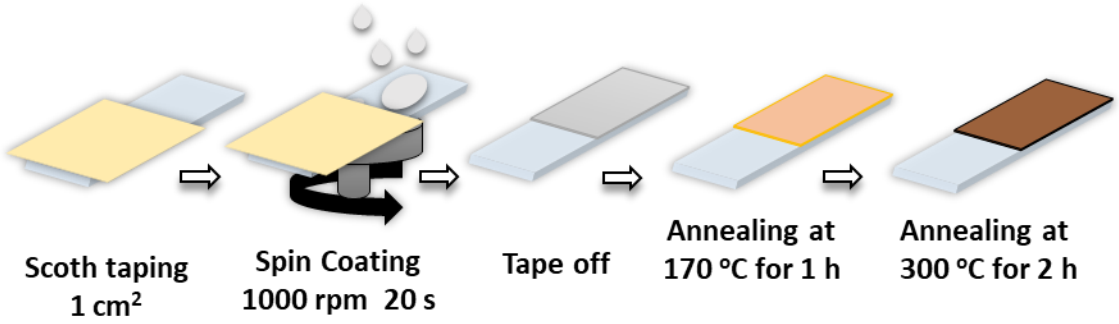

Figure 6.3 Schematic illustration of preparation of MoS_2 on FTO

6.2.5 Preparation of Mesoporous MoS_2 on Carbon Fiber

Before spin coating, carbon fibers were cleaned by ultra-sonication in absolute ethanol. The carbon fibers were cut into pieces having sizes of 0.1x2 cm. Half of it was dipped into the clear solutions of the corresponding composition. The carbon fibers were placed on the glass substrate and then spin coated at 1000 rpm for 30 seconds. The mesophase film over the carbon fiber was annealed at 170 ℃ and 300 ℃ in a nitrogen (N_2) atmosphere for one hour and two hours, respectively. Schematic illustration of the fabrication of electrodes are presented in Figure. 6.4.

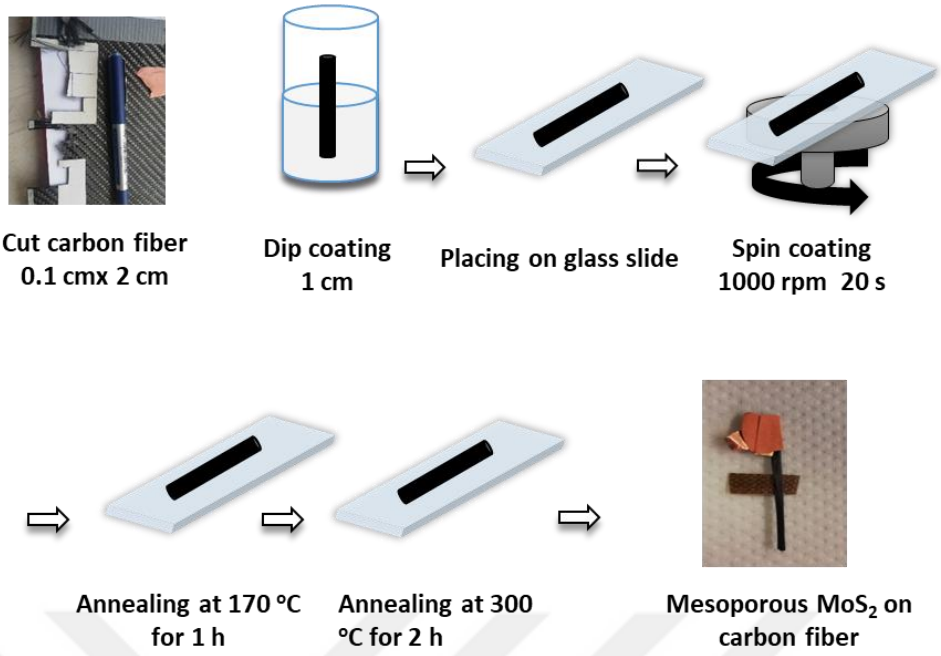

Figure 6.4 Schematic illustration of preparation of MoS_2 on carbon fiber.

6.3 Characterization

Most transition metal nitrate salts have low melting point and high solubility in water that promote the formation of lyotropic liquid crystalline mesophase with surfactants. However, there is no such Mo precursor available. Ammonium heptamolybdate tetrahydrate was rationally selected from among Mo precursors because high pH given by excess ammonia provides extra stability and solubility. However, ammonium heptamolybdate tetrahydrate does not melt at any temperature but just decomposes at 190 °C [224]. This poses a major problem for the formation of mesophase of ammonium heptamolybdate tetrahydrate with surfactants, which is a prerequisite to obtain mesoporous MoS_2. Therefore, we initially investigated the formation of liquid crystalline mesophase of ammonium heptamolybdate tetrahydrate and thiourea and two surfactants, CTAB) and $C_{12}E_{10}$. The reaction of drop-casted liquid mesophases of ammonium heptamolybdate tetrahydrate and thiourea with two surfactants was monitored by using XRD and FTIR. Drop-casted layer was annealed for half an hour at various temperatures in inert N_2 atmosphere without waiting evaporation of solvent and excess ammonia.

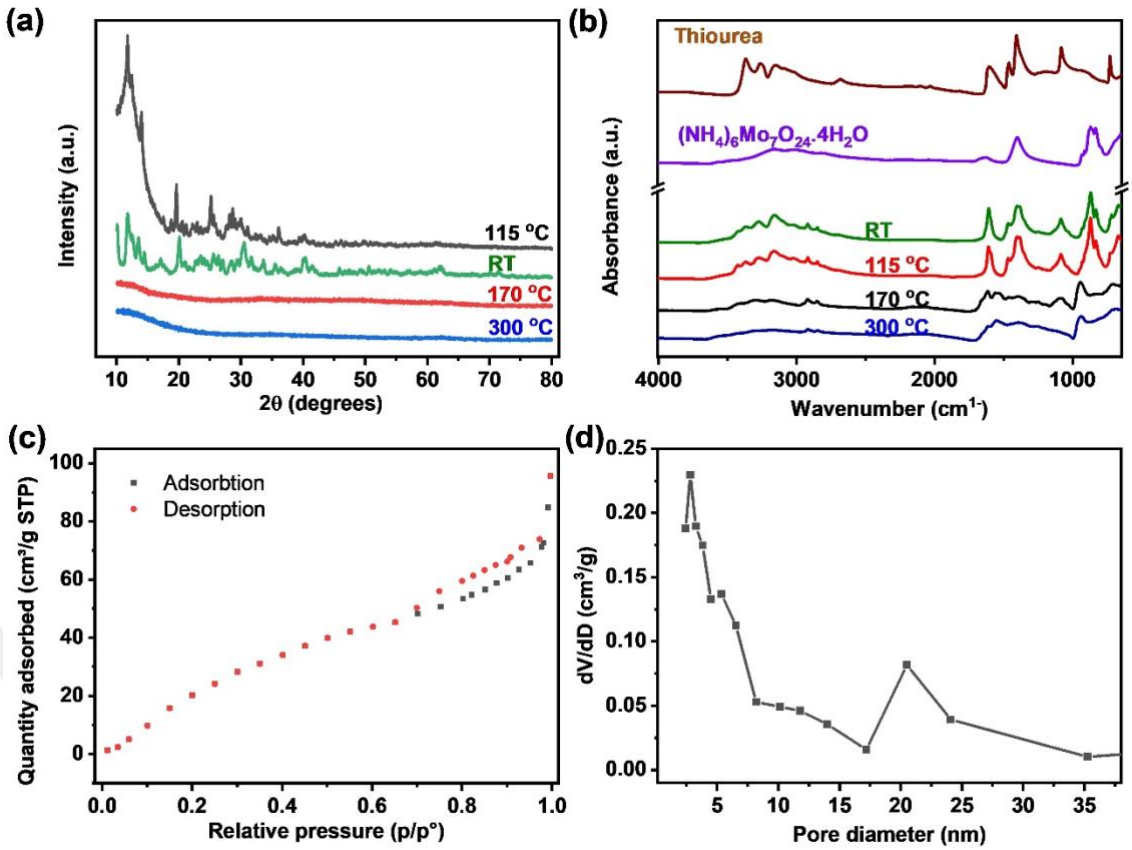

Figure 6.5 (a) XRD patterns and (b) FTIR spectra of drop-casted LLC mesophases, which were annealed at various temperatures. (c) N_2 adsorption-desorption analysis and (d) pore size distribution of the mesoporous MoS_2.

XRD analysis provides direct information about both the formation and the stability of the LLC mesophase. In the case the mesophase does not form, the precursors and surfactants crystallize after evaporation of the solvent. Many overlapped diffraction lines mostly belonging to ammonium heptamolybdate are observed in the XRD patterns of the samples annealed at 115 ℃ (see Figure 6.5a). On the other hand, the samples annealed at 170 ℃ and higher temperatures do not give any diffraction lines. FTIR spectra of the samples collected at various temperatures are presented with the reference samples of thiourea and ammonium heptamolybdate in Figure 6.5b. Tracking thiourea peaks in FTIR spectra is critical to detect the complexation of molybdate ions with sulfurous compounds. For thiourea, the peaks at 3383 and 3277 cm^{-1} are assigned to the symmetric and asymmetric stretching vibrations of N−H. The peak at 1620 cm^{-1} corresponds to N−H bending vibration. The absorption observed between 1473 and 1413 cm^{-1} is assigned to the N−C−N symmetric and asymmetric stretching modes. The sharp peak at 7316 cm^{-1}

is caused by the C−S stretching mode. Spectra obtained from the samples at room temperature and annealed at 115 ℃ are almost identical and the fingerprints of thiourea in the samples annealed at 170 ℃ and higher temperatures are not observed. This indicates that the annealing temperature of 170 ºC is adequate for the decomposition of thiourea. The samples at room temperature and 115 ℃ are opaque while their color turns greenish and dark with increasing annealing temperatures (see Figure 6.6a). The opacity of the samples correlates with XRD patterns. Crystals of ammonium heptamolybdate salt and thiourea cause opaque color. The sulfurous products from the decomposition of thiourea react with molybdate, resulting in the formation of thiomolybdates (MoS_4^{2-}) giving the samples dark red color. These observations above reveal that molybdates cannot form the LLC mesophase. However, formed thiomolybdates can be confined among the surfactant domains and form mesophase. This unique behavior is useful for the synthesis of mesoporous MoS_2 thin films.

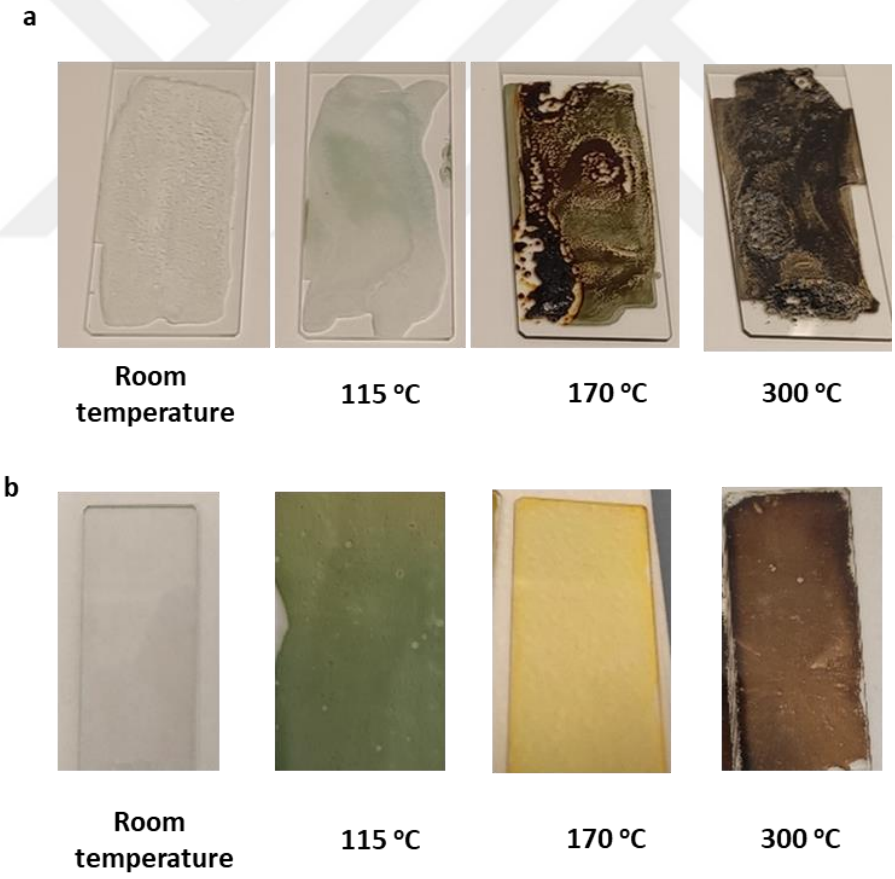

Figure 6.6 Photographs of the samples annealed at various temperatures, which were prepared using typical solution (a) without and (b) with ethylene glycol.

The spin coating method enables obtaining thinner and uniform films compared to drop and dip coating methods. Water is normally a good choice of solvent owing to its

ability to dissolve all precursors and surfactants. However, spin coating accelerates the evaporation of solvents in the liquid templating methods. Ethylene glycol, usually named as organic water, has a higher boiling point (197 ℃) and has almost the same ability to dissolve hydrophilic compounds or ionic species. The addition of ethylene glycol into a typical solution of CTAB, $C_{12}EO_{10}$, ammonium heptamolybdate, and thiourea can provide the exposure time required during spin coating. Because the viscosity of ethylene glycol is higher than that of deionized water, its amount was kept limited to get even overlayers without pits and holes.

As demonstrated in Figure 6.6b, the color of the transparent samples, which were prepared by spin coating of typical solution with ethylene glycol, turns to homogenous yellowish green after annealing at 115 ℃. Further annealing at higher temperatures changes them to yellow and then dark brown. Similar color changes were observed as the annealing temperatures of drop-casted films were raised. Besides, the crystallization of ammonium molybdate salts caused by leaching out of the mesophase was not observed as evidenced by the absence of the XRD patterns of the spin-coated samples at room temperature and further annealed at 115 ℃ (see Figure 6.7). The deionized water evaporates during spinning and the remaining ethylene glycol keeps dissolving all ingredients required for the LLC mesophase integrity. Rapid direct annealing of spin-coated samples at 170 ℃ evaporates the remaining ethylene glycol. Meanwhile, thiourea directly decomposes into sulfurous products at those temperatures (it decomposes at around 130 ℃), producing thiomolybdates. The changes in the diffraction lines at small angle XRD of the as-prepared and annealed samples presented in Figure S6a suggest that the addition of ethylene glycol to the solution prevents the crystallization of ingredients and enables the formation of LLC mesophase required for the synthesis of mesoporous MoS_2 thin films. The addition of ethylene glycol does not alter XRD patterns and thus mesoporous samples of similar crystallinity form (see Figure 6.7b). As in the protocol for the preparation of mesoporous nickel sulfides, capping during annealing cannot be applied to prevent the escape of sulfurous gasses from the mesophase without reacting molybdate ions [46]. When we apply the sandwich structure after spin coating, the sol between two substrates shrinks and aggregates randomly on the surface of the substrates during evaporation of ethylene glycol at 170 ℃. This hinders the formation of thin films.

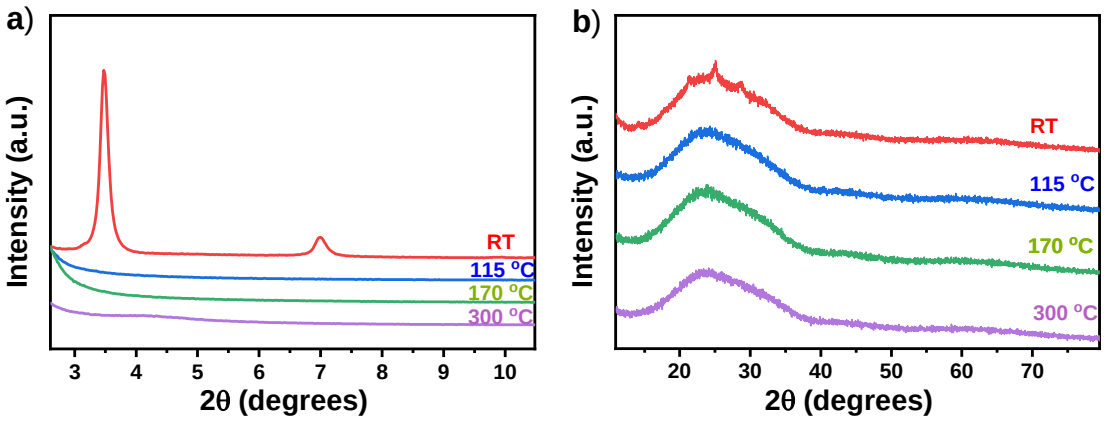

Figure 6.7 (a) Small and (b) wide XRD patterns of the samples annealed at various temperatures, which were prepared using typical solution with ethylene glycol.

To prove that fast annealing the LLC mesophase of ammonium heptamolybdate salt, thiourea, and two surfactants outcomes the mesoporous MoS_2, N_2 adsorption-desorption isotherm of the sample annealed at 300 °C was recorded (Figure 6.5c). The hysteresis on the adsorption and desorption behavior confirms the mesoporosity. BET surface area is about 182 m^2/g. The Barrett-Joyner-Halenda (BJH) analysis exhibits a narrow pore-size distribution peaking around 3 nm and a broad pore-size distribution starting to above 30 nm (Figure 6.5d). The mesopore size (~3 nm) is consistent with the size of surfactant domains in the LLC mesophase. The pore size distribution greater than the expected micelle sizes (2-3 nm) may be originating from harsh release of decomposed gaseous compounds induced by annealing.

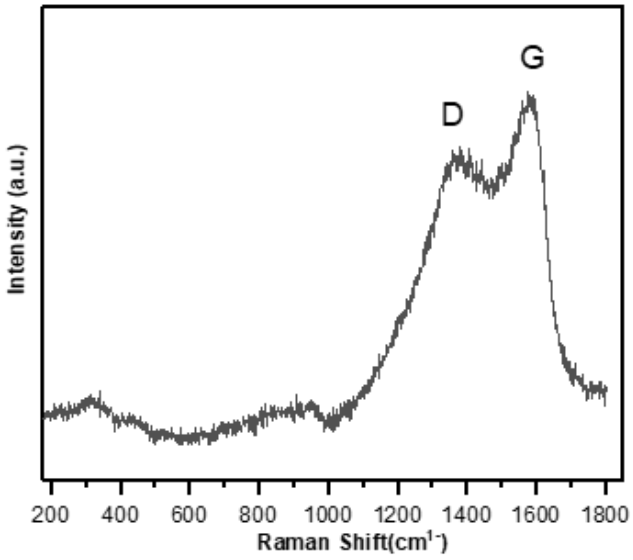

Figure 6.8 Raman spectra of mesoporous MoS_2

In order to identify the structural form of the surfactant after annealing, Raman analysis of the mesoporous MoS_2 was performed and the resulting spectrum is presented in Figure 6.8. In carbon, the Stokes phonon energy shift caused by laser excitation creates two main peaks in the Raman spectrum: graphitic peak G (1580 cm^{-1}), a primary in-plane vibrational mode, and an out-of-plane vibration, defect peak D (1350 cm^{-1}). The Raman spectrum is considered to mainly depend on sp^2/sp^3 ratio. The intensity ratio of D to G peaks is below 1, suggesting an amorphous structure. Surfactants in the mesophase structure are carbonized by annealing; mesopores are not clogged by amorphous carbon. They could be suspended in the mesoporous framework due to volumetric shrinkage during decomposition. Such a process provides an extra surface area on the sample. BET surface area, 182 m^2/g, does not belong solely MoS_2 nanocrystallites.

SEM images of scratched mesoporous MoS_2 thin film samples presented in Figure 6.9a-b show non-textured surface features. On the other hand, the interior of the films has 20-25 nm sized pores, which is consistent with pore size distribution derived from N_2 sorption analysis The imaging of smaller mesopores is under the limit of SEM. EDS of the sample performed for the compositional analysis indicates that the Mo/S atomic ratio of the sample is about 1:1, smaller than the expected ratio, 1:2 (Figure 6.10). This could indicate that a large fraction of Mo is still in its oxide form even though the Mo and S precursor ratio was adjusted to be 1:2.

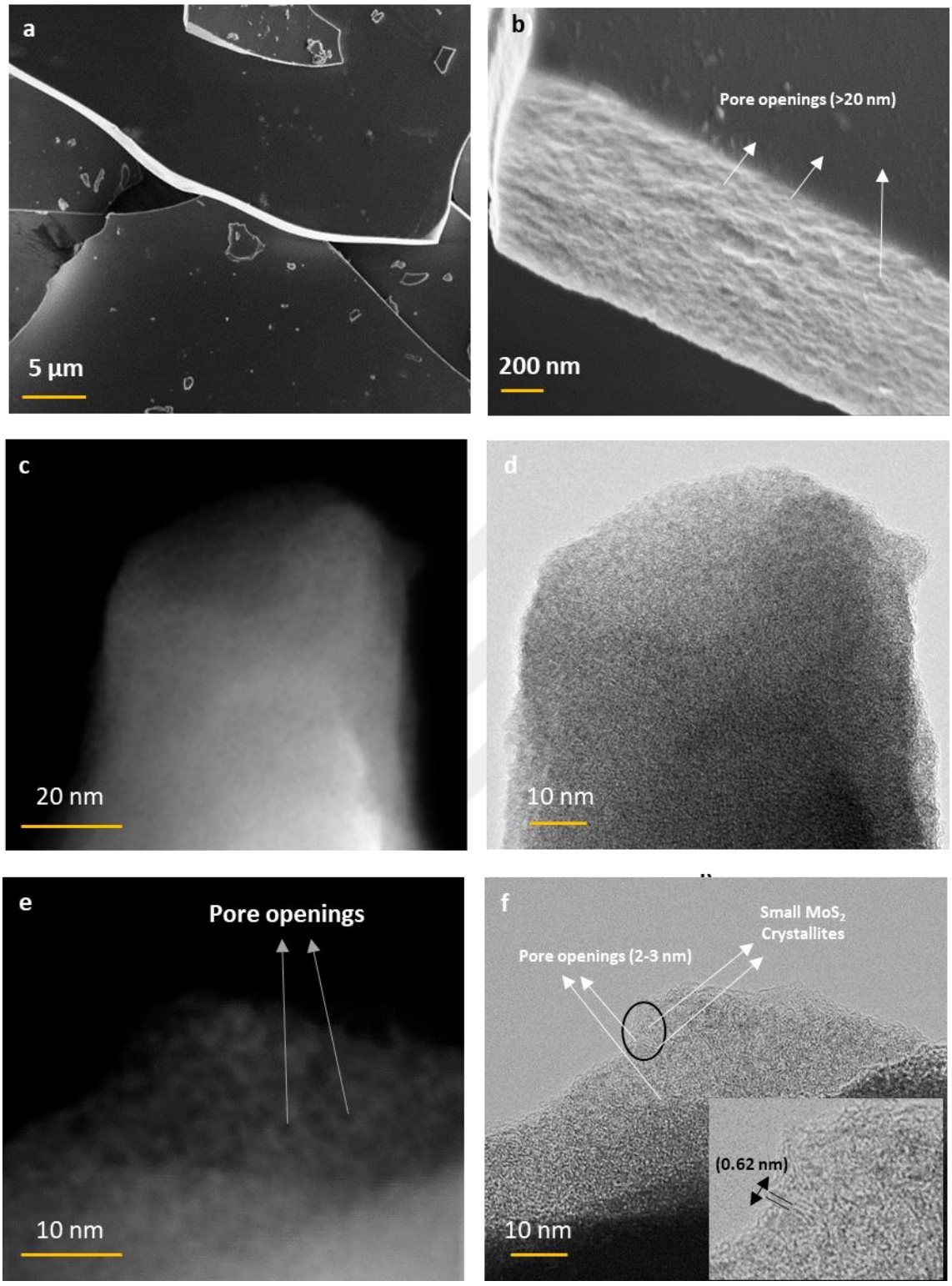

Figure 6.9 (a-b) SEM images of scratched mesoporous MoS_2 in different perspective on copper grid. (c and e) HAADF-STEM, and (d and f) low and high magnification TEM images of mesoporous MoS_2

To further understand the structural details of the mesoporous MoS_2 films, TEM images have also been collected. High angle annular dark-field (HAADF) of STEM

images, in Figure 6.9c and e, and TEM images, in Figures 6.9d and f, display the sponge-like disordered mesoporosity with pore openings 3-5 nm wide. In the selected microscopic area of the sample, the sizes of the pore openings are consistent with the sizes of the micelles formed by CTAB and $C_{12}EO_{10}$. In the high-resolution TEM images (Figure 6.9f), the lattice fringes of MoS_2 nanocrystals (0.62 nm representing (200) lattice planes) can be observed.

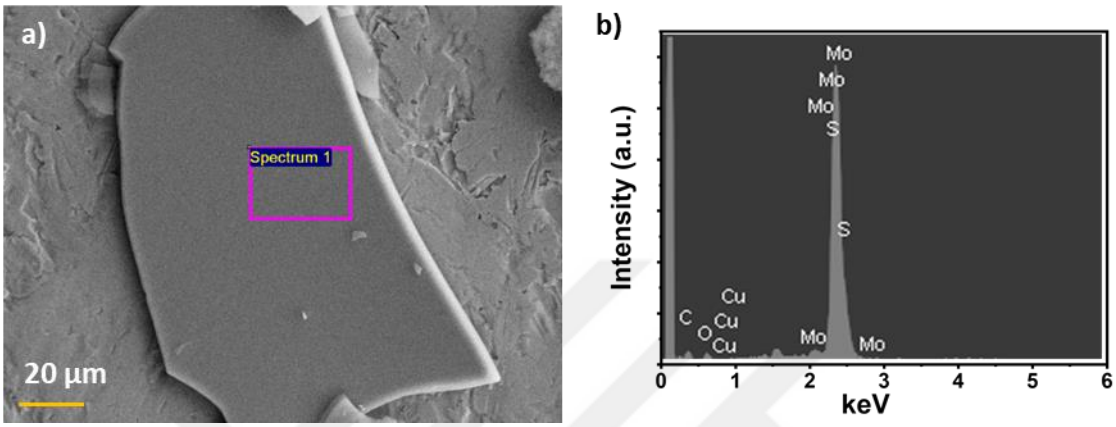

Figure 6.10 (a) SEM image of mesoporous MoS_2. (b) EDS spectrum derived from selected area of SEM image in a.

XPS measurements were performed to further identify the surface compositions of the electrodes. The results of the XPS analysis of as-prepared mesoporous MoS_2 are shown in Figure 6.11a-b. Reported XPS studies of MoS_2 formation from ammonium tetrathiomolybdate solutions is useful for assignment of Mo 3d and S 2p peaks [225] In Figure 6.11a, the Mo 3d double peaks at 232.3 and 229.1 eV are assigned to Mo^{4+} in MoS_2. Moreover, two sets of double peaks at 231.45 and 230.95 eV, and at 235.6 and 232.2 eV are observed, which originate from the MoS_3 and MoO_3 formed by unconverted molybdate ions, respectively. For S 2p XPS spectra presented in Figure 3b, the doublet peaks at 161.3/162.5 eV are ascribed to the S_2^{2-} while the major doublets at 163.8/165.0 eV were attributed to S^{2-} dimers, originating from amorphous MoS_3 and MoS_2 edges. Combining XRD, TEM, STEM, EDS, and XPS results, we can reveal that mesoporous MoS_2 thin films consist of the mixture of nano-crystalline MoS_2, amorphous MoS_3, and amorphous MoO_3 with mesoporous structure.

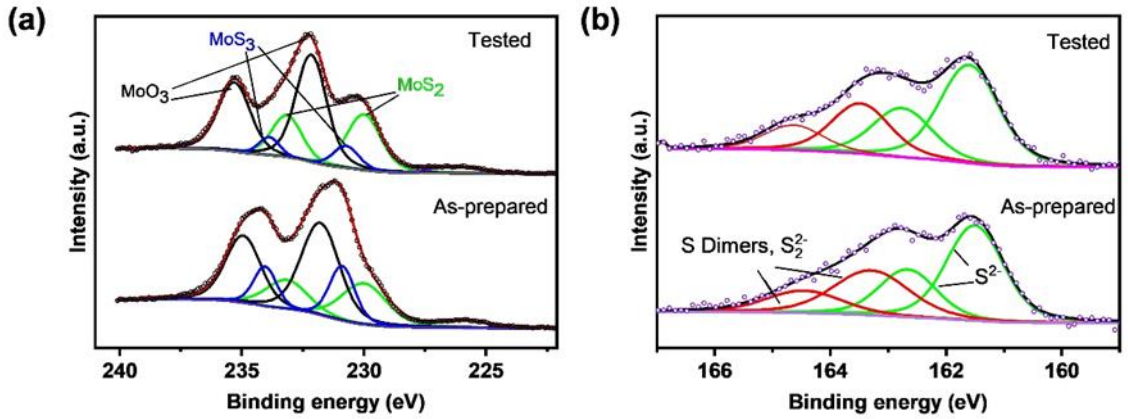

Figure 6.11 (a) Mo 3d and (b) S 2p XPS spectra of the mesoporous MoS_2 on FTO. The deconvolution of the spectra was performed by using the Doniac-Sunjic line profile. A Shirley type of background was used in all spectra. The S 2p spectra were deconvoluted using a doublet with a splitting of 1.2 eV and a 2:1 $2p_{3/2}$:$2p_{1/2}$ area ratio. The Mo 3d spectra were deconvoluted using a doublet with a splitting of 3.14 eV and a 2:3 $3d_{3/2}$:$3d_{5/2}$ area ratio.

6.4 Hydrogen Evolution Reaction in an Acidic Electrolyte

We investigated the HER activities of mesoporous MoS_2 thin films electrodes on FTO in an acidic electrolyte, 0.5 M H_2SO_4. Ten consecutive LSV scans were recorded for each electrode, the progress of the LSV curves was demonstrated in Figure 6.12a. It is observed that the HER activity of the sample annealed at 300 ℃ is dynamic, each LSV scan shows better activity in terms of lower onset potential and higher current density than the previous one. After the sixth scan, no further change in the LSV curves was observed. Ten consecutive LSV scans were also recorded for electrodes prepared at 400 and 500 ℃ to check the effect of annealing temperature on the HER activity (see Figure 6.13). The most active sample towards HER in an acidic environment is the one annealed at 300 ℃. Higher annealing temperatures reduce the HER activity dramatically. HER activities for these samples showed no improvement with LSV scans as observed in the sample annealed at 300 ℃. It was observed that consecutive LSV scans did not exhibit any significant change.

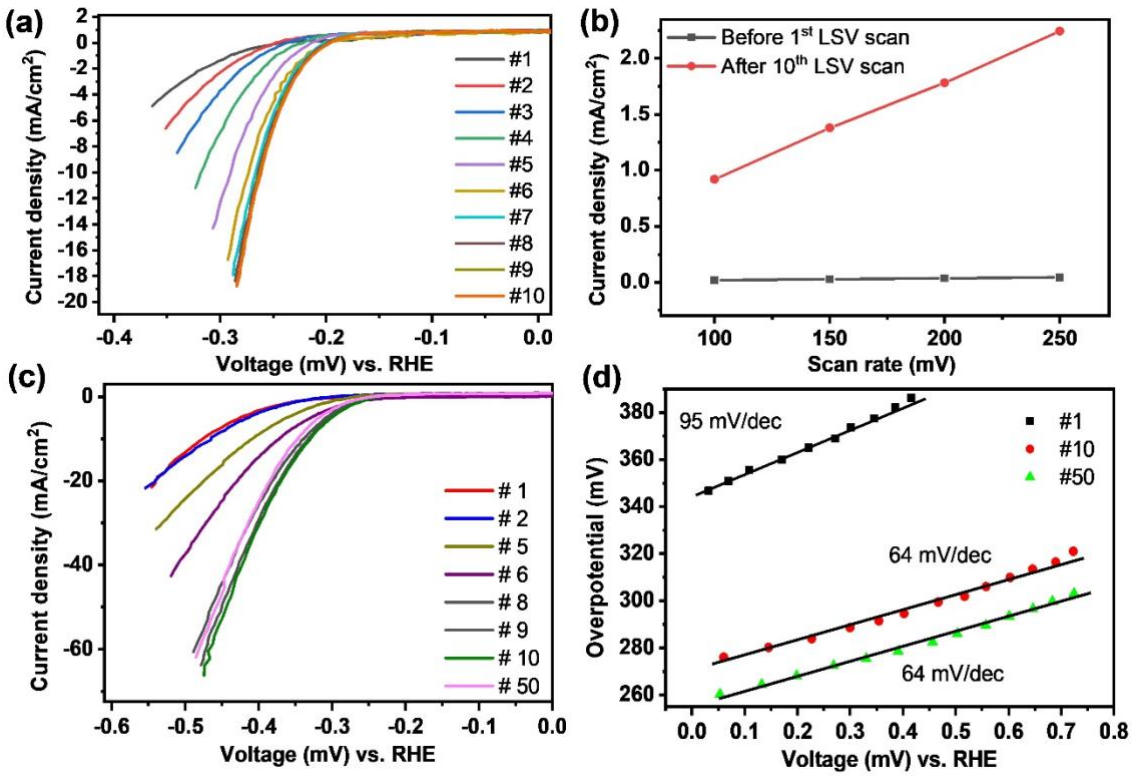

Figure 6.12 (a) Consecutive LSV plots in 0.5 M H_2SO_4 for mesoporous MoS_2 on FTO prepared at 300 °C. (b) Capacitive currents plots as a function of the scan rate for before 1st LSV san and after 10th LSV scan. (c) Long-term stability test in 0.5 M H_2SO_4. Consecutive LSV plots for mesoporous MoS_2 on FTO prepared at 300 °C. (d) Tafel plots of mesoporous MoS_2 on FTO prepared at 300 °C for various consecutive LSV plots.

ECSAs of the electrodes are typically proportional to the electric double-layer capacitance (C_{dl}), which can be derived from the CV curves in a non-faradaic region. Therefore, we track the changes in the CV curves of mesoporous MoS_2 after the stabilization performed by successive LSV scans (Figure 6.14). It was observed by comparing capacitive current plots before the 1st and after 10th LSV scan as a function of the scan rate that the ESCA of the tested sample annealed at 300 °C increased at least 5 times (Figure 6.12b). Other samples showed the same trend to a lesser extent. The calculated ECSA of tested samples annealed at 400 °C and 500 °C are around four times less than the tested sample annealed at 300 °C. We stressed that samples annealed at 400 °C and 500 °C did not show any porosity in N_2 sorption measurements. As expexted, this explains the limited HER performance of these samples. The increase in ESCA represented the correlation with the enhancement in HER activity. Apparently, there is an electrochemical activation process during HER.

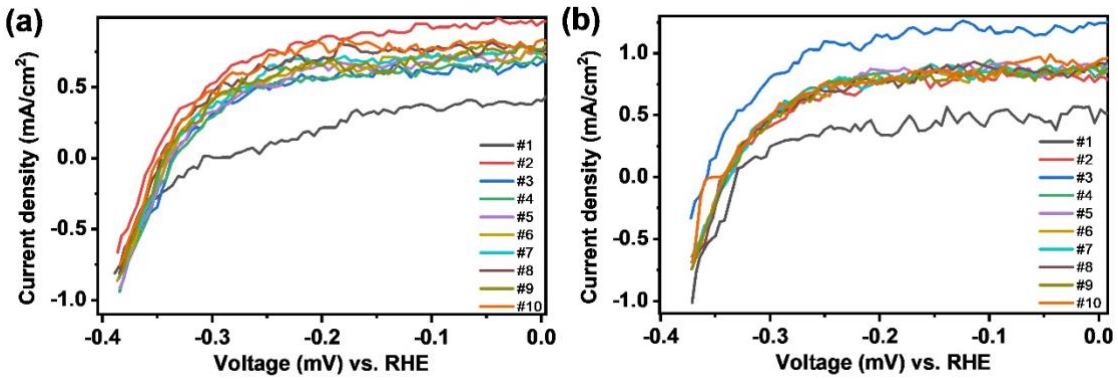

Figure 6.13 Consecutive LSV plots in 0.5 M H_2SO_4 for mesoporous MoS_2 on FTO prepared at (a) 400 ℃ and (b) 500 ℃.

To ascertain the long-term changes in HER activity, consecutive LSV curves under high potentials and current densities were recorded (Figure 6.12c). Even in working in high current densities, the HER activity was maximized at the 10^{th} cycle and then slightly lost its activity. The HER started with an overpotential of 476 mV and reduced to 332 mV at the current density of 10 mA/cm^2. It was presumed that intensified evolution of H_2 bubbles on the film structure might delaminate film structure. The Tafel plots in Figure 4d show that first LSV cycle possesses the highest Tafel slope, 95 mV/dec. in comparison to 64 mV/dec. obtained after 10^{th} and 50^{th} LSV scans, demonstrating the superior HER kinetics. Delamination of the catalyst over extensive HER was much plausible explanation since the Tafel slopes did not vary. The loss of electrocatalyst decreases only the current density and does not affect the HER kinetics. The amendment in the kinetics of HER might be related to the changes of the active sites. If the number of active species with the same characteristics is increased during HER by reasons like the dissolution of surface species blocking active HER sites, ESCA could increase but Tafel slopes do not necessarily change. Therefore, we assume that the synthesized mesoporous MoS_2 sample shows pre-catalyst property that transforms into a much superior electrocatalyst for HER.

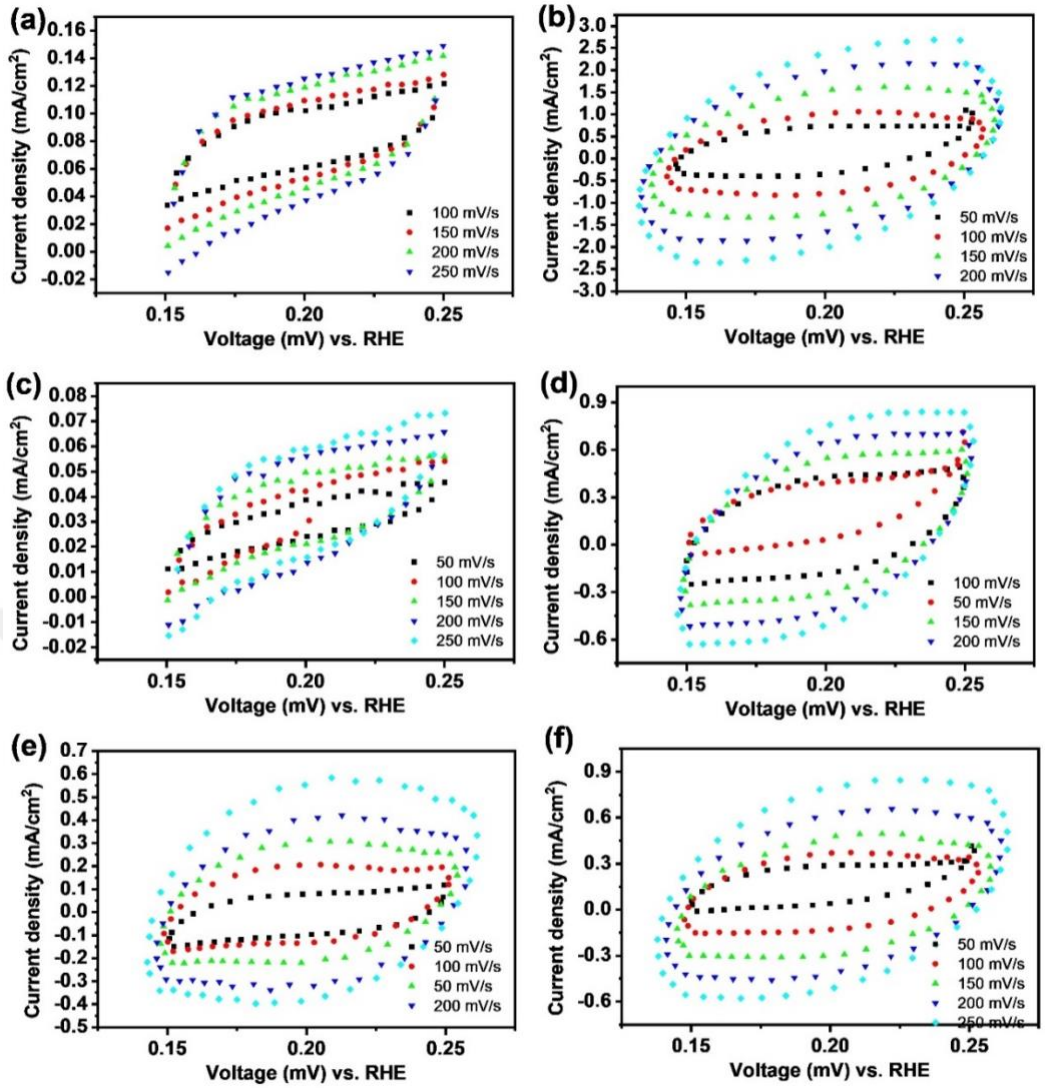

Figure 6.14 CV curves of the mesoporous MoS_2 on FTO. MoS_2 annealed at 300 ℃ (a) as-prepared / (b) tested, annealed at 400 ℃ (c) as-prepared / (d) tested, and annealed at 300 ℃ (e) as-prepared / (f) tested in a non-faradic region in 0.5 M H_2SO_4 at the scan rates of 50, 100, 150, 200, and 250 mV/s.

To further apprehend the structural change and the HER activity enhancement during HER, we performed XPS measurements on LSV tested sample. The results of the XPS analysis given in Figures 6.11a-b indicated that the intensity of double peaks at 231.4 and 231.6 eV in Mo 3d spectrum, originated from the MoS_3, decreased compared to as-prepared sample. The intensity of MoS_2 species significantly increases while those of the MoO_3 species remain largely unchanged. The relative ratio of S 2p doublet peaks at 161.3/162.5 eV and 163.8/165.0 eV slightly increases compared to the as-prepared sample. Sulfur dimers originating from MoS_3 could be converted to ultra-small nano-

crystalline MoS_2 species, because of having a high number of sulfur dimers at the edges. It is revealed that most of the amorphous MoS_3 species in the mesoporous framework are reduced to superior active species, MoS_2. It is also observed in the literature, amorphous MoS_3 undergoes in situ self-reconstruction and the formation of MoS_2 species during HER [201]–[203]. This electrochemical activation is limited by the surface. We observed that MoS_3 species cannot be electrochemically converted to MoS_2 as a whole because of the lack of contact with the electrolyte. We can presume that MoS_2 nanodomains were embedded in the amorphous MoO_3 and MoS_3 matrix of the mesoporous framework. Amorphous MoO_3 species do not present a pronounced HER activity [226] .

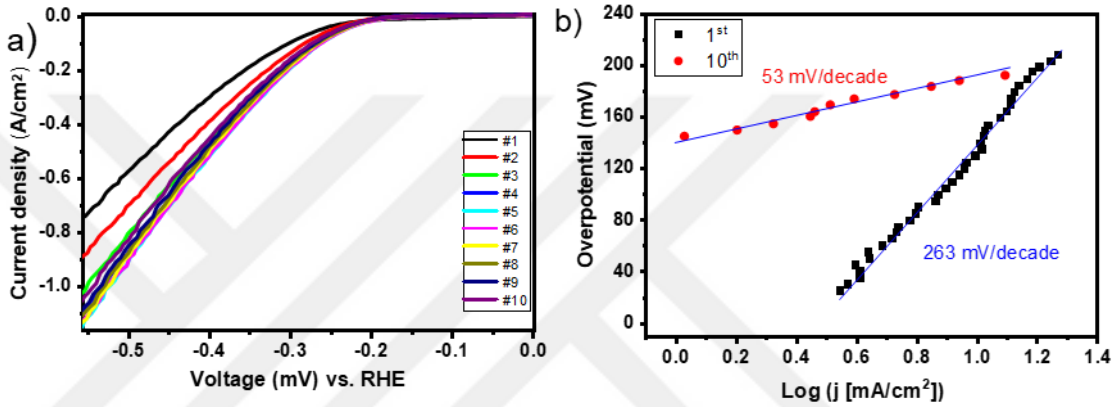

Figure 6.15 (a) Consecutive LSV plots and (b) Tafel plots for mesoporous MoS_2 on carbon fiber prepared at 300 °C, in 0.5 M H_2SO_4.

The carbon-based materials are generally used as a support material for hydrogen electrodes in order to increase the overall conductivity and surface area of the electrocatalyst. 10 consecutive LSV scans of mesoporous MoS_2 on carbon fiber within a cathodic potential window in the range of 0 to −0.6 V vs. RHE were recorded (Figure 6.15a) and the Tafel plots of first and final LSVs were calculated (Figure 6.15b). Similar to the mesoporous samples on FTO, each LSV curve exhibited better activity than the previous one. It can be seen that the 10^{th} LSV cycle showed the lowest onset overpotential of ~189 mV at 10 mA/cm^2 for the HER, beyond which the cathodic current density rises rapidly under more negative potentials. Commercial electrolyzers should operate at large current densities around 1−2 A/cm^2. The electrode on carbon fiber can reach 1 A/cm^2 with the overpotential of ~550 mV owing to the highly porous character of the electrodes. As expected, the sample on carbon fiber displayed faster HER kinetics than the sample on FTO, since the Tafel slope of the sample on carbon fiber (53 mV/dec.) was lower than

that of the sample on FTO (64 mV/dec.). As shown in Table 6.3, the values of Tafel slopes and the overpotentials at various current densities are comparable with most of the reported MoS_2 based HER electrocatalysts. In acidic media, Volmer-Heyrovsky ($H^+ + e^- \rightarrow H_{ad}$, $H^+ + H_{ad} + e^- \rightarrow H_2$) and Volmer-Tafel ($H^+ + e^- \rightarrow H_{ad}$, $H_{ad} + H_{ad} \rightarrow H_2$) processes are plausible [120]. The theoretical Tafel slope values for the Volmer reaction, Heyrovsky reaction, and Tafel reaction are 118, 39, and 29.5 mV/dec, respectively [227]. From these findings, we can suggest that the HER follows the Volmer-Heyrovsky mechanism initially when MoS_3 as precatalyst is a dominant phase. With electrochemical activation, the reduction of MoS_3 into MoS_2 nanodomains, the mechanism likely advances toward Volmer-Tafel. MoS_2 nanodomains are likely to be have abundant edge sites. Doping with high valance atoms (W, Nb, Mo, etc.) and supporting with a substrate of a superior conductive high surface area, such as carbon nanotube foam or graphene foam, our mesoporous electrodes may provide much more active sites and internal conductivity, leading to Pt like activity [219]. We can suggest that our novel soft templating method could be a promising coating technology to prepare low-cost and highly efficient MoS_2 HER binder-free electrodes on any support materials.

Table 6.3 Comparison of reported HER activities of MoS_2.

	Synthesis method	**Surface area (g/cm^2)**	**Tafel slope (mV/decade)**	**Overpotential (mV)**	**Catalyst amount (mg/cm^2)**	**Ref.**
MoS_2/Graphene foam	Hydrothermal	819	42	200 (at 100 mA/cm^2)	0.21	[218]
W-MoS_2/MoO_2/CNT foam	Thermal	N/A	44	62 (at 10 mA/cm^2)	N/A	[219]
MoS_2/MoO_2/CNT foam	Thermal	N/A	73	121 (at 10 mA/cm^2)	N/A	[219]
MoS_2/CNT foam	Thermal	N/A	120	190 (at 10 mA/cm^2)	N/A	[219]
MoS_2 on N-doped Carbon fibers	Hydrothermal	N/A	48	135 (at 10 mA/cm^2)	0.217	[213]
Mesoporous double-gyroid MoS_2	Hard Template	N/A	50	290 (at 10 mA/cm^2)	N/A	[74]
Mesoporous MoS_2/MoO_3 on Carbon fiber	Soft template	182	53	180 (at 10 mA/cm^2)	N/A	This work

6.5 Hydrogen Evolution Reaction in an Alkaline Electrolyte

We also investigated the HER activities of mesoporous MoS_2 thin films electrodes on FTO in an alkaline media. Ten consecutive LSV scans were recorded and presented in Figure 6.16. Contrary to observation of the enhancement in HER performance in acidic

media, the activity gradually decreased after each LSV scan in alkaline media. We note that the electrolyte near the electrode surface turned to blue in color during LSV cycles. Amorphous MoO_3 moiety in the mesoporous framework is probably electrochemically dissolved in alkaline media. Since the MoO_3 moiety plays a role of binding MoS_2 and MoS_3 moieties in the mesoporous framework, those active species in HER were detached from the electrode.

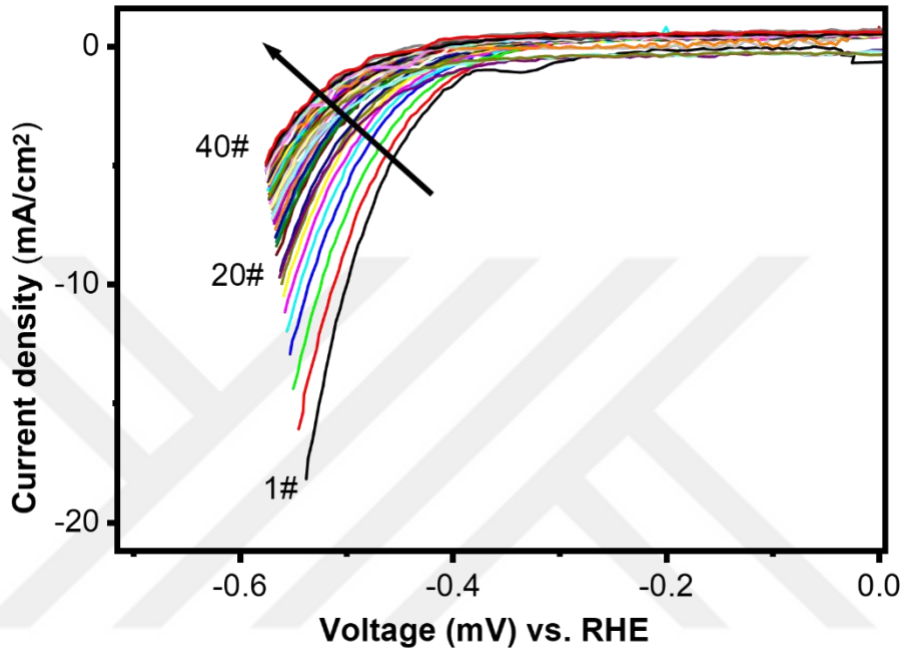

Figure 6.16 Consecutive LSV plots for mesoporous MoS_2 on FTO prepared at 300 ℃ in 1 M KOH.

6.6 General Overview

Active, durable, and abundant non-platinum group material (PGM) based electrocatalysts are crucial for green hydrogen production. MoS_2 has been one of the best candidates and most studied non-PGM electrocatalyst. Mesoporous thin-film materials also provide an ideal platform regarding improved charge transfer kinetics and reagent/product diffusion provided by their high surface area and integrated continuous nanostructure for the HER. We showed, for the first time, a novel protocol to produce mesoporous thin-film MoS_2 synthesized by a novel soft-templating method without post-sulfurization, as represented in the Figure 6.17a. The present results suggest that a mesoporous framework having a narrow pore size distribution form and consists of embedded MoS_2 nanocrystals within the continuous amorphous MoS_3 and MoO_3 moieties, as demonstrated in the Figure

6.17b. The samples exhibit superior HER activity in an acidic media after a structural transformation from MoS_3 to MoS_2 via an electrochemical reduction during HER. In-situ electrochemical activation boosts the ECSA and reduce the Tafel slopes, leading to lower overpotential and better kinetics for HER. These outcome the increases durable sulfur terminated edges of MoS_2 as HER active sites.

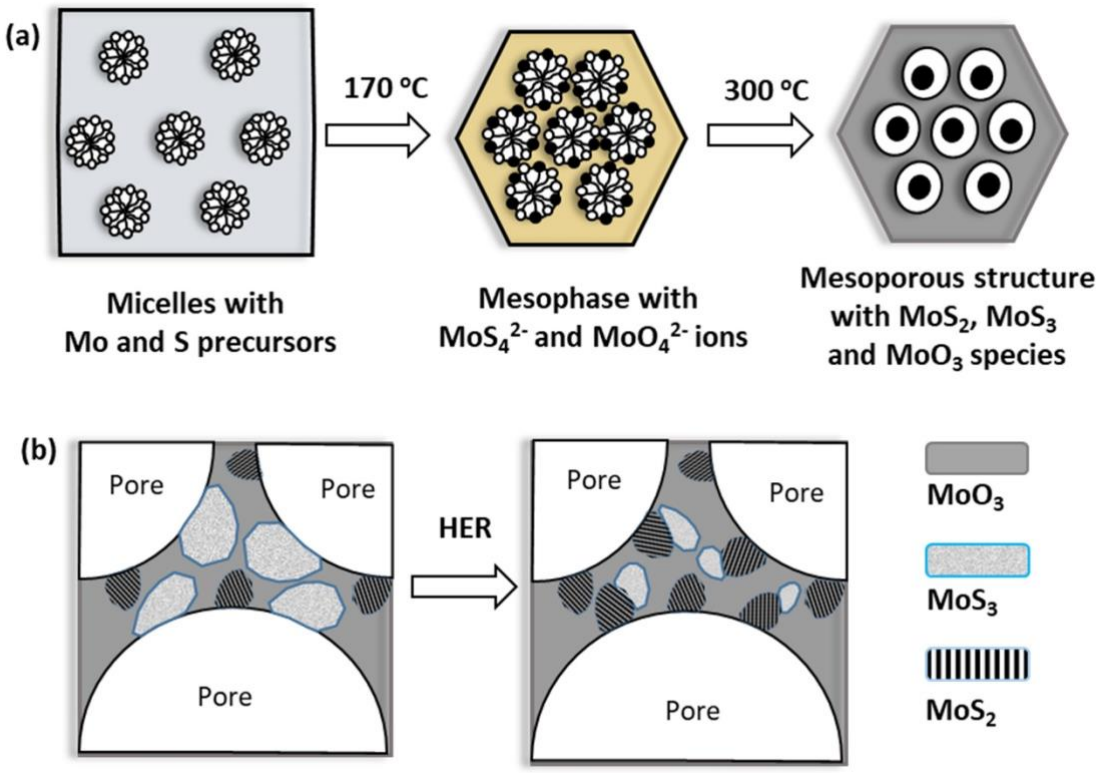

Figure 6.17 (a) The schematic diagram of the liquid templating method for mesoporous MoS_2 (b) and in-situ structural transformation during HER.

7 CONCLUSION

In this thesis, the soft templating strategy was developed and optimized to fabricate the mesoporous thin films for water reduction and oxidation.

The lyotropic liquid crystalline templating method was modified by the inclusion of sulfur precursor for obtaining mesoporous metal sulfides. It has been found that the lyotropic liquid crystalline mesophase of nickel nitrate salt with CTAB and $C_{12}EO_{10}$ can uptake the thiourea intact up to twice the mole of nickel salt. The composition and phase of mesoporous nickel sulfides was dependent on the annealing temperature and the mole ratio of precursors of Ni and S. The low annealing temperature of mesophase (<200 ^{o}C) result in the formation of mesoporous pyrite NiS_2 thin-film electrodes with ultra-thin pore walls and high surface area. The surfactant was easily removed by washing it in water. Further annealing mesoporous NiS_2 (>300 ^{O}C) transformed into mesoporous NiS. The decomposition of surfactants into carboneous materials creates mesopores. Decreasing sulfur precursor content and annealing at high temperatures produce NiS_7, Ni_3S_2 and mixed of them with NiS phase according to Ni/S content.

HER activities of mesoporous nickel sulfides were investigated for in both acidic and alkaline electrolyte. It has been found that nickel sulfides in acidic media undergoes instant dissolution and show the short-term HER activities. In addition, we reveal that nickel sulfides electrolyte under HER conditions in alkaline are electrochemically reduced. We compared the compositional changes under negative bias and related HER activities of mesoporous NiS_2 with other NiS_2 previously reported in the literature. The mesoporous NiS_2 displays superior HER activity in alkaline media after a preconditioning step that results in sulfur leaching, amorphization of the surface and collapse of the mesoporous structure. However, non-mesoporous NiS_2 structures ultimately reduces to metallic nickel, yielding a low HER activity.

Mesoporous nickel sulfides are also not stable in alkaline media for OER. They are converted to non-porous $Ni(OH)_2$ under anodic bias. We applied the lyotropic liquid crystalline strategy to fabricate mesoporous iron nickel oxide thin films for OER. We tuned the phase, composition, crystallinity of mesoporous iron nickel oxide. The trace content of iron yields mesoporous Fe-doped NiO and higher content of Fe promotes the formation $NiFe_2O_4$. We examined the OER activities of various phase and composition

of mesoporous iron nickel oxide, including neat NiO and Fe_2O_3. The OER activity trend follows $NiFeO_x$ > $NiFe_2O_4$ > NiO > Fe_2O_3.

A facile one-step soft templating method was developed to synthesize mesoporous molybdenum sulfide-oxide composite thin-film electrocatalysts directly on any substrate without using a binder or a template. Fabricated electrocatalysts contain amorphous MoS_3 and small crystallite-sized MoS_2 embedded into amorphous MoO_3 with a large surface area (around 182 m^2/g). The electrocatalyst layer undergoes in-situ electrochemical activation in which amorphous MoS_3 is reduced to MoS_2 during HER in acidic media. The electrocatalyst layer on the carbon fiber exhibits a low overpotential (~189 mV at 10 mA/cm^2) and Tafel slope (53 mV/dec.) towards HER after electrochemical activation.

In summary, we developed a facile one-step soft templating method to fabricate several electrocatalysts directly on any substrate without using a binder or a template for electrolyzers operating in both alkaline and acidic electrolytes. As future works;

- Mesoporous iron nickel oxide thin-film electrocatalysts further may be improved by doping with other transition metals such as Co, Mn and etc.
- Mesoporous molybdenum sulfide-oxide composite thin-film electrocatalysts further may be improved by doping with high valance atoms (W) and depositing on high surface are carbon support.

REFERENCES

[1] "Hydrogen: A renewable energy perspective," p. 52.

[2] H. Topsøe, B. S. Clausen, and F. E. Massoth, "Hydrotreating Catalysis," in *Catalysis: Science and Technology*, J. R. Anderson and M. Boudart, Eds. Berlin, Heidelberg: Springer, 1996, pp. 1–269. doi: 10.1007/978-3-642-61040-0_1.

[3] A. Vojvodic *et al.*, "Exploring the limits: A low-pressure, low-temperature Haber–Bosch process," *Chemical Physics Letters*, vol. 598, pp. 108–112, Apr. 2014, doi: 10.1016/j.cplett.2014.03.003.

[4] X.-M. Liu, G. Q. Lu, Z.-F. Yan, and J. Beltramini, "Recent Advances in Catalysts for Methanol Synthesis via Hydrogenation of CO and CO2," *Ind. Eng. Chem. Res.*, vol. 42, no. 25, pp. 6518–6530, Dec. 2003, doi: 10.1021/ie020979s.

[5] R. Yukesh Kannah *et al.*, "Techno-economic assessment of various hydrogen production methods – A review," *Bioresource Technology*, vol. 319, p. 124175, Jan. 2021, doi: 10.1016/j.biortech.2020.124175.

[6] G. Kakoulaki, I. Kougias, N. Taylor, F. Dolci, J. Moya, and A. Jäger-Waldau, "Green hydrogen in Europe – A regional assessment: Substituting existing production with electrolysis powered by renewables," *Energy Conversion and Management*, vol. 228, p. 113649, Jan. 2021, doi: 10.1016/j.enconman.2020.113649.

[7] S. Atilhan, S. Park, M. M. El-Halwagi, M. Atilhan, M. Moore, and R. B. Nielsen, "Green hydrogen as an alternative fuel for the shipping industry," *Current Opinion in Chemical Engineering*, vol. 31, p. 100668, Mar. 2021, doi: 10.1016/j.coche.2020.100668.

[8] S. Fawzy, A. I. Osman, J. Doran, and D. W. Rooney, "Strategies for mitigation of climate change: a review," *Environ Chem Lett*, vol. 18, no. 6, pp. 2069–2094, Nov. 2020, doi: 10.1007/s10311-020-01059-w.

[9] "Data & Statistics," *IEA*. https://www.iea.org/data-and-statistics (accessed May 03, 2021).

[10] D. Guo *et al.*, "Kinetics and mechanisms of direct reduction of iron ore-biomass composite pellets with hydrogen gas," *International Journal of Hydrogen Energy*, vol. 40, no. 14, pp. 4733–4740, Apr. 2015, doi: 10.1016/j.ijhydene.2015.02.065.

[11] E. S. Sanz-Pérez, C. R. Murdock, S. A. Didas, and C. W. Jones, "Direct Capture of CO2 from Ambient Air," *Chem. Rev.*, vol. 116, no. 19, pp. 11840–11876, Oct. 2016, doi: 10.1021/acs.chemrev.6b00173.

[12] Z. P. Cano *et al.*, "Batteries and fuel cells for emerging electric vehicle markets," *Nature Energy*, vol. 3, no. 4, Art. no. 4, Apr. 2018, doi: 10.1038/s41560-018-0108-1.

[13] E. Rivard, M. Trudeau, and K. Zaghib, "Hydrogen Storage for Mobility: A Review," *Materials*, vol. 12, no. 12, Art. no. 12, Jan. 2019, doi: 10.3390/ma12121973.

[14] P. Colbertaldo, S. B. Agustin, S. Campanari, and J. Brouwer, "Impact of hydrogen energy storage on California electric power system: Towards 100% renewable electricity," *International Journal of Hydrogen Energy*, vol. 44, no. 19, pp. 9558–9576, Apr. 2019, doi: 10.1016/j.ijhydene.2018.11.062.

[15] "Renewables 2020 – Analysis," *IEA*. https://www.iea.org/reports/renewables-2020 (accessed May 03, 2021).

[16] "Reaching Zero with Renewables," */publications/2020/Sep/Reaching-Zero-with-Renewables*. /publications/2020/Sep/Reaching-Zero-with-Renewables (accessed May 03, 2021).

[17] N.-T. Suen, S.-F. Hung, Q. Quan, N. Zhang, Y.-J. Xu, and H. M. Chen, "Electrocatalysis for the oxygen evolution reaction: recent development and future

perspectives," *Chem. Soc. Rev.*, vol. 46, no. 2, pp. 337–365, Jan. 2017, doi: 10.1039/C6CS00328A.
[18] P. C. K. Vesborg, B. Seger, and I. Chorkendorff, "Recent Development in Hydrogen Evolution Reaction Catalysts and Their Practical Implementation," *J. Phys. Chem. Lett.*, vol. 6, no. 6, pp. 951–957, Mar. 2015, doi: 10.1021/acs.jpclett.5b00306.
[19] J. O. Bockris and E. C. Potter, "The Mechanism of the Cathodic Hydrogen Evolution Reaction," *J. Electrochem. Soc.*, vol. 99, no. 4, p. 169, Apr. 1952, doi: 10.1149/1.2779692.
[20] M. Zeng and Y. Li, "Recent advances in heterogeneous electrocatalysts for the hydrogen evolution reaction," *J. Mater. Chem. A*, vol. 3, no. 29, pp. 14942–14962, Jul. 2015, doi: 10.1039/C5TA02974K.
[21] M. A. Khan *et al.*, "Recent Progresses in Electrocatalysts for Water Electrolysis," *Electrochem. Energ. Rev.*, vol. 1, no. 4, pp. 483–530, Dec. 2018, doi: 10.1007/s41918-018-0014-z.
[22] J. K. Nørskov *et al.*, "Trends in the Exchange Current for Hydrogen Evolution," *J. Electrochem. Soc.*, vol. 152, no. 3, p. J23, Jan. 2005, doi: 10.1149/1.1856988.
[23] "Hydrogénations et déshydrogénations par catalyse - Sabatier - 1911 - Berichte der deutschen chemischen Gesellschaft - Wiley Online Library." https://chemistry-europe.onlinelibrary.wiley.com/doi/abs/10.1002/cber.19110440303 (accessed May 04, 2021).
[24] S. Shiva Kumar and V. Himabindu, "Hydrogen production by PEM water electrolysis – A review," *Materials Science for Energy Technologies*, vol. 2, no. 3, pp. 442–454, Dec. 2019, doi: 10.1016/j.mset.2019.03.002.
[25] M. David, C. Ocampo-Martínez, and R. Sánchez-Peña, "Advances in alkaline water electrolyzers: A review," *Journal of Energy Storage*, vol. 23, pp. 392–403, Jun. 2019, doi: 10.1016/j.est.2019.03.001.
[26] D. M. Soares, O. Teschke, and I. Torriani, "Hydride Effect on the Kinetics of the Hydrogen Evolution Reaction on Nickel Cathodes in Alkaline Media," *J. Electrochem. Soc.*, vol. 139, no. 1, p. 98, Jan. 1992, doi: 10.1149/1.2069207.
[27] S. Anantharaj, S. R. Ede, K. Sakthikumar, K. Karthick, S. Mishra, and S. Kundu, "Recent Trends and Perspectives in Electrochemical Water Splitting with an Emphasis on Sulfide, Selenide, and Phosphide Catalysts of Fe, Co, and Ni: A Review," *ACS Catal.*, vol. 6, no. 12, pp. 8069–8097, Dec. 2016, doi: 10.1021/acscatal.6b02479.
[28] R. Kötz and S. Stucki, "Stabilization of RuO2 by IrO2 for anodic oxygen evolution in acid media," *Electrochimica Acta*, vol. 31, no. 10, pp. 1311–1316, Oct. 1986, doi: 10.1016/0013-4686(86)80153-0.
[29] S. Cherevko, "Stability and dissolution of electrocatalysts: Building the bridge between model and 'real world' systems," *Current Opinion in Electrochemistry*, vol. 8, pp. 118–125, Mar. 2018, doi: 10.1016/j.coelec.2018.03.034.
[30] J. Song *et al.*, "A review on fundamentals for designing oxygen evolution electrocatalysts," *Chemical Society Reviews*, vol. 49, no. 7, pp. 2196–2214, 2020, doi: 10.1039/C9CS00607A.
[31] T. Y. Ma, S. Dai, and S. Z. Qiao, "Self-supported electrocatalysts for advanced energy conversion processes," *Materials Today*, vol. 19, no. 5, pp. 265–273, Jun. 2016, doi: 10.1016/j.mattod.2015.10.012.
[32] F. Cheng and J. Chen, "Metal–air batteries: from oxygen reduction electrochemistry to cathode catalysts," *Chem. Soc. Rev.*, vol. 41, no. 6, pp. 2172–2192, Feb. 2012, doi: 10.1039/C1CS15228A.

[33] J. Wang, H. Zhong, Y. Qin, and X. Zhang, “An Efficient Three-Dimensional Oxygen Evolution Electrode,” *Angewandte Chemie International Edition*, vol. 52, no. 20, pp. 5248–5253, 2013, doi: https://doi.org/10.1002/anie.201301066.
[34] D. H. Everett, “Manual of Symbols and Terminology for Physicochemical Quantities and Units, Appendix II: Definitions, Terminology and Symbols in Colloid and Surface Chemistry,” *Pure and Applied Chemistry*, vol. 31, no. 4, pp. 577–638, Sep. 1972, doi: 10.1351/pac197231040577.
[35] C. T. Kresge, M. E. Leonowicz, W. J. Roth, J. C. Vartuli, and J. S. Beck, “Ordered mesoporous molecular sieves synthesized by a liquid-crystal template mechanism,” *Nature*, vol. 359, no. 6397, Art. no. 6397, Oct. 1992, doi: 10.1038/359710a0.
[36] H. Yang, A. Kuperman, N. Coombs, S. Mamiche-Afara, and G. A. Ozin, “Synthesis of oriented films of mesoporous silica on mica,” *Nature*, vol. 379, no. 6567, Art. no. 6567, Feb. 1996, doi: 10.1038/379703a0.
[37] D. Zhao, Q. Huo, J. Feng, B. F. Chmelka, and G. D. Stucky, “Nonionic Triblock and Star Diblock Copolymer and Oligomeric Surfactant Syntheses of Highly Ordered, Hydrothermally Stable, Mesoporous Silica Structures,” *J. Am. Chem. Soc.*, vol. 120, no. 24, pp. 6024–6036, Jun. 1998, doi: 10.1021/ja974025i.
[38] D. Zhao *et al.*, “Triblock Copolymer Syntheses of Mesoporous Silica with Periodic 50 to 300 Angstrom Pores,” *Science*, vol. 279, no. 5350, pp. 548–552, Jan. 1998, doi: 10.1126/science.279.5350.548.
[39] L. Mahoney and R. T. Koodali, “Versatility of Evaporation-Induced Self-Assembly (EISA) Method for Preparation of Mesoporous TiO2 for Energy and Environmental Applications,” *Materials*, vol. 7, no. 4, Art. no. 4, Apr. 2014, doi: 10.3390/ma7042697.
[40] M.-W. Xu, D.-D. Zhao, S.-J. Bao, and H.-L. Li, “Mesoporous amorphous MnO2 as electrode material for supercapacitor,” *J Solid State Electrochem*, vol. 11, no. 8, pp. 1101–1107, May 2007, doi: 10.1007/s10008-006-0246-4.
[41] Y. Li, B. Tan, and Y. Wu, “Mesoporous Co3O4 Nanowire Arrays for Lithium Ion Batteries with High Capacity and Rate Capability,” *Nano Lett.*, vol. 8, no. 1, pp. 265–270, Jan. 2008, doi: 10.1021/nl0725906.
[42] R. M. Rioux, H. Song, J. D. Hoefelmeyer, P. Yang, and G. A. Somorjai, “High-Surface-Area Catalyst Design: Synthesis, Characterization, and Reaction Studies of Platinum Nanoparticles in Mesoporous SBA-15 Silica,” *J. Phys. Chem. B*, vol. 109, no. 6, pp. 2192–2202, Feb. 2005, doi: 10.1021/jp048867x.
[43] “Liquid-crystalline phases as templates for the synthesis of mesoporous silica | Nature.” https://www.nature.com/articles/378366a0 (accessed May 03, 2021).
[44] P. Innocenzi and L. Malfatti, “Mesoporous thin films: properties and applications,” *Chemical Society Reviews*, vol. 42, no. 9, pp. 4198–4216, 2013, doi: 10.1039/C3CS35377J.
[45] H. J. Lee, K. K. Park, M. Kupnik, N. A. Melosh, and B. T. Khuri-Yakub, “Mesoporous Thin-Film on Highly-Sensitive Resonant Chemical Sensor for Relative Humidity and CO2 Detection,” *Anal. Chem.*, vol. 84, no. 7, pp. 3063–3066, Apr. 2012, doi: 10.1021/ac300225c.
[46] C. Karakaya *et al.*, “Mesoporous Thin-Film NiS2 as an Idealized Pre-Electrocatalyst for a Hydrogen Evolution Reaction,” *ACS Catal.*, vol. 10, no. 24, pp. 15114–15122, Dec. 2020, doi: 10.1021/acscatal.0c03094.
[47] J. Kibsgaard, T. R. Hellstern, S.-J. Choi, B. N. Reinecke, and T. F. Jaramillo, “Mesoporous Ruthenium/Ruthenium Oxide Thin Films: Active Electrocatalysts for the Oxygen Evolution Reaction,” *ChemElectroChem*, vol. 4, no. 10, pp. 2480–2485, 2017, doi: https://doi.org/10.1002/celc.201700334.

[48] H. J. Lee, J. Bang, J. Park, S. Kim, and S.-M. Park, “Multilayered Semiconductor (CdS/CdSe/ZnS)-Sensitized TiO2 Mesoporous Solar Cells: All Prepared by Successive Ionic Layer Adsorption and Reaction Processes,” *Chem. Mater.*, vol. 22, no. 19, pp. 5636–5643, Oct. 2010, doi: 10.1021/cm102024s.

[49] C. J. Brinker, Y. Lu, A. Sellinger, and H. Fan, “Evaporation-Induced Self-Assembly: Nanostructures Made Easy,” *Advanced Materials*, vol. 11, no. 7, pp. 579–585, 1999, doi: https://doi.org/10.1002/(SICI)1521-4095(199905)11:7<579::AID-ADMA579>3.0.CO;2-R.

[50] D. Gu and F. Schüth, “Synthesis of non-siliceous mesoporous oxides,” *Chem. Soc. Rev.*, vol. 43, no. 1, pp. 313–344, Dec. 2013, doi: 10.1039/C3CS60155B.

[51] X. Deng, K. Chen, and H. Tüysüz, “Protocol for the Nanocasting Method: Preparation of Ordered Mesoporous Metal Oxides,” *Chem. Mater.*, vol. 29, no. 1, pp. 40–52, Jan. 2017, doi: 10.1021/acs.chemmater.6b02645.

[52] A.-H. Lu and F. Schüth, “Nanocasting: A Versatile Strategy for Creating Nanostructured Porous Materials,” *Advanced Materials*, vol. 18, no. 14, pp. 1793–1805, 2006, doi: https://doi.org/10.1002/adma.200600148.

[53] Y. Deng, J. Wei, Z. Sun, and D. Zhao, “Large-pore ordered mesoporous materials templated from non-Pluronic amphiphilic block copolymers,” *Chem. Soc. Rev.*, vol. 42, no. 9, pp. 4054–4070, Apr. 2013, doi: 10.1039/C2CS35426H.

[54] K. Zhu, B. Yue, W. Zhou, and H. He, “Preparation of three-dimensional chromium oxide porous single crystals templated by SBA-15,” *Chem. Commun.*, no. 1, pp. 98–99, Jan. 2003, doi: 10.1039/B210065G.

[55] A. Rumplecker, F. Kleitz, E.-L. Salabas, and F. Schüth, “Hard Templating Pathways for the Synthesis of Nanostructured Porous Co3O4,” *Chem. Mater.*, vol. 19, no. 3, pp. 485–496, Feb. 2007, doi: 10.1021/cm0610635.

[56] H. Kim and J. Cho, “Hard templating synthesis of mesoporous and nanowire SnO 2 lithium battery anode materials,” *Journal of Materials Chemistry*, vol. 18, no. 7, pp. 771–775, 2008, doi: 10.1039/B714904B.

[57] J. S. Beck *et al.*, “A new family of mesoporous molecular sieves prepared with liquid crystal templates,” *J. Am. Chem. Soc.*, vol. 114, no. 27, pp. 10834–10843, Dec. 1992, doi: 10.1021/ja00053a020.

[58] P. Yang, D. Zhao, D. I. Margolese, B. F. Chmelka, and G. D. Stucky, “Generalized syntheses of large-pore mesoporous metal oxides with semicrystalline frameworks,” *Nature*, vol. 396, no. 6707, Art. no. 6707, Nov. 1998, doi: 10.1038/24132.

[59] D. Grosso *et al.*, “Fundamentals of Mesostructuring Through Evaporation-Induced Self-Assembly,” *Advanced Functional Materials*, vol. 14, no. 4, pp. 309–322, 2004, doi: https://doi.org/10.1002/adfm.200305036.

[60] C. Karakaya, Y. Türker, C. Albayrak, and Ö. Dag, “Assembly of Molten Transition Metal Salt–Surfactant in a Confined Space for the Synthesis of Mesoporous Metal Oxide-Rich Metal Oxide–Silica Thin Films,” *Chem. Mater.*, vol. 23, no. 12, pp. 3062–3071, Jun. 2011, doi: 10.1021/cm200932k.

[61] I. Karakaya, F. Karadas, B. Ulgut, and Ö. Dag, “Modification of Mesoporous LiMn2O4 and LiMn2−xCoxO4 by SILAR Method for Highly Efficient Water Oxidation Electrocatalysis,” *Advanced Materials Technologies*, vol. 5, no. 8, p. 2000353, 2020, doi: https://doi.org/10.1002/admt.202000353.

[62] Ö. Çelik and Ö. Dag, “A New Lyotropic Liquid Crystalline System: Oligo(ethylene oxide) Surfactants with [M(H2O)n]Xm Transition Metal Complexes,” *Angewandte Chemie International Edition*, vol. 40, no. 20, pp. 3799–3803, 2001, doi: https://doi.org/10.1002/1521-3773(20011015)40:20<3799::AID-ANIE3799>3.0.CO;2-I.

[63] C. Albayrak, A. M. Soylu, and Ö. Dag, “Lyotropic Liquid-Crystalline Mesophases of [Zn(H2O)6](NO3)2−C12EO10−CTAB−H2O and [Zn(H2O)6](NO3)2−C12EO10−SDS−H2O Systems,” *Langmuir*, vol. 24, no. 19, pp. 10592–10595, Oct. 2008, doi: 10.1021/la8022453.

[64] A. Amirzhanova *et al.*, “Synthesis and water oxidation electrocatalytic and electrochromic behaviours of mesoporous nickel oxide thin film electrodes,” *Journal of Materials Chemistry A*, vol. 7, no. 38, pp. 22012–22020, 2019, doi: 10.1039/C9TA07693J.

[65] A. Amirzhanova, N. Akmanşen, I. Karakaya, and Ö. Dag, “Mesoporous MnCo2O4, NiCo2O4, and ZnCo2O4 Thin-Film Electrodes as Electrocatalysts for the Oxygen Evolution Reaction in Alkaline Solutions,” *ACS Appl. Energy Mater.*, vol. 4, no. 3, pp. 2769–2785, Mar. 2021, doi: 10.1021/acsaem.1c00064.

[66] F. Mert Balci *et al.*, “Synthesis of mesoporous LiMn 2 O 4 and LiMn 2−x Co x O 4 thin films using the MASA approach as efficient water oxidation electrocatalysts,” *Journal of Materials Chemistry A*, vol. 6, no. 28, pp. 13925–13933, 2018, doi: 10.1039/C8TA04138E.

[67] X. Xu, W. Liu, Y. Kim, and J. Cho, “Nanostructured transition metal sulfides for lithium ion batteries: Progress and challenges,” *Nano Today*, vol. 9, no. 5, pp. 604–630, Oct. 2014, doi: 10.1016/j.nantod.2014.09.005.

[68] R. Miao *et al.*, “Mesoporous Iron Sulfide for Highly Efficient Electrocatalytic Hydrogen Evolution,” *J. Am. Chem. Soc.*, vol. 139, no. 39, pp. 13604–13607, Oct. 2017, doi: 10.1021/jacs.7b07044.

[69] E. Rodríguez-Castellón, A. Jiménez-López, and D. Eliche-Quesada, “Nickel and cobalt promoted tungsten and molybdenum sulfide mesoporous catalysts for hydrodesulfurization,” *Fuel*, vol. 87, no. 7, pp. 1195–1206, Jun. 2008, doi: 10.1016/j.fuel.2007.07.020.

[70] H. Yang *et al.*, “Trimetallic Sulfide Mesoporous Nanospheres as Superior Electrocatalysts for Rechargeable Zn–Air Batteries,” *Advanced Energy Materials*, vol. 8, no. 34, p. 1801839, 2018, doi: https://doi.org/10.1002/aenm.201801839.

[71] J. Ding, B. Hong, Z. Luo, S. Sun, J. Bao, and C. Gao, “Mesoporous Monoclinic CaIn2S4 with Surface Nanostructure: An Efficient Photocatalyst for Hydrogen Production under Visible Light,” *J. Phys. Chem. C*, vol. 118, no. 48, pp. 27690–27697, Dec. 2014, doi: 10.1021/jp508497a.

[72] B. T. Yonemoto, G. S. Hutchings, and F. Jiao, “A General Synthetic Approach for Ordered Mesoporous Metal Sulfides,” *J. Am. Chem. Soc.*, vol. 136, no. 25, pp. 8895–8898, Jun. 2014, doi: 10.1021/ja504407e.

[73] Y. Shi, Y. Wan, R. Liu, B. Tu, and D. Zhao, “Synthesis of Highly Ordered Mesoporous Crystalline WS2 and MoS2 via a High-Temperature Reductive Sulfuration Route,” *J. Am. Chem. Soc.*, vol. 129, no. 30, pp. 9522–9531, Aug. 2007, doi: 10.1021/ja072910n.

[74] J. Kibsgaard, Z. Chen, B. N. Reinecke, and T. F. Jaramillo, “Engineering the surface structure of MoS 2 to preferentially expose active edge sites for electrocatalysis,” *Nature Materials*, vol. 11, no. 11, Art. no. 11, Nov. 2012, doi: 10.1038/nmat3439.

[75] Y. Türker, C. Karakaya, and Ö. Dag, “Fabrication of Mesoporous Metal Chalcogenide Nanoflake Silica Thin Films and Spongy Mesoporous CdS and CdSe,” *Chemistry – A European Journal*, vol. 18, no. 12, pp. 3695–3705, 2012, doi: https://doi.org/10.1002/chem.201102643.

[76] J. B. Cook *et al.*, “Mesoporous MoS2 as a Transition Metal Dichalcogenide Exhibiting Pseudocapacitive Li and Na-Ion Charge Storage,” *Advanced Energy*

Materials, vol. 6, no. 9, p. 1501937, 2016, doi: https://doi.org/10.1002/aenm.201501937.

[77] J. C. Ondry, S. Robbennolt, H. Kang, Y. Yan, and S. H. Tolbert, "A Room-Temperature, Solution Phase Method for the Synthesis of Mesoporous Metal Chalcogenide Nanocrystal-Based Thin Films with Precisely Controlled Grain Sizes," *Chem. Mater.*, vol. 28, no. 17, pp. 6105–6117, Sep. 2016, doi: 10.1021/acs.chemmater.6b01681.

[78] I. Vamvasakis, K. S. Subrahmanyam, M. G. Kanatzidis, and G. S. Armatas, "Template-Directed Assembly of Metal–Chalcogenide Nanocrystals into Ordered Mesoporous Networks," *ACS Nano*, vol. 9, no. 4, pp. 4419–4426, Apr. 2015, doi: 10.1021/acsnano.5b01014.

[79] Y. Guo *et al.*, "Mesoporous Iron-doped MoS2/CoMo2S4 Heterostructures through Organic–Metal Cooperative Interactions on Spherical Micelles for Electrochemical Water Splitting," *ACS Nano*, vol. 14, no. 4, pp. 4141–4152, Apr. 2020, doi: 10.1021/acsnano.9b08904.

[80] L. B. McCusker, F. Liebau, and G. Engelhardt, "Nomenclature of structural and compositional characteristics of ordered microporous and mesoporous materials with inorganic hosts(IUPAC Recommendations 2001)," *Pure and Applied Chemistry*, vol. 73, no. 2, pp. 381–394, Jan. 2001, doi: 10.1351/pac200173020381.

[81] C. T. Kresge, M. E. Leonowicz, W. J. Roth, J. C. Vartuli, and J. S. Beck, "Ordered mesoporous molecular sieves synthesized by a liquid-crystal template mechanism," *Nature*, vol. 359, no. 6397, Art. no. 6397, Oct. 1992, doi: 10.1038/359710a0.

[82] B. T. Yonemoto, G. S. Hutchings, and F. Jiao, "A General Synthetic Approach for Ordered Mesoporous Metal Sulfides," *J. Am. Chem. Soc.*, vol. 136, no. 25, pp. 8895–8898, Jun. 2014, doi: 10.1021/ja504407e.

[83] B. Tian, J. Lei, and J. Wang, "Polyoxometalate–Surfactant Hybrids Directed Assembly of Ni3S2 into Hollow Microsphere as Pt-Comparable Electrocatalyst for Hydrogen Evolution Reaction in Alkaline Medium," *ACS Appl. Mater. Interfaces*, vol. 9, no. 46, pp. 40162–40170, Nov. 2017, doi: 10.1021/acsami.7b09634.

[84] I. Roger, M. A. Shipman, and M. D. Symes, "Earth-abundant catalysts for electrochemical and photoelectrochemical water splitting," *Nature Reviews Chemistry*, vol. 1, no. 1, pp. 1–13, Jan. 2017, doi: 10.1038/s41570-016-0003.

[85] M. A. Lukowski, A. S. Daniel, F. Meng, A. Forticaux, L. Li, and S. Jin, "Enhanced Hydrogen Evolution Catalysis from Chemically Exfoliated Metallic MoS2 Nanosheets," *J. Am. Chem. Soc.*, vol. 135, no. 28, pp. 10274–10277, Jul. 2013, doi: 10.1021/ja404523s.

[86] T. F. Jaramillo, K. P. Jørgensen, J. Bonde, J. H. Nielsen, S. Horch, and I. Chorkendorff, "Identification of Active Edge Sites for Electrochemical H2 Evolution from MoS2 Nanocatalysts," *Science*, vol. 317, no. 5834, pp. 100–102, Jul. 2007, doi: 10.1126/science.1141483.

[87] D. Kong, J. J. Cha, H. Wang, H. R. Lee, and Y. Cui, "First-row transition metal dichalcogenide catalysts for hydrogen evolution reaction," *Energy Environ. Sci.*, vol. 6, no. 12, pp. 3553–3558, Nov. 2013, doi: 10.1039/C3EE42413H.

[88] N. Jiang, Q. Tang, M. Sheng, B. You, D. Jiang, and Y. Sun, "Nickel sulfides for electrocatalytic hydrogen evolution under alkaline conditions: a case study of crystalline NiS, NiS2, and Ni3S2 nanoparticles," *Catal. Sci. Technol.*, vol. 6, no. 4, pp. 1077–1084, Feb. 2016, doi: 10.1039/C5CY01111F.

[89] J. Xie *et al.*, "Controllable Disorder Engineering in Oxygen-Incorporated MoS2 Ultrathin Nanosheets for Efficient Hydrogen Evolution," *J. Am. Chem. Soc.*, vol. 135, no. 47, pp. 17881–17888, Nov. 2013, doi: 10.1021/ja408329q.

[90] B. Hinnemann *et al.*, “Biomimetic Hydrogen Evolution: MoS2 Nanoparticles as Catalyst for Hydrogen Evolution,” *J. Am. Chem. Soc.*, vol. 127, no. 15, pp. 5308–5309, Apr. 2005, doi: 10.1021/ja0504690.
[91] D.-Y. Wang *et al.*, “Highly Active and Stable Hybrid Catalyst of Cobalt-Doped FeS2 Nanosheets–Carbon Nanotubes for Hydrogen Evolution Reaction,” *J. Am. Chem. Soc.*, vol. 137, no. 4, pp. 1587–1592, Feb. 2015, doi: 10.1021/ja511572q.
[92] Y. Sun *et al.*, “Electrodeposited Cobalt-Sulfide Catalyst for Electrochemical and Photoelectrochemical Hydrogen Generation from Water,” *J. Am. Chem. Soc.*, vol. 135, no. 47, pp. 17699–17702, Nov. 2013, doi: 10.1021/ja4094764.
[93] M. S. Faber, M. A. Lukowski, Q. Ding, N. S. Kaiser, and S. Jin, “Earth-Abundant Metal Pyrites (FeS2, CoS2, NiS2, and Their Alloys) for Highly Efficient Hydrogen Evolution and Polysulfide Reduction Electrocatalysis,” *J. Phys. Chem. C*, vol. 118, no. 37, pp. 21347–21356, Sep. 2014, doi: 10.1021/jp506288w.
[94] D. Kong, H. Wang, Z. Lu, and Y. Cui, “CoSe2 Nanoparticles Grown on Carbon Fiber Paper: An Efficient and Stable Electrocatalyst for Hydrogen Evolution Reaction,” *J. Am. Chem. Soc.*, vol. 136, no. 13, pp. 4897–4900, Apr. 2014, doi: 10.1021/ja501497n.
[95] H. Wang *et al.*, “MoSe2 and WSe2 Nanofilms with Vertically Aligned Molecular Layers on Curved and Rough Surfaces,” *Nano Lett.*, vol. 13, no. 7, pp. 3426–3433, Jul. 2013, doi: 10.1021/nl401944f.
[96] C. Tang, N. Cheng, Z. Pu, W. Xing, and X. Sun, “NiSe Nanowire Film Supported on Nickel Foam: An Efficient and Stable 3D Bifunctional Electrode for Full Water Splitting,” *Angewandte Chemie International Edition*, vol. 54, no. 32, pp. 9351–9355, 2015, doi: 10.1002/anie.201503407.
[97] H. Zhou *et al.*, “Outstanding hydrogen evolution reaction catalyzed by porous nickel diselenide electrocatalysts,” *Energy Environ. Sci.*, vol. 10, no. 6, pp. 1487–1492, Jun. 2017, doi: 10.1039/C7EE00802C.
[98] Z. Zou, X. Wang, J. Huang, Z. Wu, and F. Gao, “An Fe-doped nickel selenide nanorod/nanosheet hierarchical array for efficient overall water splitting,” *J. Mater. Chem. A*, vol. 7, no. 5, pp. 2233–2241, Jan. 2019, doi: 10.1039/C8TA11072G.
[99] R. Kumar *et al.*, “Uniformly Decorated Molybdenum Carbide/Nitride Nanostructures on Biomass Templates for Hydrogen Evolution Reaction Applications,” *ACS Omega*, vol. 4, no. 9, pp. 14155–14161, Aug. 2019, doi: 10.1021/acsomega.9b02321.
[100] N. Han, P. Liu, J. Jiang, L. Ai, Z. Shao, and S. Liu, “Recent advances in nanostructured metal nitrides for water splitting,” *J. Mater. Chem. A*, vol. 6, no. 41, pp. 19912–19933, Oct. 2018, doi: 10.1039/C8TA06529B.
[101] B. Cao, G. M. Veith, J. C. Neuefeind, R. R. Adzic, and P. G. Khalifah, “Mixed Close-Packed Cobalt Molybdenum Nitrides as Non-noble Metal Electrocatalysts for the Hydrogen Evolution Reaction,” *J. Am. Chem. Soc.*, vol. 135, no. 51, pp. 19186–19192, Dec. 2013, doi: 10.1021/ja4081056.
[102] M. Cabán-Acevedo *et al.*, “Efficient hydrogen evolution catalysis using ternary pyrite-type cobalt phosphosulphide,” *Nature Materials*, vol. 14, no. 12, Art. no. 12, Dec. 2015, doi: 10.1038/nmat4410.
[103] E. J. Popczun *et al.*, “Nanostructured Nickel Phosphide as an Electrocatalyst for the Hydrogen Evolution Reaction,” *J. Am. Chem. Soc.*, vol. 135, no. 25, pp. 9267–9270, Jun. 2013, doi: 10.1021/ja403440e.
[104] Q. Liu *et al.*, “Carbon Nanotubes Decorated with CoP Nanocrystals: A Highly Active Non-Noble-Metal Nanohybrid Electrocatalyst for Hydrogen Evolution,”

Angewandte Chemie International Edition, vol. 53, no. 26, pp. 6710–6714, 2014, doi: 10.1002/anie.201404161.

[105] J. F. Callejas *et al.*, "Electrocatalytic and Photocatalytic Hydrogen Production from Acidic and Neutral-pH Aqueous Solutions Using Iron Phosphide Nanoparticles," *ACS Nano*, vol. 8, no. 11, pp. 11101–11107, Nov. 2014, doi: 10.1021/nn5048553.

[106] E. J. Popczun, C. G. Read, C. W. Roske, N. S. Lewis, and R. E. Schaak, "Highly Active Electrocatalysis of the Hydrogen Evolution Reaction by Cobalt Phosphide Nanoparticles," *Angewandte Chemie International Edition*, vol. 53, no. 21, pp. 5427–5430, 2014, doi: 10.1002/anie.201402646.

[107] J.-T. Ren, L. Chen, C.-C. Weng, G.-G. Yuan, and Z.-Y. Yuan, "Well-Defined Mo2C Nanoparticles Embedded in Porous N-Doped Carbon Matrix for Highly Efficient Electrocatalytic Hydrogen Evolution," *ACS Appl. Mater. Interfaces*, vol. 10, no. 39, pp. 33276–33286, Oct. 2018, doi: 10.1021/acsami.8b12108.

[108] W.-F. Chen, J. T. Muckerman, and E. Fujita, "Recent developments in transition metal carbides and nitrides as hydrogen evolution electrocatalysts," *Chem. Commun.*, vol. 49, no. 79, pp. 8896–8909, Sep. 2013, doi: 10.1039/C3CC44076A.

[109] X. Xu, F. Nosheen, and X. Wang, "Ni-Decorated Molybdenum Carbide Hollow Structure Derived from Carbon-Coated Metal–Organic Framework for Electrocatalytic Hydrogen Evolution Reaction," *Chem. Mater.*, vol. 28, no. 17, pp. 6313–6320, Sep. 2016, doi: 10.1021/acs.chemmater.6b02586.

[110] P. C. K. Vesborg, B. Seger, and I. Chorkendorff, "Recent Development in Hydrogen Evolution Reaction Catalysts and Their Practical Implementation," *J. Phys. Chem. Lett.*, vol. 6, no. 6, pp. 951–957, Mar. 2015, doi: 10.1021/acs.jpclett.5b00306.

[111] J. Mohammed-Ibrahim and X. Sun, "Recent progress on earth abundant electrocatalysts for hydrogen evolution reaction (HER) in alkaline medium to achieve efficient water splitting – A review," *Journal of Energy Chemistry*, vol. 34, pp. 111–160, Jul. 2019, doi: 10.1016/j.jechem.2018.09.016.

[112] Q. Ma *et al.*, "Identifying the electrocatalytic sites of nickel disulfide in alkaline hydrogen evolution reaction," *Nano Energy*, vol. 41, pp. 148–153, Nov. 2017, doi: 10.1016/j.nanoen.2017.09.036.

[113] L.-L. Feng *et al.*, "High-Index Faceted Ni3S2 Nanosheet Arrays as Highly Active and Ultrastable Electrocatalysts for Water Splitting," *J. Am. Chem. Soc.*, vol. 137, no. 44, pp. 14023–14026, Nov. 2015, doi: 10.1021/jacs.5b08186.

[114] Y. Li *et al.*, "Facile Dynamic Synthesis of Homodispersed Ni3S2 Nanosheets as a High-Efficient Bifunctional Electrocatalyst for Water Splitting," *ChemCatChem*, vol. 11, no. 4, pp. 1320–1327, Feb. 2019, doi: 10.1002/cctc.201801960.

[115] T. A. Ho *et al.*, "Metallic Ni3S2 Films Grown by Atomic Layer Deposition as an Efficient and Stable Electrocatalyst for Overall Water Splitting," *ACS Appl. Mater. Interfaces*, vol. 10, no. 15, pp. 12807–12815, Apr. 2018, doi: 10.1021/acsami.8b00813.

[116] D. Zhang *et al.*, "Ni3S2 nanowires grown on nickel foam as an efficient bifunctional electrocatalyst for water splitting with greatly practical prospects," *Nanotechnology*, vol. 29, no. 24, p. 245402, Apr. 2018, doi: 10.1088/1361-6528/aab6ff.

[117] S. Surendran and R. K. Selvan, "Growth and Characterization of 3D Flower-Like β-NiS on Carbon Cloth: A Dexterous and Flexible Multifunctional Electrode for Supercapattery and Water-Splitting Applications," *Advanced Materials Interfaces*, vol. 5, no. 4, p. 1701056, 2018, doi: 10.1002/admi.201701056.

[118] D. Siegmund, N. Blanc, M. Smialkowski, K. Tschulik, and U.-P. Apfel, “Metal-Rich Chalcogenides for Electrocatalytic Hydrogen Evolution: Activity of Electrodes and Bulk Materials,” *ChemElectroChem*, vol. 7, no. 7, pp. 1514–1527, 2020, doi: 10.1002/celc.201902125.
[119] B. Yan, D. Krishnamurthy, C. H. Hendon, S. Deshpande, Y. Surendranath, and V. Viswanathan, “Surface Restructuring of Nickel Sulfide Generates Optimally Coordinated Active Sites for Oxygen Reduction Catalysis,” *Joule*, vol. 1, no. 3, pp. 600–612, Nov. 2017, doi: 10.1016/j.joule.2017.08.020.
[120] S. Anantharaj, S. R. Ede, K. Sakthikumar, K. Karthick, S. Mishra, and S. Kundu, “Recent Trends and Perspectives in Electrochemical Water Splitting with an Emphasis on Sulfide, Selenide, and Phosphide Catalysts of Fe, Co, and Ni: A Review,” *ACS Catal.*, vol. 6, no. 12, pp. 8069–8097, Dec. 2016, doi: 10.1021/acscatal.6b02479.
[121] X. Long *et al.*, “Metallic Iron–Nickel Sulfide Ultrathin Nanosheets As a Highly Active Electrocatalyst for Hydrogen Evolution Reaction in Acidic Media,” *J. Am. Chem. Soc.*, vol. 137, no. 37, pp. 11900–11903, Sep. 2015, doi: 10.1021/jacs.5b07728.
[122] Y. Ge *et al.*, “Insight into the hydrogen evolution reaction of nickel dichalcogenide nanosheets: activities related to non-metal ligands,” *Nanoscale*, vol. 9, no. 17, pp. 5538–5544, May 2017, doi: 10.1039/C6NR09977G.
[123] J. Staszak-Jirkovský *et al.*, “Design of active and stable Co–Mo–S x chalcogels as pH-universal catalysts for the hydrogen evolution reaction,” *Nature Materials*, vol. 15, no. 2, Art. no. 2, Feb. 2016, doi: 10.1038/nmat4481.
[124] I. Zegkinoglou *et al.*, “Operando Phonon Studies of the Protonation Mechanism in Highly Active Hydrogen Evolution Reaction Pentlandite Catalysts,” *J. Am. Chem. Soc.*, vol. 139, no. 41, pp. 14360–14363, Oct. 2017, doi: 10.1021/jacs.7b07902.
[125] X. Shang, B. Dong, Y.-M. Chai, and C.-G. Liu, “In-situ electrochemical activation designed hybrid electrocatalysts for water electrolysis,” *Science Bulletin*, vol. 63, no. 13, pp. 853–876, Jul. 2018, doi: 10.1016/j.scib.2018.05.014.
[126] Y. Zhu *et al.*, “Operando Unraveling of the Structural and Chemical Stability of P-Substituted CoSe2 Electrocatalysts toward Hydrogen and Oxygen Evolution Reactions in Alkaline Electrolyte,” *ACS Energy Lett.*, vol. 4, no. 4, pp. 987–994, Apr. 2019, doi: 10.1021/acsenergylett.9b00382.
[127] A. Goryachev *et al.*, “Stability of CoPx Electrocatalysts in Continuous and Interrupted Acidic Electrolysis of Water,” *ChemElectroChem*, vol. 5, no. 8, pp. 1230–1239, Apr. 2018, doi: 10.1002/celc.201701119.
[128] Q. Li, Z. Xing, D. Wang, X. Sun, and X. Yang, “In Situ Electrochemically Activated CoMn-S@NiO/CC Nanosheets Array for Enhanced Hydrogen Evolution,” *ACS Catal.*, vol. 6, no. 5, pp. 2797–2801, May 2016, doi: 10.1021/acscatal.6b00014.
[129] X. Shang *et al.*, “In situ cathodic activation of V-incorporated NixSy nanowires for enhanced hydrogen evolution,” *Nanoscale*, vol. 9, no. 34, pp. 12353–12363, Aug. 2017, doi: 10.1039/C7NR02867A.
[130] Y. Zhang, L. Gao, E. J. M. Hensen, and J. P. Hofmann, “Evaluating the Stability of Co2P Electrocatalysts in the Hydrogen Evolution Reaction for Both Acidic and Alkaline Electrolytes,” *ACS Energy Lett.*, vol. 3, no. 6, pp. 1360–1365, Jun. 2018, doi: 10.1021/acsenergylett.8b00514.
[131] W. Lu *et al.*, “In-Situ Transformed Ni, S-Codoped CoO from Amorphous Co–Ni Sulfide as an Efficient Electrocatalyst for Hydrogen Evolution in Alkaline Media,” *ACS Sustainable Chem. Eng.*, vol. 7, no. 14, pp. 12501–12509, Jul. 2019, doi: 10.1021/acssuschemeng.9b02216.

[132] L. He *et al.*, “Mesoporous Nanostructured CoFe–Se–P Composite Derived from a Prussian Blue Analogue as a Superior Electrocatalyst for Efficient Overall Water Splitting,” *ACS Appl. Energy Mater.*, vol. 1, no. 8, pp. 3915–3928, Aug. 2018, doi: 10.1021/acsaem.8b00663.
[133] Y. Jing *et al.*, “Mesoporous CoP Nanowire Arrays for Hydrogen Evolution,” *ACS Appl. Nano Mater.*, vol. 2, no. 9, pp. 5922–5930, Sep. 2019, doi: 10.1021/acsanm.9b01353.
[134] A. Wang *et al.*, “Integration of Theory and Experiment on Mesoporous Nickel Sulfide Microsphere for Hydrogen Evolution Reaction,” *ACS Sustainable Chem. Eng.*, vol. 6, no. 12, pp. 15995–16000, Dec. 2018, doi: 10.1021/acssuschemeng.8b04148.
[135] K. An, X. Xu, and X. Liu, “Mo2C-Based Electrocatalyst with Biomass-Derived Sulfur and Nitrogen Co-Doped Carbon as a Matrix for Hydrogen Evolution and Organic Pollutant Removal,” *ACS Sustainable Chem. Eng.*, vol. 6, no. 1, pp. 1446–1455, Jan. 2018, doi: 10.1021/acssuschemeng.7b03882.
[136] R. Miao *et al.*, “Mesoporous Iron Sulfide for Highly Efficient Electrocatalytic Hydrogen Evolution,” *J. Am. Chem. Soc.*, vol. 139, no. 39, pp. 13604–13607, Oct. 2017, doi: 10.1021/jacs.7b07044.
[137] L. Huo, B. Liu, G. Zhang, and J. Zhang, “Universal Strategy to Fabricate a Two-Dimensional Layered Mesoporous Mo2C Electrocatalyst Hybridized on Graphene Sheets with High Activity and Durability for Hydrogen Generation,” *ACS Appl. Mater. Interfaces*, vol. 8, no. 28, pp. 18107–18118, Jul. 2016, doi: 10.1021/acsami.6b05007.
[138] A. Wang, M. Zhang, H. Li, F. Wu, K. Yan, and J. Xiao, “Combination of Theory and Experiment Achieving a Rational Design of Electrocatalysts for Hydrogen Evolution on the Hierarchically Mesoporous CoS2 Microsphere,” *J. Phys. Chem. C*, vol. 123, no. 22, pp. 13428–13433, Jun. 2019, doi: 10.1021/acs.jpcc.9b01814.
[139] T. Tian, L. Huang, L. Ai, and J. Jiang, “Surface anion-rich NiS2 hollow microspheres derived from metal–organic frameworks as a robust electrocatalyst for the hydrogen evolution reaction,” *J. Mater. Chem. A*, vol. 5, no. 39, pp. 20985–20992, Oct. 2017, doi: 10.1039/C7TA06671F.
[140] J. Wang *et al.*, “NiS2 nanosheet array: A high-active bifunctional electrocatalyst for hydrazine oxidation and water reduction toward energy-efficient hydrogen production,” *Materials Today Energy*, vol. 3, pp. 9–14, Mar. 2017, doi: 10.1016/j.mtener.2017.02.002.
[141] P. Luo *et al.*, “Targeted Synthesis of Unique Nickel Sulfide (NiS, NiS2) Microarchitectures and the Applications for the Enhanced Water Splitting System,” *ACS Appl. Mater. Interfaces*, vol. 9, no. 3, pp. 2500–2508, Jan. 2017, doi: 10.1021/acsami.6b13984.
[142] H. Liu *et al.*, “Electronic Structure Reconfiguration toward Pyrite NiS2 via Engineered Heteroatom Defect Boosting Overall Water Splitting,” *ACS Nano*, vol. 11, no. 11, pp. 11574–11583, Nov. 2017, doi: 10.1021/acsnano.7b06501.
[143] Q. Ma *et al.*, “Identifying the electrocatalytic sites of nickel disulfide in alkaline hydrogen evolution reaction,” *Nano Energy*, vol. 41, no. June, pp. 148–153, 2017, doi: 10.1016/j.nanoen.2017.09.036.
[144] F. de Groot, A. Kotani, and A. Kotani, *Core Level Spectroscopy of Solids*. CRC Press, 2008. doi: 10.1201/9781420008425.
[145] H. W. Nesbitt, D. Legrand, and G. M. Bancroft, “Interpretation of Ni2p XPS spectra of Ni conductors and Ni insulators,” *Phys Chem Min*, vol. 27, no. 5, pp. 357–366, May 2000, doi: 10.1007/s002690050265.

[146] B. R. Wygant, K. Kawashima, and C. B. Mullins, “Catalyst or Precatalyst? The Effect of Oxidation on Transition Metal Carbide, Pnictide, and Chalcogenide Oxygen Evolution Catalysts,” *ACS Energy Letters*, Nov. 2018, doi: 10.1021/acsenergylett.8b01774.

[147] L.-F. Huang, M. J. Hutchison, R. J. Santucci, J. R. Scully, and J. M. Rondinelli, “Improved Electrochemical Phase Diagrams from Theory and Experiment: The Ni–Water System and Its Complex Compounds,” *J. Phys. Chem. C*, vol. 121, no. 18, pp. 9782–9789, May 2017, doi: 10.1021/acs.jpcc.7b02771.

[148] N.-T. Suen, S.-F. Hung, Q. Quan, N. Zhang, Y.-J. Xu, and H. M. Chen, “Electrocatalysis for the oxygen evolution reaction: recent development and future perspectives,” *Chem. Soc. Rev.*, vol. 46, no. 2, pp. 337–365, Jan. 2017, doi: 10.1039/C6CS00328A.

[149] C. Feng, M. B. Faheem, J. Fu, Y. Xiao, C. Li, and Y. Li, “Fe-Based Electrocatalysts for Oxygen Evolution Reaction: Progress and Perspectives,” *ACS Catal.*, vol. 10, no. 7, pp. 4019–4047, Apr. 2020, doi: 10.1021/acscatal.9b05445.

[150] T. Reier, M. Oezaslan, and P. Strasser, “Electrocatalytic Oxygen Evolution Reaction (OER) on Ru, Ir, and Pt Catalysts: A Comparative Study of Nanoparticles and Bulk Materials,” *ACS Catal.*, vol. 2, no. 8, pp. 1765–1772, Aug. 2012, doi: 10.1021/cs3003098.

[151] Y. Lee, J. Suntivich, K. J. May, E. E. Perry, and Y. Shao-Horn, “Synthesis and Activities of Rutile IrO2 and RuO2 Nanoparticles for Oxygen Evolution in Acid and Alkaline Solutions,” *J. Phys. Chem. Lett.*, vol. 3, no. 3, pp. 399–404, Feb. 2012, doi: 10.1021/jz2016507.

[152] R. Frydendal *et al.*, “Benchmarking the Stability of Oxygen Evolution Reaction Catalysts: The Importance of Monitoring Mass Losses,” *ChemElectroChem*, vol. 1, no. 12, pp. 2075–2081, 2014, doi: 10.1002/celc.201402262.

[153] C. C. L. McCrory, S. Jung, J. C. Peters, and T. F. Jaramillo, “Benchmarking Heterogeneous Electrocatalysts for the Oxygen Evolution Reaction,” *J. Am. Chem. Soc.*, vol. 135, no. 45, pp. 16977–16987, Nov. 2013, doi: 10.1021/ja407115p.

[154] H.-W. Man *et al.*, “Tailored transition metal-doped nickel phosphide nanoparticles for the electrochemical oxygen evolution reaction (OER),” *Chemical Communications*, vol. 54, no. 62, pp. 8630–8633, 2018, doi: 10.1039/C8CC03870H.

[155] J. Chen *et al.*, “Metal–Organic Framework-Derived CoxFe1–xP Nanoparticles Encapsulated in N-Doped Carbon as Efficient Bifunctional Electrocatalysts for Overall Water Splitting,” *ACS Appl. Energy Mater.*, vol. 2, no. 4, pp. 2734–2742, Apr. 2019, doi: 10.1021/acsaem.9b00065.

[156] Y.-J. Tang, L. You, and K. Zhou, “Enhanced Oxygen Evolution Reaction Activity of a Co2P@NC–Fe2P Composite Boosted by Interfaces Between a N-Doped Carbon Matrix and Fe2P Microspheres,” *ACS Appl. Mater. Interfaces*, vol. 12, no. 23, pp. 25884–25894, Jun. 2020, doi: 10.1021/acsami.0c04902.

[157] L. Trotochaud, J. K. Ranney, K. N. Williams, and S. W. Boettcher, “Solution-Cast Metal Oxide Thin Film Electrocatalysts for Oxygen Evolution,” *J. Am. Chem. Soc.*, vol. 134, no. 41, pp. 17253–17261, Oct. 2012, doi: 10.1021/ja307507a.

[158] J. Zhao, J.-J. Zhang, Z.-Y. Li, and X.-H. Bu, “Recent Progress on NiFe-Based Electrocatalysts for the Oxygen Evolution Reaction,” *Small*, vol. 16, no. 51, p. 2003916, 2020, doi: 10.1002/smll.202003916.

[159] K. Fominykh *et al.*, “Iron-Doped Nickel Oxide Nanocrystals as Highly Efficient Electrocatalysts for Alkaline Water Splitting,” *ACS Nano*, vol. 9, no. 5, pp. 5180–5188, May 2015, doi: 10.1021/acsnano.5b00520.

[160] C. Roy *et al.*, “Impact of nanoparticle size and lattice oxygen on water oxidation on NiFeOxHy,” *Nat Catal*, vol. 1, no. 11, pp. 820–829, Nov. 2018, doi: 10.1038/s41929-018-0162-x.
[161] B. Zhang *et al.*, “Homogeneously dispersed multimetal oxygen-evolving catalysts,” *Science*, vol. 352, no. 6283, pp. 333–337, Apr. 2016, doi: 10.1126/science.aaf1525.
[162] F. Dionigi *et al.*, “In-situ structure and catalytic mechanism of NiFe and CoFe layered double hydroxides during oxygen evolution,” *Nat Commun*, vol. 11, no. 1, p. 2522, May 2020, doi: 10.1038/s41467-020-16237-1.
[163] E. Fabbri *et al.*, “Dynamic surface self-reconstruction is the key of highly active perovskite nano-electrocatalysts for water splitting,” *Nature Mater*, vol. 16, no. 9, pp. 925–931, Sep. 2017, doi: 10.1038/nmat4938.
[164] M. Risch *et al.*, “Structural Changes of Cobalt-Based Perovskites upon Water Oxidation Investigated by EXAFS,” *J. Phys. Chem. C*, vol. 117, no. 17, pp. 8628–8635, May 2013, doi: 10.1021/jp3126768.
[165] P. Chen *et al.*, “Atomically Dispersed Iron–Nitrogen Species as Electrocatalysts for Bifunctional Oxygen Evolution and Reduction Reactions,” *Angewandte Chemie International Edition*, vol. 56, no. 2, pp. 610–614, 2017, doi: 10.1002/anie.201610119.
[166] G. S. Shanker and S. Ogale, “Faceted Colloidal Metallic Ni3N Nanocrystals: Size-Controlled Solution-Phase Synthesis and Electrochemical Overall Water Splitting,” *ACS Appl. Energy Mater.*, vol. 4, no. 3, pp. 2165–2173, Mar. 2021, doi: 10.1021/acsaem.0c02674.
[167] O. Mabayoje, A. Shoola, B. R. Wygant, and C. B. Mullins, “The Role of Anions in Metal Chalcogenide Oxygen Evolution Catalysis: Electrodeposited Thin Films of Nickel Sulfide as ‘Pre-catalysts,’” *ACS Energy Lett.*, vol. 1, no. 1, pp. 195–201, Jul. 2016, doi: 10.1021/acsenergylett.6b00084.
[168] M. S. Burke, M. G. Kast, L. Trotochaud, A. M. Smith, and S. W. Boettcher, “Cobalt–Iron (Oxy)hydroxide Oxygen Evolution Electrocatalysts: The Role of Structure and Composition on Activity, Stability, and Mechanism,” *J. Am. Chem. Soc.*, vol. 137, no. 10, pp. 3638–3648, Mar. 2015, doi: 10.1021/jacs.5b00281.
[169] C. C. L. McCrory, S. Jung, I. M. Ferrer, S. M. Chatman, J. C. Peters, and T. F. Jaramillo, “Benchmarking Hydrogen Evolving Reaction and Oxygen Evolving Reaction Electrocatalysts for Solar Water Splitting Devices,” *J. Am. Chem. Soc.*, vol. 137, no. 13, pp. 4347–4357, Apr. 2015, doi: 10.1021/ja510442p.
[170] D. Friebel *et al.*, “Identification of Highly Active Fe Sites in (Ni,Fe)OOH for Electrocatalytic Water Splitting,” *J. Am. Chem. Soc.*, vol. 137, no. 3, pp. 1305–1313, Jan. 2015, doi: 10.1021/ja511559d.
[171] J. Kibsgaard and I. Chorkendorff, “Considerations for the scaling-up of water splitting catalysts,” *Nat Energy*, vol. 4, no. 6, pp. 430–433, Jun. 2019, doi: 10.1038/s41560-019-0407-1.
[172] J. Zhao, J.-J. Zhang, Z.-Y. Li, and X.-H. Bu, “Recent Progress on NiFe-Based Electrocatalysts for the Oxygen Evolution Reaction,” *Small*, vol. 16, no. 51, p. 2003916, 2020, doi: 10.1002/smll.202003916.
[173] D. A. Corrigan, “The Catalysis of the Oxygen Evolution Reaction by Iron Impurities in Thin Film Nickel Oxide Electrodes,” *J. Electrochem. Soc.*, vol. 134, no. 2, p. 377, Feb. 1987, doi: 10.1149/1.2100463.
[174] J. D. Michael, E. L. Demeter, S. M. Illes, Q. Fan, J. R. Boes, and J. R. Kitchin, “Alkaline Electrolyte and Fe Impurity Effects on the Performance and Active-Phase

Structure of NiOOH Thin Films for OER Catalysis Applications," *J. Phys. Chem. C*, vol. 119, no. 21, pp. 11475–11481, May 2015, doi: 10.1021/acs.jpcc.5b02458.
[175] M. W. Louie and A. T. Bell, "An Investigation of Thin-Film Ni–Fe Oxide Catalysts for the Electrochemical Evolution of Oxygen," *J. Am. Chem. Soc.*, vol. 135, no. 33, pp. 12329–12337, Aug. 2013, doi: 10.1021/ja405351s.
[176] L. Trotochaud, S. L. Young, J. K. Ranney, and S. W. Boettcher, "Nickel–Iron Oxyhydroxide Oxygen-Evolution Electrocatalysts: The Role of Intentional and Incidental Iron Incorporation," *J. Am. Chem. Soc.*, vol. 136, no. 18, pp. 6744–6753, May 2014, doi: 10.1021/ja502379c.
[177] H. Jiang, Q. He, Y. Zhang, and L. Song, "Structural Self-Reconstruction of Catalysts in Electrocatalysis," *Acc. Chem. Res.*, vol. 51, no. 11, pp. 2968–2977, Nov. 2018, doi: 10.1021/acs.accounts.8b00449.
[178] T. Binninger *et al.*, "Thermodynamic explanation of the universal correlation between oxygen evolution activity and corrosion of oxide catalysts," *Sci Rep*, vol. 5, no. 1, p. 12167, Jul. 2015, doi: 10.1038/srep12167.
[179] E. Fabbri and T. J. Schmidt, "Oxygen Evolution Reaction—The Enigma in Water Electrolysis," *ACS Catal.*, vol. 8, no. 10, pp. 9765–9774, Oct. 2018, doi: 10.1021/acscatal.8b02712.
[180] D. Y. Chung *et al.*, "Dynamic stability of active sites in hydr(oxy)oxides for the oxygen evolution reaction," *Nat Energy*, vol. 5, no. 3, pp. 222–230, Mar. 2020, doi: 10.1038/s41560-020-0576-y.
[181] Y. Feng, H. Zhang, L. Fang, Y. Mu, and Y. Wang, "Uniquely Monodispersing NiFe Alloyed Nanoparticles in Three-Dimensional Strongly Linked Sandwiched Graphitized Carbon Sheets for High-Efficiency Oxygen Evolution Reaction," *ACS Catal.*, vol. 6, no. 7, pp. 4477–4485, Jul. 2016, doi: 10.1021/acscatal.6b00481.
[182] J. Y. C. Chen *et al.*, "Operando Analysis of NiFe and Fe Oxyhydroxide Electrocatalysts for Water Oxidation: Detection of Fe4+ by Mössbauer Spectroscopy," *J. Am. Chem. Soc.*, vol. 137, no. 48, pp. 15090–15093, Dec. 2015, doi: 10.1021/jacs.5b10699.
[183] Y.-F. Li and A. Selloni, "Mechanism and Activity of Water Oxidation on Selected Surfaces of Pure and Fe-Doped NiOx," *ACS Catal.*, vol. 4, no. 4, pp. 1148–1153, Apr. 2014, doi: 10.1021/cs401245q.
[184] J. R. Varcoe *et al.*, "Anion-exchange membranes in electrochemical energy systems," *Energy & Environmental Science*, vol. 7, no. 10, pp. 3135–3191, 2014, doi: 10.1039/C4EE01303D.
[185] D. Li *et al.*, "Highly quaternized polystyrene ionomers for high performance anion exchange membrane water electrolysers," *Nat Energy*, vol. 5, no. 5, pp. 378–385, May 2020, doi: 10.1038/s41560-020-0577-x.
[186] H. Sun, Z. Yan, F. Liu, W. Xu, F. Cheng, and J. Chen, "Self-Supported Transition-Metal-Based Electrocatalysts for Hydrogen and Oxygen Evolution," *Advanced Materials*, vol. 32, no. 3, p. 1806326, 2020, doi: 10.1002/adma.201806326.
[187] W. Ma *et al.*, "A Superlattice of Alternately Stacked Ni–Fe Hydroxide Nanosheets and Graphene for Efficient Splitting of Water," *ACS Nano*, vol. 9, no. 2, pp. 1977–1984, Feb. 2015, doi: 10.1021/nn5069836.
[188] X. Lu and C. Zhao, "Electrodeposition of hierarchically structured three-dimensional nickel–iron electrodes for efficient oxygen evolution at high current densities," *Nat Commun*, vol. 6, no. 1, p. 6616, Mar. 2015, doi: 10.1038/ncomms7616.
[189] G. Zhang, Y. Li, Y. Zhou, and F. Yang, "NiFe Layered-Double-Hydroxide-Derived NiO-NiFe2O4/Reduced Graphene Oxide Architectures for Enhanced

Electrocatalysis of Alkaline Water Splitting," *ChemElectroChem*, vol. 3, no. 11, pp. 1927–1936, 2016, doi: 10.1002/celc.201600301.
[190] C. Dong, T. Kou, H. Gao, Z. Peng, and Z. Zhang, "Eutectic-Derived Mesoporous Ni-Fe-O Nanowire Network Catalyzing Oxygen Evolution and Overall Water Splitting," *Advanced Energy Materials*, vol. 8, no. 5, p. 1701347, 2018, doi: 10.1002/aenm.201701347.
[191] C. Karakaya, Y. Türker, and Ö. Dag, "Molten-Salt-Assisted Self-Assembly (MASA)-Synthesis of Mesoporous Metal Titanate-Titania, Metal Sulfide-Titania, and Metal Selenide-Titania Thin Films," *Advanced Functional Materials*, vol. 23, no. 32, pp. 4002–4010, 2013, doi: https://doi.org/10.1002/adfm.201202716.
[192] B. S. Yeo and A. T. Bell, "In Situ Raman Study of Nickel Oxide and Gold-Supported Nickel Oxide Catalysts for the Electrochemical Evolution of Oxygen," *J. Phys. Chem. C*, vol. 116, no. 15, pp. 8394–8400, Apr. 2012, doi: 10.1021/jp3007415.
[193] K. Fominykh *et al.*, "Iron-Doped Nickel Oxide Nanocrystals as Highly Efficient Electrocatalysts for Alkaline Water Splitting," *ACS Nano*, vol. 9, no. 5, pp. 5180–5188, May 2015, doi: 10.1021/acsnano.5b00520.
[194] X. Deng, D. C. Sorescu, I. Waluyo, A. Hunt, and D. R. Kauffman, "Bulk vs Intrinsic Activity of NiFeOx Electrocatalysts in the Oxygen Evolution Reaction: The Influence of Catalyst Loading, Morphology, and Support Material," *ACS Catal.*, vol. 10, no. 20, pp. 11768–11778, Oct. 2020, doi: 10.1021/acscatal.0c03109.
[195] N. Cheng *et al.*, "Platinum single-atom and cluster catalysis of the hydrogen evolution reaction," *Nat Commun*, vol. 7, no. 1, p. 13638, Nov. 2016, doi: 10.1038/ncomms13638.
[196] C. Roukoss, D. Laurenti, E. Devers, K. Marchand, L. Massin, and M. Vrinat, "Hydrodesulfurization catalysts: Promoters, promoting methods and support effect on catalytic activities," *Comptes Rendus Chimie*, vol. 12, no. 6, pp. 683–691, Jun. 2009, doi: 10.1016/j.crci.2008.10.018.
[197] B. Hinnemann *et al.*, "Biomimetic Hydrogen Evolution: MoS2 Nanoparticles as Catalyst for Hydrogen Evolution," *J. Am. Chem. Soc.*, vol. 127, no. 15, pp. 5308–5309, Apr. 2005, doi: 10.1021/ja0504690.
[198] T. F. Jaramillo, K. P. Jørgensen, J. Bonde, J. H. Nielsen, S. Horch, and I. Chorkendorff, "Identification of Active Edge Sites for Electrochemical H2 Evolution from MoS2 Nanocatalysts," *Science*, vol. 317, no. 5834, pp. 100–102, Jul. 2007, doi: 10.1126/science.1141483.
[199] "All The Catalytic Active Sites of MoS2 for Hydrogen Evolution | Journal of the American Chemical Society." https://pubs.acs.org/doi/10.1021/jacs.6b05940 (accessed Jul. 22, 2021).
[200] C. Lv *et al.*, "An Amorphous Noble-Metal-Free Electrocatalyst that Enables Nitrogen Fixation under Ambient Conditions," *Angewandte Chemie*, vol. 130, no. 21, pp. 6181–6184, 2018, doi: 10.1002/ange.201801538.
[201] D. Merki, S. Fierro, H. Vrubel, and X. Hu, "Amorphous molybdenum sulfide films as catalysts for electrochemical hydrogen production in water," *Chem. Sci.*, vol. 2, no. 7, pp. 1262–1267, Jun. 2011, doi: 10.1039/C1SC00117E.
[202] H. G. S. Casalongue *et al.*, "Operando Characterization of an Amorphous Molybdenum Sulfide Nanoparticle Catalyst during the Hydrogen Evolution Reaction," *J. Phys. Chem. C*, vol. 118, no. 50, pp. 29252–29259, Dec. 2014, doi: 10.1021/jp505394e.
[203] S. C. Lee *et al.*, "Chemical and Phase Evolution of Amorphous Molybdenum Sulfide Catalysts for Electrochemical Hydrogen Production," *ACS Nano*, vol. 10, no. 1, pp. 624–632, Jan. 2016, doi: 10.1021/acsnano.5b05652.

[204] Y. Yu, S.-Y. Huang, Y. Li, S. N. Steinmann, W. Yang, and L. Cao, "Layer-Dependent Electrocatalysis of MoS2 for Hydrogen Evolution," *Nano Lett.*, vol. 14, no. 2, pp. 553–558, Feb. 2014, doi: 10.1021/nl403620g.

[205] Z. Lv, N. Mahmood, M. Tahir, L. Pan, X. Zhang, and J.-J. Zou, "Fabrication of zero to three dimensional nanostructured molybdenum sulfides and their electrochemical and photocatalytic applications," *Nanoscale*, vol. 8, no. 43, pp. 18250–18269, Nov. 2016, doi: 10.1039/C6NR06836G.

[206] J. Ding, Y. Zhou, Y. Li, S. Guo, and X. Huang, "MoS2 Nanosheet Assembling Superstructure with a Three-Dimensional Ion Accessible Site: A New Class of Bifunctional Materials for Batteries and Electrocatalysis," *Chem. Mater.*, vol. 28, no. 7, pp. 2074–2080, Apr. 2016, doi: 10.1021/acs.chemmater.5b04815.

[207] X. Ren, L. Pang, Y. Zhang, X. Ren, H. Fan, and S. (Frank) Liu, "One-step hydrothermal synthesis of monolayer MoS2 quantum dots for highly efficient electrocatalytic hydrogen evolution," *J. Mater. Chem. A*, vol. 3, no. 20, pp. 10693–10697, May 2015, doi: 10.1039/C5TA02198G.

[208] B. Guo *et al.*, "Hollow Structured Micro/Nano MoS2 Spheres for High Electrocatalytic Activity Hydrogen Evolution Reaction," *ACS Appl. Mater. Interfaces*, vol. 8, no. 8, pp. 5517–5525, Mar. 2016, doi: 10.1021/acsami.5b10252.

[209] X. Ren, Q. Wei, P. Ren, Y. Wang, and R. Chen, "Synthesis of flower-like MoSe2@MoS2 nanocomposites as the high efficient water splitting electrocatalyst," *Materials Letters*, vol. 231, pp. 213–216, Nov. 2018, doi: 10.1016/j.matlet.2018.08.049.

[210] Y. Yan, B. Xia, X. Ge, Z. Liu, J.-Y. Wang, and X. Wang, "Ultrathin MoS2 Nanoplates with Rich Active Sites as Highly Efficient Catalyst for Hydrogen Evolution," *ACS Appl. Mater. Interfaces*, vol. 5, no. 24, pp. 12794–12798, Dec. 2013, doi: 10.1021/am404843b.

[211] Y. Cao, "Roadmap and Direction toward High-Performance MoS2 Hydrogen Evolution Catalysts," *ACS Nano*, Jul. 2021, doi: 10.1021/acsnano.1c01879.

[212] H. Zhu *et al.*, "S-rich single-layered MoS2 nanoplates embedded in N-doped carbon nanofibers: efficient co-electrocatalysts for the hydrogen evolution reaction," *Chem. Commun.*, vol. 50, no. 97, pp. 15435–15438, Nov. 2014, doi: 10.1039/C4CC06480A.

[213] Y. Guo, X. Zhang, X. Zhang, and T. You, "Defect- and S-rich ultrathin MoS2 nanosheet embedded N-doped carbon nanofibers for efficient hydrogen evolution," *J. Mater. Chem. A*, vol. 3, no. 31, pp. 15927–15934, Jul. 2015, doi: 10.1039/C5TA03766B.

[214] Y. Yan, B. Xia, N. Li, Z. Xu, A. Fisher, and X. Wang, "Vertically oriented MoS2 and WS2 nanosheets directly grown on carbon cloth as efficient and stable 3-dimensional hydrogen-evolving cathodes," *J. Mater. Chem. A*, vol. 3, no. 1, pp. 131–135, Dec. 2014, doi: 10.1039/C4TA04858J.

[215] N. Zhang, S. Gan, T. Wu, W. Ma, D. Han, and L. Niu, "Growth Control of MoS2 Nanosheets on Carbon Cloth for Maximum Active Edges Exposed: An Excellent Hydrogen Evolution 3D Cathode," *ACS Appl. Mater. Interfaces*, vol. 7, no. 22, pp. 12193–12202, Jun. 2015, doi: 10.1021/acsami.5b02586.

[216] Y.-H. Choi *et al.*, "An in Situ Sulfidation Approach for the Integration of MoS2 Nanosheets on Carbon Fiber Paper and the Modulation of Its Electrocatalytic Activity by Interfacing with nC60," *ACS Catal.*, vol. 6, no. 9, pp. 6246–6254, Sep. 2016, doi: 10.1021/acscatal.6b01942.

[217] H. Huang *et al.*, “Strongly coupled MoS2 nanoflake–carbon nanotube nanocomposite as an excellent electrocatalyst for hydrogen evolution reaction,” *J. Mater. Chem. A*, vol. 5, no. 4, pp. 1558–1566, Jan. 2017, doi: 10.1039/C6TA09612C.
[218] L. Liao *et al.*, “MoS2 Formed on Mesoporous Graphene as a Highly Active Catalyst for Hydrogen Evolution,” *Advanced Functional Materials*, vol. 23, no. 42, pp. 5326–5333, 2013, doi: 10.1002/adfm.201300318.
[219] C. Li *et al.*, “Flexible and free-standing hetero-electrocatalyst of high-valence-cation doped MoS2/MoO2/CNT foam with synergistically enhanced hydrogen evolution reaction catalytic activity,” *J. Mater. Chem. A*, vol. 8, no. 30, pp. 14944–14954, Aug. 2020, doi: 10.1039/D0TA02538K.
[220] G. Ye *et al.*, “Defects Engineered Monolayer MoS2 for Improved Hydrogen Evolution Reaction,” *Nano Lett.*, vol. 16, no. 2, pp. 1097–1103, Feb. 2016, doi: 10.1021/acs.nanolett.5b04331.
[221] S. Kang *et al.*, “Defect-engineered MoS2 with extended photoluminescence lifetime for high-performance hydrogen evolution,” *J. Mater. Chem. C*, vol. 7, no. 33, pp. 10173–10178, Aug. 2019, doi: 10.1039/C9TC02256B.
[222] Y. Kim *et al.*, “In Situ Electrochemical Activation of Atomic Layer Deposition Coated MoS2 Basal Planes for Efficient Hydrogen Evolution Reaction,” *Advanced Functional Materials*, vol. 27, no. 34, p. 1701825, 2017, doi: 10.1002/adfm.201701825.
[223] C. Tsai *et al.*, “Electrochemical generation of sulfur vacancies in the basal plane of MoS 2 for hydrogen evolution,” *Nat Commun*, vol. 8, no. 1, p. 15113, Apr. 2017, doi: 10.1038/ncomms15113.
[224] J. Wienold, R. E. Jentoft, and T. Ressler, “Structural Investigation of the Thermal Decomposition of Ammonium Heptamolybdate by in situ XAFS and XRD,” *European Journal of Inorganic Chemistry*, vol. 2003, no. 6, pp. 1058–1071, 2003, doi: 10.1002/ejic.200390138.
[225] H. W. Wang, P. Skeldon, and G. E. Thompson, “XPS studies of MoS2 formation from ammonium tetrathiomolybdate solutions,” *Surface and Coatings Technology*, vol. 91, no. 3, pp. 200–207, May 1997, doi: 10.1016/S0257-8972(96)03186-6.
[226] L. Wu, X. Wang, Y. Sun, Y. Liu, and J. Li, “Flawed MoO2 belts transformed from MoO3 on a graphene template for the hydrogen evolution reaction,” *Nanoscale*, vol. 7, no. 16, pp. 7040–7044, Apr. 2015, doi: 10.1039/C4NR06624C.
[227] J. O. Bockris and E. C. Potter, “The Mechanism of the Cathodic Hydrogen Evolution Reaction,” *J. Electrochem. Soc.*, vol. 99, no. 4, p. 169, Apr. 1952, doi: 10.1149/1.2779692.